TECHNICAL UNIVERSITY OF DENMARK

Mechanics of Ship Grounding

Bo Cerup Simonsen
February 1997

DEPARTMENT OF
NAVAL ARCHITECTURE
AND OFFSHORE ENGINEERING

Mechanics of Ship Grounding

by

Bo Cerup Simonsen
Department of Naval Architecture
and Offshore Engineering
Technical University of Denmark

February 1997

Department of Naval Architecture
and Offshore Engineering
Technical University of Denmark
DK-2800 Lyngby, Denmark
ISBN 87-89502-34-5

Preface

This thesis is submitted as a partial fulfilment of the requirements for the Danish PhD degree. The work has been performed at the Department of Naval Architecture and Offshore Engineering, the Technical University of Denmark, during the period of September 1993 to February 1997, including 6 months' leave of absence. Professor Preben Terndrup Pedersen supervised the study.

The work was supported financially by the Technical University of Denmark and this support is greatly acknowledged.

The friendly, stimulating and dynamic work environment provided by the Department of Naval Architecture and Offshore Engineering has been exemplary. Thanks to Preben Terndrup Pedersen for guidance through numerous invaluable discussions and for providing an inspiring work space with many degrees of freedom. Thanks to Jørgen Juncher Jensen and Peter Friis Hansen for several discussions and suggestions. Thanks to the secretaries Marianne, Vivi and Linda for technical help and for providing this world of male engineers with a scent of what they call real life. Thanks to the draughtsman Hugo for skillfully preparing many of the drawings. Thanks to Jan for assistance with computers. Thanks to fellow students for all their help and inspiration. Especially thanks to Hans Jørgen Riber for introducing me to some of the wonders in the world of sailing.

In a six months' period from January to June 1995, the studies were carried out at Massachusetts Institute of Technology (MIT) under supervision of Professor Tomasz Wierzbicki in the Joint MIT-Industry Program on Tanker Safety. As much as it was a period of intensive work, it was a time of great intellectual challenge and satisfaction - the stay at MIT was definitely a highlight in my eight years as a student. Much of the work concerning grounding on rocks was carried out or started at MIT together with Tomasz. Thanks for numerous very educational discussions and for introducing me so enthusiastically to the world of crashworthiness. Thanks to Tomasz and Margaret for their kind and generous hospitality and for showing me the mountains of New England and Switzerland. Thanks to Dorothea Franzosa for giving me a real home in Arlington with all that includes of food, shelter, neighbours, family and friendships.

Special thanks to friends, to my sister, mother and father and to Linda for continuous support and understanding of lack of time on many occasions.

All in all, having had the opportunity to work for three years with the most interesting research topic, in a pleasant and dynamic work environment, and with such capacities as Preben Terndrup Pedersen, Tomasz Wierzbicki, Wlodek Abramowicz, Frank McClintock, Jørgen Juncher Jensen, and Peter Friis Hansen, it would be impossible to feel anything but very privileged. Which I utterly do.

Bo Cerup Simonsen
Lyngby, February 28 1997

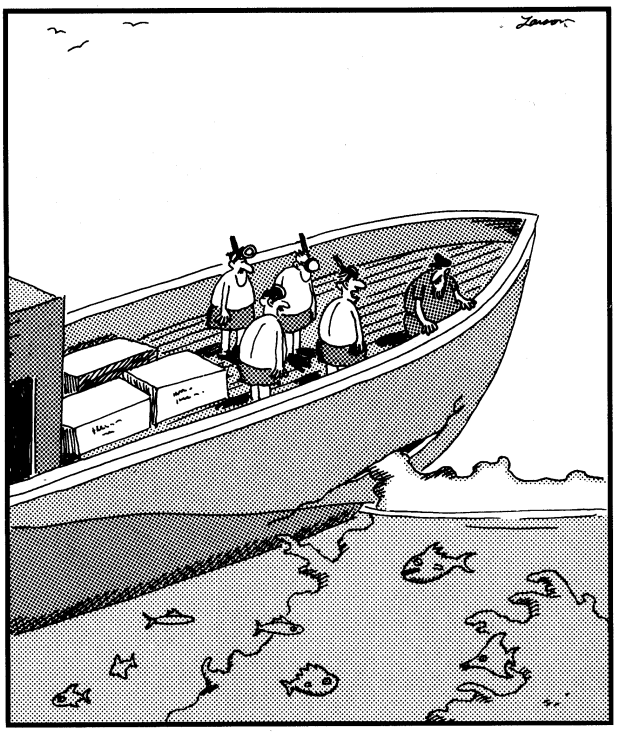

"Excuse me, Captain, but while we're waiting, would you like to join the crew and myself for a little snorkeling?"

Executive Summary

The objective of the present study has been to contribute to a rational basis for quantifying the consequences of ship grounding events. The covered main aspects are:

1. Establishment of a mathematical model for calculation of loads and hull girder response during grounding on a soft sea bed.

2. Establishment of a mathematical model for calculation of loads and hull girder response during grounding on a rock pinnacle.

In addition, a short study is presented of a theory for estimating the expected number of yearly grounding events in a certain area. A specific area in Denmark is investigated and good agreement is found between the calculated and the observed yearly number of grounding events.

The work concerning grounding on soft sea bottoms includes the following main aspects:

- Identification of the governing grounding mechanics. The hull girder is modelled as a linear elastic beam and the loads considered are gravity, hydrostatic pressure, hydrodynamic pressure and a ground reaction.

- Establishment of a model for the hydrodynamic loads which takes into account the generation of waves and shallow water effects.

- Establishment of a model for the ground response to the penetrating bow. Based on observations from laboratory experiments, the idea of this theoretical model is that the bow generates a flow of pore water in the soil. The pressure of the pore water on the bow becomes decisive for the soil reaction.

- Derivation of the governing equations for the hull girder based on the Timoshenko beam theory. The solution is found both by the finite element method and by a modal super-position approach and the results of the two approaches are shown to be equivalent.

- Verification of the model using the results of both laboratory tests at a scale of 1:60 and large scale grounding tests with a condemned fishing vessel.

- Investigation of the sectional forces compared to the strength of a VLCC in a grounding event on a soft sea bed. It is shown that the grounding-induced loads may well exceed the wave bending moment and shear force capacity of the hull girder. The effect of the hull flexibility is found to be important in a dynamic analysis because the flexible deformation of the hull girder unloads the grounding force and because the dynamic amplification of the sectional forces is significant for some grounding events. The effect of bow lift due to a receding tide is also investigated and it is shown that even a very smooth grounding event may lead to catastrophic failure if it is followed by a receding tide.

- Investigation of the grounding-induced loads compared to the strength of six different fast vessels built of steel, aluminium and fibre reinforced plastics. Grounding events of 40 knots are considered and it is shown that the hull girder strength and the grounding induced loads are of equal magnitude. Results also show that the softer the hull girder is, the smaller are the grounding induced sectional forces.

The work concerning grounding on a hard pinnacle type rock includes the following main aspects:

- Identification of the governing grounding mechanics. The grounding problem is divided into external dynamics (the global ship motion) and internal mechanics (the local response of the structure to the intruding rock). The basic approach of the internal mechanics is a type of upper bound method - i.e. from the energy dissipation rate of an assumed mode of deformation, the resistance force can be calculated. Friction, fracture and large plastic membrane and bending deformations are major basic phenomena to be depicted.

- Establishment of a model for the external dynamics. Based on time simulation of the ship motion, it is argued that the sway and yaw motion can be neglected. Then, from static equilibrium, the heave, roll and pitch motion is related to the vertical rock reaction and penetration. The surge motion is found from energy considerations.

- Investigation of the mechanics of steady-state cutting of a bare plate by a prismatic wedge. The extensive amount of literature on plate cutting is reviewed. A theoretical model is developed on the basis of an assumed mode of deformation with a crack tip zone, bending hinge lines and a zone of membrane deformation. Comparisons with three different experiments of plate cutting reveal a very good performance of the theory over a large range of cutting parameters.

- Establishment of a theory for the internal mechanics of an assembled ship bottom structure grounding on a conical rock with a rounded tip. The theory is based on a global assumed mode of deformation with compatibility between all structural members. Compared to most of the previous simplified approaches the methodology is very general, as all known ship bottom structures can be analysed. Major problems addressed and partially solved theoretically are: local plate deformation around the rock tip, frictional effects, fracture, resistance of bottom plating, resistance of longitudinal

girders, bulkheads and stiffeners and resistance of transverse frames and bulkheads. Several of the individual solutions are compared to experiments and good agreement is found.

- Comparison of the model for internal mechanics of an assembled ship bottom structure to the results of four large-scale grounding tests. Very good agreement is found as the discrepancy between measurements and theory is only in the order of 5 % for the energy absorption and 15 % for the penetration to fracture.

- Comparison of the results of the total grounding model with an accidental grounding event that happened on a reef in 1975. Uncertainties of the input data are discussed and there is shown to be very good agreement between calculated and observed damage. Calculation examples illustrate the necessity of taking proper account of the coupling between external dynamics and internal mechanics.

- A study of the energy absorption of the individual members in four different ship bottoms during a grounding event illustrates how steel can be used more or less effectively in terms of energy absorption.

Synopsis

Formålet med dette studium har været at bidrage til forståelsen af grundstødningers mekanik. Arbejdet er delt i to hovedområder:

1. Etablering af en matematisk model til bestemmelse af belastninger og skader under et skibs grundstødning på en (blød) sandbund.

2. Etablering af en matematisk model til bestemmelse af belastninger og skader under et skibs grundstødning på en klippegrund.

I tillæg præsenteres et kort studium af en teori til bestemmelse af det forventede årlige antal grundstødninger i et bestemt område. Et afgrænset område i Danmark undersøges, og der viser sig at være god overensstemmelse mellem beregnede og observerede antal grundstødninger.

De væsentligste aspekter i arbejdet vedrørende grundstødning på sandbund er:

- Identifikation af de væsentligste fysiske effekter. Skrogbjælken modelleres herefter som en lineært-elastisk Timoshenko bjælke, og de betragtede belastninger er gravitet, hydrostatisk tryk, hydrodynamisk tryk samt en reaktion fra grunden. Der ses bort fra effekter af bølger, propeller, ror, knusning af bov m.m.

- Etablering af en model til bestemmelse af de hydrodynamiske belastninger, under hensyntagen til dannelsen af bølger og lavtvandseffekter.

- Etablering af en model til bestemmelse af grundens reaktion på den indtrængende bov. Baseret på observationer fra modelforsøg er den grundlæggende ide, at boven genererer en porevandsstrømning i jorden. Trykket fra porevandet på boven viser sig at bidrage betydeligt til grundens kraft på boven.

- Udledning af de styrende ligninger for skrogbjælken baseret på Timoshenko bjælke-teori. Løsningen bestemmes både med finit-element metoden og med modal super position, og resultaterne af de to metoder vises at være ækvivalente.

- Verifikation af den teoretiske model ved hjælp af både model-forsøg i skala 1:60 samt stor skala forsøg med et fiskefartøj.

- Sammenligning af snitkræfter og styrke for en VLCC under en grundstødning. Det vises, at belastningerne induceret af en grundstødning kan overstige skrogbjælkens styrke. Skrogets fleksibilitet viser sig at være vigtig i en dynamisk analyse, idet den fleksible deformation aflaster kraften fra grunden, og idet der for visse grundstødninger viser sig at være en betydelig dynamisk forstærkning af belastningerne. Effekten af tidevand undersøges, og det vises, at selv en let grundstødning kan lede til kollaps af skrogbjælken, hvis den efterfølges af ebbe.

- Undersøgelse af belastninger og styrke af 6 hurtige fartøjer under en grundstødning. Det vises, at skrog-bjælkens styrke og de inducerede belastninger er af samme størrelse. Skibe af FRP (fibre-reinforced plastics), aluminium og stål undersøges, og det vises, at jo blødere skroget er, des mindre er belastningerne og dermed sandsynligheden for ødelæggelse af skroget.

De væsentligste aspekter af arbejdet vedrørende grundstødning på klippegrund er:

- Identifikation af de væsentligste fysiske effekter. Grundstødningsproblemet opdeles i to: den ydre dynamik (de globale skibsbevægelser) og den indre mekanik (den lokale knusningsproces omkring den indtrængende klippe). Metoden anvendt til analyse af den indre mekanik er en slags øvre-værdi-metode - d.v.s. ved hjælp af en antaget deformation kan energi dissipations-raten og dermed strukturens modstandskraft bestemmes. De væsentligste mekanismer i den indre mekanik er friktion, materiale-brud og store plastiske deformationer.

- Etablering af en teoretisk model for den ydre dynamik. Ved hjælp af tidssimulering argumenteres der for at afdrift (sway) og giring (yaw) ofte kan negligeres. En simplificeret model opstilles herefter for skibets globale bevægelse over klippen under hensyntagen til interaktionen med den indtrængende klippe. Modellen ser bort fra vertikale inertikræfter.

- Undersøgelse af mekanikken ved opskæring af en metalplade med en prismatisk kile. Eksisterende litteratur for problemet gennemgås, og tidligere udledte teorier sammenlignes. Dernæst udledes en teoretisk model baseret på en antaget deformationskinematik med en revnetip, bøjningshængsler samt membrandeformation. Sammenligning mellem den udledte teori og tre forskellige forsøg viser god overensstemmelse over et bredt spektrum af parametre.

- Etablering af en teori for den indre mekanik af en afstivet skibsbund under grundstødning på en konisk klippe med en afrundet top. Teorien er baseret på en global deformationskinematik med kompatibilitet mellem alle strukturelle elementer. I forhold til de fleste simplificerede metoder præsenteret hidtil er modellen meget generel, idet alle kendte skibsbunde kan modelleres under et. De væsentligste problemer som er identificeret og løst teoretisk er: lokal pladedeformation omkring klippens top, friktion, brud, modstandskraft fra bundplade, modstandskraft fra longitudinale stivere, skot og dragere og modstandskraft fra transversale rammer og skot. Adskillige af de udledte teoretiske løsninger er sammenlignet med forsøg, og der er fundet god overensstemmelse.

- Sammenligning af modellen for en afstivet skibsbund med resultaterne fra fire stor-skala forsøg. Overordentlig god overensstemmelse er fundet, idet afvigelsen mellem målinger og teori er omkring 5 % for energioptagelsen og omkring 15 % for klippeindtrængningen til pladebrud.

- Sammenligning af den komplette teoretiske model for grundstødning på et klippeskær med en grundstødning, som skete i 1975. Usikkerheder omkring input parametre diskuteres og det vises, at der er god overensstemmelse mellem den observerede og den beregnede skade på skibet. Beregningseksempler viser endvidere vigtigheden af at tage behørigt hensyn til koblingen mellem den ydre dynamik og den indre mekanik.

- Et studium af energioptagelsen af individuelle elementer i fire forskellige skibsbunde under en grundstødning illustrerer, hvordan stål kan benyttes mere eller mindre effektivt m.h.t energioptagelse.

Contents

List of Figures

Chapter 1

Introduction

1.1 Overview and Background

The present thesis concerning *The Mechanics of Ship Grounding* is a part of a greater study with the objective of making *Rational Design of Ship Structures for Accidental Loads*. Ship structures cover a range of constructions varying from fast vessels built of front edge technology materials to very large commercial ships built according to traditional procedures and of conventional constructional steels. With collision, grounding and fire as accidental loads, it is clear that the field of *Rational Design of Ship Structures for Accidental Loads* could focus on highly varying topics. Many problems within the field of accidental loads in marine engineering are still unsolved and it is true that even if many resources are allocated to the field, it will take years, may be even decades, before the marine community can claim to have a fully rational design basis with respect to accidental loads. The purpose of the present treatise has been to contribute to the understanding of ship grounding events.

Over the past decades there has been a continuous increase in the public concern about general risk issues. The consequence of this trend is that whenever a catastrophic accident occurs - and receives media coverage - there is an immediate political and public demand for actions to prevent the same type of catastrophe in the future. Examples of this pattern are seen in connection with the grounding of the *Exxon Valdez* and the following requirements for double hulls and in connection with the loss of the *Estonia* with the following reformulations of requirements for ferry design and operation. Many of the past improvements in safety of marine structure have been triggered by disasters but there is a change in this trend. The maritime society is beginning, albeit slowly, to think and work in terms of safety assessment of individual ships instead of the very generalized prescriptive regulations which have evolved over the past 150 years.

In line of these aspects it is clear that rational procedures for evaluating the consequenses of accidental loads are highly desirable, not to say necessary. Figure 1.1 shows the present causes of oil spill in US waters.

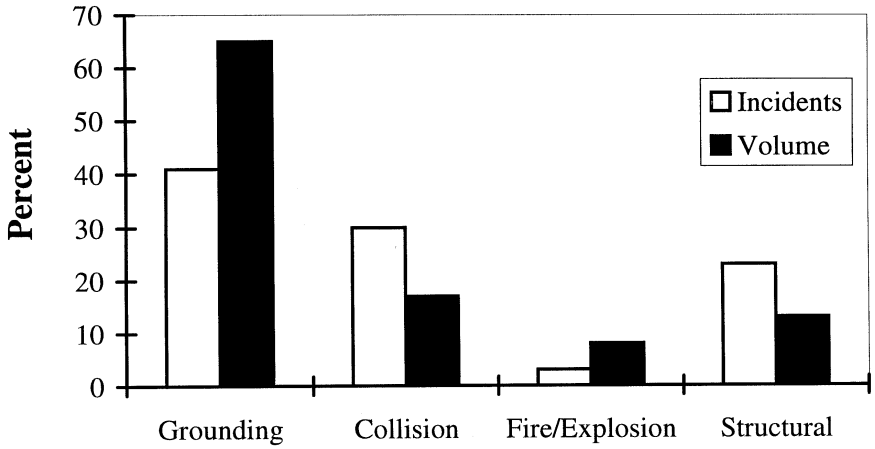

Figure 1.1: *Causes of major oil spills, [33]. 'Structural' refers to all other causes than Grounding, Collision and Fire.*

As seen in Figure 1.1 the accidental loads account for 75 % of the accidents number wise and 90 % of the pollution volume wise[1]. This reflects the fact that naval architects have accumulated a good understanding of the loads and the structural response during normal operational conditions but have not traditionally designed tank vessels to withstand groundings and collisions.

Accidents like the grounding of *Exxon Valdez* or *Braer* or the loss of both *Estonia* and *Titanic* demonstrated the potential seriousness and fatality of marine accidental loads. Yet, although the public, the governmental bodies and the marine society have long recognized the danger of accidental loads, statistics like shown in Figure 1.1 demonstrate the need for further work. A fundamental problem with rational consideration of grounding and collision in rules is that there are no simple measures of a ships defense against these loads. An idea would be to consider the statistical correlation between major design changes and the amount of oil spilled but as indicated by the clustring in Figure 1.2, the amount of oil spilled seems to be a random process, [25]. Within a reasonable time span this makes it impossible to draw cause and effect conclusions from statistics alone and attempts of doing so would most likely be highly reactionary with questionable effectiveness.

A - or perhaps *the* - methodology which rigorously takes into account the high level of uncertainty and randomness of the accidental loads is normally referred to as *Probabilistic Risk Analysis*. At least three steps are involved in such an analysis;

1. Hazard identification, i.e. what can go wrong - what are the consequences. For example this could be oil spill due to grounding of a tanker in a certain geographic area.

[1]Numbers vary some from source to source.

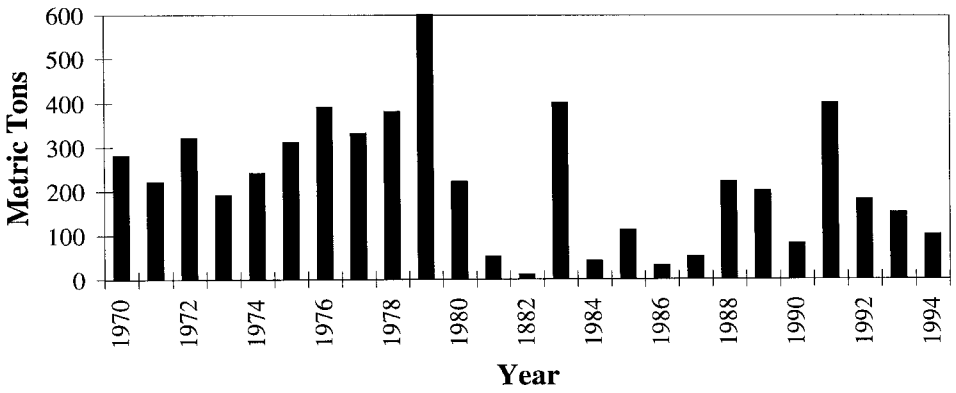

Figure 1.2: *Amount of oil spilled world wide 1970 - 1994.*

2. Scenario identification, i.e. what are the steps leading to the hazard and what is the probability of a given hazard. The so-called fault tree is a frequently applied tool in this part of the analysis.

3. Risk assessment, from the two analyses above calculate the product of consequense and probability.

As an example, the result of the analysis above could be that the probability of up to 1000 tons of oil spilled along a certain coast line in one year is 10^{-3}. Now with the risk quantified it would be up to governments, and international regulatory bodies to set up acceptance criteria. Risks cannot be eliminated but it can be reduced to a level acceptable to society. There are no universally acceptable risks so decision-makers have to identify levels of risk that are tolerable. Figure 1.3 illustrates in a simplified manner the concept of acceptable vs. unacceptable risks. The positions of examples shown in the acceptance diagram are not absolute (the cost of the clean-up after *Exxon Valdez* was estimated to be at least 2 billion US \$, [33]). Prior to risk mitigation, the risk coordinates C_1, F_1 typically fall into the 'unaccaptable' region. Then to bring the risk of a certain hazard into the acceptable region decision-makers would have the options of moving vertically or horizontally (or both) in the risk diagram, Figure 1.3.

For the example of a grounding, a vertical translation in the diagram could be obtained by requiring a stricter navigation of the ship - i.e. a higher degree of active safety. Likewise, a horizontal translation could be obtained by setting requirements for the passive safety, i.e. the response of the ship to the grounding. In aircraft and automotive industry the latter is referred to as the structural "crash-worthiness". A cost-benefit analysis would reveal the cost-optimal direction to take in the diagram Figure 1.3 and the corresponding measures.

To reduce the consequences of a given grounding - i.e. move in the horizontal direction in the diagram in Figure 1.3, governmental bodies would basically have two options; either design criteria or performance criteria. The requirements given in *OPA90* are examples of

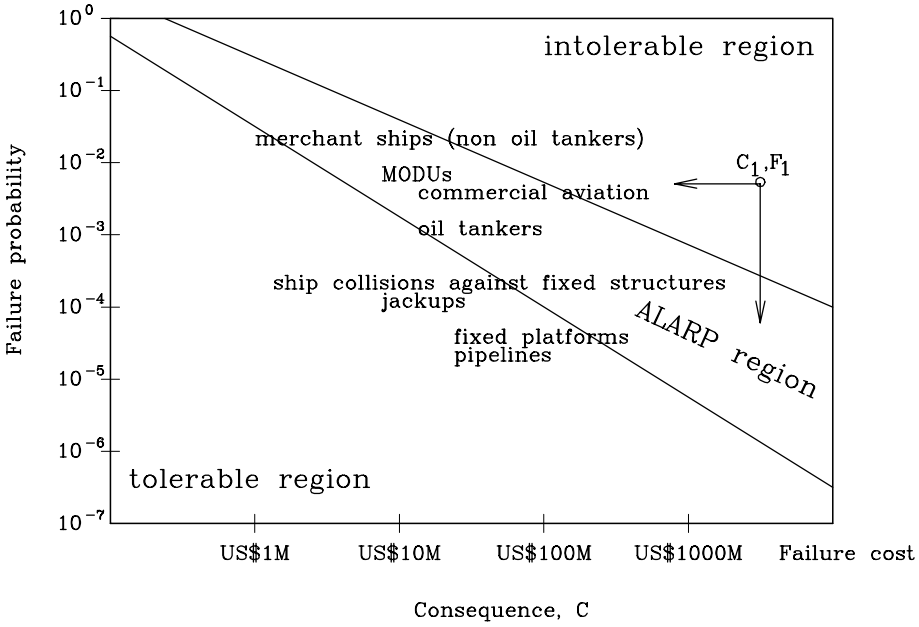

Figure 1.3: *Acceptable and unacceptable areas of risk and approximate locations of various accidents. ALARP means As Low As Reasonable Possible, and refers to generally societal and socio-economic acceptable levels of risk.*

design criteria (min. 2 m double hull spacing etc.) whereas the approach adopted by the automotive industry is based performance standards to a high degree. The development in the automotive industry is a good example of how performance standards tend to promote new development in terms of structural and operational innovations that will result in meeting or surpassing the standards. Safety standards for cars were adopted in the United States in the early 1970s. Examples of these standards are requirements of maximum deceleration during a 30 mile-per-hour head-on collision with a rigid barrier and amount of intrusion of the steering wheel into the passenger compartments. To meet the standards, each manufacturer took a slightly different approach and the highly competitive market resulted in many innovative and ingenious approaches to crashworthiness.

However, the example of the automotive industry also shows that it takes several years of intensive research to arrive at rational performance standards. Böckenhauer and Egge [72] noted the inadequacy of simple design criteria in connection with design for side collisions and presented a procedure for evaluating the collision performance of ships. The basic idea of the procedure is to evaluate the damage to a ship in eight different collision scenarios and assign them to a class according to their resistance against collision. Amdahl, [8] suggested a similar procedure for design for grounding. Figure 1.4 shows the overall idea of a procedure for evaluating a ship with respect to grounding and collision accidents. Given a specific ship and the route it will be serving, the idea of the procedure is to first identify the hazards of interest. Then, by collection of data, the input data should be specified, for example what is the ground topology around the route, which ship traffic will be met, what are

impact velocities, drafts etc. Some of these parameters are uncertain and should be given by probability density functions. Now given detailed input parameters, both the consequences and the likelyhoods of accidents should be calculated so that the risk can finally be quantified.

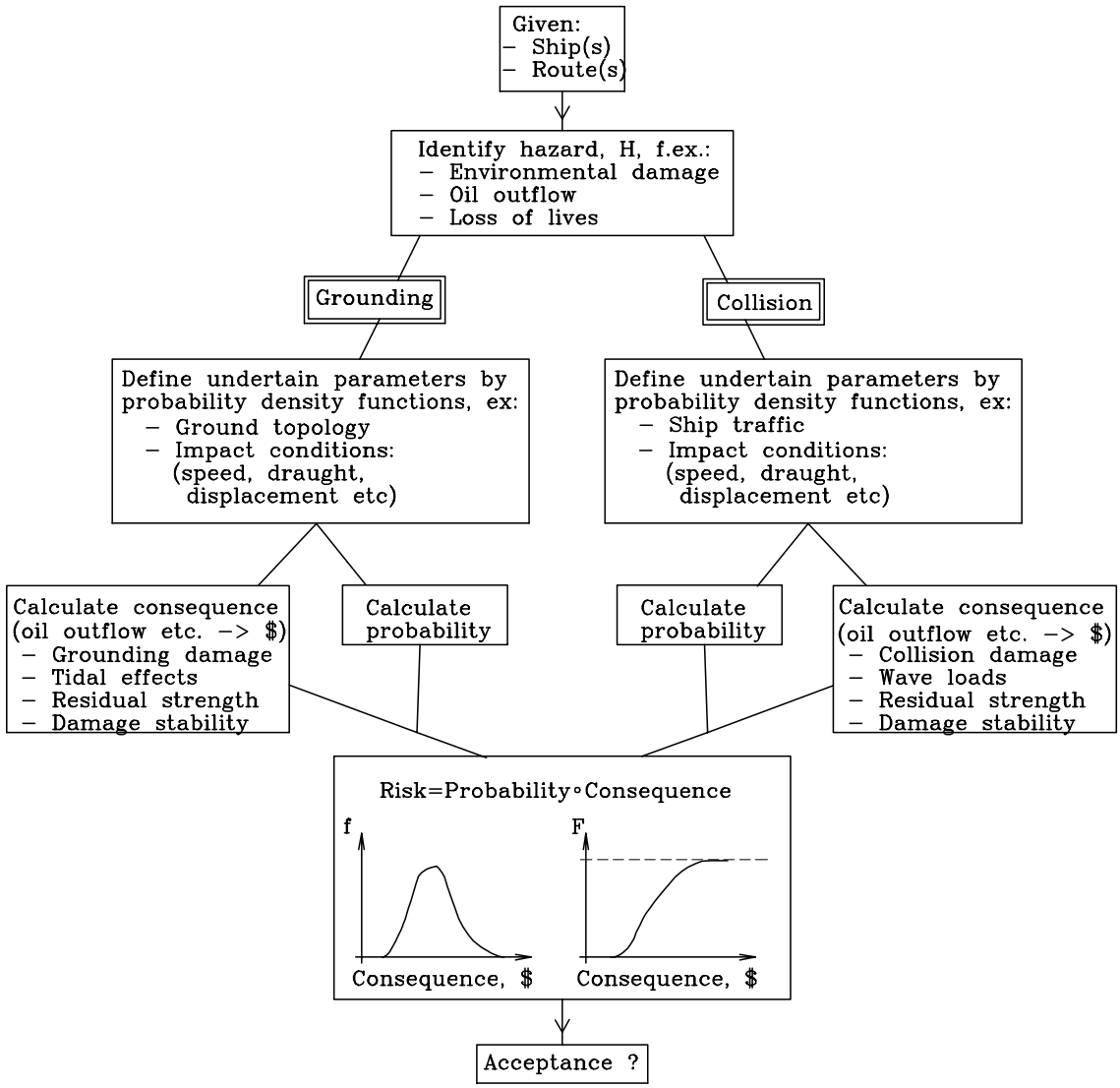

Figure 1.4: *Overall procedure for evaluating a ship with respect to the grounding and collision resistance.*

Both for the overall risk analysis and for checking the performance of individual ships as shown in Figure 1.4, it is necessary to have a methodology which defines the relation between the extent of damage and grounding parameters such as impact velocity, structural design and type of ground. In the automotive industry, full scale compliance tests ('crash tests') are mandatory but clearly this is prohibitively expensive for ships which are normally built in very small series. Model scale tests may seem to be the obvious alternative but as it will be explained later, scale tests can be difficult to interpret due to different scaling laws for plasticity and fracture. General purpose non-linear finite element codes have proved

their ability to simulate ship grounding on rocks, but their application is still prohibitively time consuming for design calculations. The main purpose of the present thesis has been to develop simplified theoretical models for predicting the structural damage in a ship grounding accident.

1.2 Objectives and Scope of the Work

With the overall objective of improving safety of ship structures with respect to accidental loads, the present treatise has merely focused on establishing a calculational procedure for evaluating the structural crashworthiness in a grounding accident. Touched only peripherically upon, the probabilistic aspects of the accidental loads has not been given high priority.

An overall view on groundings categorize the accidents in two major groups:

1. Grounding on soft sea beds, so-called *Soft Groundings*. The damage to the hull in terms of crushing at the point of ground contact is limited but the hull girder may fail in a global mode due to shear force and bending moment exceeding the hull girder capacity.
2. Grounding on hard bottoms - so-called *Hard Groundings*. The primary concern here is the local crushing and tearing of the ship bottom due to a cutting rock.

Together with analysis of the damage which can develop during grounding, it is relevant to consider the residual strength and the stability of the ship in the post-accident condition. However, the present study focuses on the loads and the damage developed during the grounding itself.

The treatise is composed as follows:

In Chapter 2 the framework for risk analysis of a certain geographic area with respect to grounding is presented. The model requires extension to cover calculation of consequences but it is shown how the expected number of groundings can be calculated. With the other results of the present treatise it should be possible to formulate a total risk assessment model with respect to grounding in a certain area.

Chapter 3 sets up a theoretical model for analysis of ship grounding on soft sea beds. The modelling of the soil response to the penetrating bow is difficult and a phenomenological model is proposed. The hull girder is modelled by a linear elastic Timoshenko beam theory.

Chapter 4 presents a verification of the theoretical soft grounding model. Analysis of results from both model and full scale tests shows good agreement between theory and measurements.

Chapter 5 presents numerical results for grounding of a large tanker and of six different fast vessels made of steel, aluminium and fibre reinforced plastics. For all ship types - and in particular for the very large tanker - it is shown that a soft grounding may lead to failure of the hull girder.

Chapter 6 gives the foundation for the theoretical model for grounding on rocks. It is argued that it is advantageous to develop models for the external dynamics and internal mechanics separately. As it is the force from the rock (the internal mechanics) that drives the global ship motion there is a strong interaction between the two models which must be taken into account. Basic equations for energy dissipation in plasticity and fracture in a moving deformation zone are also listed. Criteria for plate rupture are reviewed and the difficulty of theoretical modelling is illustrated. Based on results from sheet forming industry, it is argued that a proper criterion for plate rupture is initiation of necking.

In Chapter 7 the model for the external dynamics is discussed. A pinnacle rock may induce ship motion in all six degrees of freedom but based on results of time simulation, it is argued that it is sufficient to consider only the surge, heave, roll and pitch motions. The consequense of this simplification is that the rock can be assumed to move in a straight line along the length of the ship. Based on the neglect of certain inertia terms and the sway and yaw motions, a theoretical model for the external dynamics is subsequently proposed.

Chapter 8 presents the simplest possible internal mechanics model: cutting of a bare plate by a prismatic wedge. Despite the extreme simplicity of this problem compared to a general grounding accident, it has received the most scientific attention in the field of internal mechanics of ship grounding. Nevertheless, it is shown that the numerous proposed formulas for predicting the resistance to plate cutting give very different results, and only few of the formulas are able to predict the involved forces in experiments other than those they were derived from. A new theoretical model is proposed based on an assumed mode of deformation. Friction has received little attention in previous works but it is shown how the effect of friction and also the vertical reaction can be predicted within the framework the present theoretical approach. The theoretical model is compared to experimental results and it is shown to correspond well with experimental results from cutting of metal plates varying in thickness from 0.7 mm to 25 mm.

In Chapter 9 the problem of an assembled ship bottom structure deformed by a conical rock is adressed. Compared to cutting of a bare plate this problem is very complex. The overall idea is to assume all structural components to follow a global mode of deformation. A fundamental problem with the approach is to determine the extent of deformation around the moving rock. The extent of deformation should ideally be calculated by considering the strength of the structure around the rock but the present approach is based on failure modes observed in large scale tests. Knowing the extent of deformation, a solution is derived for the local deformation of the plating around the rock tip. The local solution gives detailed information about frictional effects and the limit penetration to fracture. From the global deformation mode, the resistance of inner bottom plating, shell plating, girders, floors, longitudinals and bulkheads is derived. Some of the derived solutions are verified through comparisons with experimental results.

In Chapter 10 the performance of the theoretical model presented in Chapter 9 is compared to four 1:5 scale experiments conducted in USA by the Naval Surface Warfare Center. The main uncertain parameter is the coefficient of friction. By choosing this parameter to be 0.4, which is reasonable, the discrepancy between the energy absorbtion in theory and experiments is maximum 6 %. An accidental grounding which happened off the coast of Singapore in 1975 is reconstructed with the theoretical model and good agreement between calculated and observed damage is found.

Chapter 2

Estimation of Grounding Frequency

2.1 Introduction

In connection with design for accidental loads it is important to quantify both frequency and consequence as the societal acceptance limits are defined by both these quantities, see Figure 1.3. Taking the equivalent example of the automotive industry, the performance standards which designers have to meet may not take into account the expected likelihood of an accident. However, if governments and regulatory bodies are to arrive rationally at rules for design, estimation of the accident frequency becomes necessary.

Although the main focus of this thesis is on consequence calculation, the results of the present chapter have been included to illustrate that the expected annual number of grounding events in a certain geographic area can be calculated by rational but simple means. No new theoretical models are derived in the present chapter, as the present analysis closely follows the approach presented by Pedersen in [98]. For further examples and descriptions of the approach, see also [19] and [91].

The pioneering work on risk models for ship grounding was conducted by Fujii and coworkers in the early seventies, [40] and [41]. Several risk analyses concerning grounding and collision have been presented since then, see e.g. [39], [43], [62] and [73].

2.2 Theoretical Model

In accordance with Pedersen [98], the starting point of the theoretical analysis is to divide the scenarios leading to grounding into four main categories, Figure 2.1:

I Ships following the ordinary direct route at normal speed. Accidents in this category are mainly due to human error, but may include ships subject to unexpected problems with the propulsion/steering system which occur in the vicinity of the fixed marine structure or the ground.

II Ships which failed to change course at a given turning point near the obstacle.

III Ships taking evasive actions near the obstacle and consequently run aground or collide with the object.

IV All other track patterns than Cat. I, II and III, for example ships completely out of course due to loss of propulsion.

Figure 2.1 shows observed grounding locations in a part of the Great Belt in Denmark over a 15-year-period. It is seen that most of the grounding events belong to category I and II but there are also category III and IV groundings which seem to be randomly scattered over the area.

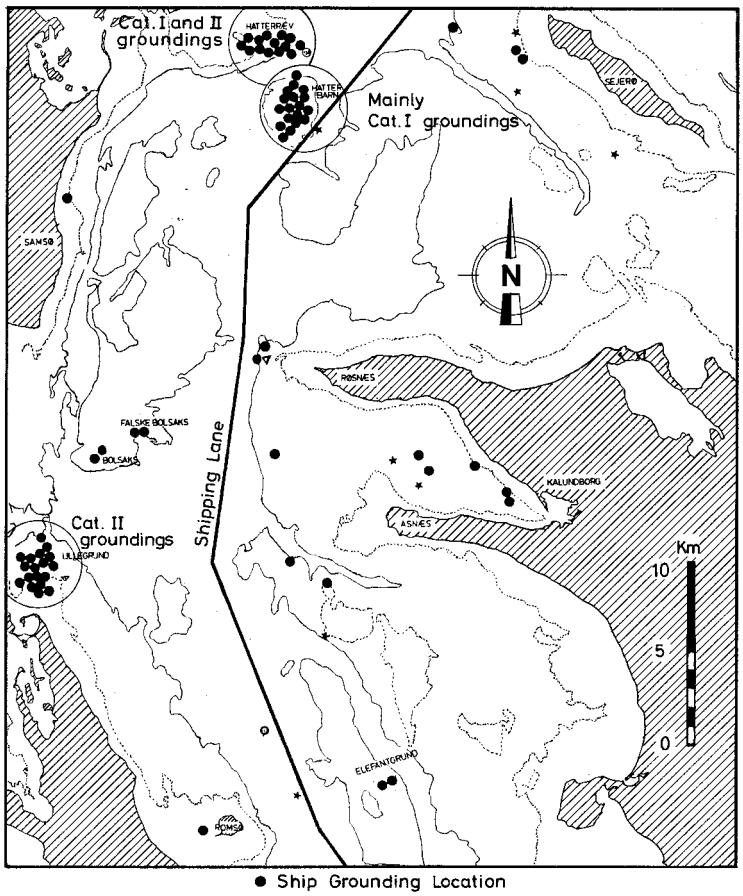

Figure 2.1: *Observed grounding events over a 15-year-period in a Danish Strait, from [98].*

In the following, expressions are presented for predicting the expected annual number of grounding events of category I and II accidents. The fault-tree methodology presented below could also be used to find the probability of category III and IV grounding events but this aspect is left for future studies. Ships in category I and II, following an ordinary route, are distributed over a transverse section of the waterway with some probability density function, $f_i(z)$, where index i refers to a ship class and z is the transverse coordinate, see Figure 2.2. The shape of f_i is a strong function of the considered waterway so a major challenge of the present approach is to define rationally $f_i(z)$ along a given route. Given f_i, the number of candidates for a grounding event can be calculated as an integral of f_i over the width, z_{min} to z_{max}, of the obstacle. This is illustrated by the hatched areas in Figure 2.2. Most of these candidates will be aware of the danger and take the necessary aversive actions before they hit the obstacle. However, a fraction, P_c, of the candidates will fail to avoid the obstacle, due to for example human and technical errors. The fraction P_c is normally referred to as the 'causation probability', and it will be shown later how it can be estimated.

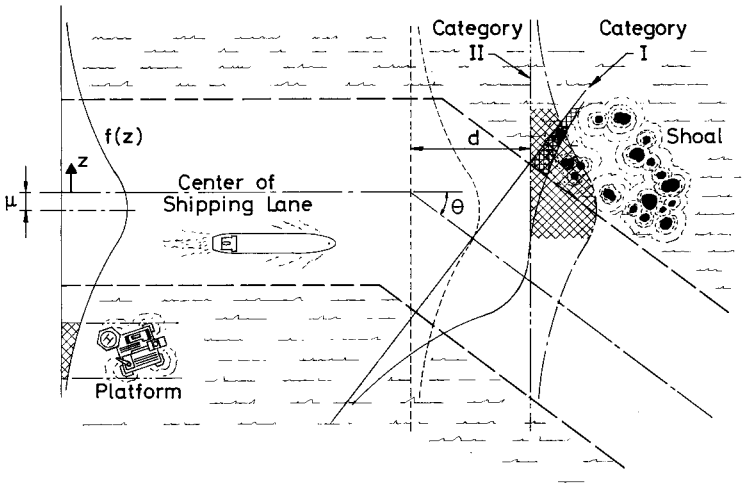

Figure 2.2: *Illustration of model for predicting the expected number of grounding events or collisions with fixed objects on a given ship route, from [98].*

According to the model described above, the expected number of grounding events in Category I and II can be calculated as

$$N_I = \sum_{Ship\ class,\ i} P_{c,i}\, Q_i \int_{z_{min}}^{z_{max}} f_i(z)\, dz \tag{2.1}$$

$$N_{II} = \sum_{Ship\ class,\ i} P_{c,i}\, Q_i\, e^{-d/a_i} \int_{z_{min}}^{z_{max}} f_i(z)\, dz \tag{2.2}$$

where the following notation has been used:

a_i	Average distance between position checks by the navigator.
d	Distance from the obstacle to the bend in the navigation route. varying with the lateral position, s, of the ship.
i	Index for ship class, categorised after vessel type and dead weight or length.
$f_i(z)$	Probability density function for the ship traffic.
N_I	Expected number of category I grounding events per year.
N_{II}	Expected number of category II grounding events per year.
$P_{c,i}$	Causation probability, i.e. ratio between ships grounding and ships on a grounding course.
Q_i	Number of ships in class i passing a cross section of the route per year.
z	Coordinate in the direction perpendicular to the route.
(z_{min}, z_{max})	Transverse coordinates for an obstacle.

Assuming that the event of checking the position of the ship can be described as a Poisson process, the factor e^{-d/a_i} represents the probability of the navigator not checking the position from the bend to the obstacle.

With the formulation above the expected number of annual grounding events becomes a function of traffic distributions, bottom topology, route layout etc. It is seen from Eq. (2.1) and Eq. (2.2) that another important parameter is the causation factor, P_C, determining how large a fraction of the accident candidates actually run aground or hit the obstacle. The parameter P_C can be estimated on the basis of available accident data collected at various locations and then transformed to the area of interest, or it can be found by use of a so-called fault-tree. A fault-tree is a logical diagram which shows the relation between system failure, i.e. an undesirable event of the tree, and failures of the components of the system. Fault tree analysis has become a very important tool for reliability and safety analysis of complex systems. An example of a fault tree for the current event of failing to avoid an obstacle is shown in Figure 2.3.

From the fault tree in Figure 2.3 the causation probability is found to be $P_c = 3.5\,10^{-4}$. The calculated expected number of yearly grounding events, $N = N_I + N_{II} + N_{III} + N_{IV}$, can be considered the intensity in a Poisson process. The probability of no grounding events in one year is then e^{-N}.

2.3 Numerical Example of Frequency Estimation

In order to illustrate the application of the theory above, the ferry route in Denmark between Esbjerg and Fanø is considered. The main data for the numerical example is given in Table 2.1. The transverse distribution of the ship traffic is assumed to follow a Gaussian distribution with a mean of μ and a standard deviation of σ. The ferry route and the

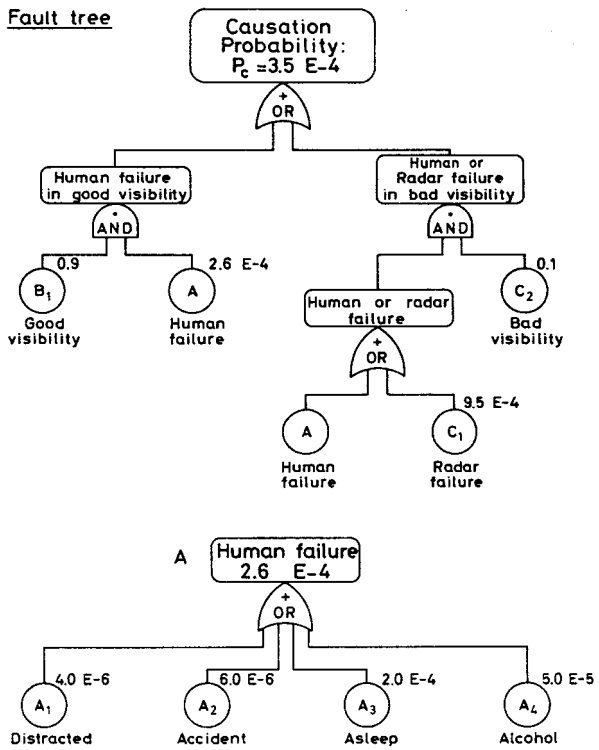

Figure 2.3: *Fault tree for determining the probability, P_C, of failing to avoid a ground or a fixed object, [98].*

surrounding banks and grounds are illustrated in Figure 2.4. The route is characterised by the harbour area in Esbjerg, an open stretch and a narrow dredged channel to Fanø.

The standard deviation, σ, of the ship traffic is a strong function of the allowable width of the route and in general it varies along the route. For the present problem, where the dredged channel *Loen* is only 30 m wide, the standard deviation is assumed to be 5 m. Hence, the distribution is such that there are three standard deviations from the centre of the shipping lane to the side of the channel and only 0.2 % of the ships are therefore assumed to be more than 15 m away from the centre of the lane. Another important parameter is the mean sailed distance between position checks. When the ship is in the channel special attention is required of the officers so the checking distance is here assumed to be 75 % of the ship length corresponding to position checks every 8 s. When the ship is between the channel and the harbour, less strict navigation is required so that the checking distance is set to one ship length. Figure 2.4 shows the result of the analysis. Due to the assumption of a standard deviation from the ship route of only 5 m, practically all the grounding events belong to Category II, i.e. they are due to failure to change course.

The calculated expected number of yearly grounding events is 3.05 giving a probability of no grounding events in one year of P(no grounding events) = 4.7 %. As the observed yearly number of grounding events from 1994-1996 was 2.3 in average, there is good agreement between theory and observations. However, the theoretical result is quite sensitive to both

Table 2.1: *Main data for calculation of the expected number of yearly grounding events for the Esbjerg-Fanø ferry route.*

Ship length, L,	49.9 m
Ship draught, T,	2.3 m
Annual number of trips (one way), Q,	12750
Assumed mean distance from route, μ,	0
Assumed standard deviation from route, σ,	5 m
Assumed ship lengths per check, a_i/L	0.75 - 1
Causation probability, P_c	$3.5\,10^{-4}$

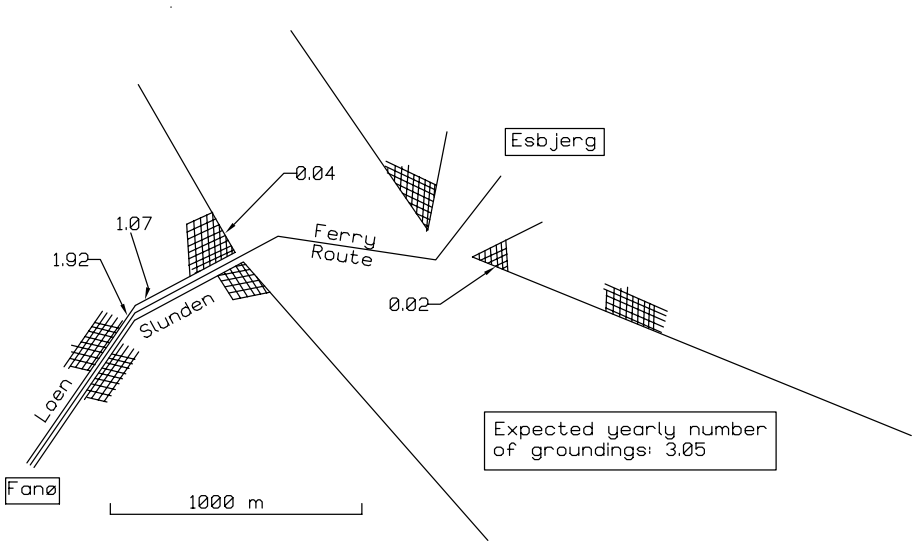

Figure 2.4: *Calculated expected yearly number of groundings on the banks and channel sides for the Esbjerg-Fanø route.*

the causation factor, P_c, and to the distance, a_i, between position checks. The expected number of grounding events is proportional to P_c, and doubling the assumed distance between checks by the navigator (1.5 ship lengths in the channel and 1 ship length on the open stretch) increases the expected yearly number of grounding events from 3.05 to 5.81. As practically none of the grounding events are of category I, the assumption of μ and σ is not critical as long as the traffic is concentrated around the centre of the lane.

In conclusion, work on theoretical frequency estimation is still needed in terms of calibration and validation. However, with further development, the model presented above could be valuable for quantifying the effects of changing route layout, pilot requirements etc. An integrated risk calculation model where frequency estimation is coupled with a model for predicting the consequences of a given grounding event would provide the necessary tool for regulatory bodies to set up rational grounding performance criteria of ships, so that the risk level is limited to an acceptable level. The remaining chapters of this thesis are de-

voted to the development of theoretical models for predicting the structural damage during a grounding event.

This page is intentionally left blank

Chapter 3

Governing Equations for a Flexible Ship in a Soft Grounding Event

3.1 Introduction

When a ship runs aground on a soft sea bed the principal energy absorbing mechanisms which stop the ship are normally:

1. Deformation of the sea bed.
2. Friction between sea bed and hull.
3. Change of potential energy of the ship and the surrounding water.
4. Deformation of the hull.
5. Hydrodynamic damping.

The solution method applied here for theoretical analysis of the soft-grounding problem is numerical integration of the equations of motion for the ship, i.e. time simulation. Alternatively, an overall simplified approach based on the conservation of energy and momentum could be applied. Such an approach was presented by Pedersen, [122], and it gives a good picture of the overall grounding mechanics. However, to obtain detailed information about loads during the impact, it is necessary to resort to time simulation. The following sections describe the load modelling corresponding to the five effects listed above and the corresponding equations of motion.

Previous experimental and numerical studies, for example [93], [112] and [117], focused on the rigid body motion of the ship. This is relevant in connection with the design of protective

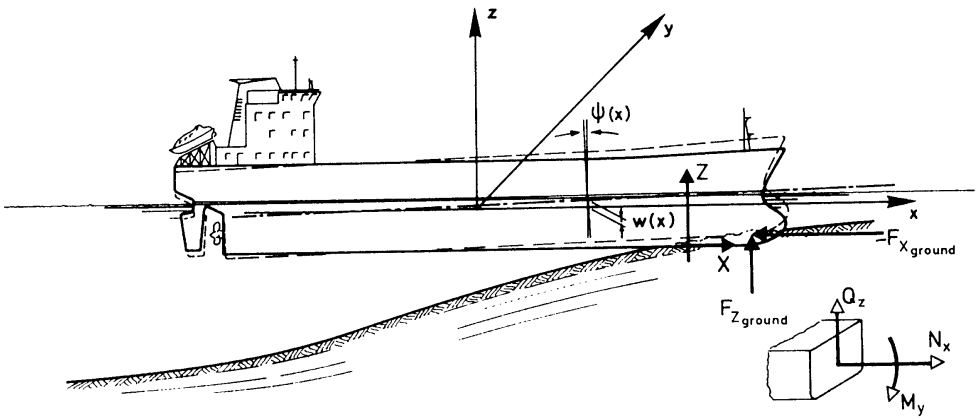

Figure 3.1: *Coordinate systems* (x, y, z) *and* (X, Y, Z) *and definition of sectional forces.*

islands for bridges and for the prediction of the tug-load necessary to refloat the ship. As the present study is focused on the loading of the ship it has been extended to incorporate enhanced modelling of the hull girder where the hull flexibility is taken into account. The finite crushing strength of the bow could also be included but as a first approximation it is assumed to be rigid. The flexible deformation of the hull girder has been determined from Timoshenko beam theory.

It is assumed that both the centre of gravity of the structural and hydrodynamic mass per unit length and the bending neutral axis of the hull girder can be considered as a straight line. This line is the $x-$axis of a coordinate system fixed with respect to the ship and with origin amidships. The $y-$axis points towards the port side and the $z-$axis points upwards, see Figure 3.1. A global coordinate system, (X, Y, Z), is fixed on the ground with origin at the point of the initial contact between bow and sea bed. Displacement and rotation in surge, heave and pitch in the (x, y, z) coordinate system is denoted (u, w, ψ). Sway and yaw is not considered. The basic idea is to calculate accelerations in the local coordinate system, transform these to the global system and perform time integration in the global system to get the time history of velocities and displacements.

3.2 Loads from Water and Gravity

3.2.1 Hydrostatic Loads

By combining the loads from the hydrostatic pressure with the gravity load on the structure in the so-called restoring load, modelling becomes simple. The ship is assumed to be in equilibrium in the initial configuration. Then, when a section is lifted out of the water, it experiences a static downward load due to the difference between weight and buoyancy. Since the weight is unchanged by lifting, the restoring force/moment is approximately given by

the change of buoyancy alone[1]. By assuming that the sides of the hull are parallel (vertical), the restoring load due to a static lift, $w(x)$, of a hull section can be expressed as

$$q_{hs,z}(x) = -\rho_w \, g \, B(x) \, w(x) \tag{3.1}$$

The assumption of vertical ship sides is good for large tankers with $C_B \approx 0.85$ but for the small fast vessels analysed later, Eq. (3.1) will only hold true during the initial impact.

3.2.2 Hydrodynamic Loads, Added Mass and Damping

Since modelling of the hydrodynamic loads on a ship is of interest in several areas of marine engineering such as manoeuverability, seekeeping and ship vibration, a substantial amount of literature has been published in this field. The characteristics for whole ships can be determined experimentally but since this is expensive and inconvenient at the design stage, many theoretical approaches have been attempted. The so-called 'strip-theory' is a convenient approach which takes advantage of the fact that ships are normally long and slender such that the overall flow pattern is two-dimensional. The ship is divided into a series of transverse sections ('strips') and each of these strips is considered separately assuming a two-dimensional flow. Determination of the two-dimensional flow is significantly less complex than the three-dimensional problem and several usable analytical solutions exist.

When an infinitely long cylinder is forced to move in an oscillating heave motion on the surface of a fluid it is subjected to hydrodynamic pressure loads. When the motion is harmonic with the frequency ω, the force working on a unit length of the cylinder can be expressed as

$$q_{hd,z}(\omega, t) = -a_z(\omega)\ddot{w}(t) - b_z(\omega)\dot{w}(t) \tag{3.2}$$

where the coefficients $a_z(\omega)$ and $b_z(\omega)$ are denoted 'added mass' and 'damping'. The added mass is seen to be the part of the force which is in phase with the acceleration and the damping is the part in phase with the velocity. Eq. (3.2) holds true for a harmonic motion with a well defined frequency. In the general case of a transient motion (Tick [126], Petersen [101]) the hydrodynamic load can be written

$$q_{hd,z}(x, t) = -\mu_z(x) \, \ddot{w}(x) - \int_0^t h_z(x, \tau) \left\{ \dot{w}(x, t-\tau) - \dot{w}(x, t-\tau=0) \right\} d\tau \tag{3.3}$$

[1] Actually, the distance from the centre of gravity, CG, to the centre of buoyancy, CB, generates a moment with the rotation of the hull, but for the pitch motion this effect is small.

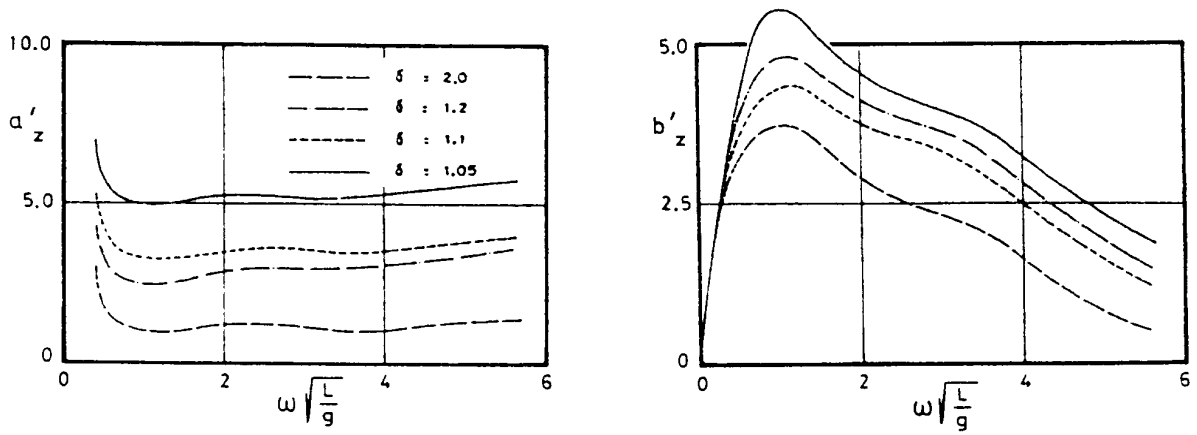

Figure 3.2: *Experimental data for added mass and damping for a 310 m tanker ($C_B = 0.85$) at restricted water depths. From Oortmerssen, [92] and [131]. The non-dimensional quantities are defined as $a'_z = a_z/\rho_w\nabla$, $b'_z = b_z/(\rho_w\nabla\sqrt{g/L})$ and $\delta = h/T$.*

where μ_z is the added mass at infinite frequency:

$$\mu_z(x) = \lim_{\omega\to\infty} a_z(x,\omega) \tag{3.4}$$

and $h_z(x,t)$ is the unit response function:

$$h_z(x,t) = \frac{2}{\pi}\int_0^\infty b_z(x,\omega)\,cos\omega t\,d\omega \tag{3.5}$$

where $b_z(x,\omega)$ is the two-dimensional damping of the cross-section in heave at frequency ω. Since the damping thus comes as a weighted integral of the velocity history from the beginning of the motion, it is often denoted a 'memory effect' - contrary to the added mass, it is a function of the past. With Eq. (3.3), the problem is now determination of the added mass and the damping coefficients, $a_z(\omega)$ and $b_z(\omega)$. As mentioned, several theoretical methods exist for unrestricted water depth but as groundings - by their very nature - occur at restricted water depths, this must be taken into account. Figure 3.2 shows results presented by Oortmerssen, [92] and [131], for added mass and damping in heave for a ship at different water depths.

It is seen that for a water depth to draught ratio of $\delta = h/T = 1.05$, the added mass is $a'_z \approx 5$, indicating an increase due to restricted water depth by a factor of approximately 5. Likewise, the effect of the restricted water depth on the damping is seen to be significant.

The approach adopted here for calculation of the damping is to use strip theory together with the data of Figure 3.2. The graphs for b'_z shown in Figure 3.2 are transformed according

to Eq. (3.5), and the unit response function for a ship section with a given depth to draught ratio, δ, is then found by interpolation.

The added mass at infinite frequency is determined by a slightly more sophisticated approach. At infinite water depth, the added mass can be determined with good accuracy by use of the results of Lewis 1929, [68]. By conformal mapping of the solution for potential flow around a cylinder, Lewis found the added mass at infinite frequency to be given by

$$\mu_z = C_V \, \rho_w \, A_s \tag{3.6}$$

where A_s is the submerged cross sectional area of the considered section and C_V is defined from the draught to breadth ratio β and the sectional area coefficient C_S as

$$\begin{aligned} C_V &= \frac{(1+a_1)^2 + 3a_3^2}{1 - a_1^2 - 3a_3^2} \\ C &= \left\{ \frac{3}{2}(1+\beta) - \sqrt{1/4(1+\beta)^2 + 2\beta(1 - 4C_s/\pi)} \right\}^{-1} \\ a_1 &= C(1-\beta) \\ a_3 &= C(1+\beta) - 1 \\ \beta &= 2T/B \\ C_S &= A_s/BT \end{aligned}$$

A semi-empirical expression for the modification of added mass due to restricted water depth was given by Prohaska, [104], as

$$\frac{\mu_z(h, T, C_S)}{\mu_z(h = \infty, T, C_S)} = 1 + 2(C_S - 0.2) \left(\frac{T}{h} \right)^2 \tag{3.7}$$

The expression is based on experiments with $\delta = h/T$ exceeding 1.5 and it is seen to have a maximum of 2.6 when $\delta = C_S = 1$. Thus, it does not depict the behaviour shown in Figure 3.2 for very small bottom clearances. The idea here is to retain Prohaska's functional dependence on the sectional geometry (i.e. the $'2(C_S - 0.2)'$ term) and find another function for the dependence on $\delta = draught/depth$ based on the results presented by both Prohaska, [104], and Oortmerssen, [92]. The final result for the modification of added mass at infinite frequency due to restricted water depth becomes

$$\frac{\mu_z(h, T, C_s)}{\mu_z(h = \infty)} = 1 + 0.54 \, (C_s - 0.2) \left(\frac{1}{\delta - 1} \right)^{0.91} \tag{3.8}$$

To limit the added mass at the point of contact ($\delta = 0$) in Eq. (3.8)) it is necessary to take into account the three-dimensional flow near the ends of the ship. Based on the results of Madsen, [74], and Oortmerssen, [92], the maximum value of the correction factor, Eq. (3.8), is here assumed to be 6.0. As this large added mass only occurs in a very limited area around the point of contact, the final results are not sensitive to this assumption so its validity will not be discussed in further detail.

3.3 Ground Reaction

The greatest challenge of developing a theoretical model for grounding on soft sea beds is establishing a model for calculation of the soil reaction. As the soil reaction induces the hull girder loads and eventually causes the ship to stop, it is of paramount importance to have a good model for the response of the ground to the penetrating bow.

In the analysis presented by Pedersen, [122], the bow was assumed to move in the plane of the undisturbed slope and an efficient coefficient of friction was adopted. To obtain a good correspondence between theory and model tests, an effective coefficient for the bow/soil interaction equal to $\mu = 0.78$ was assumed. The coefficient of friction between steel and sand is typically 0.3 - 0.4 so this effective coefficient of friction includes the normal pressure on the bow which must thus be quite significant. In the present analysis it is necessary to have a more sophisticated model for the soil behaviour so that it can be applied to a time simulation scheme.

The stopping force acting on a beaching ship is the result of ruptures in the soil in the areas of contact between bow and soil. The mechanics of this rupture is complicated, which is illustrated by an example where a ship with a cylinder bow with vertical sides is rammed horizontally into a slope of sand of 1:6, see Figure 3.3. The bow is semi-circular in shape with a radius of $r = 378mm$ and it has a flat bottom. The sand is very uniform in gradation with a mean diameter of $d_m = 0.125\ mm$, permeability coefficient $k = 9 \cdot 10^{-5}\ m/s$ and frictional angle $\varphi = 39^o$. The ship is forced with a constant velocity and it is locked in the horizontal position so that it cannot heave or pitch. Figure 3.3 shows the horizontal and vertical soil reactions for different impact velocities as functions of the horizontal position for both dry and submerged slopes.

It is noted that the force in the submerged case is 10 - 20 times greater than for the corresponding dry case. Figure 3.3 also shows that the reaction is clearly a function of impact velocity. It could be claimed that the dependence on impact velocity is due to the change in momentum of the soil being pushed by the bow but since no dependency is seen on impact velocity for the dry sand is observed, this cannot be the case. The results are important because they show that in a grounding event on a sand beach, the behaviour of the soil is strongly influenced by the pressure of the fluid present in the pores of the material. This influence of pore pressure is discussed by Zienkiewicz et al., [87].

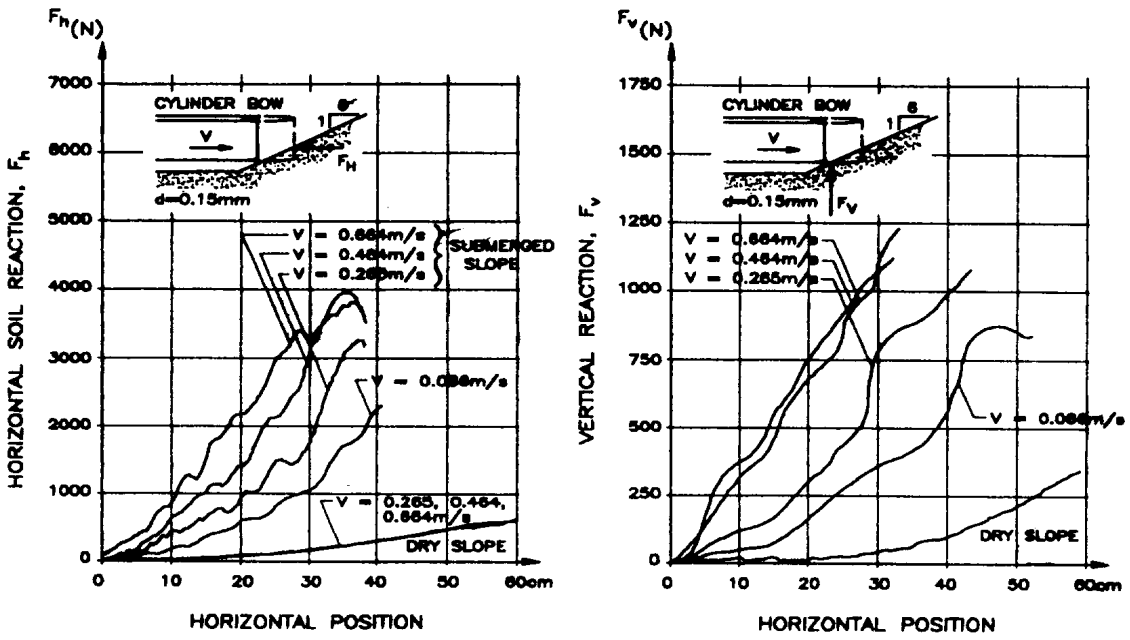

Figure 3.3: *Soil reactions on a penetrating bow. Dry and submerged slopes, different velocities, [94].*

In classical soil rupture theory, conditions are assumed to be either drained or undrained. If conditions are drained an incremental load increase on a soil element is carried solely by additional stresses in the grain skeleton ('effective stresses'), and if conditions are undrained an additional load is carried by an additional pressure in the pore fluid alone. Both drained and undrained conditions are considered independent of the time history of the load - in this case of the impact velocity. According to Figure 3.3, which shows a clear dependence on impact velocity, neither of the two theories would therefore be suited for modelling of ship grounding events. The consolidation theory is a theory which includes the time variance of loads and deformations. Biot, [20] and [21], presented a general set of equations governing the behaviour of a saturated linear elastic porous solid under dynamic conditions. For standard geotechnical consolidation problems, however, the grain skeleton is most often assumed to be linear-elastic and inertia forces neglected. Obviously, these restrictions do not apply to grounding problems where strains are far beyond the elastic limit. Biot's equations can be generalised to non-linear material behaviour if the constitutive relation is written incrementally. A fully consistent theoretical analysis of a ship grounding event would require numerical solution of these equtions, for example by use of the finite element method. The solution would include phenomena like elastic compression, rupture with very large strains, liquefaction, dilatation of the soil in rupture and flow of pore water. Use of such a model for grounding simulations would require extensive computer facilities and would be prohibitively time consuming. Therefore, the soil mechanics model used here has been based on very substantial simplifications and it is to some extent phenomenological.

The porewater creates strong effective stresses in the soil which act on the hull both

as normal and tangential stresses. The question is how these large effective stresses are generated. Two mechanisms seem possible:

1. At the rupture, the sand dilates and thus creates a large suction in the pore water in the rupture zones. This suction results in a corresponding increase in the effective stresses. This phenomenon can be observed in an undrained triaxial test.
2. During impact, the grain skeleton is compressed and pore water is squeezed out in the compression zone creating an additional pore water flow. This pore water builds up large effective stresses in areas of the grain skeleton. In other areas liquefied zones are formed.

The present approach is based on the latter hypothesis although it is recognised that the suction generated by the soil dilatation is present, [93] and [94].

3.3.1 Modelling of Soil Response

According to the hypothesis above, the soil resistance is governed by pressure in the pore water when the impact velocity is relatively high. At low velocities, on the other hand, the grain skeleton must carry the load alone corresponding to the drained case. These reflections are implemented in the present model by assuming that the total force from the soil can be found as the sum of two individual contributions:

1. A force from the pressure in the pore water around the bow. It is assumed that pore water is pressed into the grain skeleton, corresponding to the motion of the bow and that velocities of the sand can be neglected.
2. A force corresponding to a drained rupture around the bow.

The frictional stress on the bow is assumed to be a constant fraction of the normal pressure. Below the basic theory for calculation of the normal pressure is given.

Force from Pore Water Pressure

Equilibrium of the fluid phase in saturated soils can be expressed as ([21], [37])

$$-p_{,i} = \frac{\rho_w(1+e)}{e}\,\ddot{v}_i + \rho_w g\left(\frac{1}{k} + b\dot{w}_i\right)\dot{w}_i \tag{3.9}$$

where

b empirical constant accounting for non-linearities in Darcy's law at high flow velocities,
e void ratio, i.e. ratio of pore volume to grain volume,
$_{,i}$ spatial derivative with respect to the i'th component,
k permeability coefficient for laminar flow (Darcy 's law),
p pore pressure (above hydrostatic pressure),
v_i absolute average displacement of fluid phase. $\dot{v}_i$ is the absolute, filter velocity, i.e. the appropriate volume rate divided by the total area
w_i average pore water displacement relative to solid phase, $w_i = v_i - u_i$, where u_i is the absolute displacement of solid phase,
$\dot{w}_i$ relative filter velocity, i.e. appropriate volume rate divided by total area,
ρ_w density of water.

The term $b\,\dot{w}_i$ was introduced by Engelund, [37], to account for non-linearities in Darcy's law at high flow velocities. In [37] it is shown that the linear permeability coefficient can be calculated as

$$k = \frac{e^2(1+e)}{\alpha}\frac{g\,d^2}{\nu_w} \tag{3.10}$$

and the correction factor, b, as

$$b = \beta\frac{(1+e)^2}{e^3}\frac{1}{g\,d} \tag{3.11}$$

in which d is the mean diameter of grains and ν_w is the kinematic velocity of water. To account for the type and the gradation of the sand, the coefficients α and β are defined as

$$(\alpha,\beta) = \begin{cases} (800, 1.8) & \text{for spherical equal-sized grains} \\ (1000, 2.8) & \text{for uniform, round grains} \\ (1500, 3.6) & \text{for irregular, edged grains} \end{cases} \tag{3.12}$$

For a stationary flow of pore water at moderate flow velocities, Eq. (3.9) reduces to the usual form of Darcy's law,

$$-p_{,i} = \frac{\rho_w g}{k}\dot{w}_i \tag{3.13}$$

Eq. (3.9) can be linearised by introducing an effective permeability coefficient, k_e, defined as

$$\frac{1}{k_e} = \frac{1}{k} + b \cdot |\dot{w}_a| \tag{3.14}$$

where $\dot{w}_a$ is an average flow velocity. In the following it is assumed that the displacement of the grain skeleton is small compared to that of the pore water. Then $w_i = v_i$ and Eq. (3.9) becomes

$$-p_{,i} = \frac{\rho_w(1+e)}{e}\ddot{v}_i + \frac{\rho_w g}{k_e}\dot{v}_i \tag{3.15}$$

Application of the continuity condition, $\dot{v}_{i,i} = 0$, to Eq. (3.15) yields the Laplace equation:

$$\nabla^2 p = \frac{\partial^2 p}{\partial x^2} + \frac{\partial^2 p}{\partial y^2} + \frac{\partial^2 p}{\partial z^2} = 0 \tag{3.16}$$

which then becomes the governing equation for the determination of the pore water flow. Several solutions of Laplace's equation, Eq. (3.16) exist for different forms and boundary conditions. Examples for ship sections were given in the form of added mass in Eq. (3.6). Many other examples have been published, for instance by Lamb [65], Newman [84] or Landweber [66].

To illustrate how the pore water pressure acts on a bow, the simple example shown in Figure 3.4 can be considered.

A plane problem is considered but the method is the same for a three-dimensional problem. A semi-circular body of width B, is at velocity U_b and acceleration $\dot{U}_b$ pressed into a saturated soil. The boundary conditions are:

1. No fluid flow into the bow.
2. The pressure is zero at the soil surface.

The solution to this problem can be found in [88]. Expressed as a function of a radial coordinate r and an angular coordinate α, Figure 3.4, the pressure on the bow is

$$p(r,\alpha) = \frac{1}{4}\frac{B^2\,\cos\alpha}{r}\,\kappa \tag{3.17}$$

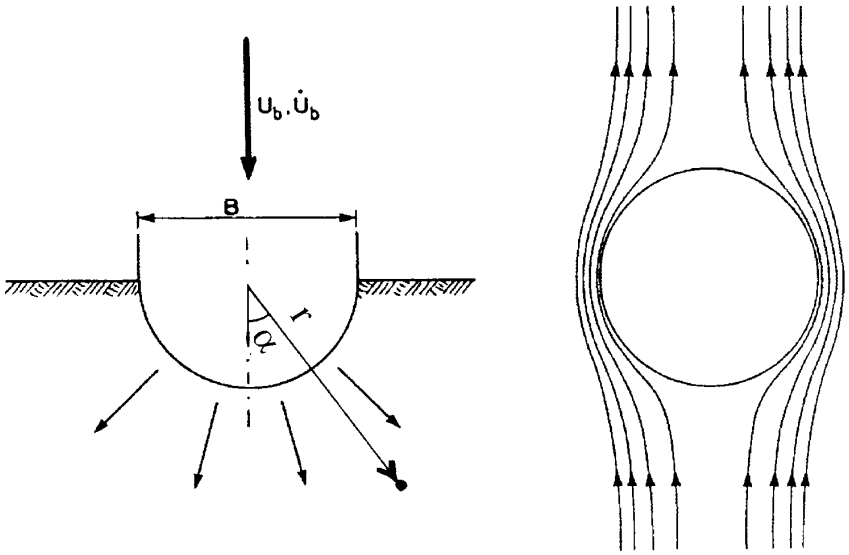

Figure 3.4: *Pore water flow around a section of a semi-circular bow.*

where

$$\kappa = \frac{\rho_w(1+e)}{e}\dot{U}_b + \frac{\rho_w g}{k_e}U_b \tag{3.18}$$

Integrating the vertical component of the pressure over the bow surface gives the total vertical force:

$$F_P = \int_{-\pi/2}^{\pi/2} (B/2)\, p(r = B/2, \alpha)\, \cos\alpha \, d\alpha = \frac{1}{2}\,\frac{\pi B^2}{4}\,\kappa \tag{3.19}$$

The resulting force is often expressed in terms of an added mass coefficient C_M (C_V in Eq. (3.6)) and a volume of reference, V_R. In the above example of a circular body with diameter B, $C_M = 1$ and $V_R = (\pi/4)B^2$ so that Eq. (3.19) could be written in a more general way as

$$F_p = \frac{1}{2}\, C_m\, V_R\, \kappa \tag{3.20}$$

The factor of $1/2$ is introduced when $C_M V_R$ is calculated for a completely immersed body subjected to fluid pressure on both sides. Added mass characteristics, $C_M V_R$, are tabulated for a large number of geometries and boundary conditions, and Eq. (3.20) therefore represents a very useful and convenient form for calculation of the result of pore water pressure

in the numerical scheme.

Force Corresponding to Drained Rupture

During grounding in normal sand, the pore water pressure is governing the soil reaction. Only at very low velocities and when the ship has stopped, the conditions are drained and the load is carried by the grain skeleton alone.

The parts of the hull penetrating the soil are approximated by a series of plane surfaces and with these assumptions, standard formulas for drained rupture in saturated sand can be used. Rupture around the bow is clearly three-dimensional but the assumption of plane strain is made here with an empirical correction due to three-dimensionality.

If it is that the rupture is fully developed and that strain hardening can be neglected, the normal effective soil pressure on the sides can be calculated by use of the theory for passive soil pressure on plane walls. The soil pressure, e_s, normal to the wall in the depth, d_p, is

$$e_s = \gamma' \, d_p \, K_\gamma \tag{3.21}$$

where γ' is the submerged weight of the soil and the rupture coefficient, K_γ, is a function of frictional angle, slope inclination and surface roughness as it is given in standard geotechnical literature (e.g. [47]). Eq. (3.21) can be integrated to give the normal force on the bulb and the ship sides.

The maximum possible drained soil reaction on the ship bottom is found from the theory of load capacities of foundations. A strip of length dl and width B can carry the load

$$d\,Q = \frac{1}{2}\gamma' \, N_\gamma \, B^2 \, dl \tag{3.22}$$

where the coefficient N_γ is given in standard geotechnical tables (e.g. [47]). Integration of Eq. (3.22) along the length of the contact area gives the load capacity, Q, based on the assumption of two-dimensional rupture. To compensate for three-dimensional effects, Q is reduced by an empirical factor of $s_\gamma = (1 - 0.4 B_{max}/L_{max})$ where B_{max} and L_{max} are, respectively, the maximum width and the maximum length of the contact area ($B_{max}/L_{max} < 1$), [48]. This maximum load, $Q_{max} = s_\gamma \, Q$, is not necessarily reached over the whole contact area of the ship bottom - in some areas the ground is elastically compressed and in other areas the rupture is fully developed. Therefore, the loading and unloading behaviour up to and from the maximum load has to be defined. This is particularly important in the final phase where equilibrium between the hydrostatic forces on the ship hull and the drained soil reaction on the ship bottom has to be reached. From tests with passive soil pressure on plane walls it is known that the maximum soil pressure is mobilised after a displacement of

approximately 1 - 5 per cent of the height of the wall. On this basis, it is assumed here that the load, Q_{max}, corresponding to the fully developed rupture is reached after a compression of a certain fraction, δ, of the foundation width, B_{max}. Correspondingly, unloading from Q_{max} is assumed to occur over a distance of $\delta\, B_{max}$. It turns out that the grounding behaviour is quite insensitive to the choice of δ so that a fixed value of $\delta = 0.03$ is used.

3.3.2 Numerical Implementation

The grounding behaviour is quite sensitive to the bow geometry and the numerical model must therefore include a reasonable representation of the actual geometry. Many bulbous bows have the shape of a half-sphere mounted on a cylinder and this is easily represented mathematically. The rest of the bow often consists of double curved surfaces. Such general shapes cannot be defined by simple analytical functions. In the present numerical model the idealisation shown in Figure 3.5 is used. The soil pressure on a V-bow is assumed to work on the ship bottom and on the plane sides defined by the points A, B and C in Figure 3.5. When a bulbous bow is considered, an additional soil reaction on the front spherical part is also calculated.

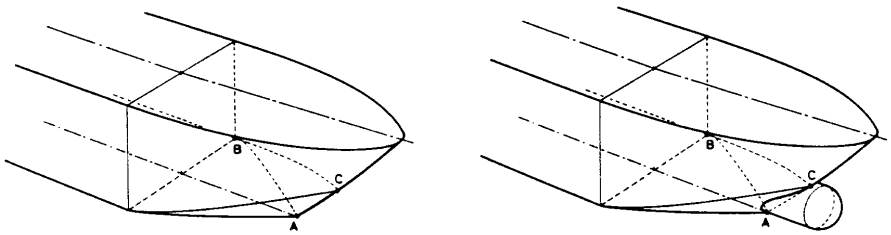

Figure 3.5: *Idealisation of V-bow and bulbous bow used in calculation model.*

As shown in Figure 3.1 the ship is assumed to sail perpendicularly onto a sloping sea bed bottom of a bi-linear shape.

3.4 Structural Response by Modal Analysis Approach

It is assumed that the structural behaviour of the ship hull can be modelled by linear Timoshenko beam theory. It is shown later that the linear elastic limit of the hull girder may actually be exceeded but it is assumed a priori that the hull girder response is purely elastic.

3.4.1 Loads

In addition to the loads from the ground and the surrounding water described previously, inertia loads are here treated as external loads in the usual manner. If the added mass in surge is denoted μ_x, the translational and angular momentum vectors for a section of unit length are

$$\vec{B}(x) = [(m+\mu_x)\dot{u}, 0, (m+\mu_z)\dot{w}] \tag{3.23}$$

$$\vec{I}_0(x) = \left[0, j_y(x)\,\dot{\psi}, 0\right] \tag{3.24}$$

where m and j_y are structural mass and moment of inertia per unit length respectively. The inertia forces acting on a segment of the hull can now be determined by expressions formulated in vector form as

$$\vec{q}_i(x) = -\frac{\partial \vec{B}}{\partial t} - \vec{\omega} \times \vec{B} \tag{3.25}$$

$$\vec{m}_i(x) = -\frac{\partial \vec{I}_0}{\partial t} - \vec{\omega} \times \vec{I}_0 - \vec{U} \times \vec{B} \tag{3.26}$$

where $\vec{U} = (\dot{u}, 0, \dot{w})$ is the translatory velocity of the section and $\vec{\omega} = (0, \dot{\psi}, 0)$ is the instantaneous angular velocity in the instantaneous moving local coordinate system. By use of Eqs. (3.23, 3.24), Eq. (3.25) and Eq. (3.26) can be transformed to scalar form:

$$q_{i,x}(x) = -(m+\mu_x)\,\ddot{u} - (m+\mu_z)\dot{\psi}\dot{w} \tag{3.27}$$

$$q_{i,z}(x) = -(m+\mu_z)\,\ddot{w} + (m+\mu_x)\dot{\psi}\dot{u} \tag{3.28}$$

$$m_{i,y}(x) = -j_y\ddot{\psi} + (\mu_z - \mu_x)\dot{u}\dot{w} \tag{3.29}$$

The reaction from the ground results from a soil pressure on a finite area of the hull but since the contact area is relatively small for the considered types of grounding, it is convenient to condense the soil pressure to a load vector, $[F_{x,G}, F_{z,G}, M_{y,G}]$, by using the Dirac delta function, δ. All in all, the distributed loads along the hull girder are then

$$q_x(x) = -(m+\mu_x)\,\ddot{u} - (m+\mu_z)\dot{\psi}\dot{w} + \delta(x_c)F_{x,G} \tag{3.30}$$

$$\begin{aligned} q_z(x) = {} & -(m+\mu_z)\,\ddot{w} + (m+\mu_x)\dot{\psi}\dot{u} - \rho_w\, g\, B(x)\, w(x) \\ & - \int_0^t h_z(x,\tau)\left\{\dot{w}(x, t-\tau) - \dot{w}(x, t-\tau=0)\right\} d\tau + \delta(x_c)F_{z,G} \end{aligned} \tag{3.31}$$

$$m_y(x) = -j_y\ddot{\psi} + (\mu_z - \mu_x)\dot{u}\dot{w} + \delta(x_c)M_{y,G} \tag{3.32}$$

where x_c is the position of the point of attack for the soil reaction force.

3.4.2 Dynamic Timoshenko Beam Equations

If the coupling between axial deformation and vertical bending of the hull beam is neglected, the condition for equilibrium of an infinitesimal element of the hull girder in the $x-$direction gives

$$\frac{\partial}{\partial x}\left[EA\left(1+\eta\frac{\partial}{\partial t}\right)\frac{\partial u}{\partial x}\right] = -q_x(x) = (m+\mu_x)\ddot{u} + (m+\mu_z)\dot{\psi}\,\dot{w} - \delta(x_c)F_{x,G} \tag{3.33}$$

Figure 3.1 shows positive directions for the sectional forces. Here E denotes Young's modulus, $A = A(x)$ is the effective cross-sectional area of the hull, η is a structural damping coefficient. If the Timoshenko beam theory is used, the corresponding equations for moment and vertical equilibrium are

$$\frac{\partial}{\partial x}\left[EI_y\left(1+\eta\frac{\partial}{\partial t}\right)\frac{\partial \psi}{\partial x}\right] - k_z GA\left(1+\eta\frac{\partial}{\partial t}\right)\left(\frac{\partial w}{\partial x}+\psi\right) = \tag{3.34}$$

$$-m_y(x) = j_y\,\ddot{\psi} + (\mu_x-\mu_z)\dot{u}\dot{w} - \delta(x_c)\,M_{y,G}$$

and

$$\frac{\partial}{\partial\, x}\left[-k_z GA\left(1+\eta\frac{\partial}{\partial t}\right)\left(\frac{\partial w}{\partial x}+\psi\right)\right] = -q_z(x) = \tag{3.35}$$

$$(m+\mu_z)\,\ddot{w} - (m+\mu_x)\dot{\psi}\,\dot{u} + \rho_w\, g\, B\, w -$$

$$\delta(x_c)\,F_{z,G} + \int_0^t h_z(x,\tau)\,\{\dot{w}(x,t-\tau) - \dot{w}(x,t-\tau=0)\}\,d\tau$$

Here $I_y = I_y(x)$ denotes the cross sectional moment of inertia, $k_z A = k_z A(x)$ is the vertical shear area, G is the material shear modulus.

3.4.3 Solution Methodology

The solutions of Eqs. (3.33, 3.34, 3.35) will be sought in the form

$$\begin{aligned} u(x,t) &= \tilde{u}_0(t) + \sum_{i=1}^{N} g_i(t)\,u_i(x) \\ w(x,t) &= \tilde{w}_0(t) - x\,\tilde{\psi}_0(t) + \sum_{i=1}^{M} f_i(t)\,w_i(x) \\ \psi(x,t) &= \tilde{\psi}_0(t) + \sum_{i=1}^{M} f_i(t)\,\psi_i(x) \end{aligned} \tag{3.36}$$

where $\tilde{u}_0(t)$, $\tilde{w}_0(t)$ and $\tilde{\psi}_0(t)$ denote rigid body surge, heave and pitch motions, respectively, and $\{(u_i(t), w_i(t), \psi_i(t)),\ i = 1, 2, \ldots\}$ are the normalised eigenfunctions associated with free vibrations of the ship in water.

The eigenfunctions $u_i(x)$ are determined from the eigenvalue problem consisting of the differential equation and the boundary conditions, respectively:

$$-\left(EAu_i'\right)' = \Omega_{a,i}^2 \left(m + \mu_x\right) u_i \tag{3.37}$$

$$\left(EAu_i'\right)_{x=x_{aft}} = \left(EAu_i'\right)_{x=x_{forw}} = 0 \tag{3.38}$$

where $\Omega_{a,i}$ is the i'th eigenfrequency for the longitudinal vibration and $'$ denotes differentiation with respect to x. Note that the added mass, μ_x, is at infinite frequency, i.e. it is independent of $\Omega_{a,i}$. The eigenfunctions can be normalised so that they satisfy the orthonormality condition:

$$\int_L u_i \left(m + \mu_x\right) u_j \, dx = \delta_{ij} \tag{3.39}$$

Similarly, the eigenfunctions (w_i, ψ_i) are determined from the following differential equations:

$$-(EI_y\psi')' + k_z GA\left(w' + \psi\right) = \Omega^2 j_y \psi \tag{3.40}$$

$$-\left[k_z GA\left(w' + \psi\right)\right]' = \Omega^2 \left(m + \mu_z\right) w \tag{3.41}$$

with the boundary conditions

$$\left(EI_y\psi'\right)_{x=x_{aft}} = \left(EI_y\psi'\right)_{x=x_{forw}} = 0 \tag{3.42}$$

$$\left[k_z GA\left(w' - \psi\right)\right]_{x=x_{aft}} = \left[k_z GA\left(w' - \psi\right)\right]_{x=x_{forw}} = 0 \tag{3.43}$$

Since this eigenvalue problem is self-adjoint, the normalised eigenfunctions $\{w_i, \psi_i\}$ and $\{w_j, \psi_j\}$ corresponding to the eigenvalues Ω_i^2 and Ω_j^2, respectively, fulfil the following orthonormality relations:

$$\int_L \left\{\psi_i j_y(x) \psi_j + w_i \left(m + \mu_z\right) w_j\right\} \, dx = \delta_{ij} \tag{3.44}$$

$$\int_L \left\{\psi_i \left(EI\psi_j'\right)' + \psi_i k_z GA\left(w_j' + \psi_j\right) + w_i \left[k_z GA\left(w_j' + \psi_j\right)\right]'\right\} \, dx = \Omega_i^2 \, \delta_{ij} \tag{3.45}$$

where δ_{ij} is Kronecher's delta.

The boundary conditions in Eqs. (3.38, 3.42 and 3.43) imply that the axial force, the bending moment and the shear force are zero at the forward end of the hull. The axial deformation turns out to be negligible and certainly, the bending moment at the forward end is small compared to the maximum bending moment in the hull girder. The shear force, on the other hand, attains its maximum value at the point of contact, so by using the eigenfunctions for a free-free beam a somewhat erroneous representation of the shear deformation at the forward part of the hull must be expected. The validity of the modal super-position approach was therefore checked by a finite element approach, as described later.

The solution assumption, Eq. (3.36), is now substituted into the governing equations, Eqs. (3.33, 3.34, 3.35). Multiplication of the resulting Eq. (3.33) with one eigenfunction at the time followed by integration over the length of the ship leads to the governing equation for the longitudinal rigid body motion:

$$M_{xx}\ddot{\tilde{u}}_0 + M_{zz}\left\{\dot{\tilde{w}}_0\dot{\tilde{\psi}}_0 - x_{gz}\dot{\tilde{\psi}}_0^2\right\} = F_{x,G}(t) \tag{3.46}$$

where

$$M_{xx} = \int_L \{m(x) + \mu_x(x)\}\, dx \tag{3.47}$$

$$M_{zz} = \int_L \{m(x) + \mu_z(x)\}\, dx \tag{3.48}$$

$$x_{gz} = \int_L \{m(x) + \mu_z(x)\}\, x dx / M_{zz} \tag{3.49}$$

It is assumed that the quadratic terms $(\dot{w}\dot{\psi})$ can be neglected. The amplitude functions $g_i(t)$ for the longitudinal vibrations can then be found by solving the following second order differential equations:

$$\ddot{g}_i(t) + \eta\Omega_{ai}^2\dot{g}_i(t) + \Omega_{ai}^2 g_i(t) = F_{x,G}\cdot u_i(x_c) \tag{3.50}$$

Performing analogous multiplications and integrations to Eqs. (3.34, 3.35) gives the following equations for the heave and pitch rigid body motions:

$$\begin{aligned} J_y\ddot{\tilde{\psi}}_0 + (M_{xx} - M_{zz})\,\dot{\tilde{u}}_0\dot{\tilde{w}}_0 + x_{gz}M_{zz}\left(\dot{\tilde{u}}_0\dot{\tilde{\psi}}_0 - \ddot{\tilde{w}}_0\right) \\ -\rho_w\, g\, S_w\tilde{w}_0 + \rho_w\, g\, I_w\,\tilde{\psi}_0 = M_{y,G} + x_c\, F_{z,G} \\ + \int_0^t h_{zx}(\tau)\left\{\dot{\tilde{w}}_0(t-\tau) - \dot{\tilde{w}}_0(t-\tau=0)\right\} d\tau \\ - \int_0^t h_{zx^2}(\tau)\left\{\dot{\tilde{\psi}}_0(t-\tau) - \dot{\tilde{\psi}}_0(t-\tau=0)\right\} d\tau \end{aligned} \tag{3.51}$$

and

$$\begin{aligned} M_{zz}\ddot{\tilde{w}}_0 - M_{xx}\dot{\tilde{u}}_0\dot{\tilde{\psi}}_0 - x_{gz}M_{zz}\ddot{\tilde{\psi}}_0 - \rho_w\, g\, S_w\tilde{\psi}_0 + \rho_w\, g\, A_w\, \tilde{w}_0 = \\ F_{z,G} + \int_0^t h_z(\tau)\left\{\dot{\tilde{w}}_0(t-\tau) - \dot{\tilde{w}}_0(t=0)\right\} d\tau \\ + \int_0^t h_{zx}(\tau)\left\{\dot{\tilde{\psi}}_0(t-\tau) - \dot{\tilde{\psi}}_0(t=0)\right\} d\tau \end{aligned} \tag{3.52}$$

where

$$\begin{aligned} J_y &= \int_L \left\{j_y(x) + x^2\,(m(x) + \mu_z(x))\right\} dx \\ A_w &= \int_L B(x)\, dx \\ S_w &= \int_L x\, B(x)\, dx \\ I_w &= \int_L x^2\, B(x)\, dx \\ h_z(\tau) &= \int_L h_z(x,\tau)\, dx \\ h_{zx}(\tau) &= \int_L x\, h_z(x,\tau)\, dx \\ h_{zx^2}(\tau) &= \int_L x^2\, h_z(x,\tau)\, dx \end{aligned}$$

It must be noted here that the governing equations for the rigid body motion, Eqs. (3.46, 3.51 and 3.52), correspond to those derived for example by Abkowitz, [1].

Utilising the orthonormality relations, Eq. (3.44), gives the governing equations for the amplitude functions of the transverse vibration modes:

$$\ddot{f}_i(t) + \eta\Omega_i^2\,\dot{f}_i(t) + \Omega_i^2\, f_i(t) = F_{z,G}(t)\, w_i(x_c) + M_{y,G}(t)\, \psi_i(x_c) \tag{3.53}$$

In the derivation of Eq. (3.53), the terms which are quadratic in the structural vibration amplitudes are neglected and it is assumed that the natural frequencies, Ω_i, are so high that the memory effects represented by the convolution integrals can be neglected.

3.5 Structural Response by the Finite Element Approach

With the capabilities of modern computers, the finite element method has become the most popular numerical approach in structural mechanics. It was included in the present study to check the validity of the modal analysis approach. As for the modal analysis, the structural response is here modelled by application of the linear Timoshenko beam theory in accordance with Pedersen and Jensen, [89].

3.5.1 Solution Methodology

The overall idea of the method is to discretize the structure into a series of nodal points and connecting elements. The deformation of the structure is defined by the displacements and the rotations of the nodal points and the assumed deformation fields for the elements. Since each nodal point has six degrees of freedom at the most, the problem of finding the deformation of a continuous structure has been reduced to calculating the displacement and rotation of a finite number of points.

Knowing the stiffness and inertia of the connecting elements, global equilibrium for the structure can be expressed in matrix form as

$$\boldsymbol{M} \cdot \ddot{\boldsymbol{q}} + \boldsymbol{C} \cdot \dot{\boldsymbol{q}} + \boldsymbol{K} \cdot \boldsymbol{q} = \boldsymbol{Q} \tag{3.54}$$

where $\boldsymbol{M}$, $\boldsymbol{C}$ and $\boldsymbol{K}$ are the inertia, damping and stiffness matrices, $\ddot{\boldsymbol{q}}$, $\dot{\boldsymbol{q}}$ and $\boldsymbol{q}$ are the second, first and zeroth derivatives of the displacement and rotation vector and $\boldsymbol{Q}$ is a vector containing global external loads (i.e. forces and moments) on the structure.

Eq. (3.54) can be set up for general systems and examples of impressive solutions for very complex problems of structural crashworthiness are shown in Chapter 10. The most commonly used method for solving Eq. (3.54) for very dynamic problems like a car crash or a ship collision is normally referred to as 'the explicit method'. It is the least ingenious method (and the one used here): simply put everything except inertia terms into $\boldsymbol{Q}$, solve for the accelerations and integrate these twice to obtain velocities and displacements as a function of time. As mentioned, the method has proved applicable to highly dynamic problems, but it is normally not efficient for finding a (near) static equilibrium where inertia terms are not dominant.

3.5.2 Stiffness and Inertia of a Timoshenko Beam Element

Due to the varying stiffness and mass of the hull girder, it is divided into a number of beam elements. If the longitudinal deformation (not displacement) is ignored, each beam element has only two degrees of freedom, $(w_z, \theta_y) = (w, \theta)$, for the flexible deformation. Cubic interpolation functions are used in accordance with the approach of Jensen and Pedersen [89]. By means of the notation M and l for the element mass and the length, G for the material shear modulus and

$$\begin{aligned}
\eta_y &= EI_y/k_z GAl^2 \\
\rho_y &= 1/(1+12\,\eta_y) \\
\alpha_y &= (1+3\,\eta_y)\rho_y \\
\beta_y &= (1-6\,\eta_y)\rho_y
\end{aligned}$$

the element stiffness matrix can be written as

$$[k] = \begin{bmatrix}
\frac{12EI_y}{l^3}\rho_y & \frac{-6EI_y}{l^2}\rho_y & \frac{-12EI_y}{l^3}\rho_y & \frac{-6EI_y}{l^2}\rho_y \\
 & \frac{4EI_y}{l}\alpha_y & \frac{6EI_y}{l^2}\rho_y & \frac{2EI_y}{l}\beta_y \\
 & & \frac{12EI_y}{l^3}\rho_y & \frac{6EI_y}{l^2}\rho_y \\
 & & & \frac{4EI_y}{l}\alpha_y
\end{bmatrix} \tag{3.55}$$

and the elements of the inertia matrix as

$$\begin{aligned}
m_{1,1} &= M\rho_y^2\left[\frac{13}{35}+\frac{42}{5}\eta_y+48\eta_y^2+\frac{6}{5}\left(\frac{r_y}{l}\right)^2\right] \\
m_{1,2} &= M\rho_y^2 l\left[\frac{11}{210}+\frac{11}{10}\eta_y+6\eta_y^2-(6\eta_y-1/10)\left(\frac{r_y}{l}\right)^2\right] \\
m_{1,3} &= M\rho_y^2\left[\frac{9}{70}+\frac{18}{5}\eta_y+24\eta_y^2-\frac{6}{5}\left(\frac{r_y}{l}\right)^2\right] \\
m_{1,4} &= M\rho_y^2 l\left[\frac{13}{420}+\frac{9}{10}\eta_y+6\eta_y^2+(6\eta_y-1/10)\left(\frac{r_y}{l}\right)^2\right] \\
m_{2,2} &= M\rho_y^2 l^2\left[\frac{1}{105}+\frac{1}{5}\eta_y+\frac{6}{5}\eta_y^2+\left(\frac{2}{15}+2\eta_y+48\eta_y^2\right)\left(\frac{r_y}{l}\right)^2\right] \\
m_{2,3} &= -M\rho_y^2 l\left[\frac{13}{420}+\frac{9}{10}\eta_y+6\eta_y^2+(6\eta_y-1/10)\left(\frac{r_y}{l}\right)^2\right] \\
m_{2,4} &= M\rho_y^2 l^2\left[\frac{1}{140}+\frac{1}{5}\eta_y+\frac{6}{5}\eta_y^2+\left(\frac{1}{30}+2\eta_y-24\eta_y^2\right)\left(\frac{r_y}{l}\right)^2\right]
\end{aligned}$$

$$
\begin{aligned}
m_{3,3} &= M\rho_y^2\left[\frac{13}{35}+\frac{42}{5}\eta_y+48\eta_y^2+\frac{6}{5}\left(\frac{r_y}{l}\right)^2\right]\\
m_{3,4} &= -M\rho_y^2 l\left[\frac{11}{210}+\frac{11}{10}\eta_y+6\eta_y^2-(6\eta_y-1/10)\left(\frac{r_y}{l}\right)^2\right]\\
m_{4,4} &= M\rho_y^2 l^2\left[\frac{1}{105}+\frac{1}{5}\eta_y+\frac{6}{5}\eta_y^2+\left(\frac{2}{15}+2\eta_y+48\eta_y^2\right)\left(\frac{r_y}{l}\right)^2\right]
\end{aligned}
\tag{3.56}
$$

No transformations are needed, so the element matrices are assembled directly into the global stiffness and inertia matrices, which become banded with a width of four. Note that the element mass includes the added mass so that $M = \int_l (m+\mu_z)dx$.

3.5.3 Loads

As mentioned previously, the loads acting during the grounding are the ground reaction and the hydrostatic and hydrodynamic pressure. Hydrodynamic damping is neglected for reasons given in Chapter 4 and the hydrodynamic loads therefore enter the equations of motion as added mass in M. As in the modal analysis, the ground reaction is assumed to attack the structure in a nodal point (the foremost point) and is thus easily included in the system of equations. The hydrostatic loads are calculated from Eq. (3.1). By denoting the intensity of the vertical line load at the two nodal points of an element p_{z1} and p_{z2} and assuming a linear variation between the nodal points, the corresponding nodal forces are derived in [89]:

$$
\begin{aligned}
Q_{z,1} &= \rho_y\, l\,\left[\left(\frac{7}{20}+4\eta_y\right)p_{z1}+\left(\frac{3}{20}+2\eta_y\right)p_{z2}\right]\\
M_{y,1} &= \rho_y\, l^2\,\left[\left(\frac{1}{20}+\frac{1}{2}\eta_y\right)p_{z1}+\left(\frac{1}{30}+\frac{1}{2}\eta_y\right)p_{z2}\right]\\
Q_{z,2} &= \rho_y\, l\,\left[\left(\frac{3}{20}+2\eta_y\right)p_{z1}+\left(\frac{7}{20}+4\eta_y\right)p_{z2}\right]\\
M_{y,2} &= \rho_y\, l^2\,\left[\left(\frac{1}{30}+\frac{1}{2}\eta_y\right)p_{z1}+\left(\frac{1}{20}+\frac{1}{2}\eta_y\right)p_{z2}\right]
\end{aligned}
$$

3.6 Grounding-Induced Sectional Forces

The following two sections present theory for calculating the grounding induced sectional forces. The theory is divided into two parts although the governing equations are the same. The first section deals with the sectional forces during the grounding process, i.e. during those few seconds while the ship is being brought to a stop by the ground reaction. As

indicated above, the equilibrium of the hull girder during this process is determined both by static and dynamic effects. After the ship has stopped it rests on the sea bed until it is refloated and meanwhile the hull is subjected to the forces of wind, waves and tidal action. The sectional forces during this period, which may be up to several days, are considered in the second part. The analysis is split into two parts because the solution methodology is fundamentally different. During the grounding the accelerations are relatively large and the solution can be found by explicit integration of accelerations over time. The static solution after the grounding is independent of time and is considered as the equilibrium position of the ship where the bow lift is equal to the bow lift when the ship velocity has diminished to 1/1000 of the initial velocity.

3.6.1 Sectional Forces during the Grounding Process

The equations governing the ship motion during the grounding were set up above. Once the rigid body displacements and the flexible deformations are known, the sectional forces could be found from the constitutive relations

$$N_x = EA\frac{\partial u}{\partial x} \tag{3.57}$$

$$Q_z = k_z GA\left(\frac{\partial w}{\partial x} + \psi\right) \tag{3.58}$$

$$M_y = EI_y\frac{\partial \psi}{\partial x} \tag{3.59}$$

This approach works for the finite element solution but it turns out that in a modal analysis, a very large number of eigenfunctions and stations are needed for accuracy and convergence of Q_z and M_y. This problem, which is caused by the necessity of using derivatives of approximate eigenfunctions, is efficiently overcome by considering the overall equilibrium of the aft part of the hull, thus by working with integrals instead of derivatives. Equilibrium is formulated as

$$\frac{dN_x}{dx} = -q_x \tag{3.60}$$

$$\frac{dQ_z}{dx} = -q_z \tag{3.61}$$

$$\frac{dM_y}{dx} = Q_z - m_y \tag{3.62}$$

Since the boundary conditions at the aft end of the ship are very simple:

$$N_x(x = -L/2) = 0 \tag{3.63}$$
$$Q_z(x = -L/2) = 0 \tag{3.64}$$
$$M_y(x = -L/2) = 0 \tag{3.65}$$

it is convenient to integrate Eqs. (3.60 - 3.62) from $x = -L/2$ with the loads given by Eqs. (3.30 - 3.32).

3.6.2 Sectional Forces in Final Stopping Position

Even if a ship hull survives the loads during the actual grounding, the following additional loads from tide and waves may be fatal. In several of the large disastrous grounding accidents (for example that of the Braer), the hull damage was continuously increased over a long period of time due to waves acting on the ship while stuck on the cliffs. Modeling of such a behaviour would be very difficult to present in a generally applicable form, so the present study does not include any attempts to establish models for such a behaviour. Instead, the much simpler case of grounding followed by a receding tide is considered.

Figure 3.6 shows an example of a ship grounding event where the effect of a receding tide was very significant. The shown ship, the *Else Terkol*, is supported at two points close to the ends. This condition would be critical for the strength of the hull girder for many ships.

The sectional forces after the ship has stopped will be analysed here simply by considering loads due to an instance of static lifting at a certain point of the hull. This lifting arises partly from the grounding itself and partly from a tide following the grounding.

In the analysis presented by Pedersen, [122], where the hull was assumed to be rigid and have vertical sides, linear expressions were derived for the maximum sectional forces due to the static lift at a certain point of the ship bottom. For a flexible hull girder, however, the sectional forces give rise to a deformation which changes the loads. In the present section, the effect of this flexible deformation is investigated. As in the previous sections, it is assumed that the ship runs aground on a slope and rests on the bow, i.e. $x_c \approx L/2$. The displacement of a section of the hull is written in a form similar to Eq. (3.36):

$$w(x) = w_0 - x\,\psi_0 + w_f(x) \tag{3.66}$$

Figure 3.6: *Grounding of the Else Terkol in the Bristol Channel. The tide is 8 m.*

where $(w_0,\, \psi_0)$ is the rigid body lift and rotation measured amidships and $w_f(x)$ is the additional flexible deformation. The kinematic boundary conditions of the flexible problem are chosen to be $w_f = 0$ at $x = \pm L/2$. The flexible deformation is found by use of the finite element method. Faster and more sophisticated solution methods could be found but for the present analysis, which only requires few calculations, the finite element method is considered easy to implement. The element stiffness matrix for a prismatic Timoshenko beam element was given in Section 3.5. Generally, the finite element or stiffness method proves impractical for problems where insufficient kinematic boundary conditions are present - for example in an overall analysis of an aeroplane or a ship as in this case. The global stiffness matrix is then singular and artificial boundary conditions - for example based on symmetry conditions - have to be introduced. This introduction of boundary conditions was not necessary for the dynamic part of the grounding because the inertia matrix in Eq. (3.54) is non-singular, regardless of boundary conditions. In the present analysis, the problem is overcome by considering a beam, which is simply supported in both ends. The beam is indeed simply supported at the fore end but the final solution must have zero reaction at the aft support. An example of the loads, which are the distributed restoring load, q, and the ground reaction, $F_{z,G}$, is shown schematically in Figure 5.7. Vertical equilibrium gives

$$\begin{aligned} F_{z,G} &= -\int_{-L/2}^{L/2} q_z(x)\, dx \\ &= \rho_w\, g \int_{-L/2}^{L/2} \{w_0 B(x) - x\, \psi_0\, B(x) + B(x)\, w_f(x)\}\, dx \end{aligned} \tag{3.67}$$

Likewise, moment equilibrium around midship gives

$$
\begin{aligned}
x_c\, F_{z,G} &= -\int_{-L/2}^{L/2} x\, q_z(x)\, dx \\
&= \rho_w\, g \int_{-L/2}^{L/2} \left\{ x\, w_0\, B(x) - x^2\, \psi_0\, B(x) + x\, B(x)\, w_f(x) \right\} dx
\end{aligned} \tag{3.68}
$$

Due to the flexible deformation, w_f, the solution to this problem cannot be found immediately. The load on the beam and thus the deformation is a function by the deformation itself so an iterative solution is applied. Although not trivial the system is still linear, and if it is found to be necessary, a closed-form solution could be found for the considered flexible problem, which is actually the problem of a beam on an elastic foundation. The reduced force, F_z' and the moment M_y' are defined as

$$
F_z' = \frac{F_{z,G}}{\rho_w g} - \int_{-L/2}^{L/2} w_f(x) B(x)\, dx \tag{3.69}
$$

$$
M_y' = \frac{x_c\, F_{z,G}}{\rho_w g} - \int_{-L/2}^{L/2} x\, w_f(x)\, B(x)\, dx \tag{3.70}
$$

With a trial flexible deformation $w_{f,k}(x)$, an estimate of the rigid body displacement and rotation is found by solving Eq. (3.67) and Eq. (3.68) for w_0 and ψ_0:

$$
w_0 = \frac{F_z' - M_y'\, S_w / I_w}{A_w - S_w^2 / I_w} \tag{3.71}
$$

$$
\psi_0 = \frac{-M_y' + F_z'\, S_w / A_w}{I_w - S_w^2 / A_w} \tag{3.72}
$$

A definition of A_w, S_w and I_w was given in Section 3.4.3. The line load can now be calculated for this configuration and the corresponding refined flexible deformation, $w_{f,k+1}(x)$, can be found by solving the static finite element equations, $\boldsymbol{K} \cdot \boldsymbol{q} = \boldsymbol{Q}$. As a measure of the residual load the quantities

$$
F_{z,resid} = F_{z,G} + \int_{-L/2}^{L/2} q_z(x)\, dx \tag{3.73}
$$

$$
M_{y,resid} = x_c\, F_{z,G} + \int_{-L/2}^{L/2} x\, q_z(x)\, dx \tag{3.74}
$$

are chosen and a convergence criterion is formulated as

$$max\left\{\left|\frac{F_{z,resid}}{F_{z,G}}\right|,\left|\frac{M_{y,resid}}{x_c\,F_{z,G}}\right|\right\}\leq\epsilon \tag{3.75}$$

The problem converges very fast and an accuracy corresponding to $\epsilon = 10^{-5}$ is reached within 2 - 3 iterations.

When the displacement, w, of sections along the hull is known, the distribution of the *grounding-induced* shear force and bending moment are easily found from Eqs. (3.1, 3.61, 3.62).

Considering a rigid ship with vertical sides, Pedersen, [122], derived approximate expressions for the maximum shear force and bending moment around midship. When the distance from the longitudinal centre of flotation to the contact point is $L/2$, the expressions are

$$\begin{aligned} Q_{ext} &= \frac{Z_{bow}\,\rho_w\,g\,A_w}{4\left(1+(L/2r)^2\right)}\left(2-\frac{1}{4}\frac{L^2}{r^2}-\frac{4\,r^2}{L^2}\right) && \text{at } x=-r^2/l \\ M_{ext} &= -\frac{1}{27}Z_{bow}\,\rho_w\,g\,A_w\,L && \text{at } x=L/2-2r^2/l \end{aligned} \tag{3.76}$$

where Z_{bow} is the lift of the bow, l is the distance from the longitudinal centre of flotation to the contact point and r is an inertia radius defined from the longitudinal metacentric height GM_L, the water plane area A_w and the submerged volume ∇ as

$$r=\sqrt{\frac{\nabla\,GM_L}{A_w}} \tag{3.77}$$

3.7 Hull Girder Strength

In order to apply the theory presented above to risk assessment in connection with ship grounding, the ship strength in reserve for the grounding loads must be known. Numerous methods have been presented for prediction of the ultimate strength of a hull girder, for example Caldwell [26], Smith [116], Yao and Nikolov, [143]. It is important to note, however, that it is the *reserve* strength which is relevant to a comparison with the calculated grounding-induced loads. Hence, the still-water loads (and perhaps some wave loading) have to be considered together with the grounding loads. The importance of this is exemplified by the fact that ships have been lost due to hull girder failure even when floating freely in calm

water. For example the VLCC the *Energy Concentration* collapsed during discharge of oil in Rotterdam in 1980, [107].

In principle, the analysis could be done in two ways. The total ultimate strength of the hull girder could be compared to the grounding-induced loads together with still water loads and perhaps some wave or tidal load. If all information about a given grounding is available this approach is attractive because it contains the choice of very accurate analysis. The ultimate strength of ship sections exposed to both bending and shear could be considered as indicated by Hansen, [46].

Alternatively, since the design of the ship is often based on a still-water load and a wave load, it is meaningful to compare the design wave load to the grounding-induced load on the basis of the idea that the actual wave load in a grounding situation is probably small. To get a first estimate of how the grounding-induced loads compare with the strength of certain ship types, the simplicity of this approach makes it the most attractive. The current study is based on this approach which was also presented by Pedersen in [122].

Large Vessels

In [85] results were presented for the maximum wave loads predicted to occur during the life of a large ship, based on a probability level of 10^{-8} and maximum wave-induced bending and shear stresses of 110 N/mm^2. An analysis by Bai et al., [18], showed that for bulk carriers without significant corrosion, the sagging moment at the ultimate collapse is about 28 % higher than the allowable bending moment specified by the IACS. To get a first idea of how grounding-induced loads compare with ship strength, however, the formulas adopted by the IACS are considered to be sufficiently accurate.

According to the sign convention shown in Figure 3.1, the wave-induced bending moment is given by

$$M_W = \begin{cases} 0.19F_0(x)CL^2BC_B & \text{for sagging moment} \\ 0.11F_0(x)CL^2B(C_B+0.7) & \text{for hogging moment} \end{cases} \tag{3.78}$$

where M_W is in kNm, L and B should be in metres and C_B should not be less than 0.6. F_0 is a distribution factor which varies between 0 and 1 (0 at ends and 1 around midship). The maximum wave-induced shear force (in kN) to be expected over the lifetime at the given probability level is

$$Q_W = \begin{cases} 0.3F_1(x)CLB(C_B+0.7) & \text{for } Q_W > 0 \\ 0.3F_2(x)CLB(C_B+0.7) & \text{for } Q_W < 0 \end{cases} \tag{3.79}$$

where $F_1(x)$ and $F_2(x)$ are 0 at the hull ends and between 0 and respectively 1 and 0.92 over the hull length. The coefficient C is a function of length:

$$C = \begin{cases} 10.75 - \left(\frac{300-L}{100}\right)^{1.5} & \text{for } 90 \leq L \leq 300 \\ 10.75 & \text{for } 300 < L < 350 \\ 10.75 - \left(\frac{L-350}{150}\right)^{1.5} & \text{for } 350 \leq L \end{cases} \tag{3.80}$$

High-Speed Vessels

The increasing popularity of fast vessel concepts has made a study of this category of ships relevant. The environmental damage following hull failure of a fast ferry will most likely be very limited compared to that of a large tanker, but accidental groundings have demonstrated the potential fatality of this type of accident, [86]. A high-speed vessel is defined as one where $V/\sqrt{L} > 4.2$ (V is the maximum ship speed in knots and L is ship length in metres). Unfortunately, classification societies do not separate design loads in still-water and bending contributions, so the present study compares the grounding-induced loads to the total strength, neglecting still-water loads. Det Norske Veritas, [134], gives the following values for the total design bending moment (in kNm) as:

$$M_b = \begin{cases} 0.125L^2BC_W(C_B + 0.7)\left(0.85 + k_1\frac{V}{\sqrt{L}}\right) & \text{for hogging moment} \\ 0.3L^2BC_WC_B & \text{for sagging moment} \end{cases} \tag{3.81}$$

where $k_1 = 0.25$ at unrestricted service, and the wave coefficient C_W is considered according to

$$C_W = \begin{cases} 0.08L & \text{for L} < 100 \\ 6 + 0.02L & \text{for L} > 100 \end{cases} \tag{3.82}$$

Following DNV, [134], a vertical shear force (in kN) can be related to the bending moment from Eq. (3.82) by the relation

$$Q_b = \frac{4\,M_b}{L} \tag{3.83}$$

which is connected to requirements for the bending moment through $Q_b = dM_b/dx$. The equations presented above will be used later for the reserve strength of the hull girder. As already mentioned, the application of these formulas introduces uncertainties about the still-water loads but as a first conservative estimate of the magnitudes of the grounding loads compared to the strength, the formulas are considered sufficiently accurate.

Chapter 4

Verification and Discussion of the Theoretical Soft-Grounding Model

The objective of the present chapter is to discuss and validate the presented theoretical model. In connection with the construction of the fixed link across the Great Belt in Denmark, a series of model- and large-scale tests was conducted to investigate the mechanics of soft grounding. Some results of these experiments were already shown in Figure 3.3 and below more results are presented to validate the theoretical model.

4.1 Model Tests

4.1.1 Experimental Set-up

Figure 4.1 shows the experimental set-up. A tanker model in scale 1:60 was forced into a sand beach at a constant horizontal velocity. The bow of the ship was connected to the rest of the hull by a dynamometer making it possible to measure the vertical shear force at this cross section of the ship. Based on the measured vertical shear force, the heave and pitch motions and the hydrostatic properties, the vertical ground reaction acting on the bow during the grounding could be determined. The horizontal reaction was measured directly as the force necessary to push the ship onto the ground. Some of the main data for the experiments is given in Table 4.1.

4.1.2 Results and Validation

The calculated ground reaction is sensitive to the modelling of the ground response, hydrodynamic loads and hydrostatic loads, so it is well suited for comparison between measurements and calculations.

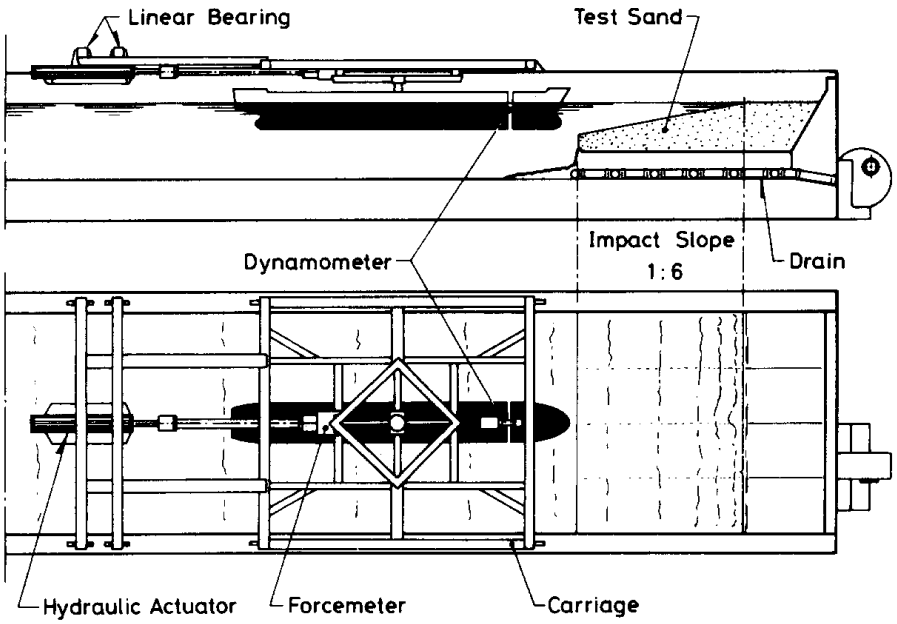

Figure 4.1: *Experimental setup for model testing of soft grounding.*

Table 4.1: *Main data for model scale grounding experiments.*

Length, L	2.57 m
Beam, B	0.378 m
Initial Draft, T	0.117 m
Ship mass, M_s	78.4 kg
Impact velocity, V	0.265 - 0.664 m/s
Slope inclination	1 : 6
Mean grain size, d_m	0.125 mm

Figure 4.2 shows the measured and the calculated vertical soil reaction for two tests where the impact velocity was 0.664 m/s. Very good correspondence between measurements and calculations is observed.

As it will be shown later, the behaviour of an initial peak followed by a continuous increase in the soil reaction is more or less characteristic of soft groundings. The initial peak of the soil reaction transfers momentum to the ship, so that the motion is changed from surge to a mode of motion where the bow somewhat follows the slope. The following gradual increase is due to the continuous lifting of the bow as the ship moves forward.

For analysis of the dynamic response of the hull girder, it is the initial peak of the soil reaction, which induces the hull vibration, so it is important that this peak is correctly modelled. Figure 4.3 shows the measured and the calculated vertical ground reaction for different impact velocities. The calculated soil reactions show a more dynamic behaviour

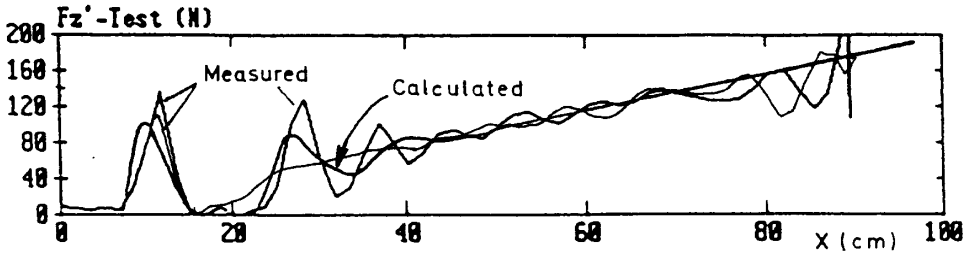

Figure 4.2: *Vertical ground reaction vs. horizontal position of ship. Theoretical prediction and results of two tests where the impact velocity was 0.664 m/s.*

after the first peak but other experiments actually also showed this behaviour, see for example Figure 4.2. All in all the agreement between measurements and calculations is very good.

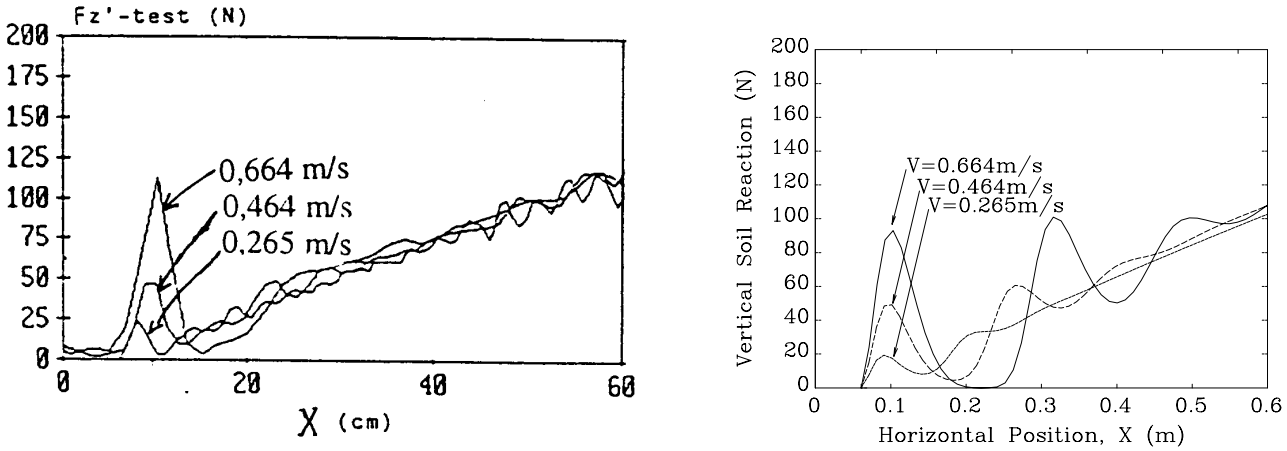

Figure 4.3: *Measured and calculated vertical ground reaction vs. horizontal position of ship for different impact velocities.*

Experiments were also carried out with a larger grain size corresponding to gravel in full scale and the theoretical model depicts the behaviour of this material with all its main characteristics but with greater errors for the peak forces. All in all, however, the comparisons indicate that the theoretical model is capable of predicting the vertical ground reaction from normal beach material. With a good theoretical prediction of the vertical soil reaction it is interesting to compare measured and calculated values for the effective coefficient of friction. This coefficient of friction is defined as the ratio of the soil reaction in the direction of the bow motion to the soil reaction in the normal direction. Figure 4.4 shows measured and calculated values for this quantity in experiments with different impact velocities. Some scatter of the experimental results is observed but the overall agreement with the theoretical predictions is good. Again, it is worth noting that the effective coefficient of friction is about 0.6 - 1.0, indicating a significant contribution of the passive soil pressure in front of the bow to the total resistance.

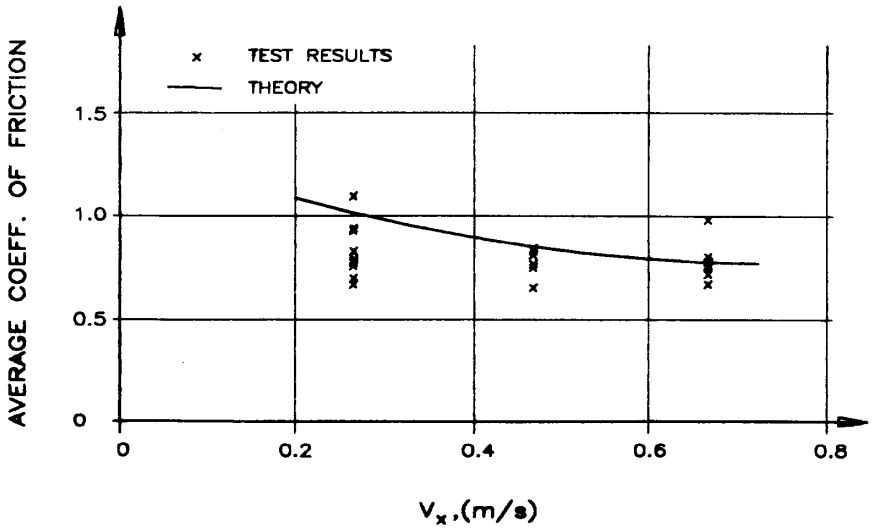

Figure 4.4: *Effective coefficient of friction vs. model ship velocity.*

4.2 Large-Scale Tests

Being able to predict the grounding response in model scale, the Great Belt Link Ltd conducted a series of large scale tests in March 1993 to verify model tests and the mathematical model. The test results were most recently published by Sterndorff and Pedersen [117].

4.2.1 Experimental Set-up

The tests were conducted by running a condemned fishing vessel up on selected beaches at impact velocities ranging between 2 m/s and 5.5 m/s. During the tests, surge, heave and pitch accelerations were measured as well as deformations of the beach and the ship bow. Based on the accelerations, rigid body velocities and motions were determined. The forces arising from the interaction between the bow of the vessel and the soil were determined by the accelerometer recordings and the equations of motion for the ship.

Figure 4.5 shows the vessel in a grounded position after test no. 1. The waves were small the first day (tests nos. 1 and 2) but significant the other days.

Main data for the experiments is given in Table 4.2.

4.2.2 Results and Validation

Measured and calculated rigid body accelerations, vertical and horizontal ground reaction forces, the effective coefficient of friction and stopping distances are compared below. All

Figure 4.5: *Grounded ship in large-scale test no. 1.*

test data is from [117] and all calculated results - including those published in [117] - were produced by the author with the theoretical model presented above.

Figure 4.6 shows the rigid body accelerations for the vessel during grounding test no. 4. Some difference is observed between the peak values of the acceleration but the overall behaviour of the measured and the calculated response is identical.

Figure 4.7 shows measured and calculated values for the vertical and the horizontal soil reaction during the impact. First it is noted that the overall behaviour is similar to that shown in Figure 4.2 for the model tests - an initial peak is followed by a gradual increase in forces. It is seen that the overall behaviour of the measured and the calculated forces

Table 4.2: *Main data for large scale grounding experiments.*

Length, L	29.55 m
Beam, B	6.60 m
Initial Draught, T	3.30 m
Displacement, M_s	298.6 t
Metacentric height, GM_L	28.9 m
Impact velocity, V	2.0 - 5.5 m/s
Slope inclination	1 : 20 - 1 : 4
Mean grain size, d_m	1.0 - 2.0 mm

is identical. A closer look, however, reveals a difference in the magnitude of the peak soil reactions and also in the duration of the initial peak. The difference in peak force can be due to uncertainties in the modelling of hydrodynamic loads. The difference in the duration of the initial peak is most likely due to the difficulty of modelling the complex double curved hull shape by a plane ship side and a plane ship bottom as shown in Figure 3.5. This is a limitation of the theoretical model which could be removed in future studies.

As regards comparison of measured and calculated values, it must be noted that derivation of the required quantities from the measured data is a cumbersome task which is associated with uncertainties - for example the added mass, the point of attack for the ground force and the effect of waves. Therefore, a discrepancy between measured and calculated values does not necessarily indicate an erroneous theoretical model - it also indicates the difficulty of the deterministic approach to a partly stochastic problem. The content of the soil should be described by a distribution function rather than just a mean diameter. Moreover, some of the large scale tests revealed a rather significant dependence of the grounding behaviour on the waves. Finally, it should be noted that due to uncertainties, such as modelling of added mass and the soil permeability, some parameters of the theoretical model could be changed to enhance the agreement with measured quantities, but the presented results are based on the theory given in previous sections.

Figure 4.8 shows a comparison between measured and calculated values for the effective coefficient of friction in test no. 1. Good agreement is seen during most of the grounding.

To give an overall picture of the prediction of the theory compared to measurements, Table 4.3 shows measured and calculated values for the stopping distance. Due to the uncertain measurements of the underwater slope, calculations are performed with both the largest and the smallest slope estimated. There is seen to be a tendency towards overprediction of the stopping distance for the theoretical model but the overall agreement is good. The bad agreement for test no. 7 waves is most likely due to the effect of the waves.

Table 4.3: *Measured and calculated stopping distances in large scale tests.*

Test no.	Impact vel. (m/s)	Slope 1:X	Measured dist. (m)	Calculated dist. (m)
1	2.5	12-14	9.6	10.9 - 11.6
2	5.1	9-11	16.4	16.6 - 18.1
3	5.1	4-6	12.1	9.9 - 13.4
4	4.1	4-6	8.1	8.3 - 11.1
5	4.1	10-15	16.6	14.7 - 17.3
6	5.0	8-15	17.3	16.7 - 19.8
7	4.5	11-18	13.2	17.2 - 20.7

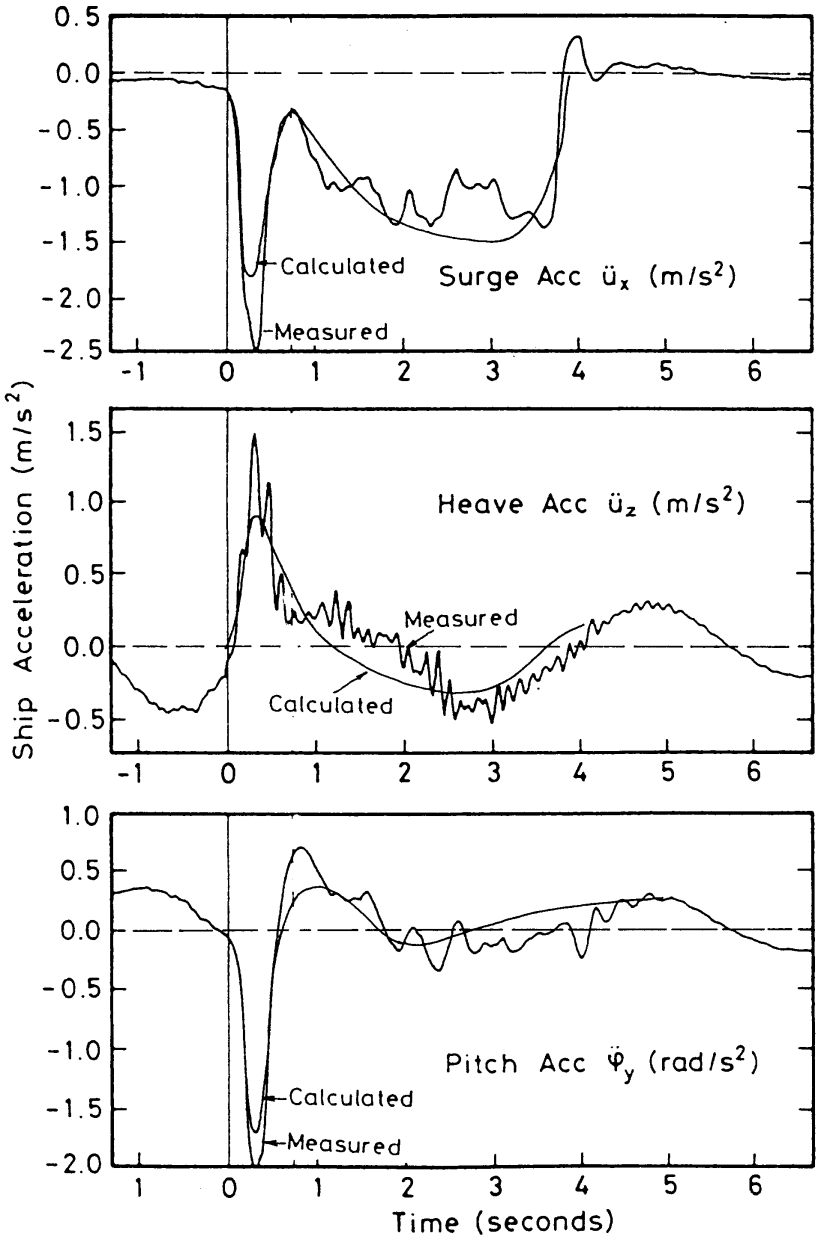

Figure 4.6: *Measured and calculated rigid body surge, heave and surge accelerations in test no. 4.*

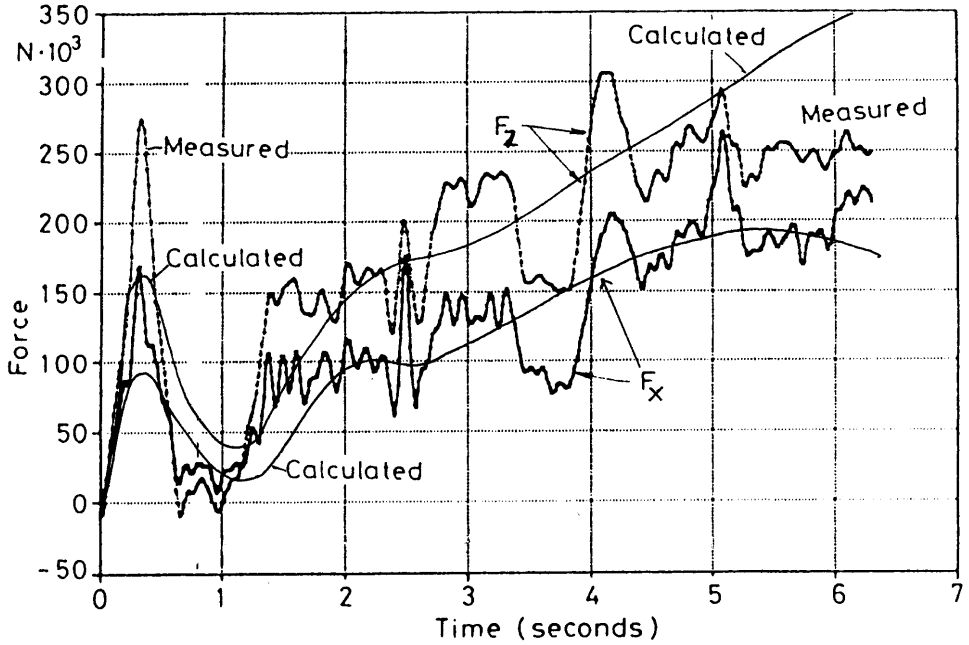

Figure 4.7: *Measured and calculated behaviours of vertical and horizontal ground reaction vs. time in test no. 1.*

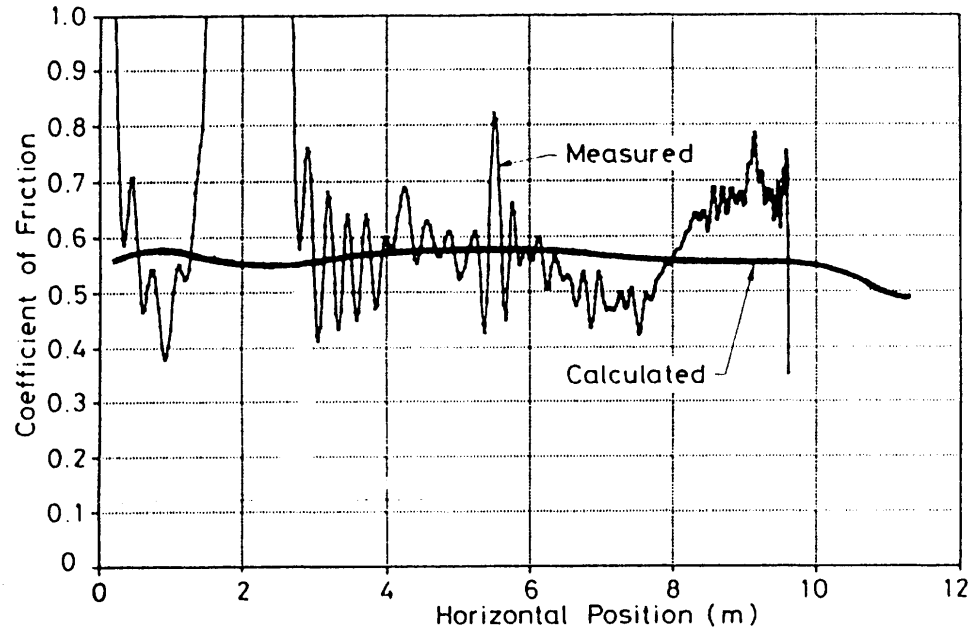

Figure 4.8: *Effective coefficient of friction vs. ship velocity in test no. 1. Measured and calculated values.*

4.3 Numerical Solution Methodology: Modal Analysis vs. Finite Element Method

As mentioned previously, the modal analysis is often an efficient approach because the solution is found in a space where the governing equations are decoupled. The cost of the method is to find the base of this space, i.e. the appropriate eigenmodes. If a large number of eigenmodes are necessary, as would certainly be the case if the ground reaction did not act near the end of the beam, the method is not necessarily the most efficient. For the present application the method is expected to be efficient but it is difficult to assess the error introduced by using modes of a free-free beam with zero shear force at the point of contact: The shear deformation at the front end cannot be included regardless of how many modes are summed up. Therefore, it is interesting to see how the solution of the modal analysis compares with that of the stiffness method. Figure 4.9 shows the soil reaction vs. time calculated by the two methods for the specific grounding example of a VLCC considered later in Section 5.1. The soil reaction is suited for comparison of solutions because it is highly sensitive to the response of both structure, soil and water. It is seen that the flexible ship gives a highly different response and that the modal analysis and the finite element method lead to equivalent results.

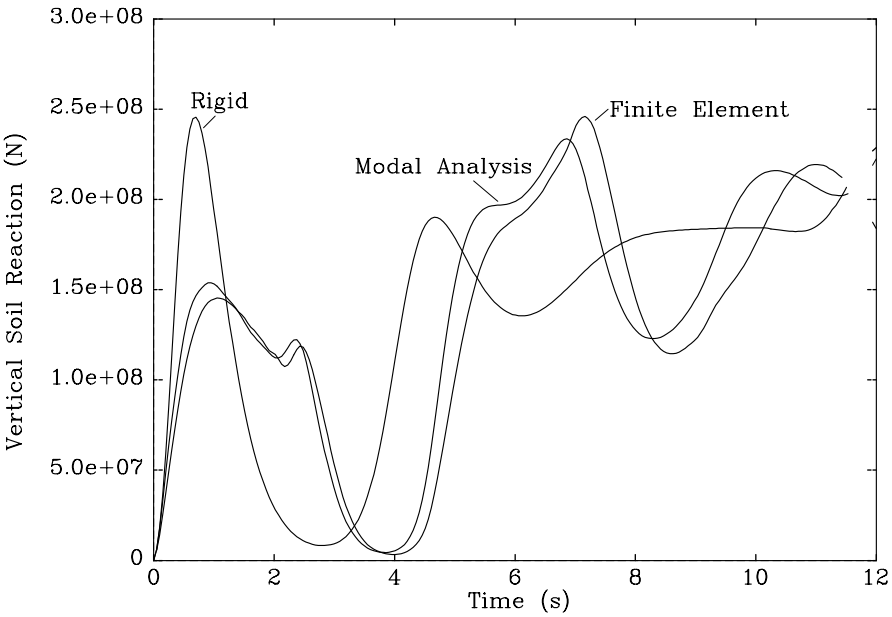

Figure 4.9: *Vertical component of soil reaction vs. time. The structural response of the ship is calculated both by modal analysis and by the finite element method.*

Figure 4.10 shows the position of the hull girder base line after 0.95 s calculated by the two methods. As seen from Figure 4.9 and Figure 4.10, there is very good agreement between the two calculated responses indicating that the modal analysis, which is significantly faster (50 - 100 times with the present implementations), is sufficiently accurate. The results presented in the following sections are calculated by the modal analysis approach.

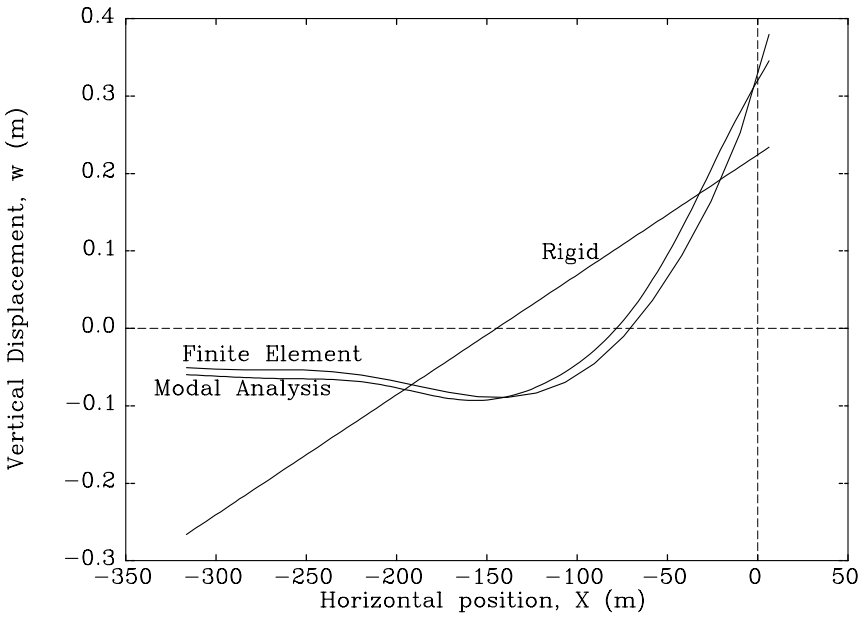

Figure 4.10: *Position of ship base line at $t = 0.95\,s$. The structural response for the flexible case is calculated both by modal analysis and by the finite element method.*

Chapter 5

Examples: Soft Grounding of a Large Tanker and Fast Vessels

With the theoretical model presented and validated in the previous sections, the foundation is given for investigation of the grounding response of different categories of ships. The grounding types considered in the following are

- a large loaded tanker at an impact speed of up to 15 knots,
- fast vessels of up to 100 m in length grounding at a speed of up to 40 knots.

For both kinds of ships the grounding-induced sectional forces in the hull girder will be compared to the reserve strength.

5.1 Grounding of a Large Tanker

Both accidents and analyses have shown that the grounding-induced sectional forces are potentially critical for large tankers, [122]. The present section therefore focuses on the grounding response of a large tanker.

5.1.1 Main Particulars of Ship and Ground

The main data for the considered grounding example is given in Table 5.1.

The mass distribution including added mass is shown in Figure 5.1. The added mass is calculated according to Eq. (3.6) and Eq. (3.8). The increase in mass near the bow is due to the diminishing water depth. The distribution of stiffnesses, EI_y and k_zGA, is shown in Figure 5.2 as $k_s(x)$. The stiffness distributions are then

$$\begin{aligned} EI_y(x) &= k_s(x)\, EI_y(x=0) \\ k_zGA(x) &= k_s(x)\, k_zGA(x=0) \end{aligned}$$

Table 5.1: *Main data for the considered VLCC.*

Length, L	322.7 m
Beam, B	58.2 m
Initial Draught, T	20.8 m
Block coefficient, C_B	0.81
Bulb radius, R_b	4.0 m
Water line area, A_w	$1.70 \cdot 10^4\ m^2$
First moment of area w.r.t. $x = 0$, S_w	$-2.98 \cdot 10^4\ m^3$
Second moment of area w.r.t. $x = 0$, I_w	$1.25 \cdot 10^8\ m^4$
Mass, incl. added mass, M_{zz}	$7.64 \cdot 10^8\ kg$
Moment of inertia, incl. added mass, J_y	$4.95 \cdot 10^{12}\ kg\,m$
Longitudinal centre of gravity, x_{gz}	18.5 m
Shear stiffness amidships, k_zGA	$1.71 \cdot 10^{11}\ N/m^2$
Bending stiffness amidships, EI_y	$2.23 \cdot 10^{14}\ N/m^2$
Lowest 'wet' eigen freq. (bending/shear), Ω_1	$2.35\ rad/s$

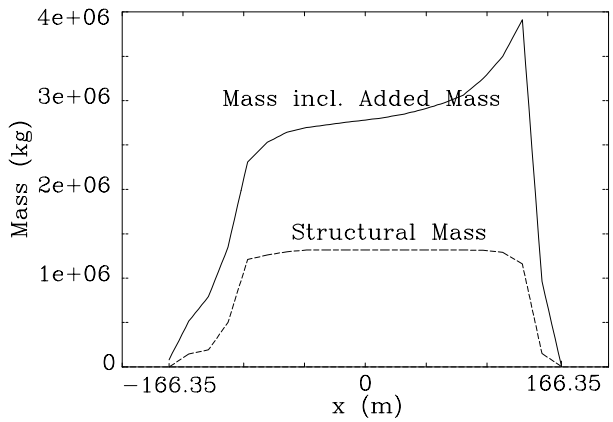

Figure 5.1: *Mass distribution for a VLCC grounding on a slope with the inclination 1:6.*

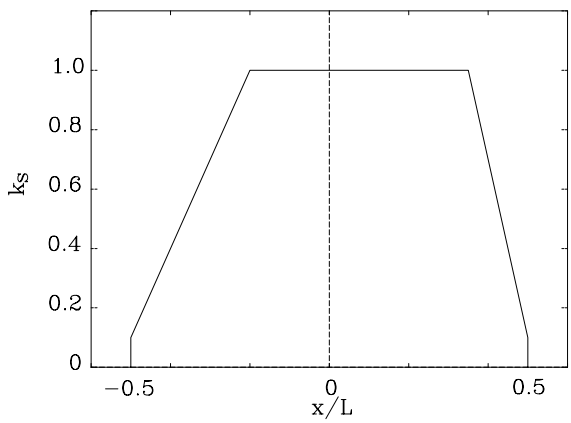

Figure 5.2: *Stiffness distribution, k_s, for the considered VLCC.*

In the basic example the ship is assumed to run aground with a velocity of 6 m/s on a sand slope with the inclination 1:6. The sand is relatively coarse ($d_m = 2\ mm$) with a frictional angle of $\varphi = 37^o$. Before the induced sectional forces are compared to the reserve strength of the hull, some of the characteristics of the solution are investigated.

5.1.2 Effect of Hydrodynamic Damping

The effect of hydrodynamic damping was investigated in [99] and as shown there, the damping force contributes little to the total force equilibrium of the ship. Figure 5.3 shows the unit response function, $h_z(x,t)$, for the considered VLCC grounding on a slope of 1:6. The increase of $h_z(x,t)$ near the bow is due to the diminishing water depth.

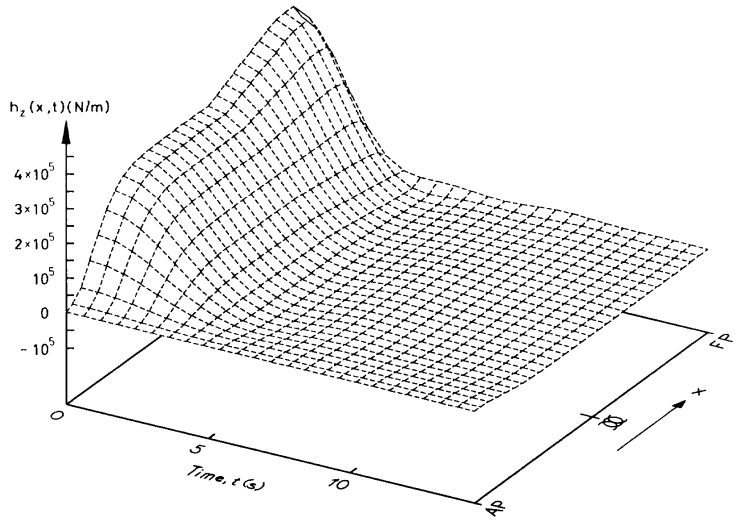

Figure 5.3: *Unit response function, $h_z(x,t)$, for a VLCC grounding on a slope of 1:6.*

Figure 5.4 shows the soil reaction calculated for a rigid hull with and without the hydrodynamic damping (denoted 'memory effect').

Since the damping loads arise as a weighted integral of the history of the vertical velocity of the hull sections, it does not come into play until after a while - thus the term 'memory effect'. The damping reduces the stopping length in this grounding example by less than 5 %. As the effect of damping loads on the maximum sectional forces was shown to be even less (about 1-2 %), [99], the damping loads are neglected in the following.

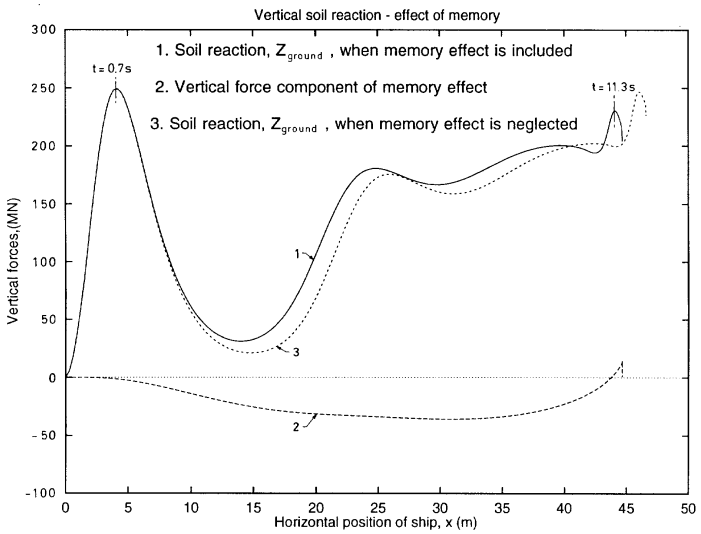

Figure 5.4: *Vertical components of soil reaction and memory effects, rigid hull*

5.1.3 Effect of Hull Flexibility on Grounding Dynamics

It was already shown in Figure 4.9 that introduction of hull flexibility changes the grounding response significantly as the grounding force in the first peak was reduced by about 40 % and the period of the initial impact was prolonged. The purpose of the present section is to illustrate the effect of hull flexibility on the grounding response in more detail. Figure 5.5 shows the profile of the bottom of the furrow generated by the penetrating bow.

It is seen that the furrow depth of the initial impact is smaller for the flexible ship, corresponding to the lower peak force shown in Figure 4.9. Although the flexible deformation gives a smaller initial peak soil reaction and a furrow depth, the hull 'bounces back' later and gives rise to a soil reaction and furrow depth which is even larger than for the rigid ship. An important conclusion from Figure 5.5 is that the stopping distance (which is also the furrow length) is practically the same for the rigid and the flexible ship.

Figure 5.6 shows the maximum bending moment in the hull girder as a function of time for a flexible and a rigid VLCC. First, it is noted that the hull is in a state of sagging during the entire grounding. The bending moment during the initial impact is largest for the rigid ship but, as it was the case for the soil reaction shown in Figure 4.9, a dynamic amplification for the flexible ship induces a larger maximum bending moment later ($t = 6.4s$). It is also important to note that this maximum bending moment is 45 % larger than the bending moment in the final resting position. This means that, although it is possible to predict the final resting position with good accuracy assuming a rigid ship, the maximum bending moment during the grounding has to be found by taking proper account of the hull flexibility - at least for some types of groundings. With a gentler slope, a smaller impact velocity or a softer soil than considered here, the hull flexibility will be less important.

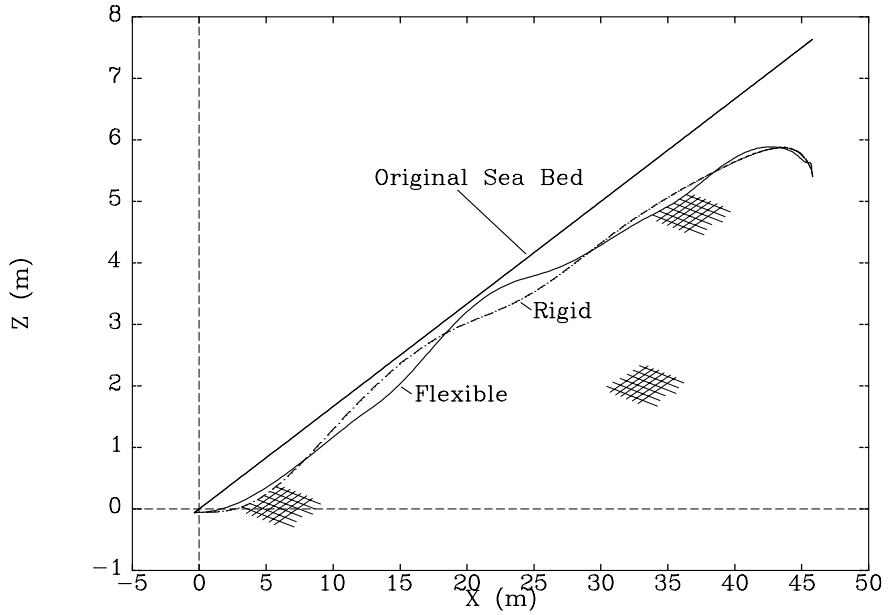

Figure 5.5: *Profile of original sea bed and furrow generated by the penetrating bow. Results for both rigid and flexible hulls are shown.*

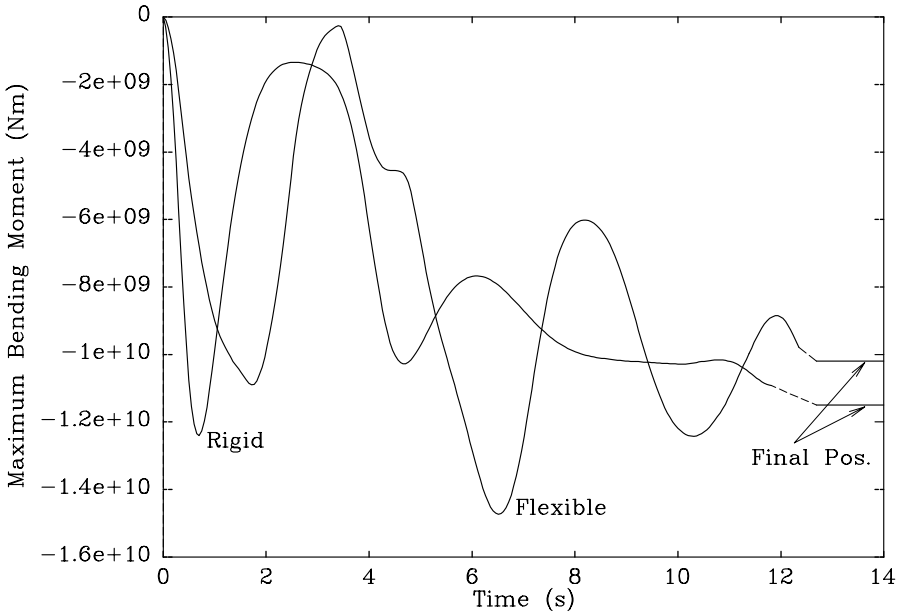

Figure 5.6: *Maximum bending moment in the hull girder of a VLCC as a function of time.*

5.1.4 Effect of Hull Flexibility on Final Resting Position

In the final resting position, the grounding-induced loads induce a sagging of the hull as discussed in Section 3.6. The loads acting on the hull in the final resting position at a bow lift of 1 m are given in Figure 5.7. The corresponding deformed configuration of the considered VLCC is shown in Figure 5.8.

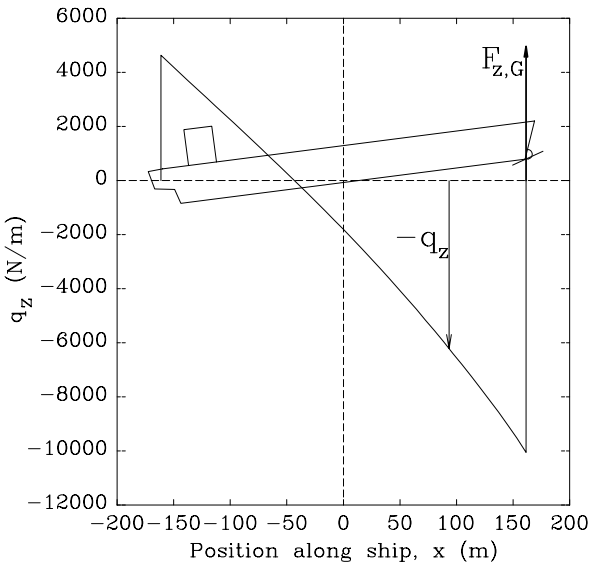

Figure 5.7: *Static loads on a VLCC hull in the final resting position. The bow lift is 1 m ($x_c = L/2$) and $F_{z,G} = 33.7\,MN$. Flexible hull.*

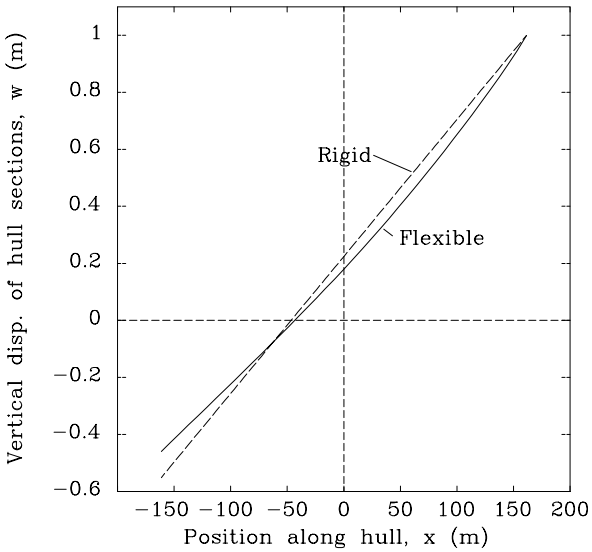

Figure 5.8: *Vertical displacement of sections along a VLCC which is lifted at the bow due to a grounding. Solutions for both rigid and flexible hulls are shown.*

Figure 5.9 and Figure 5.10 show the shear force and the bending moment in the hull girder at a bow lift of 1 m for a rigid and a flexible VLCC.

The differences between the rigid and the flexible hull response are quantified in Table 5.2. It is seen here that introduction of the hull flexibility reduces forces and moments in the final resting position by 10 - 15 %. Except for the maximum shear force around midship, the accuracy of the formulas presented by Pedersen in [122], Eq. (3.76), is also seen to be at this level.

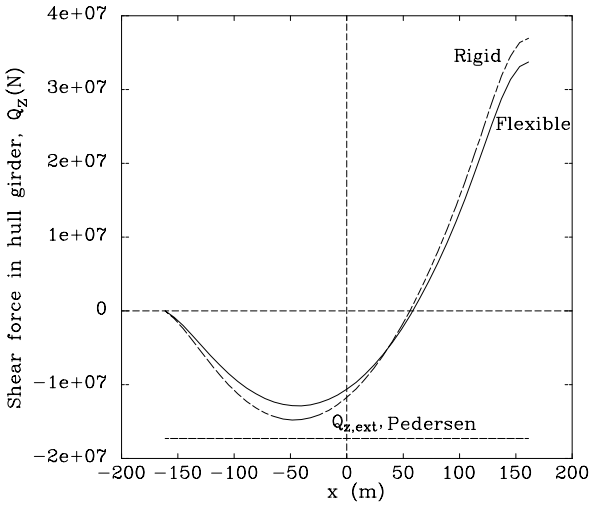

Figure 5.9: *Shear force in hull girder at* $1\,m$ *bow lift.*

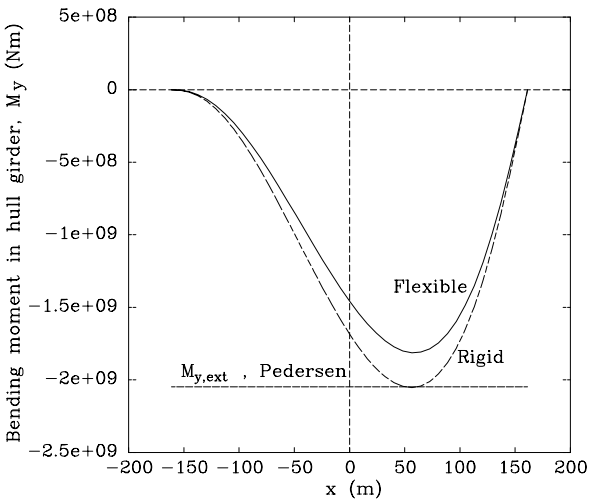

Figure 5.10: *Bending moment in hull girder at* $1\,m$ *bow lift.*

Table 5.2: *Effect of flexibility in final resting position. The bow lift is* $1\ m$.

Soil reaction (max. shear force) $F_{zG}(rigid)/F_{zG}(flex)$	$37.0\,MN/33.7\,MN$	1.10
Max. shear force around midship $Q(max, rigid)/Q(max, flex)$	$-14.8\,MN/-12.9\,MN$	1.15
Max. bending moment $M(max, rigid)/M(max, flex)$	$-2.05\cdot10^9\,Nm/-1.81\cdot10^9\,Nm$	1.13
Bending moment, Pedersen [122] $M_{ext}/M(max, flex)$	$-2.05\cdot10^9\,Nm/-1.81\cdot10^9\,Nm$	1.13
Bending moment, Pedersen [122] $M_{ext}/M(max, rgd)$	$-2.05\cdot10^9\,Nm/-2.05\cdot10^9\,Nm$	1.00
Shear force, Pedersen [122] $Q_{ext}/Q(max, flex)$	$-17.3\,MN/-12.9\,MN$	1.35

5.1.5 Sectional Forces and Strength

The maximum shear force in the hull girder occurs at the point of contact with the ground and, as this point of contact is assumed to be at the bow in the present analysis, the shear force is equal to the ground reaction. It is therefore relevant to consider the distribution of shear force at the instants of maximum soil reaction. As seen from Figure 4.9, the soil reaction attains extremum values at $t = 0.95\,s$ and $t = 6.86\,s$. Figure 5.11 shows the distribution of shear force in the hull girder at these times of maximum ground reaction and in the final resting position (the bow lift is 5.6 m). When compared to the IACS wave load strength requirement it is quite clear that shear loading of the hull girder may be critical. The strength of the hull is exceeded in the midship section but even more pronouncedly so in the forward end of the hull. It should be mentioned here that, as the shear strength comes from the side shell and longitudinal bulkheads it does not actually drop to zero at the fore end as indicated in Figure 5.11. Still, even if the shear strength of the midship section was attained throughout the length of the hull, Figure 5.11 indicates possible shear failure over a significant part of the hull.

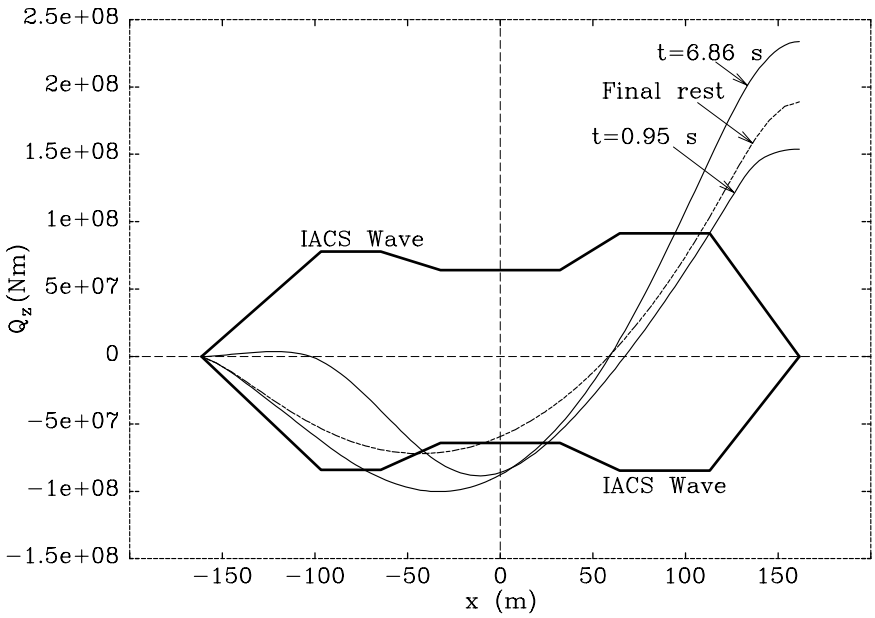

Figure 5.11: *Shear force in hull girder at selected times.*

Figure 5.6 showed that the maximum bending moment in the hull girder attains several pronounced peaks as a function of time. Figure 5.12 shows the distribution of bending moments in the hull girder at three of these peaks ($t = 1.72\,s$, $t = 6.51\,,s$ and $t = 10.31\,s$) and in the final resting position. As for the shear force, it is seen that the bending moment capacity is exhausted in the considered grounding example.

As seen in Figure 5.5, the furrow generated by the penetrating bow is only about 1 m deep which indicates a stiff ground. Figure 5.13 shows the maximum bending moment in the hull girder as a function of time for soils with different permeabilities - given as different

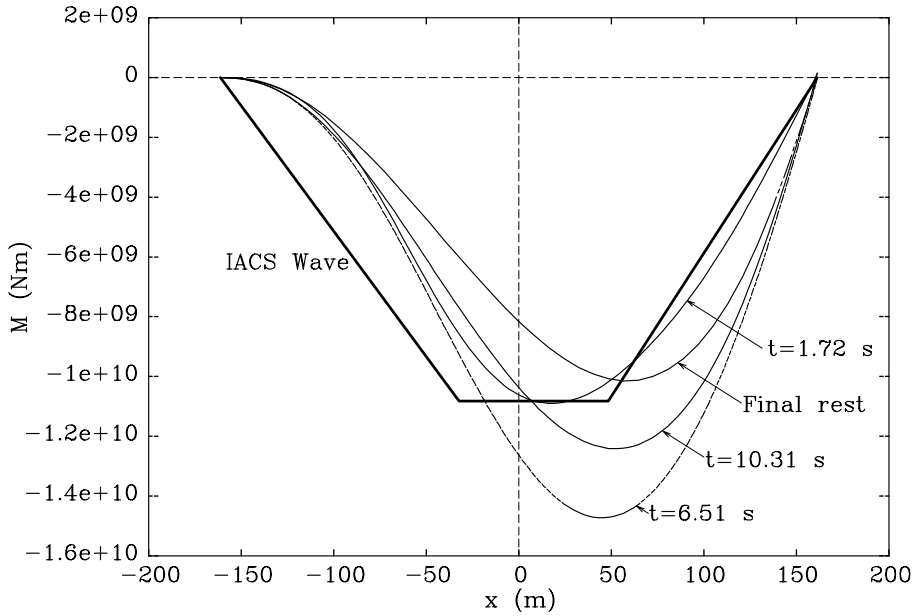

Figure 5.12: *Bending moment in hull girder at selected times.*

grain mean diameters. It is seen that decreasing the soil permeability ('$d = 1\ mm$') gives higher peak bending moments and vice versa, increasing the soil permeability gives a lower level for the maximum bending moment. In fact, Figure 5.13 shows that, for a soil with a hardness corresponding to $d = 10\ mm$, the bending moment capacity of the IACS wave load is not exceeded.

As illustrated by the model experiment results in Section 4.1.2, the impact loads are a strong function of the impact velocity. Figure 5.14 shows the maximum bending moment as a function of the impact velocity. It is seen that, for impact velocities of up to about 5 m/s, the bending moment capacity about midship is not exceeded. For small impact velocities the critical period is therefore not during the grounding itself, but rather in the period between the grounding and the refloating where a receding tide may increase the bow lift significantly.

Figure 5.15 and Figure 5.16 show the maximum shear force and bending moment in the final resting position vs. bow lift. It is seen here that if the IACS wave load shear strength amidships is attained over the length of the hull, lifting of the bow of only 1.9 m is enough to cause the shear strength in the forward end of the ship to be exceeded. For the shear strength about midship and the bending moment, the corresponding critical values for bow lift are 5.0 m and 6.0 m, respectively.

Figure 5.17 and Figure 5.18 show stopping distance and bow lift for different impact velocities. For example, if the considered VLCC runs aground at a velocity of 2.5 m/s which is a typical velocity in a difficult manoeuvre, the bow lift is 1.7 m and it the ship is not refloated the water level can only lower by 0.2 m before the shear force at the fore end reaches a critical level.

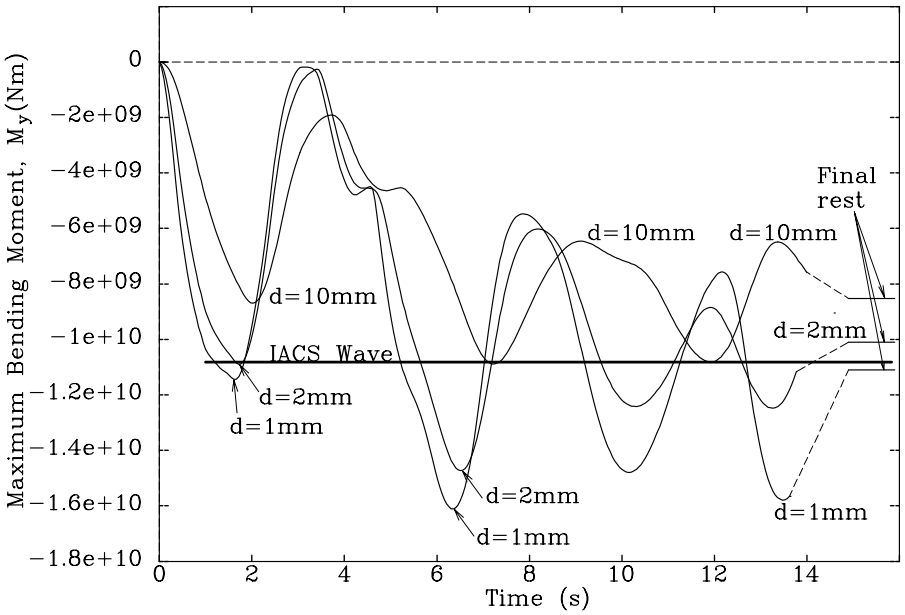

Figure 5.13: *Maximum bending moment vs. time for different soils (d is mean grain diameter).*

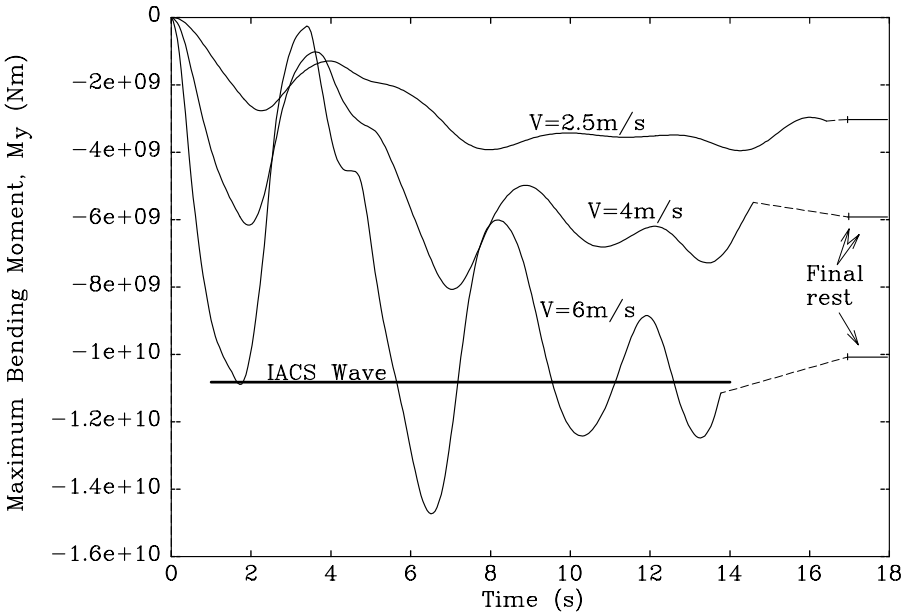

Figure 5.14: *Maximum bending moment vs. time for different impact velocities.*

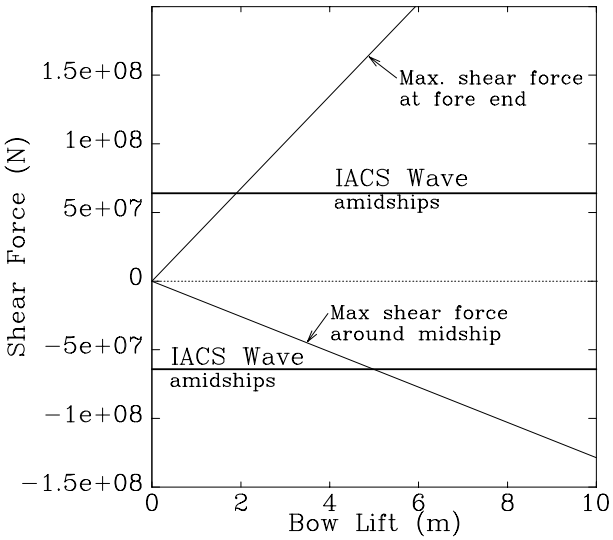

Figure 5.15: *Maximum shear forces in hull girder as a function of the bow lift.*

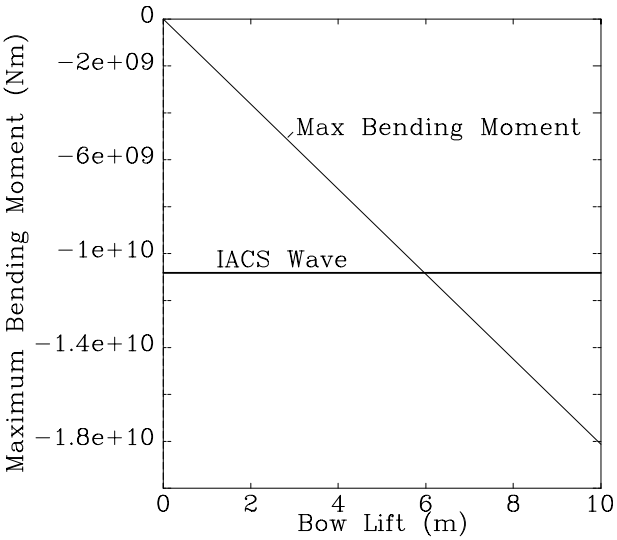

Figure 5.16: *Maximum bending moment in hull girder as a function of the bow lift.*

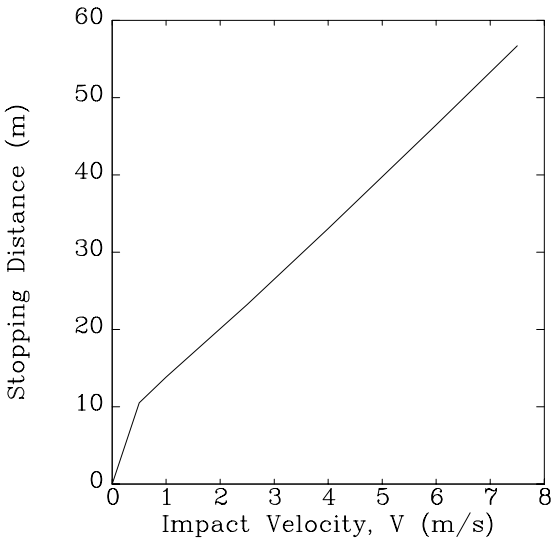

Figure 5.17: *Stopping distance as a function of impact velocity.*

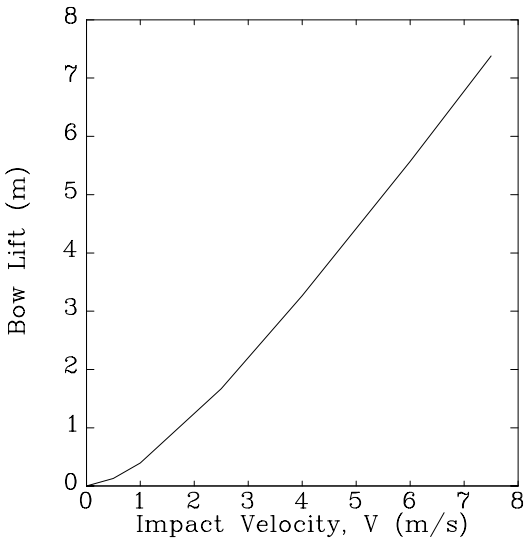

Figure 5.18: *Bow lift as a function of impact velocity.*

5.2 Dynamics of Fast Ships

Incidents of grounding of fast ships on hard ground have demonstrated the potential fatality of this type of accidents, [86]. When the impact speed is 35 - 40 knots and the stopping mechanism for the ship is crushing of the bow structure, accelerations reach a potentially fatal level. For the type of grounding considered here where the stopping mechanism is relatively smooth, the damage concerned with regards structure rather than human lives. Below, the grounding responses of six different fast vessels are compared and as for the VLCC considered above, the grounding-induced sectional forces are compared to approximate strength values taken from class requirements.

5.2.1 Ship and Ground Main Particulars

The main data for the ships is given in Table 5.3.

Table 5.3: *Main data for 50 m and 100 m fast ships of steel, aluminium and fibre-reinforced plastic (FRP).*

	50 m ship	100 m ship
Length, L	50.0 m	100.0 m
Beam, B	7.20 m	14.4 m
Initial draught, T	1.82 m	3.64 m
Block coefficient, C_B	0.355	0.355
Water line area, A_w	$2.52 \cdot 10^2\ m^2$	$1.06 \cdot 10^3\ m^2$
Second moment of area, I_w	$4.08 \cdot 10^4\ m^4$	$6.53 \cdot 10^5\ m^4$
Long. C. of flotation, LCF	- 5.86 m	- 11.71 m
Mass, incl. added mass, M_{zz}	$7.72 \cdot 10^5\ kg$	$6.18 \cdot 10^6\ kg$
Mass, incl. added mass, M_{xx}	$2.50 \cdot 10^5\ kg$	$2.00 \cdot 10^6\ kg$
Moment of inertia, incl. added m., J_y	$1.11 \cdot 10^8\ kg\,m^2$	$3.54 \cdot 10^9\ kg\,m^2$
Long. centre of gravity, x_{gz}	-4.70 m	- 9.40 m
Shear stiffness amids., k_zGA, steel hull	$3.75 \cdot 10^8\ N/m^2$	$3.00 \cdot 10^9\ N/m^2$
Bending stiffness amids., EI_y, steel hull	$1.88 \cdot 10^{10}\ N/m^2$	$6.00 \cdot 10^{11}\ N/m^2$
Lowest eigen freq., Ω_1, steel hull	$10.94\ rad/s$	$7.74\ rad/s$
Shear stiffness amids., k_zGA, alu. hull	$1.19 \cdot 10^8\ N/m^2$	$9.50 \cdot 10^8\ N/m^2$
Bending stiffness amids., EI_y, alu. hull	$5.95 \cdot 10^9\ N/m^2$	$1.90 \cdot 10^{11}\ N/m^2$
Lowest eigen freq., Ω_1, alu. hull	$6.16\ rad/s$	$4.35\ rad/s$
Shear stiffness amids., k_zGA, FRP hull	$5.60 \cdot 10^7\ N/m^2$	$4.50 \cdot 10^8\ N/m^2$
Bending stiffness amids., EI_y, FRP hull	$2.80 \cdot 10^9\ N/m^2$	$9.00 \cdot 10^{10}\ N/m^2$
Lowest eigen freq., Ω_1, FRP hull	$4.23\ rad/s$	$3.00\ rad/s$

The ships are assumed to run aground on a slope of 1:10 consisting of relatively coarse sand ($d_m = 2\ mm$). In this type of grounding the ships may run completely up on the beach and rest on the keel. If the penetration into the ground is neglected and the ship sides are assumed to be wall-sided, the sliding length which gives contact over the length of the keel is approximately

$$\Delta X = l + \frac{I_w - S_w\, l}{A_w l + S_w} \tag{5.1}$$

where l is the distance from the longitudinal centre of flotation to the point of contact. As in the previous sections, A_w, S_w and I_w are the zeroth to second moment of the water plane around midship. For a large tanker with an (almost) rectangular water plane, the sliding length giving keel contact is simply $\Delta X = 2/3L$. For the two ship sizes analysed here, Eq. (5.1) predicts keel contact after 40 m and 80 m, respectively (i.e. after about $\Delta t \approx \Delta X/V = 2s, 4s$). Eq. (5.1) was derived from static considerations. In the dynamic simulation, complete keel contact is found to take place after 1.6 s and 3.4 s and 31.6m and 63.5 m, respectively. Only the period before keel contact is considered in the following.

5.2.2 Accelerations, Sectional Forces and Strength

The horizontal accelerations for the two aluminium ships are shown in Figure 5.19. It is seen that the accelerations during the initial impact reach a level around only 2 m/s^2. This is less than what can be experienced by braking a car and it is unlikely to cause fatalities.

Concerning loads in the hull girder, Figure 5.20 shows the maximum shear forces in the hull girder during the initial impact. The maximum shear force at the fore end is equal to the vertical component of the ground reaction, and the maximum shear force around midship normally occurs at a small distance behind the midship section, as shown in Figure 5.11 for the considered VLCC.

As discussed in Section 3.7, the strength curve in Figure 5.20 is approximate but the figure illustrates that the grounding loads and the hull girder strength are of the same order of magnitude and, once again, that the hull flexibility has great influence on the grounding-induced sectional forces. This latter point is also illustrated in Figure 5.21 and Figure 5.22, which show the hull displacement at the initial stages of the grounding for the considered rigid and flexible ships.

Figure 5.23 shows the maximum bending moment in the hull girder as a function of time for the 100 m ships. The figure indicates that the bending moment is not critical either for the flexible ships during the initial impact. For the steel ship, though, a peak bending moment is seen after about 2.3 s, which exceeds the strength of the hull girder according to the DNV requirements. The bow lift at this point is about 5 m, and since the initial draught

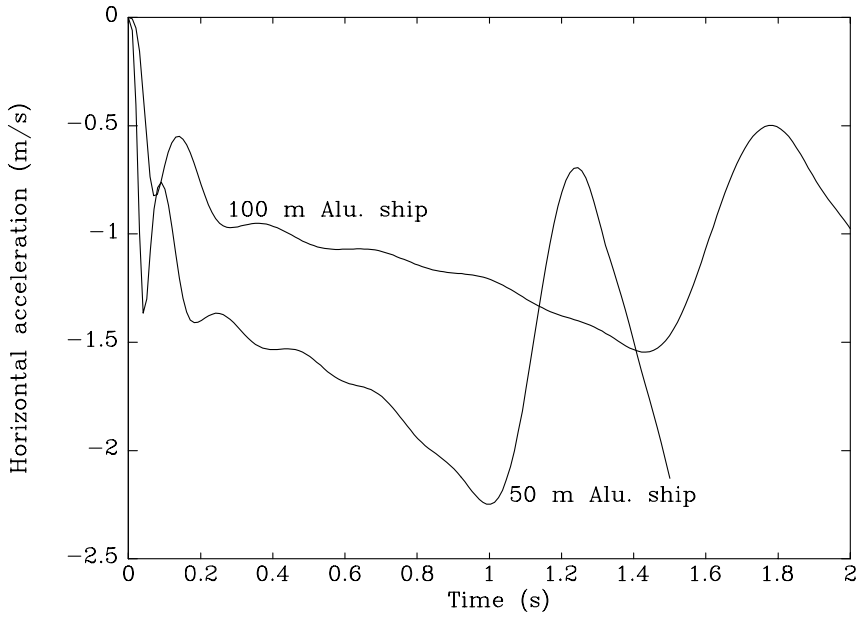

Figure 5.19: *Horizontal accelerations of aluminium ships of 50 m and 100 m during initial impact.*

of the ship was 3.5 m, the range of validity of the model for calculation of restoring loads is exceeded. If the restoring loads were taken accurately into account the sectional loads would be smaller than presented in this section because the loss of buoyancy is exaggerated here.

Figure 5.24 and Figure 5.25 show shear forces and bending moments for the 50 m ships. The comments given above for the 100 m ships hold true for these ships as well: The grounding-induced loads and the hull girder strength are at the same level and the hull flexibility is seen to reduce significantly shear forces and bending moments during the impact.

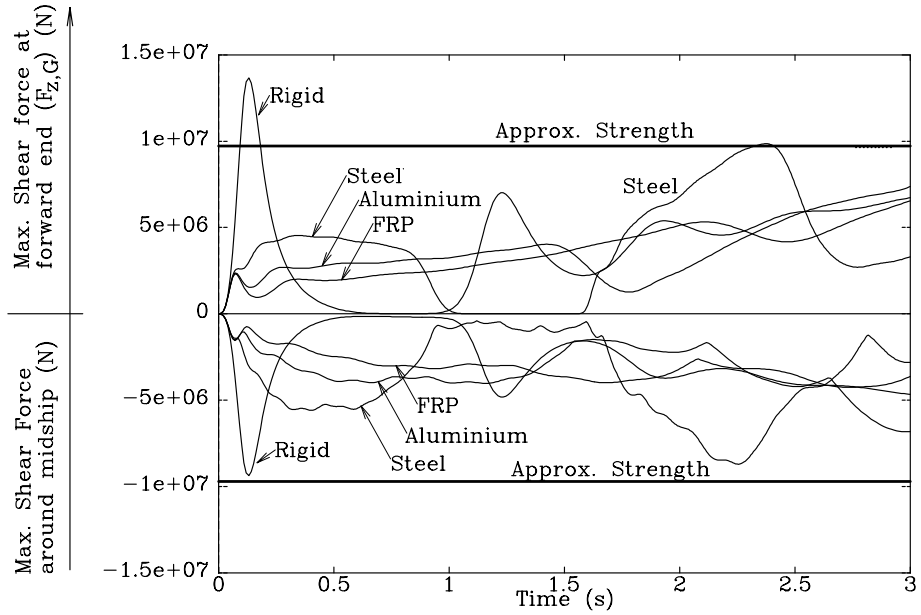

Figure 5.20: *100 m ships. Extremum shear forces in hull girders of FRP, aluminium, steel and rigid ships as a function of time. Maximum shear force at the fore end is equal to the vertical component of ground reaction.*

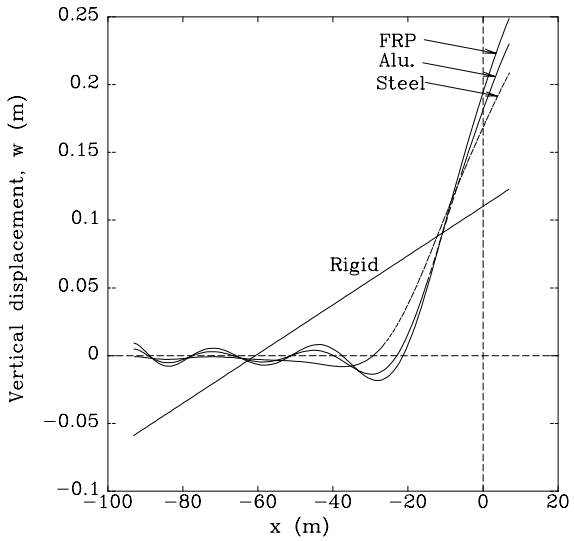

Figure 5.21: *Vertical displacement of hull at $t = 0.2$ s. 100 m ships.*

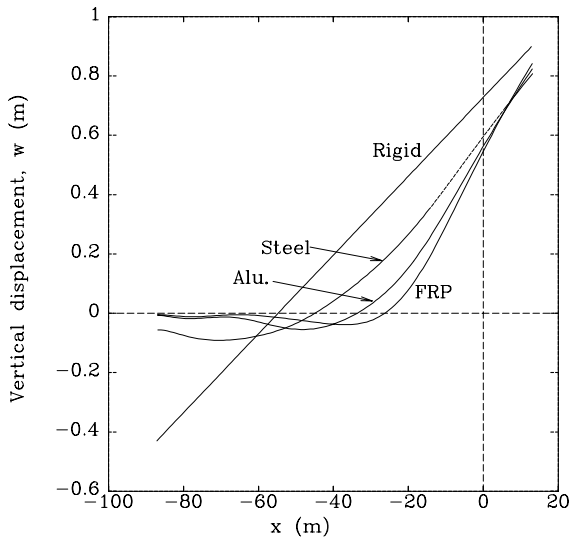

Figure 5.22: *Vertical displacement of hull at $t = 0.5$ s. 100 m ships.*

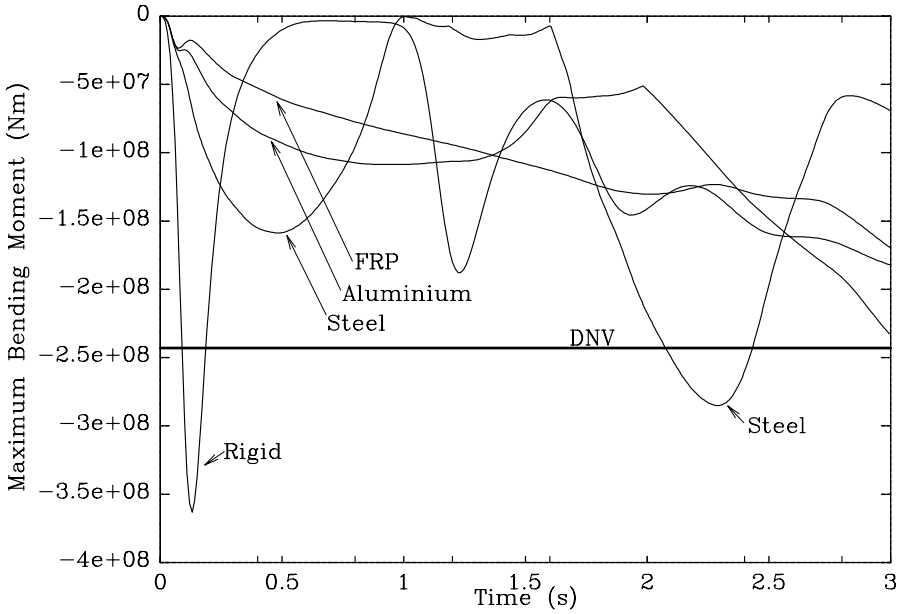

Figure 5.23: *100 m ships. Extremum bending moment in hull girders of FRP, aluminium, steel and rigid ships as a function of time.*

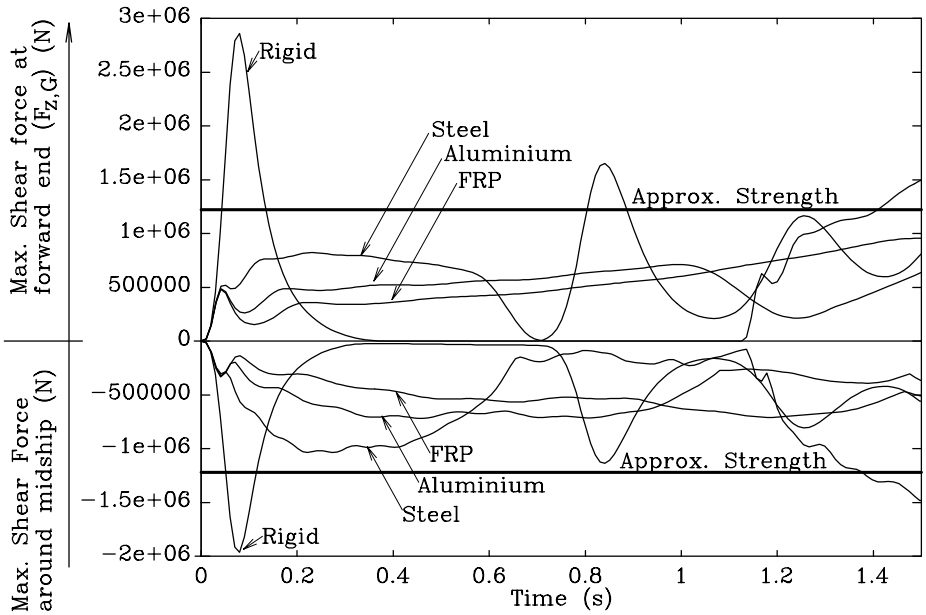

Figure 5.24: *50 m ships. Extremum shear forces in hull girders of FRP, aluminium, steel and rigid ships as a function of time. Maximum shear force at the fore end is equal to the vertical component of ground reaction.*

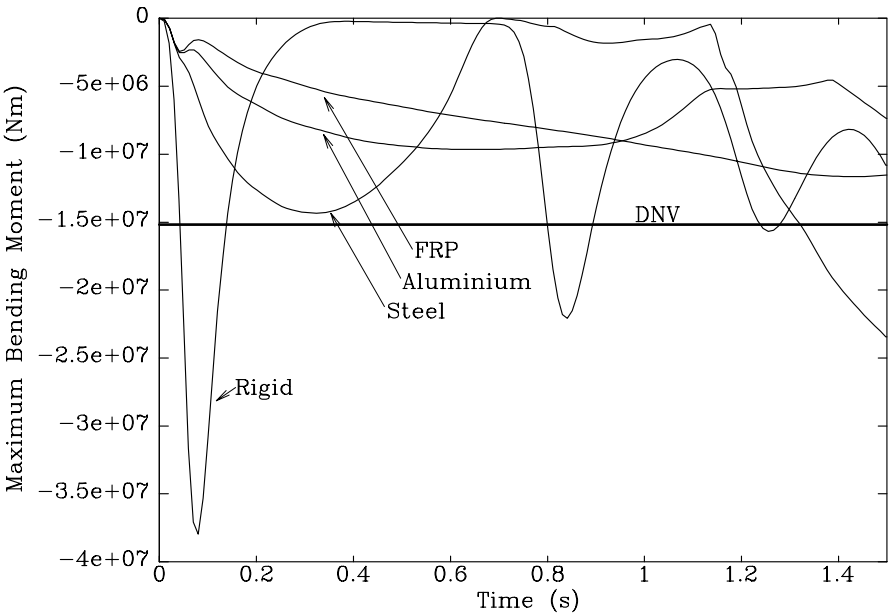

Figure 5.25: *50 m ships. Extremum bending moment in hull girders of FRP, aluminium, steel and rigid ships as a function of time.*

This page is intentionally left blank

Chapter 6

Theoretical Basis for the Hard Ground Model

6.1 Introduction

The remaining chapters are concerned with ship grounding on hard ground, for example a rock pinnacle. As for the soft grounding problem described in the previous chapters the coupling is strong between the behaviour of the ground, the ship hull and the surrounding water. Theoretical analyses, e.g. Lenselink and Thung [67] and Mizukami et al. [81], have shown that it is possible to solve this type of problem in an integrated way by describing the behaviour of each of the three components by structural or fluid elements and solving the complete set of equations simultaneously. To gain insight into the overall mechanics of the problem, however, it is highly advantageous to divide it into the external dynamics and the internal mechanics. This approach was taken by Minorsky in 1959 [80] for the ship collision problem. An example for ship grounding was presented by Kuroiwa in 1996 [63], where a strip theory model for the ship motion was coupled with an explicit finite element model (LS-DYNA3D) for the local damage process. The present solution method is based on the same overall approach of dividing the problem into two parts. However, a primary objective of the present model has been easy modelling and small computational effort. Therefore, the model for the internal mechanics is here based on simplified deformation mechanisms and the model for the external dynamics on static equilibrium. When compared to the results of Kuroiwa [63], these simplifications reduce significantly pre- and post processing and also reduce the CPU time from 450 hours to less than 1 second, i.e. by a factor of more than 10^6. As it will be discussed later, however, the finite element methodology has certain advantages in terms of accuracy and consistency at a detailed level.

Figure 6.1 illustrates the division of the grounding problem into external dynamics and internal mechanics. The model for the external dynamics calculates the rigid body ship motion given a force on the hull and the model for the internal mechanics calculates the

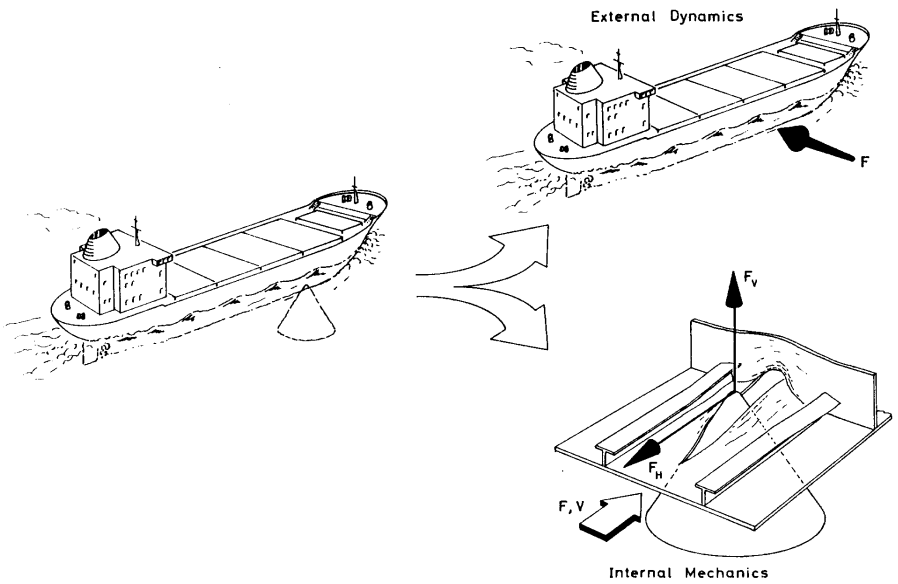

Figure 6.1: *Division of the grounding problem into external dynamics and internal mechanics. The internal mechanics is divided into energy dissipation in plasticity and fracture and energy dissipation in friction.*

force on the hull given a certain penetration of the rock into the hull. As it is shown later, it is also convenient to separate the internal mechanics into energy dissipation by plastic deformation and fracture and energy dissipation by friction.

Due to this division, it is necessary to develop only one model for the external dynamics and one for the internal mechanics for each class of structural deformations. In accordance with this overall dissection of the problem, the subsequent three chapters describe, respectively, the developed theoretical models for the external dynamics, the internal mechanics for a ship grounding on a wedge type reef, and the internal mechanics for a ship grounding on a cone type rock.

Although the structural behaviour is strongly dependent on the type of rock encountered, the underlying theory of structural resistance due to plasticity, fracture and friction is the same. After a sketchy review of existing methods, the present chapter describes this basic theory, which is the foundation of the two types of rocks considered in Chapters 8 and 9.

6.2 Internal Mechanics, Outline of Existing Methods

Since the overall objective of the theoretical model is to predict structural damage and potential oil outflow in a given grounding event, the model for the internal mechanics must be able to predict the ground reaction and the initiation and the termination of shell plate

fracture (i.e. opening of tanks). Several attempts to predict damage in collision accidents have been published over time - the amount of literature on grounding is very limited. Many of the involved failure mechanisms are the same, though. The basic difference between grounding and collision is that grounding is rather a steady state process and friction plays an important role whereas a collision is characterised by a completely transient response of the structure with little influence of friction. Phenomena like deformation far into the post-buckling region, large plastic deformations and fracture are involved in both collision and grounding processes and the proposed models for predicting the damage are as numerous as the phenomena are complex. The models can be divided into five categories:

1. Statistical methods.
2. Experimental methods.
3. Continuum based finite element method.
4. Energy method.
5. Hybrid and idealised structural unit method.

Statistical Methods. In the area of structural damage due to collisions Minorsky's article from 1959 [80] is most frequently quoted and referred to. Minorsky analysed 50 collisions and found a linear relationship between the energy dissipated in the structure and the volume of displaced material, see Figure 6.2.

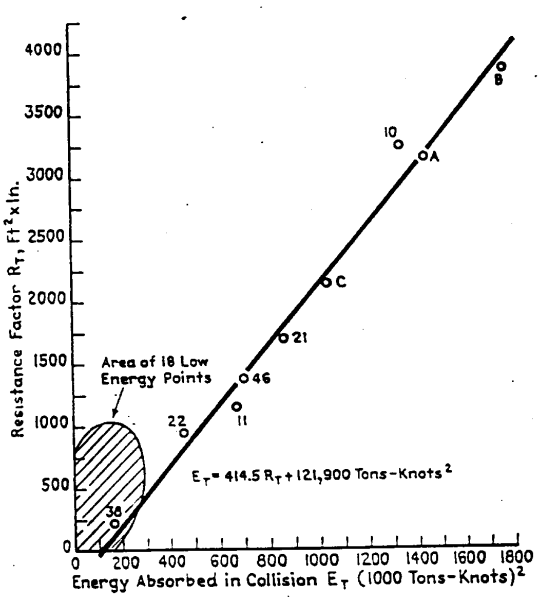

Figure 6.2: *Linear relationship between the volume of deformed material (Resistance Factor, R_T) and the energy dissipated in the structure (E_T), [80].*

Minorsky recognised the complexity of the internal mechanics and made comments which give food for thought for the present analytical approach: "... It is also rather obvious that the resistance forces which develop during the impact period do not lend themselves to analytical methods of calculation..." and "...as an analytical solution would of necessity rest on many doubtful assumptions, it was preferable to follow a semi-analytical approach based on the facts of actual collisions...".

The amount of reported statistical research in the area of grounding damage is very scarce. It seems that, since the first statistical investigation of grounding was reported in 1975 by Card [27], no further statistical studies have been published in open literature. In connection with a viability study on double bottom and segregated ballast tankers, Card analysed 30 grounding accidents in US waters between 1969 and 1973. A major conclusion of Card's work was that, in 27 of the 30 accidents, the maximum vertical extent of damage was less than $B/15$, indicating that a double bottom with this height would prevent oil outflow in 90 % of the accidents.

In general, statistical analyses are hampered by insufficient or incomplete data such as vessel speed, extent of damage, and the shape of the underwater obstacle in the case of a grounding event. In addition, the information is often considered proprietary or is unavailable due to litigation.

A fundamental problem of statistical analyses for determining the grounding response of completely new structural arrangements or materials is that prediction of the behaviour is questionable when done by extrapolation from existing ships.

Experimental Methods. Over the years a large number of experiments have been carried out in order to shed light on the internal mechanics of grounding and collision. Most of this work concerns the very simplified example of wedge cutting of a bare plate. A thorough literature review is given in Chapter 8. Recently Astrup, [10], reported on cutting experiments with plates of up to 25 mm thickness. An example of such a large-scale cutting experiment is shown in Figure 6.3.

Due to the escalation of test expenses with scale, most experiments with assembled ship structures were carried out at a relatively small scale (1:30 - 1:10). Recently, however, series of large-scale (1:5 - 1:4, t=3-5mm) grounding experiments were conducted, [9], [106]. Some of these tests will be further discussed in Chapter 10.

The necessity of performing scaled tests constitutes a fundamental problem in experimental analysis of grounding and collision: The energy dissipation for a fracture process is proportional the square of the length scale ($\sim R_c\dot{A}$), whereas the plastic flow is proportional to the cube of the length scale ($\sim \sigma_0\dot{V}$). Therefore, the energy absorption of a given structure cannot be scaled by elementary scaling laws when the plastic flow is accompanied by fracture. Moreover, if dynamic effects are significant, which they are likely to be in grounding events as well as in collisions, it has been demonstrated that scale effects may be severe: Experiments have shown that the impact energy absorbed for a given amount of damage in

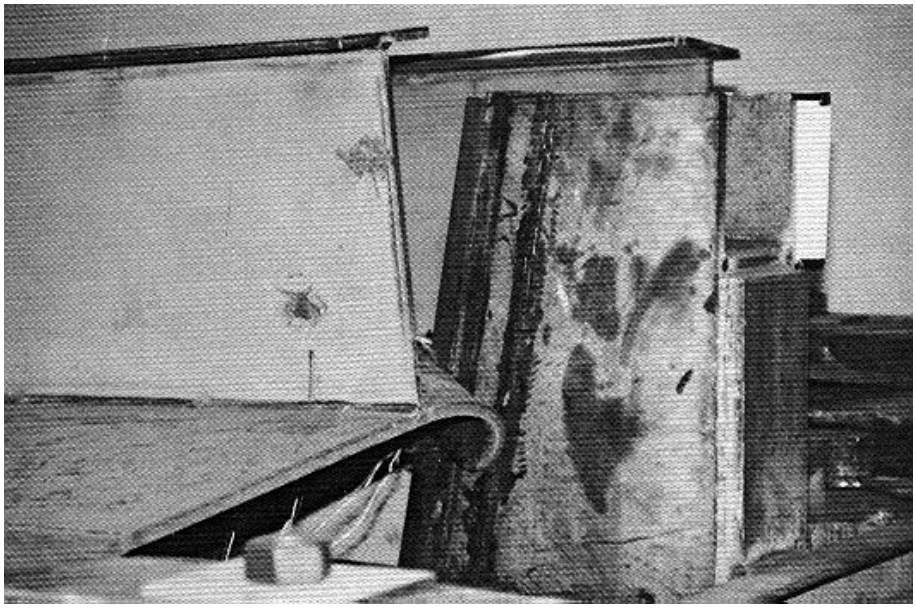

Figure 6.3: *Cutting of a 20 mm thick plate by a wedge, [10].*

a full-scale steel structure is less than 50 % of that expected from a one-quarter scale model which suffers the same scaled damage, [52], [56], [24].

Continuum-Based Finite Element Method. This approach represents the most general of the five listed procedures, in the sense that it can be applied to any kind of structural problem, practically without prior knowledge of the global structural behaviour. Several commercial codes are available, for example LS-DYNA3D, PAMCrash, ABAQUS, ADINA and MSC/DYTRAN and the list of problems solved successfully by this method seems endless. Relatively few have reported on successful attempts at modelling collision and - in particular - grounding events, though. Some finite element simulations could be mentioned: Side collision by Lenselink and Thung [67], stranding bottom damage by Amdahl and Kavlie [7], high-speed ferry bow collision by Kim et al. [61], grounding on a pinnacle by Kuroiwa et al. [64], [63]. Figure 6.4 shows part of the grounding model used by Kuroiwa, [63].

Since the finite element method is based on discretizing the structure into relatively small structural elements and solving the dynamic equilibrium equations incrementally, it can consistently take into account the coupled effects of elasticity, plasticity, strain hardening, strain rate sensitivity and temperature dependencies. The finite element method is considered to be so accurate that it has replaced model tests in several areas, but it is true to say that the problem of predicting fracture is not yet fully solved.

For the probabilistic design methodology described in Chapter 1, where a large number of grounding scenarios have to be evaluated, the method is still prohibitively expensive in terms of man and computer power, see the comments of the introduction to this chapter.

Energy Method. This class of approaches rests on more or less consistent extensions of the 'upper bound theorem of plasticity' to finite deformations. The method is based on

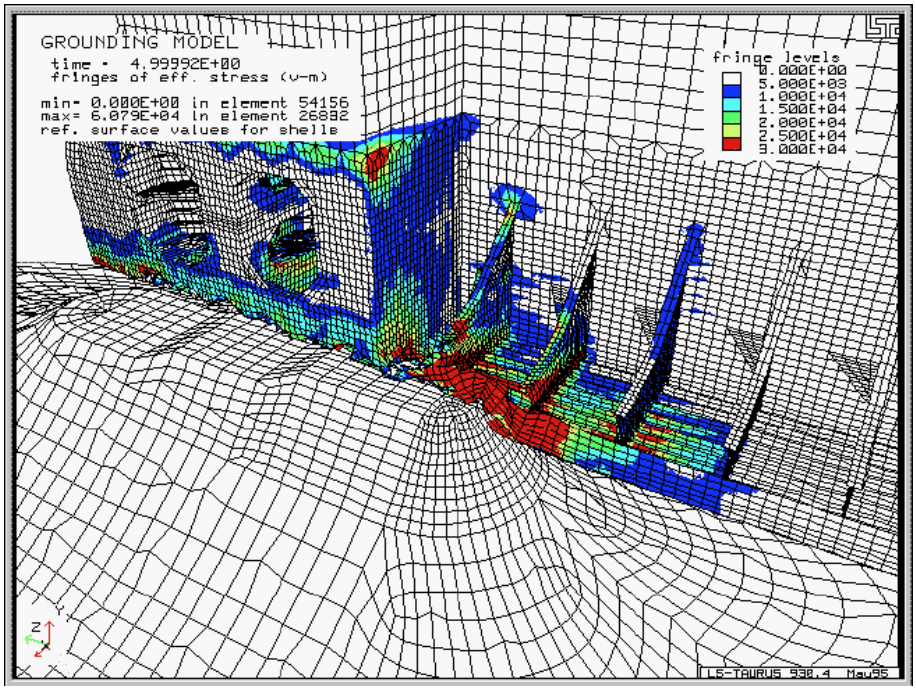

Figure 6.4: *Simulated rock and single hull VLCC with the finite element method, [63].*

the idea that the work rate (the *power*) of an external force must equal the rate of internal energy dissipation in the structure. Thus, the method is also known as the "balance-of-power approach", [22]. The procedure is to find the kinematically admissible deformation of the structure which yields the lowest force ('least upper bound').

The method was applied to crushing of thin-walled structures for the first time by Alexander, [5], in 1959. Alexander developed a simple kinematic model for axial crushing of thin cylindrical shells and humbly noted, "...In view of the approximate nature of the analysis, it is surprising that there is such good agreement with experiment...". Figure 6.5 shows the deformation mode assumed in the analysis by Alexander, [5].

Several significant applications of the method have been published since then, for example in the area of crashworthiness of vehicles, [137], and in the field of machining and metal forming, [22].

Once the deformation mode is known, the method can predict the involved forces with very good accuracy. For statically indeterminate systems, however, it may be difficult to find an appropriate deformation mode. This is a major limitation of the method. For a space frame it is possible to investigate all possible idealised failure modes and choose the one which gives the lowest failure load ("least upper bound"), but for a complex structure like a double bottom this becomes an extremely cumbersome task. A way of overcoming this problem would be to combine the simplified idealised collapse mechanisms of the upper bound method with the finite element method in a so-called *hybrid* approach, see below.

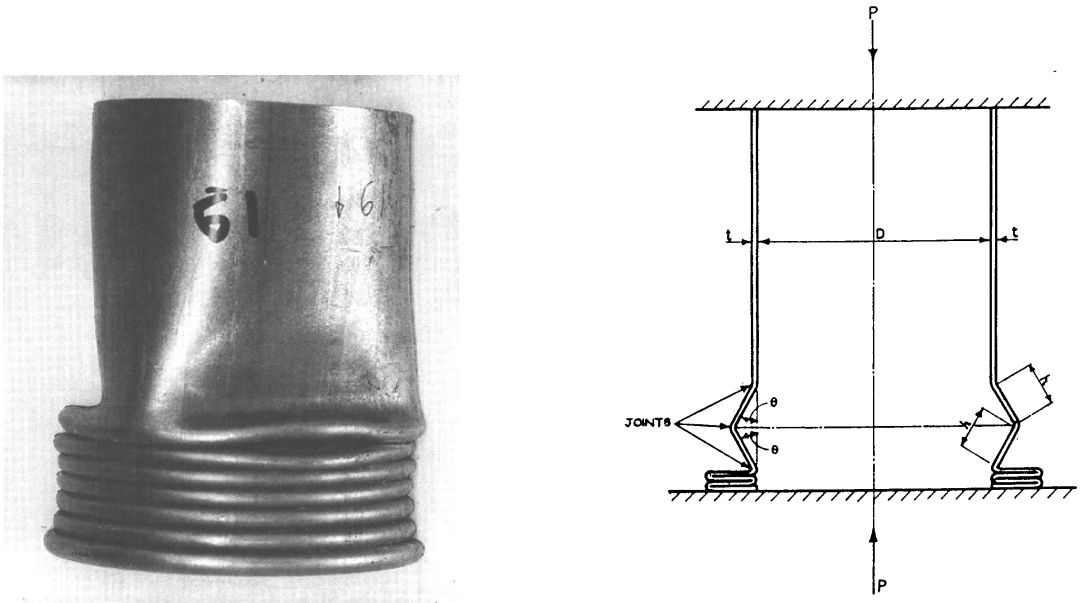

Figure 6.5: *A crushed circular tube, [53], and the corresponding idealised deformation mode, [5].*

Hybrid and Idealised Structural Unit Method. As seen above, the empirical, analytical and numerical methods all have advantages and disadvantages. The Idealised Structural Unit Method (ISUM) has the potential of utilising the strong points of each of the other methods. Like the finite element method it is based on the stiffness method, but instead of using continuum based elements, it uses relatively large structural elements. The element stiffness is defined as a function of deformation and stresses so observed behaviour like plastic deformation, buckling, and tearing can be included. The behaviour of each of the structural units can be found from any of the methods above and by applying these 'intelligent' units, the computational time can ideally be reduced by orders of magnitude compared to the finite element method, see for example Weijde and Haug, [130].

Ueda was among the first to introduce the concept in a computer program (for example Ueda and Rashed, [129]) and over time it has been applied to many different structural problems in marine engineering. Paik and Pedersen, [97], recently presented a study on the internal mechanics of side collisions based on this approach. Figure 6.6 shows an example from [97] of the deformation of the side structure. The elements shown are the actual elements of the calculational model so, compared to the detailed finite element model shown in Figure 10.9, the crude *ISUM*-model obviously requires much less computational effort.

6.3 Basic Idea of Present Internal Mechanics Model

The approach adopted here is the *"Energy Method"* or the *"Balance of Power Method"*. When external loads are applied to a deformable structure, the power (the work rate) of

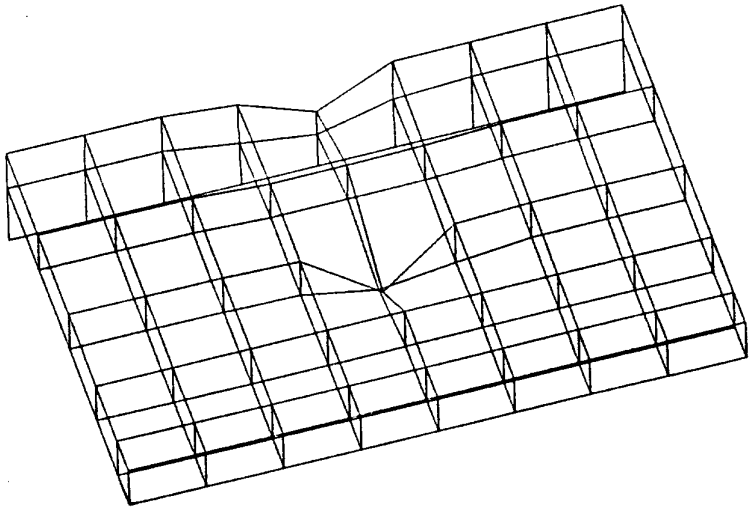

Figure 6.6: *Computational model for side collision by the ISUM, [97].*

these loads must be equal to the incremental energy stored elastically or dissipated in the structure. If a rigid-plastic structure is assumed, no elastic energy can be stored and the power of the external loads thus equals the rate of energy dissipated by plastic deformations, fracture and frictional effects on the surface of the structure. This can be expressed as:

$$F_H \cdot V = \dot{E}_p + \dot{E}_c + \dot{E}_f = F_P \cdot V + \int_S p\,\mu\,V_{rel}\,dS \tag{6.1}$$

where

F_H	is the resisting force of the structure in the direction of V. In the present thesis this direction will normally be referred to as horizontal.
V	is the relative velocity between ship and rock.
$\dot{E}_p$	is the rate of plastic energy dissipation.
$\dot{E}_c$	is the rate of energy dissipation in the crack tip zone.
$\dot{E}_f$	is the rate of energy dissipated by frictional forces. on the surface of the structure.
F_P	is the so-called plastic resistance which here includes. both plasticity and fracture.
μ	is the Coulomb coefficient of friction.
p	is the normal pressure on the rock from the plate element dS.
S	denotes the contact area between rock and plate.
V_{rel}	is the relative velocity between rock and plate element, dS.

The idea is to postulate the displacement and the strain fields of the ship bottom structure passing over a given rock and then, by use of Eq. (6.1), find the resisting force. The

advantage of this type of approach over a purely experimental one is that, once the major deformation and energy dissipating mechanisms are identified, it should be possible to consider consistently an assembled structure and find the energy dissipation and resisting force of the total assembled structure. To derive general expressions for the resistance of such a hull bottom assembly from experimental data alone seems to be an overwhelming task. The idea of smearing longitudinal stiffeners is tempting, see e.g. [95], but for use in the design of complex structures it would seem unable to capture effects of structural details or other structural arrangements.

The difficulty of the present approach is to select a realistic deformation mode. When this deformation mode is identified, the energy dissipation and the reaction force are found from the theory of the next section. The basic idea of the deformation mode adopted here is sketchily illustrated in Figure 6.7 for a pinnacle type rock. The hull bottom structure passes over the pinnacle leaving a path of deformed structure in the wake.

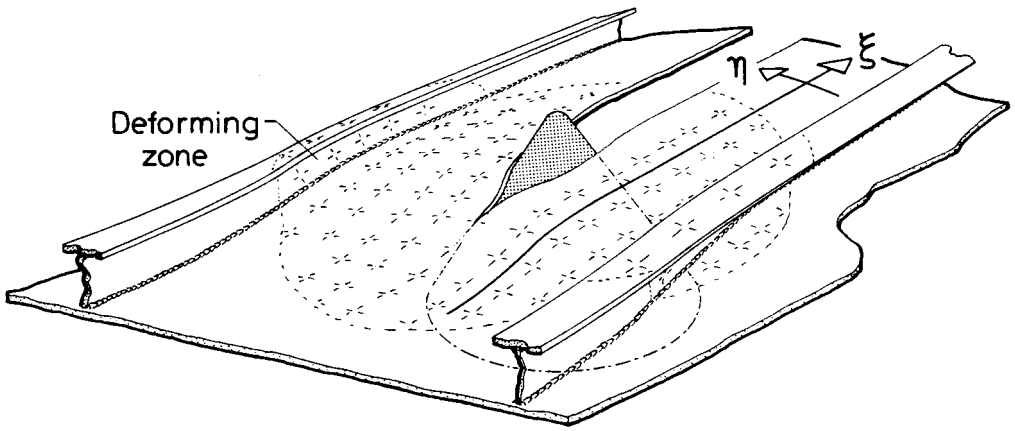

Figure 6.7: *Sketch of the idea of a moving deformation zone.*

The process is assumed to be in a quasi-static state so that the instantaneous rate of energy dissipation is found by considering a constant penetration and a constant mode of deformation. The rock penetration actually changes over time but the primary motion is clearly in the longitudinal direction[1]. Thus, it is sufficient to consider the instantaneous penetration. Transverse members also disturb the quasi-static picture but, as it will be explained later, this effect is smeared out in the longitudinal direction. Dynamic effects are not included in the present analysis although it has been shown, see e.g. Jones, [54], that these could be significant for full-scale grounding problems where the impact speed may be up to 45 knots (23 m/s).

There are three energy-dissipating mechanisms in any of the considered deformation modes:

- Bending in the form of (moving) hinge lines.

[1] Typically, the damage length is 50 - 100 times larger than the penetration, see for example [27].

- Membrane deformation of plate fields.
- Material separation in a crack tip zone, if the plate material has fractured.

Actually, there is no clear distinction between these mechanisms, but it has been shown in several areas of sheet metal deformation and fracture that such a separation of energy absorbing mechanisms often adequately represents the observed behaviour leading to great simplifications of the theoretical analysis, see e.g. Alexander, [5], Atkins, [11], and Wierzbicki and Abramowicz, [137].

It must be emphasised that the present approach assumes that the structure only fractures at the rock tip - for example there is assumed to be no separation of longitudinals, girders, floors or bulkheads from the shell plating. In many of the simplified approaches presented in the field of crashworthiness, this assumption of no fracture at element intersections has been implicitly used without further justification, for example [60], [97], [100]. A large part of the simplified theory was developed for car body parts, which normally have a plate thickness of less than 1 mm. Most of the experimental evidence therefore shows a considerably more ductile behaviour than is the case for ship structures built of plates in the order of 10-20 mm. To shed light on this problem Thomsen [124], recently performed crushing experiments with large-scale aluminium cruciforms (full-scale according to a newly built fast ferry), Figure 6.8.

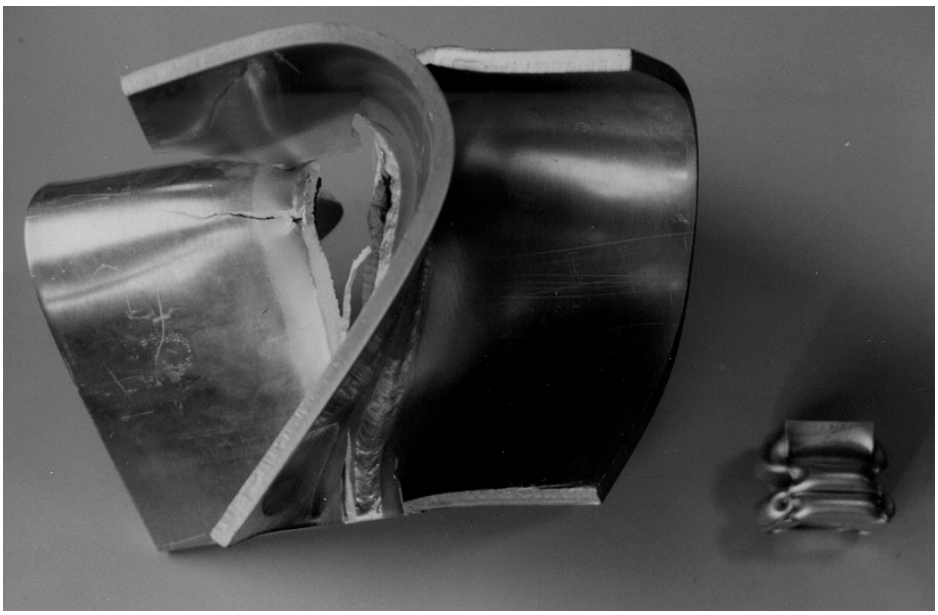

Figure 6.8: *Photograph of crushed aluminium specimens. The collapse of the full-scale specimen to the left was dominated by fracture (t = 8 mm). The small specimen to the right collapsed without fracture as seen in several previous tests, [113].*

As shown in Figure 6.8, the experiments revealed a significant portion of fracture for the full scale specimens with a plate thickness of 8 mm and the simplified theory overestimated

the energy absorption by a factor of two, see also [113]. For equivalent 4 mm specimens practically no fracture was observed and the simplified theory was found to agree with the experimental results. The example above illustrates the importance of including fracture and strength of intersections in a consistent manner and it encourages further research in this area.

6.4 Basic Equations for Energy Dissipation in Plasticity and Fracture

It is worth noting that the material flows *through* the deformation zone shown in Figure 6.7 in contrast to many structural problems where the volume of deformation is stationary within the structure. This means that any straining of material or bending of a plate section has to move continuously forward. In fact, the present deformation pattern resembles one of steady fluid flow around a blunt body. Therefore, similar to most fluid flow solutions an Eulerian description of material motion is used. The material flow is described in a (ξ, η) coordinate system where ξ follows the streamlines and η is in the perpendicular direction, Figure 6.7. The theory is divided into energy dissipation in the far field and in the tip zone. The latter is the small plastic zone right around the crack tip and the far field is the rest of the deforming zone. Inertia and strain rate effects are neglected.

Plastic Energy Dissipation in Far Field
With rigid-plastic material obeying von Mises' yield criterion, the plane stress yield condition can be written as

$$F_{vm} = \sigma_{xx}^2 + \sigma_{xx}\sigma_{yy} + \sigma_{yy}^2 + 3\sigma_{xy}^2 - \sigma_0^2 = 0 \tag{6.2}$$

where σ_0 is the uniaxial yield stress. For real construction materials σ_0 is a function of strain history and strain rate. Here, σ_0 is considered to be constant and equal to an average flow stress for the process concerned. Thus, the flow stress is higher than the initial yield stress but lower than the ultimate stress, σ_u. In the following a flow stress of $\sigma_0 = (\sigma_y + \sigma_u)/2$ is used but more advanced approaches taking into account the specific deformation process could be taken. Depending on the process other values have been suggested, for example $\sigma_0 = 0.92 \cdot \sigma_u$, [2].

For a deforming plate of area S, the rate of internal energy dissipation can be expressed as

$$\dot{E}_P = \dot{E}_m + \dot{E}_b = \int_S N_{\alpha\beta}\dot{\varepsilon}_{\alpha\beta}\, dS + \int_S M_{\alpha\beta}\dot{\kappa}_{\alpha\beta}\, dS \tag{6.3}$$

where $N_{\alpha\beta}$, $M_{\alpha\beta}$ are components of the membrane force and bending moment tensors, and $\dot{\varepsilon}_{\alpha\beta}$, $\dot{\kappa}_{\alpha\beta}$ are the corresponding generalised strain and curvature rates calculated in the deformed configuration. The two terms in the above equation represent the rate of membrane and bending energy dissipation, $\dot{E}_m$ and $\dot{E}_b$, respectively. In general, $N_{\alpha\beta}$ and $M_{\alpha\beta}$ in Eq. (6.3) are related by the yield condition, Eq. (6.2). However, this interaction between moments and membrane forces is very cumbersome to handle analytically and it is neglected in the present analysis.

It is assumed that the deformation zone consists of a series of discrete moving hinge lines and a number of deforming plate elements. If the rock is regarded as stationary, the hull deformation can be thought of as a steady-state flow of hull material past the rock. Since the material moves *through* a deformation zone, it is convenient to introduce the spatial-Eulerian coordinate system (ξ,η) shown in Figure 6.7, where ξ is directed along the material stream lines and η is perpendicular to them.

The material derivative of a given field variable $X = X(x,t)$ is in general composed of two parts [42], [75] (x refers to space and t to time):

$$\frac{D\,X}{D\,t} = \frac{\partial\,X}{\partial\,t} + \nabla\,X \cdot \mathbf{V}_\alpha{}^T \tag{6.4}$$

where the components of the gradient vector, ∇, and the velocity vector, $\mathbf{V}_\alpha$, are

$$\nabla = \begin{bmatrix} \partial/\partial\xi \\ \partial/\partial\eta \end{bmatrix} \qquad \mathbf{V}_\alpha^{\mathbf{T}} = \left[\frac{\partial\xi}{\partial t}, \frac{\partial\eta}{\partial t}\right] \tag{6.5}$$

For a steady-state process, the change in time of any quantity, X, at a given location is zero. Therefore, the first term in Eq. (6.4) vanishes. Furthermore, since material points follow the stream lines at a velocity of V, $\partial\eta/\partial t = 0$ and $\partial\xi/\partial t = V$. For steady state flow Eq. (6.4) thus reduces to

$$\frac{D\,X}{D\,t} = V\,\frac{\partial\,X}{\partial\,\xi} \tag{6.6}$$

The rate of membrane energy dissipation in Eq. (6.3) for a plate strip of width $d\eta$ can be expressed as

$$d\dot{E}_m = t \int_{\xi_a}^{\xi_b} \sigma_{\alpha\beta}\,\dot{\varepsilon}_{\alpha\beta}\,d\xi\,d\eta \tag{6.7}$$

where t is now plate thickness and (ξ_a, ξ_b) are boundaries of the local plastically deforming zone. By application of the yield condition, Eq. (6.2), and the associate flow rule, Eq. (6.7) can be written as

$$d\dot{E}_m = \frac{2}{\sqrt{3}}\sigma_0\, t \int_{\xi_a}^{\xi_b} \sqrt{\dot{\varepsilon}_{\xi\xi}^2 + \dot{\varepsilon}_{\eta\eta}^2 + \dot{\varepsilon}_{\xi\xi}\dot{\varepsilon}_{\eta\eta} + \dot{\varepsilon}_{\xi\eta}^2}\; d\xi\, d\eta \tag{6.8}$$

For a steady-state process Eq. (6.6) can be used to transform the time derivatives of the strain in Eq. (6.8) into space derivatives. By assuming that the strains are varying linearly along a stream line, the expression under the square root in Eq. (6.8) becomes a constant. Then, performing the integration over the length of the deformaton zone from ξ_a to ξ_b, the expression for the rate of membrane energy dissipation becomes

$$d\dot{E}_m = \sigma_0 V t[\varepsilon_{eq}]\; d\eta \tag{6.9}$$

where $[\varepsilon_{eq}]$ is the change in equivalent strain of a material element from entering to leaving the deformation zone. The equivalent strain is given by

$$\varepsilon_{eq} = \frac{2}{\sqrt{3}}\sqrt{\varepsilon_{\xi\xi}^2 + \varepsilon_{\eta\eta}^2 + \varepsilon_{\xi\xi}\varepsilon_{\eta\eta} + \varepsilon_{\xi\eta}^2} \tag{6.10}$$

By use of Eq. (6.6) it can be shown [114] that the rate of bending energy dissipation, $d\dot{E}_b$, for a plate strip of width $d\eta$ is

$$d\dot{E}_b = V_n M_0[\kappa_{nn}]dL = V M_0[\kappa_{nn}]\; d\eta \tag{6.11}$$

where dL is the length of the hinge line, $[\kappa_{nn}]$ is the jump in curvature over a hinge line, V_n the normal velocity of the hinge line, and M_0 is the plane strain fully plastic bending moment per unit length

$$M_0 = \frac{2}{\sqrt{3}}\frac{\sigma_0\, t^2}{4} \tag{6.12}$$

The expression Eq. (6.11) should be integrated over all hinge lines in the given problem.

Note that the equations above should be used with consistent definitions of stresses, strains and the volume of integration. In the present approach stress and strain is related to the original volume of material.

Energy Dissipation in Crack Tip Zone
A major challenge of developing a simplified method for the prediction of grounding damage is to include fracture consistently. Section 6.5 below discusses criteria for predicting the onset and the termination of fracture. When the shell plating fractures the global mode of deformation changes because large transverse membrane stresses in the plating are released. At the same time, an additional energy-dissipating mechanism is introduced: material separation. Different views on how to determine theoretically the tip zone process have been presented over time, see for example [13], [70].

One approach is to use the ductile fracture toughness, R_c, giving a rate of energy dissipation in the tip zone of

$$\dot{E}_c = R_c \, \dot{A} = R_c \, t \, V \tag{6.13}$$

where $\dot{A} = t\,V$ is the rate by which new area is generated.

Eq. (6.13) poses the disadvantage and difficulty that R_c is highly dependent on the actual strain history up to the point of fracture. For mild steel, R_c varies from 200 to 1000 kJ/m^2 depending on the mode of fracture, [12].

In special cases - for example the wedge cutting considered in Chapter 8, the plate is not separated in a true fracture mode, but the material is rather forced to *flow* around the rock (the wedge) making the use of a fracture toughness parameter questionable. The rate of energy dissipation for this alternative mode of purely plastic flow is an integral of the plastic energy dissipation over the volume of the tip zone:

$$\dot{E}_c = \int_S \sigma_0 \, \dot{\varepsilon}_{eq} \, t \, dS_{tip\,zone} \tag{6.14}$$

The question of whether fracture should be included or not is further discussed in Chapter 8. For an assembled plate bottom structure being deformed by a rock, the choice of crack tip process modelling is not critical because the energy dissipation of the crack tip is not significant. However, it is significant which global deformation mode to choose depending on the fracture state of the plate material, as further described in Section 6.5.

6.5 Onset of Fracture

As noted above, a major challenge in any theoretical hard grounding analysis is prediction of the onset and the termination of fracture in the shell plating. Prediction of fracture is important because it determines which compartments are torn open, as well as it influences the overall deformation mode and thus the amount of damage to the hull. The problem of predicting the onset of fracture can be divided into two parts:

1. Determination of the strain history of material elements up to fracture.

2. Determination of the fracture locus, i.e. the limiting length of the strain path (in a strain space) which causes fracture.

The present section is concerned with the latter, i.e. the general failure behaviour of a plate material element. Item 1 is dealt with in the specific chapter about grounding resistance of an assembled ship bottom, Chapter 9. In a detailed numerical solution, the first item does not constitute a major problem apart from the fact that calculated stress and strain concentrations generally increase with decreasing element size. Prediction of fracture therefore normally becomes sensitive to the discretization.

Since a simplified approach like the present is based on overall deformation mechanisms it is not possible to trace accurately the stress/strain history of material elements at a very detailed level. Hence, it has proved necessary in many simplified analyses to use unrealistically low values for the fracture strain, for example $\varepsilon_{cr} = 3$ % by Kierkegaard [60] or 5 % by Paik and Pedersen [97]. A similar problem is encountered in the following section concerning friction because the detailed deformation of the plate on the rock and the corresponding pressure distribution does not come from the simplified solution. For friction and fracture it is therefore necessary to couple the overall deformation model with more detailed local solutions. Such a local solution for the failure of shell plating attached to a rigid structure like a bulkhead was presented by Atmadja and McClintock, [17] and [78]. For the present problem, a local solution for a sphere indentation into a circular plate is presented in Chapter 9.

Item 2, determination of the fracture locus, is an even more difficult task than the first. Fracture often follows closely after necking, and as shown below this necking can be predicted with a good level of accuracy if the strain hardening properties of the material are known. The mechanism leading to the final material separation, however, is not yet fully understood and it has proved very difficult to make a theoretical or empirical model which applies to fracture problems in general.

Due to the difficulties mentioned above, it is too ambitious at the present stage to try to incorporate advanced models for the fracture mechanics of the ship bottom structure. In the work presented by Simonsen et al. [114], a critical penetration to rupture was calculated from the rock tip radius, the spacing between longitudinals and the fracture strain from a uniaxial tension test. Although based on a very simple one-dimensional model of the material straining in the wake of the rock, the model included some of the major parameters of the problem and it could probably be tuned to give reasonable overall prediction of fracture. The plate deformation around the rock is clearly 3-dimensional, however. In recognition of this complication, the present approach is based on theory and experience gained in the field of plate forming. Our problem of fracture in sheet metals after extensive plastic flow is also of concern to metal formers who attempt to make pressings like sinks or car body parts. The strain distribution in such complicated pressings is inevitably non-uniform and it can

be highly non-uniform in certain regions of the pressings. Regions of high local strain or high strain gradients are critical with respect to plate failure and there has long been an urge in this area of engineering to understand the failure mechanisms. Some industries use large deformation elasto-plastic finite element codes with thermodynamically coupled constitutive equations to identify critical areas of plate straining. At a more simple level, metal formers extensively use the so-called 'Forming Limit Diagram', *FLD*. The FLD shows the locus of necking in a diagram of the major in-plane strain pairs, $(\varepsilon_1, \varepsilon_2)$. Several authors have used the idea of showing the fracture locus in the same diagram - then a *Fracture Forming Limit Diagram, FFLD*. An example of an *FFLD* is given later in Figure 6.12.

6.5.1 Plastic Instabilities

Plastic instabilities can be seen in a uniaxial tension test, see Figure 6.9. When the plate specimen is deformed, the deformation initially spreads along the length of the specimen. At a certain point, the forming of a *diffuse neck* is initiated and at further deformation the neck is strongly localised in a *local neck*.

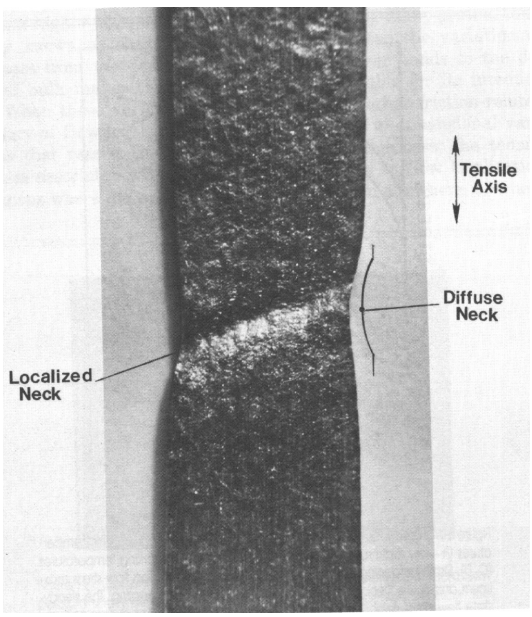

Figure 6.9: *Diffuse and local necks formed in a uni-axial tension test of a plate specimen, [108].*

The diffuse neck corresponds to a very gradual and mild thinning of the sheet, the extent of which is many times the sheet thickness. Because, in many sheet forming operations such as stretching, the sheet is clamped around its entire periphery, the symmetry profile radius observed during diffuse necking in a sheet tensile test is often not detectable. Moreover, substantial amounts of deformation is frequently obtainable even after the onset of diffuse necking. For this reason, the process of diffuse necking is normally considered as merely a

precursor to the second necking mode, that of the localised neck, which actually determines the formability of the sheet metal.

Initiation of the diffuse necking was predicted first by Consideré, [32]. If elastic deformations are neglected, the volume of the test specimen is constant during the deformation:

$$d(l \cdot A) = 0 \qquad \Rightarrow \tag{6.15}$$

$$l\,dA + A\,dl = 0 \qquad \Rightarrow \tag{6.16}$$

$$\frac{dl}{l} = -\frac{dA}{A} = d\varepsilon \tag{6.17}$$

where l and A represent the length and the cross-sectional area of the specimen, respectively. The axial load in the specimen is equal to the true stress times the area, $P = \sigma \cdot A$. During the deformation, the material hardens and σ increases but at the same time A decreases. As long as the decrease in cross sectional area is counterbalanced by a larger increase in σ the process is stable. The deformation is distributed along the length of the specimen. At some point, however, the geometric softening takes over, and the deformation will localize in the diffuse neck. At further deformation the local through-thickness neck is formed. The forming of the diffuse neck is initiated when $d\,P = d\,(\sigma\,A) = 0$, i.e.

$$\frac{d\sigma}{\sigma} + \frac{dA}{A} = 0 \tag{6.18}$$

Combining Eq. (6.17) and Eq. (6.18) gives

$$\frac{d\sigma}{d\varepsilon} = \sigma \tag{6.19}$$

The actual point of instability depends on the material hardening characteristics. Plastic behaviour of normal construction materials can often be modelled by the power law, according to which the equivalent stress $\bar{\sigma}$ is related to the equivalent strain $\bar{\varepsilon}$ by the relation

$$\bar{\sigma} = C\ \ (B + \bar{\varepsilon})^n \tag{6.20}$$

where n, B and C are material constants. In particular, n is the hardening exponent. Eq. (6.20) is often used with $B = 0$. For a material following Eq. (6.20), Eq. (6.19) gives the axial strain at the initiation of diffuse necking:

$$\varepsilon = \ln\left(\frac{l_0 + \Delta l}{l_0}\right) = n - B \tag{6.21}$$

The strain limits for diffuse necking in sheets can be found from a similar approach, again with the instability limit as the point where the increase in stress due to strain hardening is equilibrated by the decrease in the cross-sectional area, i.e. $d(\sigma_x A_x) = d(\sigma_y A_y) = 0$. The criterion, often referred to as *'Swift's Criterion for Diffuse Necking'*, [35], is the biaxial equivalent to Eq. (6.21) and it can be expressed as:

$$\begin{aligned} \bar{\varepsilon} &= \frac{2}{\sqrt{3}}\sqrt{\varepsilon_1^2 + \varepsilon_2^2 + \varepsilon_1\varepsilon_2} = Z_d\, n - B \\ Z_d &= \frac{4(1 - X + X^2)^{3/2}}{4 - 3X - 3X^2 + 4X^3} \\ X &= \frac{\sigma_2}{\sigma_1} = \frac{2\varepsilon_2/\varepsilon_1 + 1}{2 + \varepsilon_2/\varepsilon_1} \end{aligned} \tag{6.22}$$

Several attempts at predicting the local necking which follows the diffuse necking in biaxially loaded sheets have been presented over time. As shown below, classical plasticity theory predicts the existence of necking in the drawing region ($\dot{\varepsilon_1} > 0$, $\dot{\varepsilon_2} < 0$) whereas the problem in the stretching region ($\dot{\varepsilon_1} > 0$, $\dot{\varepsilon_2} > 0$) has proved to be more difficult. For the drawing region Hill, [49], presented the following results for localised necking: As necks are normally in a state of plane strain the neck must form along a characteristic line of zero extension in the plane of the sheet, i.e. $\varepsilon_{yy} = 0$ in Figure 6.10.

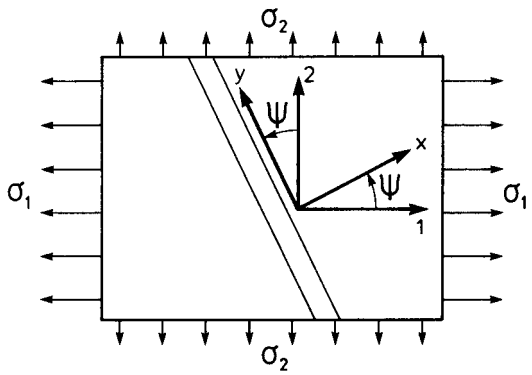

Figure 6.10: *Onset of a necking band of zero extension, according to Hill's analysis for localised necking in sheets.*

This uniquely defines the orientation of the neck as

$$\tan\psi = \sqrt{\frac{-\dot{\varepsilon}_2}{\dot{\varepsilon}_1}} \tag{6.23}$$

For the conditions of a uniaxial test ($\dot{\varepsilon}_1/\dot{\varepsilon}_2$ = -2), Eq. (6.23) gives $\psi = 35^o$, which corresponds well with the orientation of the neck in Figure 6.9. It can be shown, for example

[38], that if simultaneous stationarity is required, $d(\sigma_{xx}\, t) = d(\sigma_{xy}\, t) = 0$, and a power-law material (Eq. (6.20) with $B = 0$) is assumed, the limiting strain pair at necking is

$$\varepsilon_1 + \varepsilon_2 = n \qquad \text{for } \varepsilon_2 < 0 \tag{6.24}$$

It is evident from Eq. (6.23) that Hill's prediction of local necking is restricted to the deep-drawing range ($\dot{\varepsilon_1} > 0$, $\dot{\varepsilon_2} < 0$). It is also worth noting that the instability limits given by Eqs. (6.21) and (6.24) are independent of the assumed yield locus but dependent on the material hardening law.

A major difficulty is encountered in theoretical prediction of local necking in the stretching range ($\dot{\varepsilon_1} > 0$, $\dot{\varepsilon_2} > 0$). With flow theory and in the absence of a pointed vertex on the yield surface, forming limits can be predicted only by postulating the existence of initial defects in the sheet, [76], or by making use of a perturbation analysis for studying the rate of growth of instabilities, [36]. In another approach initiated by Stören and Rice, [119], it is shown how deformation theory can be used to simulate the destabilising effect of a vertex on the yield surface, see also [51]. As discussed by Ferron and Zeghloul, [38], however, the theory only applies to metals with no strain rate sensitivity and it can therefore hardly be applied to metals in general.

For the present grounding analysis where the actual strain, strain rates, curvatures, imperfections etc. cannot be quantified, implementation of complicated models for the material in the stretching range cannot be justified. Instead, according to Atkins, [14], an empirical formula which relates the necking locus to the material in the stretching range is simply

$$\varepsilon_1 - 1/2\, \varepsilon_2 = n \qquad \text{for } \varepsilon_2 > 0 \tag{6.25}$$

The necking locus for the shell plating is now fully defined by Eqs. (6.24 and 6.25). Figure 6.11 shows this empirical relation together with the Hill and Swift criteria for local and diffuse necking, respectively.

It should be emphasised that the effects of strain rate and geometry on the necking and the fracture are truely profound and consequently a simple locus as that defined by Eqs. (6.24) and (6.25) cannot be accurate in general. As an example of the severe effect of geometry, it can be mentioned that Mellor, [79], and Hill, [50], have shown that, for cylindrical shells exposed to tension/compression and an internal pressure, the necking locus is

$$\begin{aligned} \varepsilon_1 + 2\, \varepsilon_2 &= n \qquad \text{for } \varepsilon_2 > 0 \\ \varepsilon_1 &= n \qquad \text{for } \varepsilon_2 < 0 \end{aligned}$$

rather than the locus defined by Eqs. (6.24 and 6.25) for a plane plate.

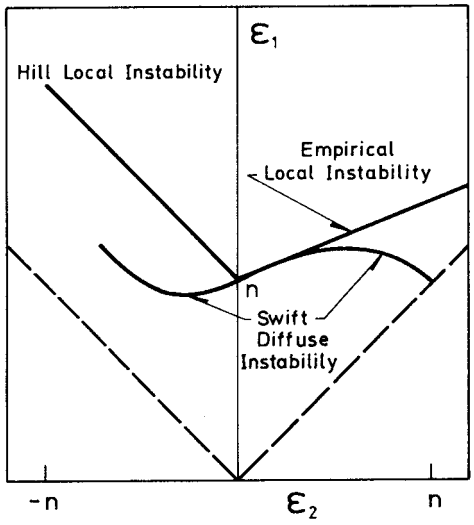

Figure 6.11: *Necking criteria: Swift, Hill and empirical.*

6.5.2 Ductile Fracture

The range of engineering problems in which fracture has relevance is enormous and the list of attempts at predicting fracture seems endless. Much of the work has been devoted to prediction of fatigue failure, which is characterised by cyclic successive development and growth of cracks at a relatively low level of plastic straining. In the present problem, fracture is preceded by a significant plastic flow and much of the theory developed for fatigue failure does not apply.

A thorough review of empirical criteria for ductile fracture is given by Atkins and Mai, [15]. These criteria include simple maximum stress or maximum strain theories, critical combinations of stress and strain and variations on these themes. Some of the criteria are entirely empirical, some are based on micromechanical models. Simple empirical criteria may represent the failure data of the particular experimental conditions from which they were derived but experiments show that many of these most simple theories cannot be true in general. The straining path up to the point of fracture is important. This observation has also been adopted in several of the empirical models by assuming that fracture occurs when some product of stress and strain, for example $\int \sigma_H \, d\bar{\varepsilon}$, reaches a critical value (σ_H is the hydrostatic stress).

The theoretical approach which has gained most popularity is that of void coalescence and growth. The basic idea is that holes are nucleated from inclusions or hard second-phase particles and that these grow and coalesce to give fracture. The holes grow in size and also change their shape. The average radial growth is proportional to the mean (hydrostatic) stress σ_H, and the change of shape depends on the shear stress field. Some of the theoretical models for void coalescence and growth are implemented as standard options in commercial non-linear finite element codes. For example Yu [144] used the model by Gurson [45] within

the framework of *MARC* and showed good agreement between measured and theoretically predicted initiation of rupture. The early models, for example proposed by McClintock and coworkers and Rice and Tracey in the 1960s, were based on ideas and solutions from viscous solids. Inclusions are modelled as regular arrays of cylindrical holes with known spacing-to-size ($l/2r$) ratios and fracture is assumed to occur when holes touch each other. In its simplest form the McClintock criteria can be written as

$$\int \frac{\sigma_H}{\bar{\sigma}} d\bar{\varepsilon} = ln(l/2r) \tag{6.26}$$

A valuable simplification of the McClintock type of criteria arises as it surprisingly turns out that the integral is somewhat path-independent. Using von Mises' yield surface, Atkins [15] has shown that the McClintock criterion for a plate in plane stress reduces to a very convenient form:

$$\varepsilon_1 + \varepsilon_2 = -\varepsilon_3 = \frac{3}{2} \ln\left(\frac{l}{2r}\right) \tag{6.27}$$

This simple result corresponds well to the experimental evidence that fracture in sheets under different load biaxialities often takes place at a specific through-thickness strain characteristic of the material.

An alternative approach is to assume fracture when the plastic work per unit volume has attained a certain critical value. When the material is strained to a state just at fracture, the energy dissipated at the (virtual) crack tip $R_c dA$, where R_c is the fracture toughness and dA is area of the new surface which is generated. The volume in which this energy is absorbed is $H dA$ where H is some measure of the in-plane width of the plastic zone. The critical work per unit volume is therefore $E_{crit} = R_c dA / H dA = R_c / H$. For a material that follows the power law, the plastic work per unit volume is

$$E = \int \bar{\sigma} d\bar{\varepsilon} = \frac{\sigma_0 \bar{\varepsilon}^{n+1}}{(n+1)} \tag{6.28}$$

The effective strain at fracture is therefore defined by the locus

$$\bar{\varepsilon} = \frac{2}{\sqrt{3}} \sqrt{\varepsilon_1^2 + \varepsilon_2^2 + \varepsilon_1 \varepsilon_2} = \left(\frac{(n+1) R_c}{\sigma_0 H}\right)^{1/(n+1)} \tag{6.29}$$

The fracture toughness, R_c can be determined by a double edged notch test, see e.g. [15] or [16]. The effective width of the plastic zone, H, is basically unknown, however. In a theoretical discussion by Atkins and Mai [16], it is suggested using the plate thickness, i.e. $H = t$. Figure 6.12 shows fair agreement between experiments and Eq. (6.29) for $H = t$.

6.5.3 Failure Criteria Adopted in the Present Analysis

As indicated above, a significant amount of scientific work has been devoted to understanding metal plate failure. Most of the proposed theoretical models require input parameters completely unknown to the practising naval architect, and they are at a level of detail and complexity which presently does not comply with the uncertainties in an assembled ship bottom structure. It is clear that the input data for the theoretical model must be at a relatively simple level, ideally only a traditional uniaxial stress-strain diagram should be given as material data input. Based on the idea that the far field displacements from necking to fracture are small due to the localisation of deformation, the present analysis adopts local necking as the governing failure mode. In summary, the necking locus is therefore given by

$$\begin{aligned} \varepsilon_1 + \varepsilon_2 &= n \qquad \text{for } \varepsilon_2 < 0 \\ \varepsilon_1 - 1/2\,\varepsilon_2 &= n \qquad \text{for } \varepsilon_2 > 0 \end{aligned} \tag{6.30}$$

An example of measured necking and fracture strains is shown in Figure 6.12 which also shows the failure locus adopted in the present analysis, Eq. (6.30) together with Eq. (6.22), Eq. (6.27) and Eq. (6.29).

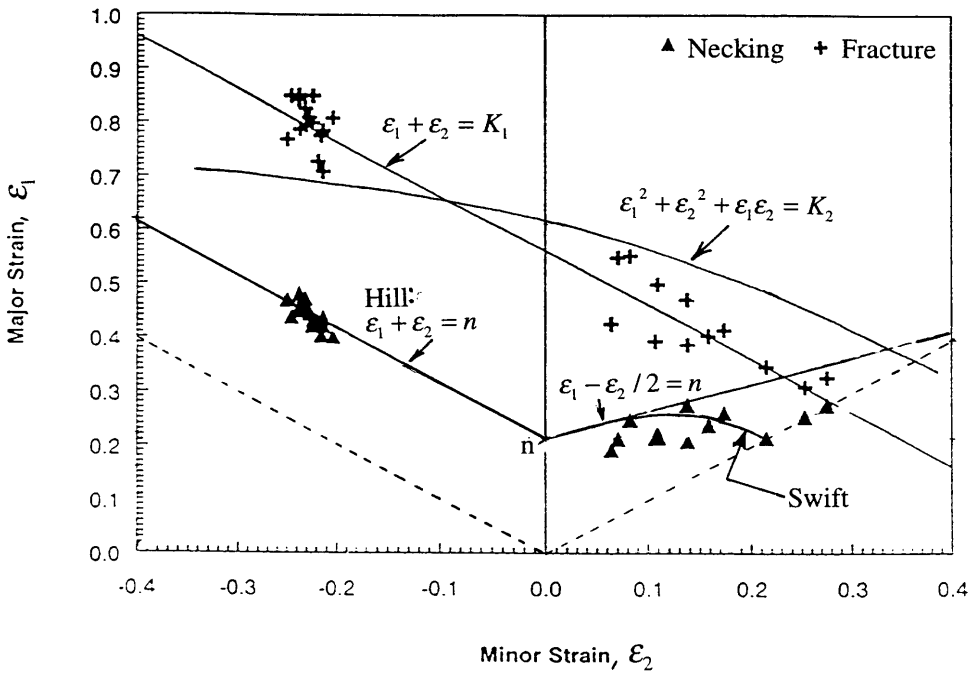

Figure 6.12: *Failure of a plate sheet under different proportional biaxial loading paths. Comparison between measurements, [82], and theory for necking and fracture. K_1 is taken to give a best fit of Eq. (6.27). K_2 is calculated from Eq. (6.29) corresponding to $H = t$.*

The results were presented in [82] and are for a low-carbon steel plate with a thickness of $t = 0.8\ mm$. The material can be described by the power law, Eq. (6.20) with $B = 0$,

$C = 548\ N/mm^2$ and $n = 0.21$. The fracture toughness was measured in a double edged notch test, see e.g. [15], to be $R = 240\ kJ/m^2$.

6.6 Friction and Perpendicular Reaction

Friction is an important energy dissipating mechanism in a grounding event. For cutting of a plate by a wedge with the semi-angle, θ, Wierzbicki and Thomas, [140], and Ohtsubo and Wang, [90], used a factor for the effect of friction on the plate resistance, F:

$$g = \frac{F_H}{F_P} = 1 + \frac{\mu}{tan\theta} \tag{6.31}$$

which indicates that friction increases the resistance by 52 % for the example of $\mu = 0.3$ and $\theta = 30^o$. In a study of tube splitting on a flat die, Stronge et al. [121], used a friction factor of $g = 1/(1-\mu)$. For the case of aluminium against a steel die, they measured a coefficient of friction of $\mu = 0.56$ giving a friction factor of $g = 2.27$.

As indicated by Eq. (6.1), the present study assumes a Coulomb type of friction where the frictional stress at the interface between plate and rock is proportional to the normal pressure. The friction factor, g, can then be consistently derived from Eq. (6.1) and the requirement of equilibrium in the direction of the overall plate motion if the distribution of normal pressure on the rock is known. Below, this is illustrated for the example of a prismatic wedge cutting through a plate which is perpendicular to the wedge edge. The approach can be extended to any rock geometry. The critical point is to determine the distribution of normal pressure, as this is not predicted by the upper bound method. For a wedge with plane surfaces, however, the whole normal pressure works in the same direction[2] so this distribution has no relevance for the solution. If it is noted that the surface, S, in Eq. (6.1) is plane and it is assumed that V_{rel} is constant over this surface the balance of work rates can be expressed as

$$F_H\, V = F_P\, V + 2\,\mu\, N\, V_{rel} \tag{6.32}$$

where N is the normal force on the front wedge sides, i.e. the integral of the normal pressure. The relative velocity, V_{rel}, between the plate and the wedge in the contact area is assumed to be inclined an angle, ζ, from the plane of the plate, Figure 6.13. This angle depends on the rolling of the plate curls on the wedge and it can be shown geometrically that ζ must be bound by 0 and θ, $0 \leq \zeta \leq \theta$. In reality, the direction of motion (ζ) for material on the wedge face changes: First there is an upward component but around the wedge shoulder, material flows horizontally.

[2] Effects of the wedge shoulders are neglected.

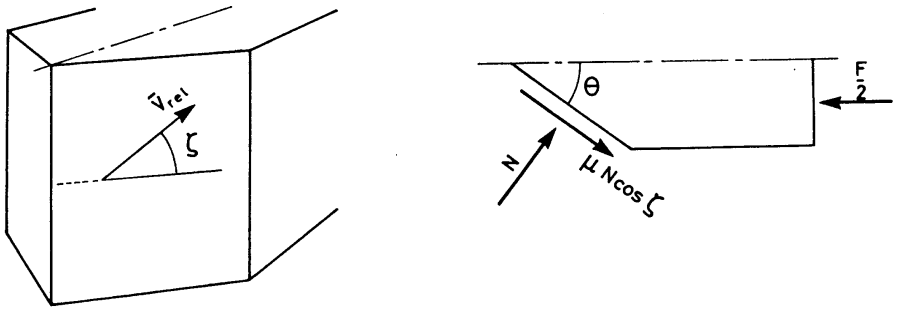

Figure 6.13: *Definition of the direction of relative velocity and free body diagram for a wedge.*

Pippenger, [103], reported scouring traces on a $\theta = 45^o$ wedge with $\zeta = 22.5^o$ and $\zeta = 17.9^o$ for experiments with wedges inclined respectively $\alpha = 70^o$ and $\alpha = 45^o$ from perpendicular. As an estimate it is therefore reasonable to use $\zeta = \theta/2$, which also makes sense intuitively.

The tangential friction force on the wedge is in the same direction as V_{rel}. Figure 6.13 shows the direction of V_{rel} and a free body diagram of the wedge. It is seen that horizontal equilibrium can be expressed as

$$\frac{F_H}{2} = N\,sin\theta + \mu\,N\,cos\theta\,cos\zeta \Rightarrow \tag{6.33}$$

$$N = \frac{F_H}{2(sin\theta + \mu\,cos\theta\,cos\zeta)} \tag{6.34}$$

Insertion of $V_{rel} = V$ into Eq. (6.32) gives

$$F_H = F_P \left(1 - \frac{\mu}{sin\theta + \mu\,cos\theta\,cos\zeta}\right)^{-1} \tag{6.35}$$

For the example of $\theta = \pi/2$ and $\zeta = \pi/2$, corresponding to the tube splitting process, the friction factor becomes $g = 1/(1-\mu)$, which is the same expression as used by Stronge et al. [121]. Inserting $\zeta = \theta/2$ in Eq. (6.34) gives the final expression for the friction factor;

$$g(\mu,\theta) = \frac{F_H}{F_P} = \left(1 - \frac{\mu}{sin\theta + \mu\,cos\theta\,cos(\theta/2)}\right)^{-1} \tag{6.36}$$

It is seen that this expression is different from that used by Wierzbicki and Thomas, [140], and Ohtsubo and Wang, [90], Eq. (6.31) which gives lower values for g than Eq. (6.36). At $\mu = 0.3$ and $\theta = 10^o, 30^o, 45^o$ the difference is 3.2 %, 9.0 % and 13 % respectively.

The reaction force, F_V, on the plate perpendicular to the direction of motion is the vertical component of the friction force μN:

$$\begin{aligned} F_V &= -2\,\mu\,N\,sin\zeta \\ &= F_H \frac{-\mu\,sin\zeta}{sin\theta + \mu\,cos\theta\,cos\zeta} \end{aligned} \tag{6.37}$$

Note that the vertical force on the plate is downward due to the upward rolling of the plate flaps. With $\zeta = \theta/2$ the ratio between the vertical reaction and the horizontal resistance thus becomes

$$k(\mu,\theta) = \frac{F_V}{F_H} = \frac{-\mu\,sin(\theta/2)}{sin\theta + \mu\,cos\theta\,cos(\theta/2)} \tag{6.38}$$

This method for finding the friction factor, g, and the vertical to horizontal force ratio, k, is also adopted in Chapter 8 and Chapter 9. A very significant shortcoming of the present friction modelling is that the coefficient of friction, μ, on which the whole formulation rests, is basically unknown as it has been reported to vary between 0.3 and 0.8. Future studies are needed to quantify coefficients of friction for different ship platings, coatings and rock types.

This page is intentionally left blank

Chapter 7

External Dynamics of Grounding on a Pinnacle

As it was discussed in Chapter 6 it is convenient to divide theoretical modelling of a grounding scenario into external dynamics and internal mechanics, see Figure 6.1. In the first part of the thesis concerning grounding on sand banks, the two-dimensional character of the ground allowed for considerations of only surge, heave and pitch, neglecting the other three degrees of freedom. When a ship runs aground on a sharp rock like a pinnacle, however, it is clear that, if the rock is not exactly at the centre line, all six degrees of freedom are activated. The vertical component of the ground reaction causes the ship to heave, roll and pitch, while the horizontal component influences the surge, sway and yaw motions. In the present chapter a simplified model for the external mechanics is proposed. From an analysis of the ship motion in the horizontal plane (surge, sway and yaw), it is first argued that the sway and yaw motions can be neglected. The surge motion can be determined from energy considerations. Then, in a separate analysis, the motion (heave, pitch and roll) due to the vertical ground reaction is considered and a relationship between ship motion and ground reaction is developed on the basis of static equilibrium.

7.1 Ship Motion in the Horizontal Plane - Damage Path

When a ship runs aground on a rock which is not in the symmetry plane, the ship begins to rotate as illustrated in Figure 7.1. It would clearly be most convenient to immediately neglect the sway and yaw motions but in order to justify such an assumption at least three items must be investigated:

1. Can the damage path be assumed to be linear?

2. Does the damage path stay within the ship or leave it?

3. Does a substantial part of the initial kinetic energy go into a rotation mode of the ship?

In order to answer these questions accurately, it is necessary to solve the equations of motion for the ship numerically. If it is found necessary, closed-form expressions for the above-mentioned effects can be developed subsequently. It should be emphasised here that the objective of the present analysis is not to determine the damage length of a given grounding event, but rather to find the ship motion and the shape of the damage path given a certain damage length.

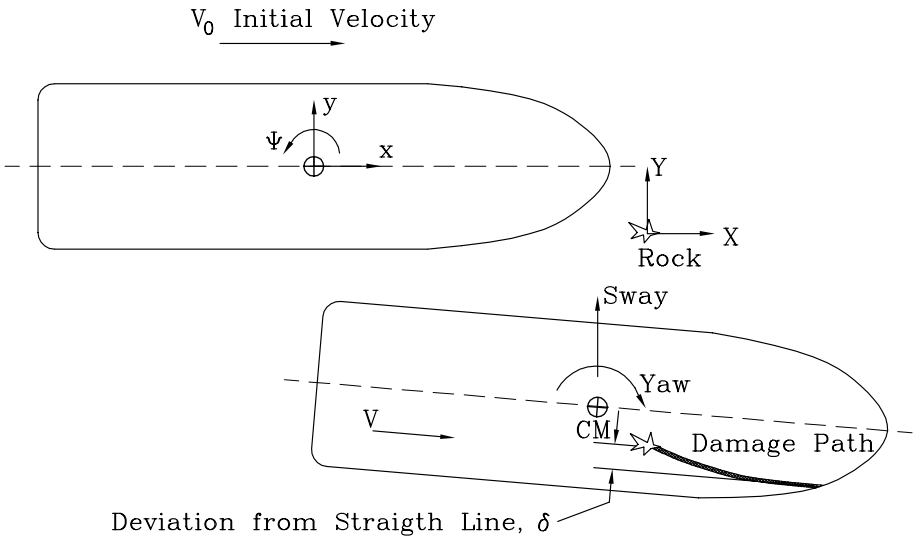

Figure 7.1: *Horizontal ship motion in a grounding scenario where the rock is not at the symmetry plane. Definition of local and global coordinate systems, xyz and XYZ.*

For the numerical solution with finite rotations, it is convenient to introduce two coordinate systems: a local coordinate system, xyz, which is fixed in the ship, and a global coordinate system, XYZ, which is fixed on the rock, see Figure 7.1. The local coordinate system has its origin in the hull symmetry plane amidships. The x-axis points forward, the y-axis points horizontally towards the port side and the direction of the z-axis is upwards. The global system has its origin at the rock centre. The X-axis points in the direction of the initial velocity of the ship, the Z-axis points upward as the z-axis and the Y-axis is perpendicular to the X and Z axes, Figure 7.1.

In the planar motion the two displacements and the rotation in the xyz-coordinate system are described by u, v and Ψ, respectively. The coordinates of the local origin ($(x, y) = (0, 0)$) in the global coordinate system are (X_S, Y_S) and the rotation Ψ is the same as in the local system.

Since only the motion in the horizontal plane is considered, gravitational and hydrostatic loads do not affect the motion, and the loads to be considered are therefore contact forces

from the rock and hydrodynamic pressure. In the following two sections these loads are discussed before the equations of motion are presented.

7.1.1 Loads on Hull from Ground

The ground reaction force depends strongly on the structure and on the rock. At this point in the analysis, certain assumptions are therefore necessary. The magnitude of the grounding force is here assumed to be constant throughout a grounding event, and the direction is assumed to coincide with the rock velocity relative to the hull. This is illustrated in Figure 7.2. In a real ship structure, major longitudinal members give significant resistance against the rock moving in the transverse direction and the present analysis therefore gives an upper bound for the deviation of the damage path from a straight line.

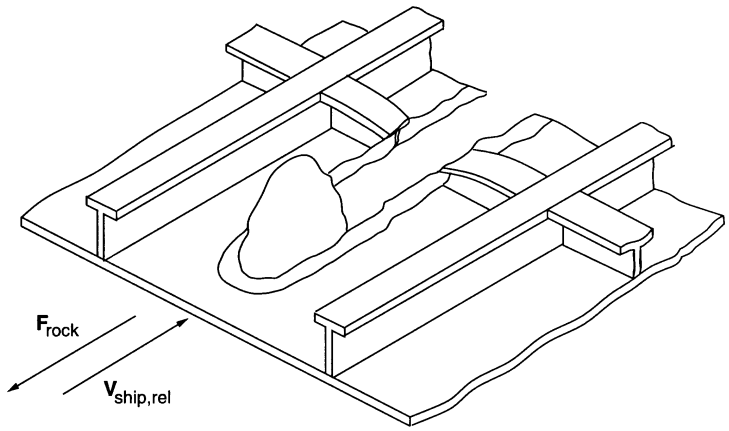

Figure 7.2: *Assumption of ground reaction force acting in the opposite direction of the relative velocity between rock and ship bottom.*

Consistent with the above definition of the coordinate systems, the velocity of the rock relative to the ship bottom at the position of the rock is given by:

$$V_{rel,X} = -\left(\dot{X}_S + Y_S\dot{\Psi}\right) \tag{7.1}$$

$$V_{rel,Y} = -\left(\dot{Y}_S - X_S\dot{\Psi}\right) \tag{7.2}$$

Hence, the total relative velocity between the rock and the ship bottom at the position of the rock is

$$V_{rel} = \sqrt{V_{rel,X}^2 + V_{rel,Y}^2} \tag{7.3}$$

The components of the grounding force in the global coordinate system can now be expressed as

$$F_{G,X} = \frac{V_{rel,X}}{V_{rel}} F_G \tag{7.4}$$

$$F_{G,Y} = \frac{V_{rel,Y}}{V_{rel}} F_G \tag{7.5}$$

where F_G is the magnitude of the grounding force. As mentioned, this force is assumed to be constant throughout the analysis and equal to an average grounding force. Actually, the magnitude of the force may change with the rock position. This changes the calculated trajectory slightly without altering the main conclusion. The direction of the force varies according to Eq. (7.4) and Eq. (7.5) above.

7.1.2 Hydrodynamic Loads

The hydrodynamic loads are modelled by a two dimensional strip theory and the application of an impulse response technique as in Chapter 6, Section 3.2.2. The transverse hydrodynamic load on a segment of the hull per unit length can be expressed as

$$q_{hd,y}(x,t) = -\mu_y(x)\ddot{v}(x,t) - \int_0^\infty h_y(x,\tau)\dot{v}(x,t-\tau)d\tau \tag{7.6}$$

where $\mu_y(x)$ is the added mass at infinite frequency;

$$\mu_y(x) = \lim_{\omega\to\infty} a_y(x,\omega) \tag{7.7}$$

and the unit response function, $h_y(x,t)$, is the cosine transformation of damping;

$$h_y(x,t) = \frac{2}{\pi}\int_0^\infty b_y(x,\omega)\cos(\omega t)d\omega \tag{7.8}$$

Added mass, $a_y(x,\omega)$, and damping, $b_y(x,\omega)$, is found by use of conformal mapping. The specific numerical example considered here is taken from Petersen [102]. The convolution integral of Eq. (7.6) can be expressed in a computationally more convenient form as

$$\int_0^\infty h_y(x,\tau)\dot{v}(x,t-\tau)d\tau = \int_0^t h_y(x,\tau)\left(\dot{v}(x,t-\tau) - \dot{v}(x,0)\right)d\tau \tag{7.9}$$

The hydrodynamic loads on the entire ship hull at a given time can now be found by integration of Eq. (7.6) along the ship length, L.

7.1.3 Equations of Motion

By treating the hydrodynamic loads as described above, the system of equations of motion in the ship coordinate system can be expressed as in Chapter 3:

$$\begin{bmatrix} M_{xx} & 0 & 0 \\ 0 & M_{yy} & x_{gy}M_{yy} \\ 0 & x_{gy}M_{yy} & J_{zz} \end{bmatrix} \begin{Bmatrix} \ddot{u} \\ \ddot{v} \\ \ddot{\Psi} \end{Bmatrix} =$$

$$\begin{Bmatrix} F_x \\ F_y \\ M_z \end{Bmatrix}_{ground} + \begin{Bmatrix} F_x \\ F_y \\ M_z \end{Bmatrix}_{damp} + \begin{Bmatrix} M_{yy}\left(\dot{v}\dot{\Psi} + x_{gy}\dot{\Psi}^2\right) \\ -M_{xx}\dot{u}\dot{\Psi} \\ \left(M_{xx} - M_{yy}\right)\dot{u}\dot{v} + x_{gy}M_{yy}\dot{u}\dot{\Psi} \end{Bmatrix} \tag{7.10}$$

where

$$\begin{aligned} M_{xx} &= \int_L \left(m(x) + \mu_x(x)\right) dx \\ M_{yy} &= \int_L \left(m(x) + \mu_y(x)\right) dx \\ J_{zz} &= \int_L x^2 \left(m(x) + \mu_y(x)\right) dx \\ x_{gy} &= \int_L x \left(m(x) + \mu_y(x)\right) dx / M_{yy} \end{aligned}$$

where $m(x)$ is the mass of the ship per unit length and μ_x and μ_y denote added mass at infinite frequency in the longitudinal and the transverse direction, respectively. The added mass in the longitudinal direction cannot be determined by simple means so as for the soft grounding problem described in Chapter 3, it is taken to be 5 % of the ship mass.

The grounding load in Eq. (7.10) is found by transforming Eq. (7.4) and Eq. (7.5) into the ship coordinate system:

$$\begin{Bmatrix} F_x \\ F_y \\ M_z \end{Bmatrix}_{ground} = \begin{Bmatrix} F_{G,X}\cos\Psi + F_{G,Y}\sin\Psi \\ -F_{G,X}\sin\Psi + F_{G,Y}\cos\Psi \\ F_{G,X}Y_s - F_{G,Y}X_s \end{Bmatrix} \tag{7.11}$$

The damping load resulting from the generation of waves can be expressed as:

$$\begin{Bmatrix} F_x \\ F_y \\ M_z \end{Bmatrix}_{damp} = \begin{Bmatrix} 0 \\ -\int_0^t h_y(\tau)\left(\dot{v}(t-\tau) - \dot{v}(0)\right) d\tau - \int_0^t h_{yx}(\tau)\left(\dot{\Psi}(t-\tau) - \dot{\Psi}(0)\right) d\tau \\ -\int_0^t h_{yx}(\tau)\left(\dot{v}(t-\tau) - \dot{v}(0)\right) d\tau - \int_0^t h_{yx^2}(\tau)\left(\dot{\Psi}(t-\tau) - \dot{\Psi}(0)\right) d\tau \end{Bmatrix}$$

where

$$\begin{aligned} h_y(\tau) &= \int_L h_y(x,\tau)dx \\ h_{yx}(\tau) &= \int_L x h_y(x,\tau)dx \\ h_{yx^2}(\tau) &= \int_L x^2 h_y(x,\tau)dx \end{aligned}$$

Eq. (7.10) is solved for the accelerations in the ship coordinate system and these local accelerations are transformed into the global coordinate system by the relations

$$\begin{aligned} \ddot{X}_s &= \ddot{u}\cos\Psi - \ddot{v}\sin\Psi - \dot{\Psi}\left(\dot{u}\sin\Psi + \dot{v}\cos\Psi\right) \\ \ddot{Y}_s &= \ddot{u}\sin\Psi + \ddot{v}\cos\Psi - \dot{\Psi}\left(-\dot{u}\cos\Psi + \dot{v}\sin\Psi\right) \\ \ddot{\Psi}_s &= \ddot{\Psi} \end{aligned} \tag{7.12}$$

Given the initial conditions, the global accelerations, $\left\{\ddot{X}_s, \ddot{Y}_s, \ddot{\Psi}_s\right\}$, can then be integrated numerically to give the velocity and position of the ship as a function of time.

The time simulation is stopped when the relative velocity between ship bottom and rock is zero, i.e. $V_{rel} = 0$, see Eq. (7.3). At this point the ship rotates around the rock and the damage does not increase further in the longitudinal direction. This corresponds to the approach most often used in the analysis of side collisions: The collision damage is assumed to stop when the relative velocity at the contact point between the struck and the striking ship has diminished to zero.

7.1.4 Numerical Example and Results of Calculations

In this section the motion of a 300,000 DWT tanker is investigated. The main particulars of the considered vessel are:

Length between perpendiculars, L	322.7 m
Beam, B	58.2 m
Draught, T	21.0 m
Block Coefficient, C_B	0.81
Displacement, M_S	327,000 tons

The unit response functions for the considered ship, $h_y(\tau)$ and $h_{yx^2}(\tau)$, are shown in Figure 7.3.

The initial distance from the rock to the ship symmetry plane (the so-called rock eccentricity) is 26 m, which is the maximum possible distance from the ship symmetry plane. The

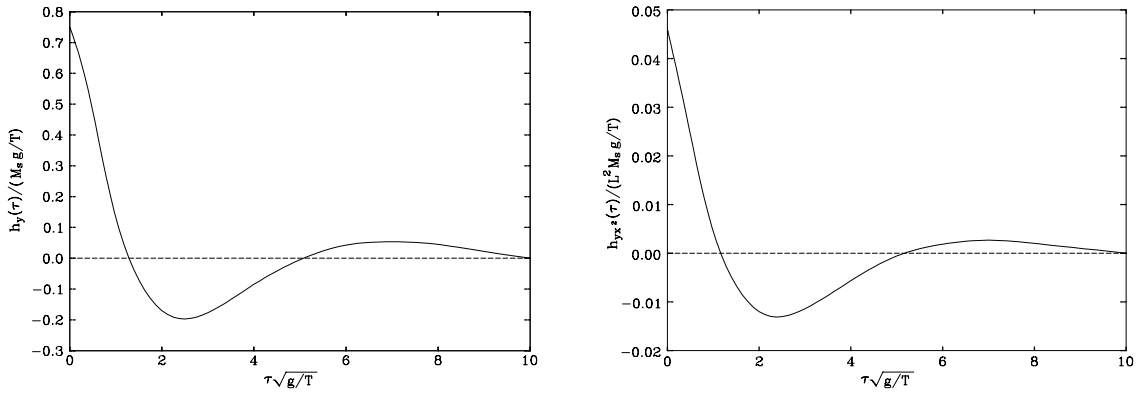

Figure 7.3: *Unit response functions $h_y(\tau)$ and $h_{yx^2}(\tau)$*

analysis will therefore give an upper bound estimate of the effect of ship rotation. The rock does not touch the hull until 12 m aft of FP.

Consider first a series of groundings at an initial velocity of 12 knots. The initial kinetic energy of the ship is the $E_{kin,init} = 1/2 M_{xx} V^2 = 6.55\ 10^9\ J$. The force level is chosen to give stopping distances of approximately 25 m, 50 m, 75 m, 100 m and 150 m. For example, for a desired stopping distance of approximately 100 m, the grounding force should be

$$F_G = \frac{6.55\ 10^9\ J}{100\ m} = 6.55\ 10^7\ N$$

In Table 7.1 below, the results are summarised for five numerical simulations. The following notation is used:

F_G	Magnitude of the grounding force used in numerical simulation.
$\frac{E_{kin,init}}{F_G}$	This quantity would be stopping distance if the ship was restrained from rotation.
ΔX_S	The calculated length (so-called 'stopping distance').
$\frac{E_{kin,term}}{E_{kin,init}}$	The ratio between the kinetic energy when the grounding has terminated and the initial kinetic energy. If the ship was restrained from rotation, this quantity would be zero.
δ_{max}	The maximum deviation of the damage path from a straight line.
Ψ_{term}	The yaw angle of the ship when the grounding terminates.

Figure 7.4 shows the damage for the five considered cases. The damage path is shown as the deviation of the path from a straight line as a function of distance from the point of first contact. Positive deviation means that the damage path has moved towards the symmetry plane of the ship.

Table 7.2 summarises results for the analysis of the effect of impact velocity. An analysis equivalent to the one above is carried out for impact velocities of 4 knots, 8 knots, 12 knots,

Table 7.1: *Summary of the results for analysis of the effect of force level on the horizontal motion. The initial velocity is 12 knots (6.17 m/s).*

	F_G (MN)	$\frac{E_{kin,init}}{F_G}$ (m)	ΔX_S (m)	$\frac{E_{kin,term}}{E_{kin,init}}$ $(\%)$	δ_{max} (m)	Ψ_{term} (deg)
1	262.0	25.0	25.1	1.13	2.15	1.6
2	131.0	50.0	50.2	1.51	3.93	3.6
3	87.3	75.0	75.3	2.01	5.03	6.2
4	65.5	100.0	100.0	2.66	4.93	9.2
5	43.7	150.0	149.1	3.75	2.49	15.7

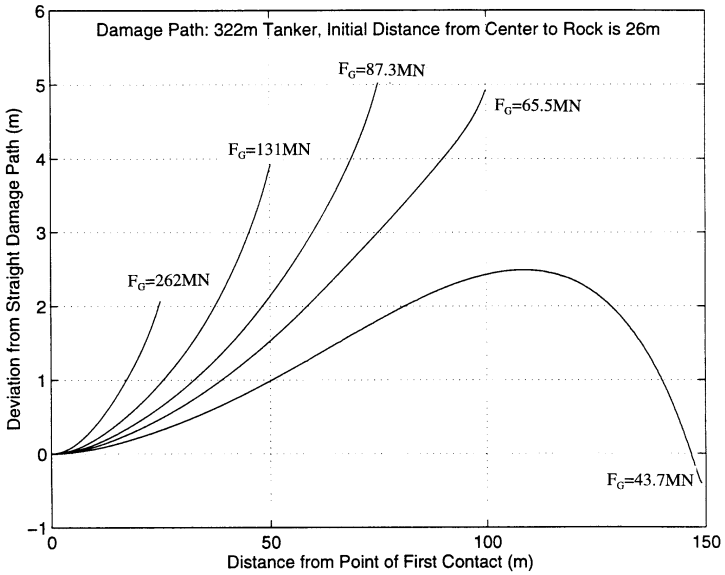

Figure 7.4: *Calculated damage paths for the five levels of the ground reaction force considered in Table 7.1. The impact velocity is 12 knots.*

and 16 knots. The grounding force is chosen to be one which led to the maximum deviation of the damage path from a straight line in the previous analysis, i.e. $F_G = 87.3\ MN$.

Figure 7.5 shows the calculated damage paths for the different impact velocities. It is seen that the shapes of these paths are similar to the paths found in Figure 7.4 for different grounding forces.

An important conclusion from the analysis is that the rock initially moves towards the ship symmetry line (if initial contact is forward of amidships). This means that if a ship just barely strikes a rock with the bilge, the rock will "lock" onto the ship and the rotation of the ship will cause the damage to extend further into the hull structure - the rock will not tend to leave the structure, as might be expected.

Concerning the question of whether the damage path leaves the ship at some point, the present analysis suggests that, if the initial point of contact is at the fore end of the ship and

Table 7.2: *Summary of the results for analysis of the effect of impact velocity on horizontal motion. The grounding force is* $F_G = 87.3\ MN$

	$V\ (knots)$	$\frac{E_{kin,init}}{F_G}\ (m)$	$\Delta X_S\ (m)$	$\frac{E_{kin,term}}{E_{kin,init}}\ (\%)$	$\delta_{max}\ (m)$	$\Psi_{term}\ (deg)$
6	4.0	8.33	8.40	0.95	0.75	0.48
7	8.0	33.3	33.6	1.25	2.84	2.2
8	12.0	75.0	75.3	2.01	5.03	6.2
9	16.0	133.3	132.8	3.72	2.91	13.4

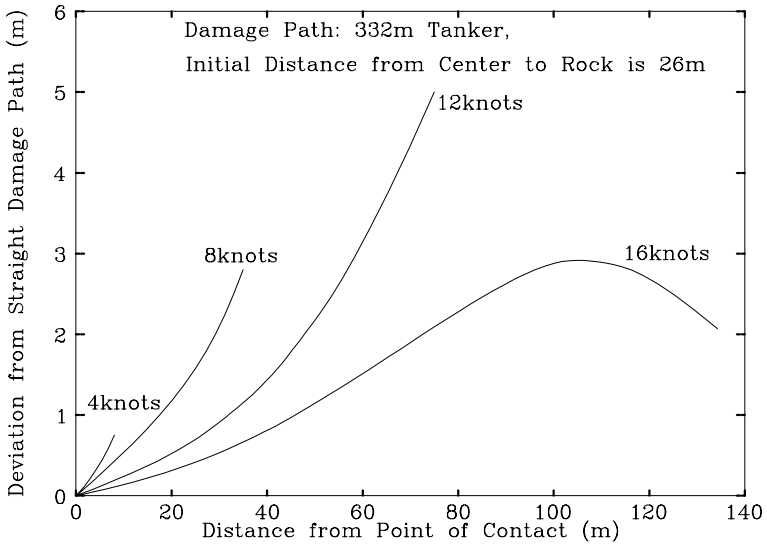

Figure 7.5: *Calculated damage paths for the four different impact velocities considered in Table 7.2. The ground reaction force is 87.3 MN.*

the expected stopping distance (i.e. $E_{kin,init}/F_G$) is between $L/2$ and L, the damage path leaves the ship. However, this part of the analysis requires further investigation because the strength of the structure in the transverse direction must be properly included in the present model. It should also be noted that considering the rock at the bilge gives the highest possible ship rotation. The rotation vanishes if the rock is in the ship symmetry plane.

It is seen from Table 7.1 and Table 7.2 that the deviation of the damage path from a straight line, δ_{max}, has a maximum of approximately 5 m and that the maximum amount of the initial kinetic energy that goes into the rotation is 3.72 %. Comparing columns 3 and 4, the analysis also shows that, if the horizontal force can be determined, the stopping distance can be found with very good accuracy by ignoring the rotation mode and simply equating the initial kinetic energy to the work of horizontal force. This observation supports the validity of the energy balance approach proposed below, where the yaw and sway motions of the ship are neglected.

7.2 Static Equilibrium of a Grounding Ship

In this section a relationship is established between the vertical component of the ground reaction and the heave, roll and pitch of the ship. As mentioned, this relationship is based on static equilibrium so that the horizontal reaction force does not contribute to the equilibrium equations. The effect of neglecting vertical inertia forces is believed to be small although it is recognised that, when sturdy transverse members are encountered, inertia will invariably have some effect which cannot be taken into account in a purely static approach. A natural future expansion of the model would be to solve the equations of motion taking account of inertia terms.

Consider a ship (initially floating freely) which is exposed to a vertical force, F_Z, at an arbitrary position on the ship bottom. The objective is to find changes in heave, surge and pitch from the initial equilibrium position corresponding to equilibrium in the new position. Changes in heave, pitch, and roll are here denoted w_h, θ_p and φ_r. The change in heave is measured at the Longitudinal Centre of Flotation, LCF, and the position of the point of contact, P, is measured from the symmetry plane at the LCF. The longitudinal and transverse distances to P are denoted l and s respectively, see Figure 7.6.

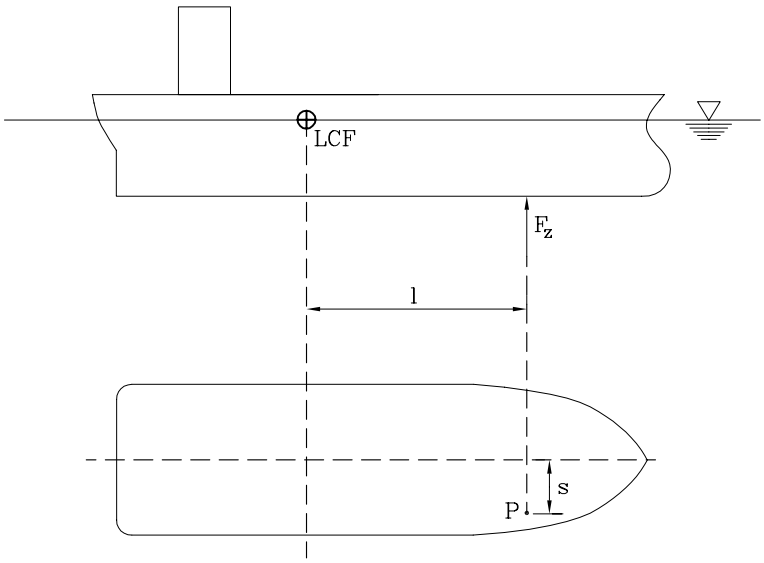

Figure 7.6: *Definition sketch for static equilibrium.*

For small rotations and displacements, the lift of the hull, ΔZ, at the point P can in terms of heave, pitch and roll be expressed as:

$$\Delta Z = w_h + l\theta_p + s\varphi_r \tag{7.13}$$

The condition for static equilibrium can be expressed as

$$F_Z \;=\; \rho_w\, g\, A_{wp}\, w_h \tag{7.14}$$

$$M_x = \rho_w\, g\, \nabla\, GM_T\, \varphi_r \quad , \quad M_x = F_Z\, s \tag{7.15}$$

$$M_y = \rho_w\, g\, \nabla\, GM_L\, \theta_p \quad , \quad M_y = F_Z\, l \tag{7.16}$$

On the basis of Eqs. (7.13 - 7.16), the relation between the vertical reaction and the lift of the hull at the position of the rock can now be expressed as

$$F_Z = \frac{\rho_w g A_{wp}}{1 + \dfrac{l^2}{r^2} + \dfrac{s^2}{p^2}} \Delta Z \tag{7.17}$$

Two new parameters are introduced here, the equivalent radii of inertia:

$$r^2 = \frac{\nabla GM_L}{A_{wp}} \quad \text{and} \quad p^2 = \frac{\nabla GM_T}{A_{wp}} \tag{7.18}$$

where

∇	is the displacement volume of the ship.
A_{wp}	is the area of the water plane.
GM_L	is the longitudinal metacentric height.
GM_L	is the transverse metacentric height.

7.2.1 Numerical Example

In order to illustrate how the vertical reaction force depends on the point of attack, P, for the ground reaction, consider Eq. (7.17) in a non-dimensional form:

$$F'_Z = \frac{F_Z}{\rho_w g A_{wp} \Delta Z} = \frac{1}{1 + \left(\dfrac{l}{r}\right)^2 + \left(\dfrac{s}{p}\right)^2} \tag{7.19}$$

For the tanker considered in the previous section in a fully loaded condition, the following maximum values were found

$$\frac{l}{r} = 2.0 \qquad \text{at FP in the ship symmetry plane}$$

$$\frac{s}{p} = 2.8 \qquad \text{at the foremost point at the bilge}$$

For a unit displacement at different locations on the ship bottom, the vertical force (equivalent to the 'stiffness' of the floating ship) can then be found from Eq. (7.19), see also Figure 7.7:

Force at symmetry line amidships (max. force)	$F'_Z = 1$
Force at symmetry FP	$F'_Z = 0.20$
Force at bilge amidships	$F'_Z = 0.11$
Force at bilge at fore end	$F'_Z = 0.078$

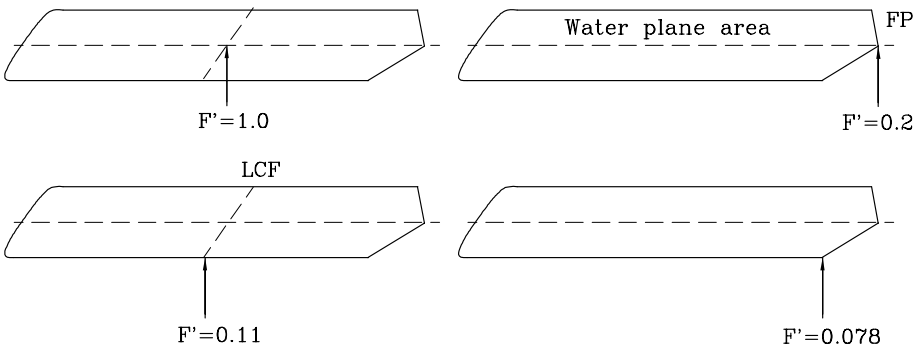

Figure 7.7: *Illustration of the vertical force required to lift the ship a unit displacement at different locations on the ship bottom. The four figures illustrate the ship water plane and the force at the four positions considered above.*

The results above illustrate the significant decrease in 'stiffness' of the floating ship as the distance from the LCF to the contact point increases. It is clear from these results that the penetration of the rock into the ship structure will be largest if the rock is at the ship symmetry plane and smallest if the rock is at the bilge.

The potential energy due to a grounding-induced lift, ΔZ, of the ship can be found from Eq. (7.17) as the work of the external force, F_Z, required to bring the ship to the given condition:

$$E_{pot} = \int_0^{\Delta Z} F_Z(Z)dZ = \frac{1}{2}\frac{\rho_w g A_{wp}}{\left(1 + \frac{l^2}{r^2} + \frac{s^2}{p^2}\right)} \ (\Delta Z)^2 \tag{7.20}$$

The next section describes how Eq. (7.17) and Eq. (7.20) can be used in a simplified model for the external dynamics.

7.3 Simplified Model for the External Dynamics

The main results of the analyses of global ship motion presented above can be summarised as follows:

- The sway and yaw motions can be neglected with little loss of accuracy for most grounding events. Thus, the damage path can be assumed to be linear and the kinetic energy of the rotation mode can be neglected.

- The relation between the vertical component of the ground reaction and heave, pitch, and roll was established on the basis of static equilibrium, Eq. (7.17).

- The expression for the potential energy of the ship due to the grounding event was derived, Eq. (7.20).

Based on these results the present section presents a simplified theoretical model for determination of the equilibrium path and determination of the point when the ship has been brought to a stop.

Figure 7.8 defines the main parameters of the problem. In consistency with the analysis above, the X-axis points forward and has its origin at the rock centre. The longitudinal position of the ship is described by the coordinate amidships, X_S, and the position of the ship at the initial contact is denoted X_0.

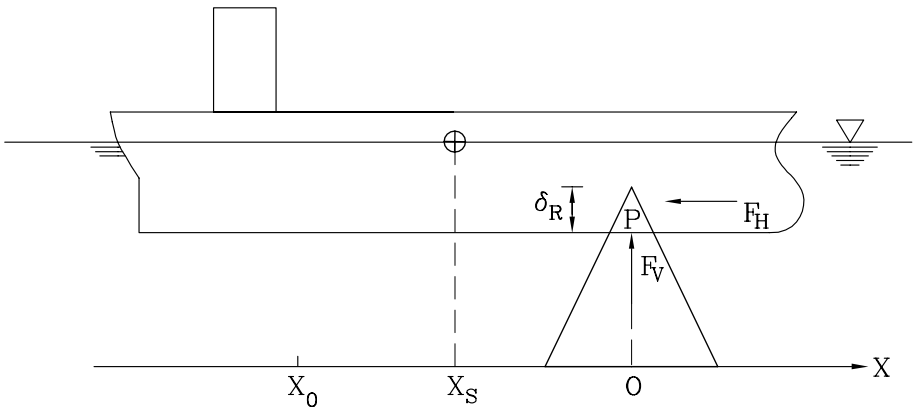

Figure 7.8: *Definition sketch for determination of equilibrium path and stopping position of ship.*

The basic idea is to increment the ship forward and at each increment find the rock penetration, the ground reaction, and the heave, pitch and roll motion corresponding to the static equilibrium of the ship. As the ship is incremented forward the work of the horizontal force tracked all along. When the work of the ground reaction plus the potential energy of the ship equals the initial kinetic energy, the ship has been brought to a stop.

The structural model derived in the subsequent chapters expresses the horizontal and the vertical components of the ground reaction, (F_H, F_V), in terms of the rock penetration, δ_R, into the hull. It is assumed that the contact area between the hull and the rock is a point, P, on the ship bottom. The rock penetration at point P if there were no heave, pitch and

roll is denoted δ_{R0} and, as before, the vertical rigid body lift at point P is called ΔZ. The net penetration into the hull is then:

$$\delta_R = \delta_{R0} - \Delta Z \tag{7.21}$$

The condition for equilibrium can now be expressed as the solution, ΔZ, to the non-linear equation:

$$F_Z(\Delta Z) = F_V(\delta_{R0} - \Delta Z) \tag{7.22}$$

where $F_Z(\Delta Z)$ is given by Eq. (7.17) and $F_V(\delta_{R0} - \Delta Z)$ is the vertical reaction force. Expressions for $F_V(\delta_R)$ are derived in the subsequent chapters about internal mechanics. Due to fracture in the structure, the function $F_V(\delta_R)$ is a discontinuous function, which causes certain complications of determining the global equilibrium because several points may satisfy the equilibrium conditions. This is illustrated in Figure 7.9, which, in principle, shows the two functions of Eq. (7.22). The problem of several equilibrium paths is often encountered in the solution of non-linear differential equations. It complicates the analysis because the solution can be very sensitive to the initial conditions.

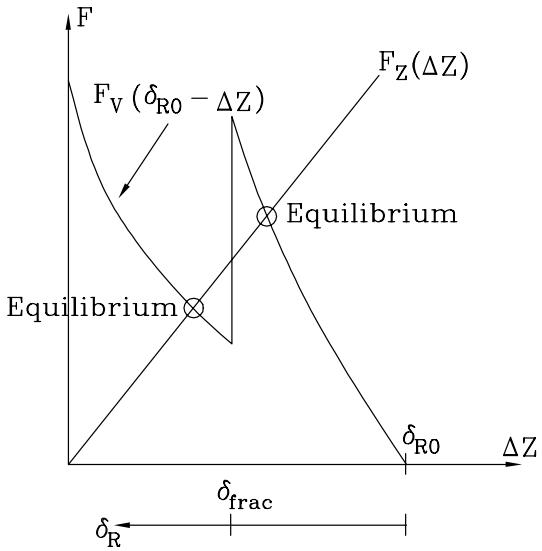

Figure 7.9: *Illustration of multiple root equation for global equilibrium.*

The procedure for the external dynamics can be summarised as follows:

1. When contact is initially established, determine the equilibrium condition which is first encountered when the rock penetrates the hull (i.e. the largest possible root, ΔZ in Eq. (7.22), see Figure 7.9). Calculate the horizontal resistance, F_H.

2. The ship position is incremented forward by a distance ΔX_S.

3. A new equilibrium position is sought around the previously found equilibrium configuration. If more equilibria are found, the new equilibrium is considered to be the one closest to the previous.

4. When the appropriate equilibrium is found, the horizontal component of the ground reaction F_H and the potential energy of the ship can be calculated. The current kinetic energy of the ship can then be calculated from the principle of conservation of energy:

$$E_{kin}(X_S) = E_{kin,init} - E_{pot}(X_S) - \int_{X_0}^{X_S} F_H(X)dX \tag{7.23}$$

When $E_{kin}(X_S) = 0$, the ship has been brought to a stop and the calculation is terminated. The damage length of the hull is then $\Delta X_S = X_S - X_0$. If $E_{kin}(X_S) > 0$ the loop is entered at point 2.

This page is intentionally left blank

Chapter 8

Internal Mechanics for a Bare Plate Cut by a Wedge

8.1 Introduction

One of the energy-absorbing mechanisms in a grounding or collision event is the so-called plate cutting process. However, considering the complexity of an assembled ship bottom structure deformed in a grounding event, the problem of only plate cutting seems to be of minor importance. Nevertheless, many experimental results and much work have been devoted to this problem and it is also treated here. Most authors use the terms 'cutting' or 'tearing' although some of the observed failure modes are quite complex and bear little resemblance to the original meaning of these words. The mechanics of the cutting process is complicated as it may involve plastic flow of the plate in the vicinity of the wedge tip, ductile fracture, friction between wedge and plate, membrane deformation of the plate, and large-scale bending of the plate 'flaps' remote from the wedge tip into various scroll motifs and other folding patterns.

In this chapter, the plate cutting phenomenon is described qualitatively, some of the most significant previous work is discussed and summarised, and new theories are derived for steady-state plate cutting by a wedge.

Depending on the deformation mode which develops, the plate cutting phenomena described in the literature can be divided into three categories, see Figure 8.1:

1. Stable or clean curling cut. The plate is separated at the tip or in front of the wedge and rolls and folds to the same side during the entire process.

2. Braided cut. The plate separates at the wedge tip as in the clean curling cut but the deformed flaps fold back and forth.

3. Concertina tearing. The plate folds back and forth in front of the wedge while it is torn at remote boundaries.

The experimental and theoretical analyses of these three classes fall into two main categories:

- "Initiation or transient wedge penetration". The wedge penetration is considered from the point of initial contact between wedge tip and plate edge to the point where the mean resistance force reaches a constant level. Normally, the initiation phase can be assumed to terminate when the shoulders of the wedge enter the plate, [69]. Since the maximum width of the penetrator into the plate increases with the penetration, the reaction force is also an increasing function of the penetration. This process was initially considered as an idealisation of a rigid ship bow penetrating into the deck-plating of another ship in a collision but, recently, it has also been applied to groundings. Several authors, for example [90], [10] and [95], have applied results or models for this process as an approximation to problems of 'steady-state penetration' described below.
- "Steady-state penetration". If the penetrator has a finite width, the plate reaction force reaches a constant mean level after a certain penetration and the process is then said to be in a steady state. This process is considered to be an idealisation of a rock pinnacle or ice reef cutting through a ship bottom in a grounding or ice collision event.

For each of the three examples shown in Figure 8.1, the deformation was large enough for the steady state to be reached, so the figure shows the deformation and the reaction in both the initiation and the steady state phases.

The present chapter is concerned with the steady state clean curled cutting. Whenever the term 'cutting' is used in the following without further explanation it refers to this specific cutting mode.

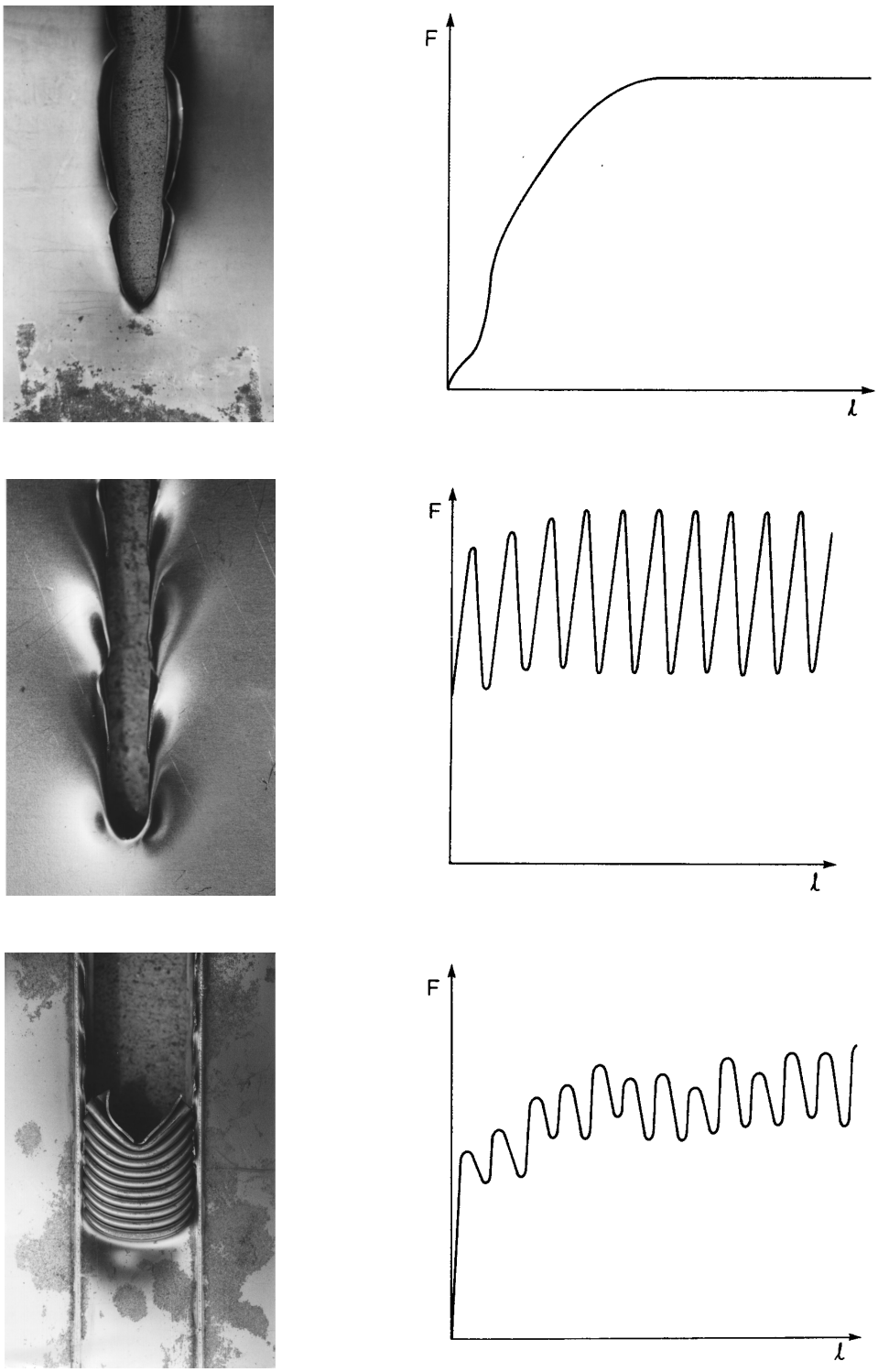

Figure 8.1: *Photographs of three cutting modes: clean curling cut, braided cut, and concertina tearing with corresponding force-displacement (F, l)-diagrams.*

8.2 Previous Work

A thorough literature review was presented by Lu and Calladine, [69], but since then the list of relevant publications has been expanded. A brief summary of literature pertinent to the field of plate cutting is given below.

The basic geometric features of the cutting set-up used in the reported experimental work is shown in Figure 8.2.

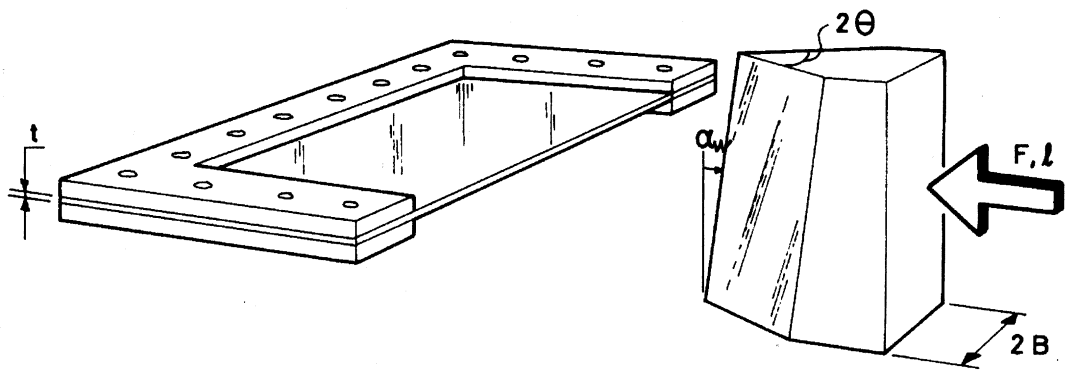

Figure 8.2: *Cutting set-up.*

The definition of the inclination angle, α_w, varies. Some perform experiments with an inclined plate and some incline the cutting edge as shown in Figure 8.2.

Earlier experiments were performed with drop-hammer tests but to eliminate dynamic effects - which are difficult to interpret - most recent work is based on quasi-static testing.

Several authors developed simple formulas giving the energy absorption, W, as a function of the penetration, l, into the plate. The reaction force, F, is then calculated from $W(l)$ as $F(l) = \frac{dW}{dl}$ with a correction factor when needed, due to the inconsistency of the dimensions. In the next section the formulas are compared.

The notation used in the present chapter is given below.

F	Reaction force from plate on wedge (N).
W	Absorbed energy (Nm).
l	Length of penetration into plate (mm).
t	Plate thickness (mm).
δ_t	Crack tip opening displacement (mm).
$\overline{\delta}_t$	Non dimensional crack tip opening displacement, $\overline{\delta}_t = \delta_t/t$.
2θ	Wedge angle, i.e. angle between wedge faces.
$2B$	Shoulder width of wedge.
b	Spacing between longitudinal stiffeners.
μ	Coefficient of friction.
α_w	Angle between cutting edge and normal to plate.
σ_y	Initial yield stress.
σ_0	Energy equivalent flow stress.

Not all of the empirical formulas listed in the following are dimensionally consistent, i.e. they are not independent of the dimensions of the involved parameters. If not defined otherwise, F is in $[N]$, W is in $[Nm(=J)]$, and l, t is in $[m]$.

Akita, Ando, Fujito and Kitamura (1972), [3] and [4], conducted tests with penetration of a rigid wedge ($\theta = 30,\ 40^0$) into a 3.2 mm steel plate to analyse the response of a ship side in collision. They proposed a simple conceptual model in which the plate exerts a normal compressive stress of σ_y onto the plate over the nominal contact area. From static equilibrium the plate resistance force becomes

$$F = 2.0\sigma_y\, t\, l\, tan\theta \tag{8.1}$$

Since the portion of the plate in contact with the wedge is deformed due to tearing and denting it was proposed to reduce the resistance force by 20 %. However, the analysis does not take the actual deformation mode of rolling plate flaps consistently into account and, as it is shown in Figure 8.3 of the next section, the proposed formula, Eq. (8.1), over predicts the actual plate resistance.

Vaughan (1978,80), [132], [133], used the experimental data of Akita and Kitamura, [4], together with Minorsky's formula, [80], to estimate the damage suffered by a ship bottom cut by a reef or ice. Vaughan assumed that the energy would be absorbed in two mechanisms, plastic deformation and creation of new surfaces by fracture, and thus came up with an two term empirical expression for the energy absorption and plate resistance force:

$$W = 3.3 \cdot 10^7\, l\, t + 9.3 \cdot 10^7\, l^2\, t\, tan\theta \tag{8.2}$$

$$F = 3.3 \cdot 10^7\, t + 1.9 \cdot 10^8\, l\, t\, tan\theta \tag{8.3}$$

Vaughan subsequently performed sixty-four drop-hammer experiments with plates of mild steel, [133], with $t = 0.752,\ 0.958,\ 1.181,\ 1.867\ mm$ and $\theta = 5,\ 15,\ 30^0$. Based on the same idea of two major energy-absorbing mechanisms, he obtained an expression for the energy absorption:

$$W = 1.7 \cdot 10^8\, l\, t^{1.5} + 4.4 \cdot 10^9\, l^2\, t^2\, tan\theta \tag{8.4}$$

$$F = 1.7 \cdot 10^8\, t^{1.5} + 8.8 \cdot 10^9\, l\, t^2\, tan\theta \tag{8.5}$$

All experiments were performed with the plate tilted at an angle, of $\alpha_w = 10^0$, because it was discovered that, with this orientation, the cutting of the plates occurred by flaps rolling up on one side ('clean curling cut'), in contrast to the more complicated back-and-forth bending ('braided cut'), which is characteristic when $\alpha_w = 0^0$.

The expression for the reaction force, Eq. (8.5), is seen to have a finite value at zero penetration so that for small penetrations, these formulas do not correspond to actual reaction forces.

Woisin (1982), [141], analysed drop-hammer tests reported by GKSS in Germany. In a series of 13 tests, two equal plates ($t = 2 - 10\ mm$) cut into each other and Woisin proposed the following formula for the energy absorption:

$$W = 6.0 \cdot 10^8\, l\, t^{1.7} \tag{8.6}$$

$$F = 6.0 \cdot 10^8\, t^{1.7} \tag{8.7}$$

In a series of 19 tests, rigid wedges ($\alpha_w = 0^0$, $\theta = 15,\ 35,\ 50^0$) were forced into plates of mild steel with thicknesses between 2 and 4 mm. In seven of these tests the plate did not rupture although the penetration amounted to $l/t = 30$. The resistance of a plate of mild steel before fracture was found to be well approximated by the expression

$$F = 6.0 \cdot 10^9\, t^2 \tag{8.8}$$

when $12 \leq l/t \leq 30$ and $5\ mm \leq t \leq 10\ mm$.

In the remaining cases where the plate ruptured the proposed expressions are

$$W = 2.5 \cdot 10^9\, l\, t^2 \left\{0.5 + 30\left(\frac{t}{l}\right) + \frac{\theta - 20^0}{15^0}\left(0.05 + 0.002\frac{l}{t}\right)\right\} \tag{8.9}$$

$$F = 2.5 \cdot 10^9\, t^2 \left\{0.5 + \frac{\theta - 20^0}{15^0}\left(0.05 + 0.004\frac{l}{t}\right)\right\} \tag{8.10}$$

for $20^0 \leq \theta \leq 50^0$ and $24 \leq l/t \leq 60$.

By considering the cutting response of plates of different thicknesses the complexity of scaling was noted.

Jones, Jouri, and Birch (1984-87), [52] , [55], and [56], performed drop-hammer tests on plates of mild steel. In the most recent work, [55], eighty-four specimens were cut with $\alpha_w = 0^0$, $t = 1.501 - 5.95\ mm$, and $2\theta = 30$, 45, and 60^0. The energy-absorbing mechanisms - cutting, bending, elasticity and friction - were identified and an attempt was made to partition between them the energy delivered. The bending and the friction energies were found to amount to about 10 % each, elasticity effects were negligible, and the remaining - i.e. the energy absorbed in cutting - was found to be given by the formulas

$$W = 8.1 \cdot 10^7\, l\, t^{1.44} \tag{8.11}$$

$$F = 8.1 \cdot 10^7\, t^{1.44} \tag{8.12}$$

for $t = 1.501\ mm$ and $\sigma_0 = 255\, MPa$ and

$$W = 5.9 \cdot 10^7\, l\, t^{1.305} \tag{8.13}$$

$$F = 5.9 \cdot 10^7\, t^{1.305} \tag{8.14}$$

for $t = 3.25,\ 4.955,\ 5.95\ mm$ and $\sigma_0 = 398.5\, MPa$.

It is seen that the reaction force is not a function of the penetration. This does not correspond to observations from quasi-static tests where the reaction force is a continuously increasing function of the penetration, see Figure 8.1.

It is argued that material strain rate effects are insignificant for the test results. Scaling is discussed and it is illustrated that the geometrically similar scaling principles are not satisfied for the plate cutting problem.

Atkins (1988), [11], presents the scaling laws for bodies undergoing simultaneous plastic flow and crack propagation. If rigid-plastic behaviour is assumed the energy scaling for the prototype (p) and the model (m) follows:

$$\frac{W_p}{W_m} = \frac{\lambda^2(\lambda\chi + 1)}{(\chi + 1)} \tag{8.15}$$

where λ is the geometric scale factor and χ is the ratio between the rate of energy dissipation in the far field deformation and the rate of energy in the crack tip zone in one scale (provided

the energy dissipation at the crack tip is proportional to the length scale squared and the energy dissipation in the far field is proportional to the length scale cubed).

It is argued that fracture is a governing parameter for the plate cutting process, see also [13]. By analysing the results of Jones, Jouri and Birch, [55], [56], and Lu and Calladine, [69], Atkins made an attempt to separate the energy dissipating mechanisms and find the variance of χ. Several difficulties were encountered, though, and it seems that more experimental data is needed before an approach of scaling is applicable to practical problems. It should be noted that in the work outlined below (for example Lu and Calladine, [69]) all energy is assumed to be dissipated in plastic flow, so that the scaling of energy, W_p/W_m, follows λ^3 corresponding to $\chi = \infty$.

Lu and Calladine (1990), [69], performed quasi-static cutting tests with 35 hardened plates of mild steel ($t = 0.72 - 2.0\,mm$, $\alpha_w = 0^0, 10^0, 20^0$ and $2\theta = 20^0, 40^0$) and by using Buckingham's dimensional analysis they found the formula

$$\begin{array}{ll} W = C_{1.3}\,\sigma_y\,l^{1.3}\,t^{1.7} & \text{for } 5 < l/t < 150 \\ F = 1.3\,C_{1.3}\,\sigma_y\,l^{0.3}\,t^{1.7} & \text{for } 5 < l/t < 150 \end{array} \tag{8.16}$$

where $C_{1.3}$ is a purely empirical constant, which depends on the cutting conditions such as wedge and tilt angles. Unlike Eqs. (8.2-8.14), the formulas by Lu and Calladine are seen to be dimensionally consistent.

As it will be discussed in more detail later, Lu and Calladine made valuable contributions to the field by discussing the effect of friction, fracture and dynamics. [69] also presents the first attempt to investigate the effect of a finite shoulder width and thus the phase of steady-state cutting.

Wierzbicki and Thomas (1993), [140], developed an analytical model for prediction of the cutting force and derived an expression, identical in form and characteristics to the results presented by Lu and Calladine:

$$F = 3.28\,\sigma_0\,\mu^{0.4}\,l^{0.4}\,t^{1.6}\,\overline{\delta}_t^{0.2} \tag{8.17}$$

for a coefficient of friction, $0.1 < \mu < 0.4$, and a wedge angle, $10^0 < \theta < 30^0$. It is the first publication where a coefficient of friction, μ, and a fracture parameter, $\overline{\delta}_t$, enter the expression explicitly.

Paik (1994,95), [95] and [96], investigated the cutting response of stiffened steel plates. In [95], the analysis is based on dimensional analysis, fifty cutting experiments ($t = 3.4 -$

$7.8\,mm$, $2\theta = 15,\ 45,\ 60^0$), and the hypothesis that longitudinal stiffeners can be included by using an area-equivalent plate thickness, t_{eq}. Applying a least-square best fit to the experimental data, Paik expressed the energy absorption and the cutting force as

$$W = C_{1.5} C_f \sigma_0\, t_{eq}^{1.5}\, l^{1.5} \tag{8.18}$$

$$F = 1.5\, C_{1.5} C_f \sigma_0\, t_{eq}^{1.5}\, l^{0.5} \tag{8.19}$$

with the coefficient, $C_{1.5}$, being a function of wedge angle alone:

$$C_{1.5} = 1.112 - 1.156\theta + 3.760\theta^2 \tag{8.20}$$

and the dynamic correction factor, C_f, expressed as a function of the initial impact velocity, V, as

$$C_f = 1.0 - 0.042V + 0.001V^2 \tag{8.21}$$

In accordance with Lu and Calladine, [69], Paik considered inertia effects to be negligible whereas strain rate effects tend to raise the load level and dynamic effects on friction tend to lower the load. All in all, it is interesting to note that C_f is found to be a decreasing function of the impact velocity, for example $C_f = 1$ at $V = 0\,m/s$ and $C_f = 0.67$ at $V = 8m/s$. It should be noted that the correction factor, C_f, is found from the drop-hammer results of Jones and Jouri, [55]. In drop-hammer tests the velocity decreases from V to zero but this change in velocity has not been taken into account in the derivation of C_f. Thus, Eq. (8.21) cannot necessarily be used in Eq. (8.19) for an instantaneous velocity.

In [96], Paik and Lee discuss the effect of transverse stiffeners and it is proposed that these should be included in the analysis in a discrete manner (as opposed to the continuous 'smearing' technique proposed for longitudinal members).

Wierzbicki (1994), [135], developed a closed form solution for the reaction force when a concertina tearing deformation mode (see Figure 8.1) develops. By assuming a deformation mode and applying the principle of virtual work, the mean resistance force was found to be

$$F = 2\sqrt{3}\sigma_0 t^2 \left[\frac{2}{\sqrt{3}} \left(\frac{b}{t} \right)^{1/3} + \frac{\delta_t}{t} \right] \tag{8.22}$$

Experimental results with plates of mild steel ($t = 0.74 - 1.14\,mm$) are presented for validation of the model.

Astrup (1994), [10], conducted experiments ($2\theta = 60^0$, $\alpha_w = 10^0$, $2B = 250\ mm$, $t = 15, 20\, mm$) to investigate the cutting of thick plates with a wedge of finite width. The observed failure modes were quite complex in that both stable plate cutting and concertina tearing modes were seen. It is noted in [10] that the measured reaction force was generally 60 - 75 % higher than that predicted by the formula of Lu and Calladine. It is argued that this difference is due to strain rate effects and frictional effects. Another reason is that the test wedge had a finite shoulder width whereas the formula of Lu and Calladine is based on the initial penetration. This means that, after the wedge shoulders have entered the plate, a cutting mode different from that observed in Lu and Calladine's experiments develops. Large scours were observed on the cut specimens and it is argued that a coefficient of friction equal to 0.5 - 0.55 seems reasonable. By comparison of the energy absorption in the *initial* deformation with the drop-hammer tests of Jones et al., [55], it is found that there are no significant size effects in the cutting phenomenon.

Zheng and Wierzbicki (1995), [145], developed a closed-form solution for the reaction force after the steady state has been reached. It is assumed that the cutting process consists of three different energy absorbing mechanisms:

1. Ductile fracture in a small zone in front of the wedge.
2. Bending of the plate in moving hinge lines.
3. Membrane deformation.

A suitable model was postulated for the kinematics with one free parameter, the so-called plate rolling radius, R. The rate of energy dissipation in each of the three mechanisms listed above is expressed as a function of this rolling radius. In compliance with the idea of a least upper bound, the total resistance is found by minimising the total resistance force with respect to the rolling radius.

The resistance force is given by

$$F = \frac{\sigma_0 t^2}{4}\left[2\frac{B+R}{R} + 1.27\frac{R}{t}\ \cos\theta + 1.28\theta^2\frac{\cos(\theta/2)}{\cos\theta}\frac{(R+B)^2}{Rt}\right](1+\mu cot\theta) \tag{8.23}$$

with the rolling radius

$$R = B\sqrt{\frac{2(t/B) + 1.28\theta^2\cos(\theta/2)/\cos\theta}{1.27\cos\theta + 1.28\theta^2\cos(\theta/2)/\cos\theta}} \tag{8.24}$$

Ohtsubo and Wang (1995), [90], present an analysis method somewhat similar to that of Wierzbicki and Thomas, [140]. A kinematic model is proposed and the energy dissipation of the plastic flow in the tip zone and in the rolling hinge lines is calculated. The proposed expression for the cutting force is

$$F = 1.51\,\sigma_0 t^{1.5} l^{0.5} \sin^{0.5}(\theta)\,\left(1 + \frac{\mu}{\tan\theta}\right) \tag{8.25}$$

8.3 Comparison of Formulas for Initiation Cutting

As a general comparison of the proposed formulas is difficult, this section compares the formulas for two specific set-ups: Cutting of a thin (0.9 mm) plate of mild steel and cutting of a high-strength steel plate with a thickness (15 mm) relevant for ship building. It should be noted that a few of the formulas are shown outside the proposed range of validity.

Figure 8.3 shows a comparison of the proposed formulas with the results of one of the experiments reported in [69]. The input data for the calculations is given in Table 8.1.

Table 8.1: *Main data for comparison with the experiment of Lu and Calladine, [69].*

Plate thickness, t	0.9 mm
Wedge angle, $2\,\theta$	40 ^{o}
Flow stress, $\sigma_0 = \sigma_y$	272 MPa
Coefficient of friction, μ	0.3
Non-dimensional crack opening displacement, $\overline{\delta}_t$	1 .
Length of penetration, l	0-80 mm

It is seen that there is a significant difference between the formulas. However, the latest formulas proposed by Lu and Calladine, Wierzbicki and Thomas, Paik, and Ohtsubo and Wang show a similar trend which corresponds quite well with the experimental result.

Figure 8.4 shows a comparison of the proposed formulas with the results of one of the experiments reported in [10]. The input data for the calculations is given in Table 8.2.

As in the case of Figure 8.3, Figure 8.4 shows a considerable scatter between theoretical predictions. It is seen that up to the point ($l = 216\ mm$) where the wedge shoulders enter the plate, there is a fair correspondence between most of the formulas and the experimental curve.

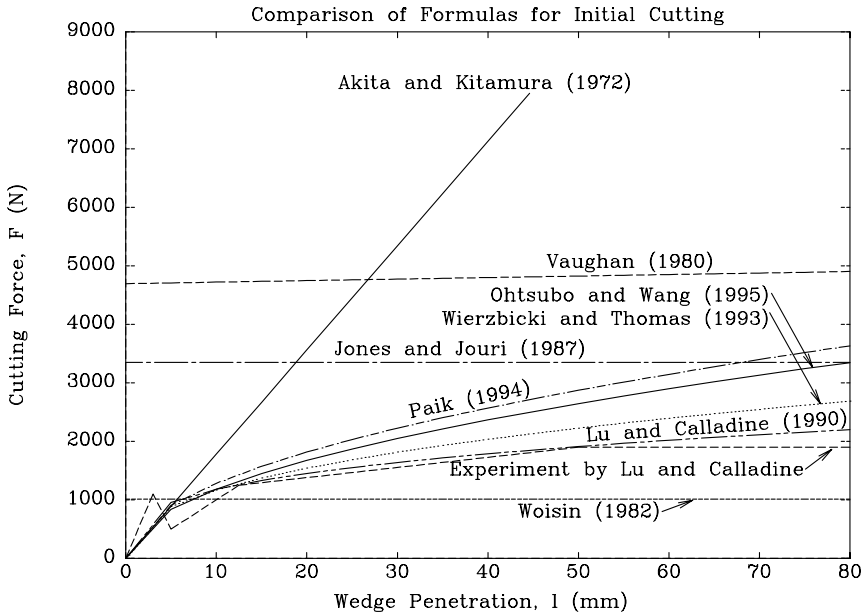

Figure 8.3: *Comparison of several formulas proposed in the literature with the result of one of Lu and Calladine's experiments, [69].*

Table 8.2: *Main data for comparison with the experiment of Astrup, [10].*

Plate thickness, t	15.0 mm
Wedge angle, 2θ	60 ^{o}
Yield stress, σ_y	417 MPa
Flow stress, $\sigma_0 = \sigma_u$	544 MPa
Coefficient of friction, μ	0.3
Non-dimensional crack opening displacement, $\overline{\delta}_t$	1 .
Length of penetration, l	0-432 mm

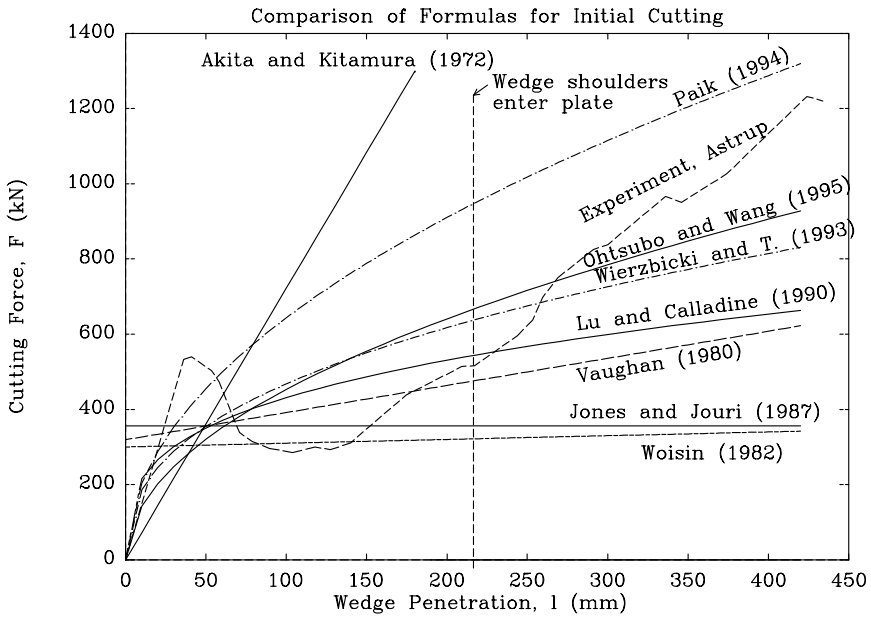

Figure 8.4: *Comparison of several formulas proposed in the literature with the result of one of Astrup's experiments, [10], for a 15 mm plate. The wedge shoulders enter the plate at* $l = 216\,mm$.

8.4 Prediction of Steady State Cutting Force with Existing Formulas

Lu and Calladine, [69], and Paik and Lee, [96], Astrup, [10], Yahiaoui et al., [142], and Zheng and Wierzbicki, [145], performed tests with wedges of finite width but the only formula in which the wedge width enters explicitly is due to Zheng and Wierzbicki, [145]. The experimental results of Lu and Calladine, [69], Yahiaoui et al., [142], and Astrup, [10], are summarised in Table 8.3. In all of the reported tests, the wedge angle was inclined at an angle of $\alpha_w = 10^0$ in order to obtain the clean curling cutting mode shown in Figure 8.1.

Table 8.3: *Experimental results for steady-state cutting. In all experiments the wedge was inclined at an angle of,* $\alpha_w = 10^o$.

Experiments by	σ_0 (Mpa)	θ $(^o)$	$2\,B$ (mm)	t (mm)	F (kN)
1. Lu & Calladine, [69]	272	10	10	1.6	6.0
2. Yahiaoui et al., [142]	270	45	19	0.75	2.5
3. Astrup, [10]	526	30	250	20	2250

Lu and Calladine, [69], observed that the main features of the physical behaviour and of the resulting load-deformation curve are of the same kind as in the initiation cutting, until the upper edge of the plate reaches the shoulder of the wedge whereupon the resisting force remains practically constant, as the wedge penetrates further. On the other hand, Thomas, [123], found that the initiation phase goes beyond the point where the shoulders enter the plate - it is rather twice as long as suggested by Lu and Calladine. The experimental curve of Astrup shown in Figure 8.4 does not show a distinct penetration at which steady state is reached, because the deformation initiates a mode of braided cutting, see Figure 8.1. On the observations of Thomas and Lu and Calladine, it seems realistic to use the proposed formulas for initiation cutting up to a certain point of penetration, l, and assume that the load level is retained from this point of penetration throughout the rest of the deformation. This penetration, l, is then

$$l = \kappa_{ini} \frac{2\,B}{\tan\,\theta} \tag{8.26}$$

with $\kappa_{ini} = 1 - 2$. Table 8.4 below presents results of this approach, i.e. the penetration, l, of Eq. (8.26) is used in the formulas for initiation cutting, Eqs. (8.16, 8.17, 8.19, 8.25). Corresponding to the findings of Lu and Calladine and Thomas, the value of κ_{ini} is taken to be respectively 1 and 2 in Table 8.4. Clearly, the approach is approximative because the deformation pattern shifts from a mode of cutting and curling in the initiation mode to a mode of cutting, curling and membrane deformation in the steady-state phase. The particular deformation mode of the steady-state phase was considered by Zheng and Wierzbicki, [145], who derived Eq. (8.23).

The input values of the formulas used in Table 8.4 (B, t etc.) are taken in agreement with the experimental results presented in Table 8.3. The coefficient of friction is assumed to be μ=0.3.

Table 8.4: *Theoretical prediction of steady-state cutting for the experimental results of Table 8.3. The following abbreviations are used for the formulas: L/C: Lu and Calladine, W/T: Wierzbicki and Thomas, O/W: Ohtsubo and Wang, Z/W: Zheng and Wierzbicki.*

Theoretical Prediction, $\kappa_{ini} = 1$

Experiments by	L/C Eq. (8.16) (kN)	W/T Eq. (8.17) (kN)	Paik Eq. (8.19) (kN)	O/W Eq. (8.25) (kN)	Z/W Eq. (8.23) (kN)
1. Lu & Calladine, [69]	5.81	5.88	6.37	7.05	3.81
2. Yahiaoui et al., [142]	1.14	1.12	2.89	1.26	3.28
3. Astrup, [10]	1514	1459	2258	1588	1580

Theoretical Prediction, $\kappa_{ini} = 2$

Experiments by	L/C Eq. (8.16) (kN)	W/T Eq. (8.17) (kN)	Paik Eq. (8.19) (kN)	O/W Eq. (8.25) (kN)	
1. Lu & Calladine, [69]	7.15	7.76	9.01	9.97	
2. Yahiaoui et al., [142]	1.41	1.48	4.08	1.78	
3. Astrup, [10]	1864	1925	3193	2246	

As in Figure 8.3 and Figure 8.4, the difference between various theoretical predictions is seen to be quite remarkable. It is interesting to note that the formula of Paik, Eq. (8.19), corresponds well with all of the observed results when $\kappa_{ini} = 1$ is used. It should be noted that, if the coefficient of friction is increased to $\mu = 0.55$ as proposed by Astrup, [10], the theoretical prediction for Astrup's results of Ohtsubo/Wang ($\kappa_{ini} = 1$) and Zheng/Wierzbicki rises from 1588 kN, 1580 kN to 2041 kN and 2030 kN, respectively. These results are seen to correspond quite well to the experimental value of 2250 kN.

8.5 Problem Statement and Basic Idea of New Theoretical Model

The remainder of the present chapter is concerned with the derivation and the verification of a new theoretical model for the analysis of steady-state cutting of an unstiffened metal plate by a prismatic wedge. The ultimate goal of these studies is to be able to analyse an assembled ship bottom structure which is significantly more complex than just a bare plate.

A picture from a plate cutting experiment is shown in Figure 8.5. A prismatic wedge cuts through a ductile plate which separates at the line of symmetry.

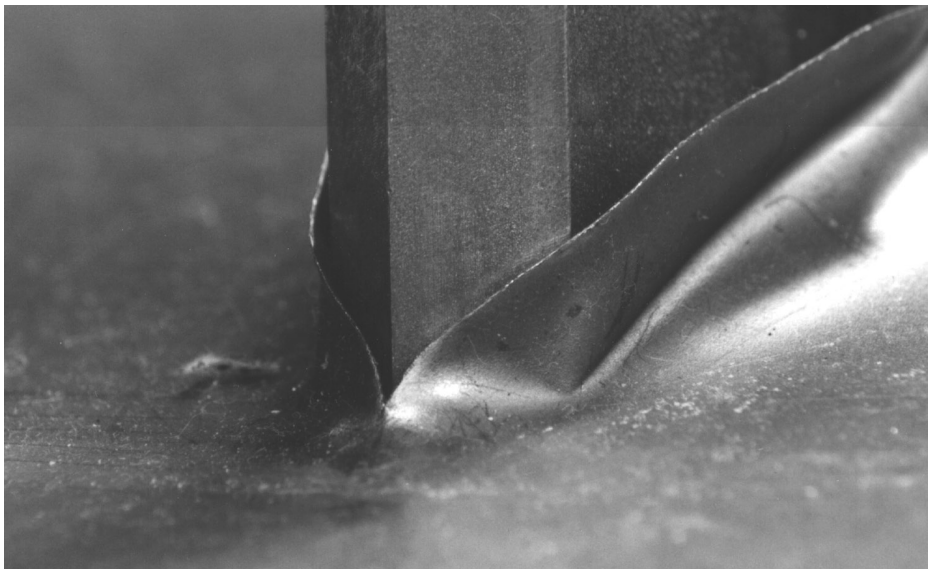

Figure 8.5: *Picture of plate cutting by a wedge.*

To quantify the energy dissipation according to Eq. (6.1), the plate is assumed to deform as shown in Figure 8.6. The necessary amount of membrane straining is illustrated in Figure 8.7 which could be constructed of paper (which is not extensible). The assumed mode of deformation with plane flaps conforming to the wedge corresponds well to the experimental observations of Astrup, [10], Yahiaoui, [142], Rodd and MacCampbell, [106], and Lu and Calladine, [69]. The assumed kinematics of the deformation has one free parameter, the plate rolling radius R, and it is postulated that the actual deformation mode minimises the total rate of energy dissipation.

Supporting the present approach, Atkins, [11], [12], has shown that the rigid-plastic approximations to tearing problems often adequately represent observed behaviour when fracture is accompanied by, or preceded by, extensive plastic flow. Examples (other than plate cutting) which include both fracture and far field deformation are tensile tearing of a deep double-edge notched specimen and trouser tearing. The basic idea of the methods for finding the specific work of fracture, R_c, is to perform experiments to determine all

parameters except $\dot{E}_c$ in Eq. (6.1). Then, from $\dot{E}_c$ and the kinematics of the specific problem, R_c can be determined. As mentioned, the distinction between a crack tip zone and the far field presented by Atkins is also applied in the present analysis.

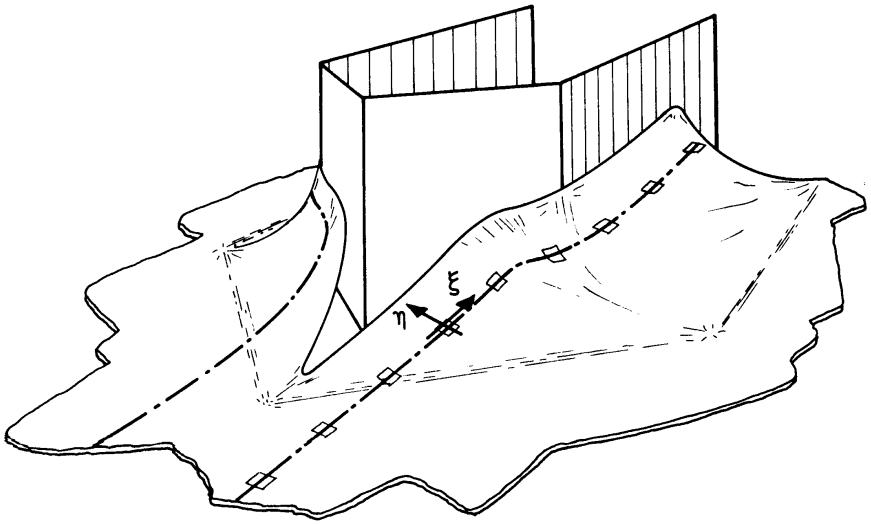

Figure 8.6: *Assumed mode of deformation.*

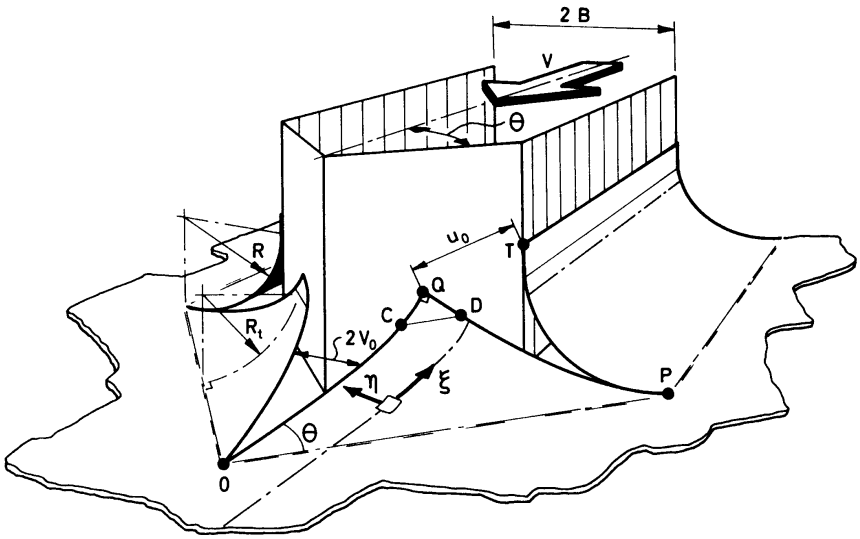

Figure 8.7: *Necessary straining illustrated by gap width.*

8.6 Energy Dissipation in Plasticity and Fracture

The basics of the development of the expressions for the rate of energy dissipation in the tip zone and in the far field have been described in the previous Section 8.5 and in Chapter 6, Section 6.4. The final expressions are derived below. The deformation in the far field is divided into bending (moving hinge lines and membrane deformation).

Far Field, Moving Hinge Lines

As illustrated by Figure 8.7, the steady-state cutting process involves several areas of bending. The relevant bending radii are the radius at the side of the wedge, R, and the radius in front of the wedge, R_t.

The three primary bending mechanisms are:

1. Initial curling. The curvature of the undeformed plate changes from 0 to $1/R_t$ (hinge line OP).
2. Hinge lines at wedge front. The plate is straightened out so that the curvature reverts from $1/R_t$ to 0 for a part of the plate (hinge line CD).
3. Bending around the wedge shoulder (line PT).

The hinge lines of point 2 and 3 above are in areas of high membrane straining so, if the true interaction on the yield curve (Eq. (6.2)) was taken into account, these hinges would give very limited resistance and they are therefore neglected in the following.

The rolling radius, R_t, is kept as a variable in the formulation and taken to be the value which gives the lowest rate of energy dissipation. In the wake of the wedge, the rolling radius is $R = R_t/\cos\theta$.

Since the jump in curvature is $[\kappa_{nn}] = 1/R_t = 1/R\cos\theta$ and the total width of the hinge line perpendicular to the direction of motion is $B + R$, the final expression for the rate of energy dissipation due to bending becomes (see Eq. (6.11))

$$\dot{E}_b = 2\int V\, M_0\, [\kappa_{nn}]\, d\eta \tag{8.27}$$

$$= \frac{\sigma_0\, t^2\, (B+R)\, V}{\sqrt{3}\, R\cos\theta} \tag{8.28}$$

Far Field, Membrane Deformation

Figure 8.7 shows the geometry which is observed if the plate is cut at the centre line and

along the edges PT, PQ and folded without membrane deformation of the plate (this could be done with a piece of paper and a pair of scissors). Then, the gaps between the plate edges PT and PQ are indicative of the amount of membrane straining necessary for material continuity during the cutting process. In the large scale tests of Astrup, [10], a few lateral cracks were also observed (along line PT in Figure 8.7) but for thin plates this is not seen.

The necessary straining can be accommodated by an infinite number of possible strain fields. The actual strain rate field is the one which minimises the instantaneous rate of energy dissipation of material flow, fracture and friction. Little is published about the strain field in steady-state cutting but useful information can be obtained from inspection of cut specimens. The cut plate transmits direct tensile (or compressive) stresses in the ξ direction, and likewise tensile strains develop. This can be deduced from Figure 8.1 for the curled cut where the deformed plate is seen to be buckled. During the cutting process, the longitudinal plate fibres are stretched in the deforming zone at the wedge front, and instead of recompressing to the original length, leaving straight flaps in the wake, the plate buckles. As mentioned, however, the plating of a ship structure has stiffeners, attached to it and the presence of longitudinal stiffeners which are often quite substantial, tends to prevent the development of tensile deformation in the longitudinal direction of the hull structure when the deformation is large enough for the longitudinals to be involved.

The hull plating rather deforms in a mode where longitudinal fibres are sheared with respect to each other. Such a deformation mode of predominant shear in the (ξ, η) coordinate system (see Figure 8.6) was reported by Turgeon, [128], for small-scale tests without fracture and by Rodd and MacCampbell, [106], for large scale grounding tests with a double bottom being deformed by a conical rock.

Moreover, in the large-scale cutting tests of Astrup, [10], the deformed plate flaps were seen to be nearly plane, indicating shear rather than tensile deformation, see Figure 8.8. Based on these observations, the present formulation for the membrane deformation rests on the assumption that the in-plane strains in the far field are all shear strains (in the (ξ, η) coordinate system) . It is recognised that this is not always the case but, as it will be argued later, this assumption greatly simplifies the analysis. Since longitudinal fibres are not stretched, the present model also provides a realistic basic deformation pattern model for the case of a longitudinally stiffened plate.

Figure 8.8: *Cutting of a 20 mm plate by a wedge, [10].*

With this assumption of dominant shear strains, $\varepsilon_{\xi\eta}$, the rate of energy dissipation can be derived. From Eq. (6.9) the rate of energy dissipation is found as an integral of the equivalent strain over the width of the plastic zone in the wake of the wedge, for example along the PT-line, see Figure 8.7:

$$\dot{E}_m = 2\,\sigma_0\,V\,t\int_{\eta_P}^{\eta_T}\left[\frac{2}{\sqrt{3}}\varepsilon_{\xi\eta}\right]d\eta \tag{8.29}$$

$$= 2\,\sigma_0\,V\,t\int_{\eta_P}^{\eta_T}\left[\frac{2}{\sqrt{3}}\frac{1}{2}\left(\frac{\partial u}{\partial \eta}+\frac{\partial v}{\partial \xi}\right)\right]d\eta \tag{8.30}$$

$$= \frac{2}{\sqrt{3}}\sigma_0\,V\,t\,[u_P-u_T] = \frac{2}{\sqrt{3}}\sigma_0\,V\,t\,u_0 \tag{8.31}$$

where u_0 is the distance between Q and T in Figure 8.7. In Appendix A it is shown that $u_0 \approx B\,\theta$ so that the final expression becomes

$$\dot{E}_m = \frac{2}{\sqrt{3}}\,\sigma_0\,V\,t\,B\,\theta \tag{8.32}$$

Near Tip Plate Separation. Although the process of the near tip crack zone has been considered explicitly by several authors no-one has yet applied a theory to the problem of plate cutting which covers in detail and in general the material splitting process. Lu

and Calladine, [71], argue that the cutting process can be described at a sufficient level of accuracy with the flow stress as the only material parameter. A discussion on this topic is given by Atkins and Lu and Calladine in [13] and [70]. Stronge et al., [120], [121], performed an experimental and theoretical study on the problem of tube splitting and concluded that the relative contribution of the tearing energy to the total energy dissipation is small. This supports those of the presented analyses of Section 8.2 where fracture parameters are not included. Several authors leave material fracture parameters out of the analysis based on the observation that the crack tip stays right at the wedge tip so that the separation process is one of plastic flow rather than fracture. For highly ductile specimens being cut by a sharp wedge as those thin plates of mild steel used in several of the reported model tests, it is true and not too surprising that the plate separates at the cutting edge. However, for less ductile specimens - for example thick hull plating, [10], or other types of material, [69] - or blunt nosed wedges, [106], [77], the crack was observed to run ahead of the wedge and a general theory should therefore cover this situation and thus consider the fracture toughness of the material.

In the large-scale double bottom grounding tests reported in [106], an unstable crack was seen to unzip a part of the structure in front of the wedge. A stable crack in the outer bottom propagated with the penetration of the rock but, at a certain point of penetration, the crack suddenly propagated through a transverse bulkhead far into the inner hull plating. To capture this complex type of behaviour would require very detailed elasto-plastic calculations. Theoretically, the finite element method would be applicable but for practical use in design it is too labour-intensive.

The question of whether fracture should be included or not is handled in the present mathematical model by choosing between purely plastic flow or fracture, depending on which of the two alternative modes gives the lowest energy dissipation. This corresponds to normal fracture criteria for ductile materials, see for example Atkins, [12].

The energy dissipation rates for these different plate separation processes are given by Eqs. (6.13) and (6.14). In order to evaluate the integral of Eq. (6.14), it is assumed that the strain field is dominated by tensile strains in the lateral (η) direction. This is not fully consistent with the assumption that the PT-PQ gap in Figure 8.7 is accommodated by shear strains alone but estimates indicate that the effect of shear in the tip zone is small. Indeed, due to symmetry, the shear must be zero at the centre line.

According to Eq. (6.14) it is sufficient to consider the total equivalent strain of the material in the wake of the cutting edge. With $\varepsilon_{\xi\xi} = \varepsilon_{\xi\eta} = 0$, the final expression is found as an integral over the width of the plastic zone in the wake of the cutting edge:

$$\dot{E}_c = 2\,\sigma_0\,V\,t\int[\varepsilon_{eq}]\,d\eta \tag{8.33}$$

$$= 2\,\sigma_0\,V\,t\int_{\eta_l}^{\eta_u}\left[\frac{2}{\sqrt{3}}\varepsilon_{\eta\eta}\right]d\eta \tag{8.34}$$

$$= \frac{4}{\sqrt{3}}\sigma_0 \, V \, t \, v_0 \tag{8.35}$$

where η_l and η_u denote lower and upper boundaries for the strain field in the lateral direction on one side of the centre line and v_0 is half of the maximum gap width between the plate curls in front of the wedge.

In Appendix A it is shown that

$$v_0 \approx 0.16 \, R \, \cos^2\theta \, (1 + 0.55\,\theta^2) \tag{8.36}$$

giving the final expression as

$$\dot{E}_c = \frac{0.64}{\sqrt{3}} \, \sigma_0 \, V \, t \, R \, \cos^2\theta \, (1 + 0.55\,\theta^2) \tag{8.37}$$

8.7 Friction

Using the approach described in Section 6.6, Pippenger, [103], derived the relations corresponding to Eqs. (6.36, 6.38) for the case of a wedge which is inclined at an angle α_w (see Figure 8.2), from the direction perpendicular to the plate. Keeping the relations in their most general form but modifying Pippenger's expressions according to the assumption $V_{rel} = V$ gives:

$$\frac{F_H}{F_P} = g(\mu, \theta, \alpha_w) = \left(1 - \frac{\mu}{\sin\beta \, \sin\theta' + \mu \, (\cos\theta' \cos\zeta + \sin\zeta \, \cos\beta \, \sin\theta')}\right)^{-1} \tag{8.38}$$

$$\frac{F_V}{F_H} = k(\mu, \theta, \alpha_w) = \frac{\cos\beta - \mu \sin\zeta \, \sin\beta}{\sin\beta \, \sin\theta' + \mu \, (\cos\theta' \cos\zeta + \sin\zeta \, \sin\theta' \, \cos\beta)} \tag{8.39}$$

where θ' is the projected wedge angle and β is an intermediate value:

$$\theta'(\theta, \alpha_w) = \tan^{-1}(\tan\theta \, \cos\alpha_w) \tag{8.40}$$

$$\beta(\theta, \alpha_w) = \tan^{-1}(1/(\sin\theta' \, \tan\alpha_w)) \tag{8.41}$$

For $\alpha_w = 0$, it is seen that $\theta' = \theta$, $\beta = \pi/2$ and with $\zeta = \theta/2$ Eqs. (8.38, 8.39) reduce to Eqs. (6.36, 6.38) as expected.

Figure 8.9 shows the friction factor, g, as a function of the wedge angle, θ, for $\mu = 0.3, 0.45, 0.6$ and $\alpha_w = 10^o$. Taking $\mu = 0.3$, $\alpha_w = 10^o$ and $\theta = 10^o$, 30^o and 45^o gives

friction factors, g, of 2.8, 1.7 and 1.5, respectively, indicating a very significant contribution of friction to the total plate resistance.

It should be noted that the effect of friction comes as a factor which is independent of the rolling radius, R. Likewise, the plastic/fracture resistance derived in the previous section was found to be independent of μ so that the radius which minimises the resistance force becomes independent of μ. This does probably not reflect reality[1] but at present there is not sufficient information available about this problem to improve the model in this respect.

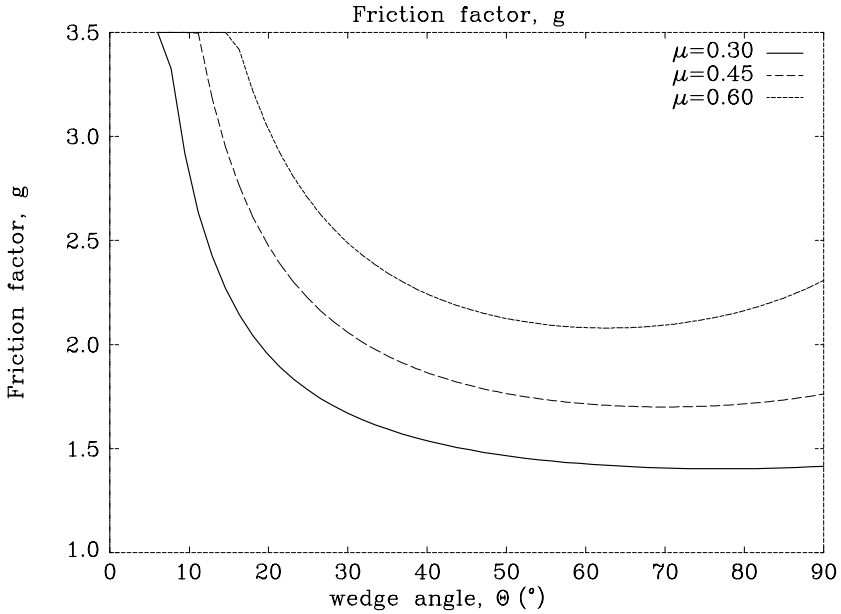

Figure 8.9: *Friction factor, g.* $\mu = 0.3, 0.45, 0.6$ *and* $\alpha_w = 10^o$.

Moreover, it should be noted that the whole contact pressure is assumed to be on the front plane sides of the wedge. However, the corner point at the shoulders and the front tip might transmit some force. The effect of the shoulders tends to increase the friction factor whereas the force on the front tip tends to lower it. For wedges with sharp edges, the effect of these edge irregularities is believed to be small but for some types of idealised rocks, like for example the cone shaped rock analysed by Rodd and MacCampbell, [106], these effects are dominant and prediction of g and k becomes a cumbersome task.

Figure 8.10 shows k as a function of the wedge inclination angle, α_w, for $\theta = 45^o$ and $\mu = 0.3, 0.45, 0.6$. For small inclination angles, α_w, the vertical component of the frictional force dominates over the normal force, and the total vertical force is thus negative.

[1] For the tube splitting process, Stronge et al., [121] use, an expression for the plate rolling radius which is a strong function of μ.

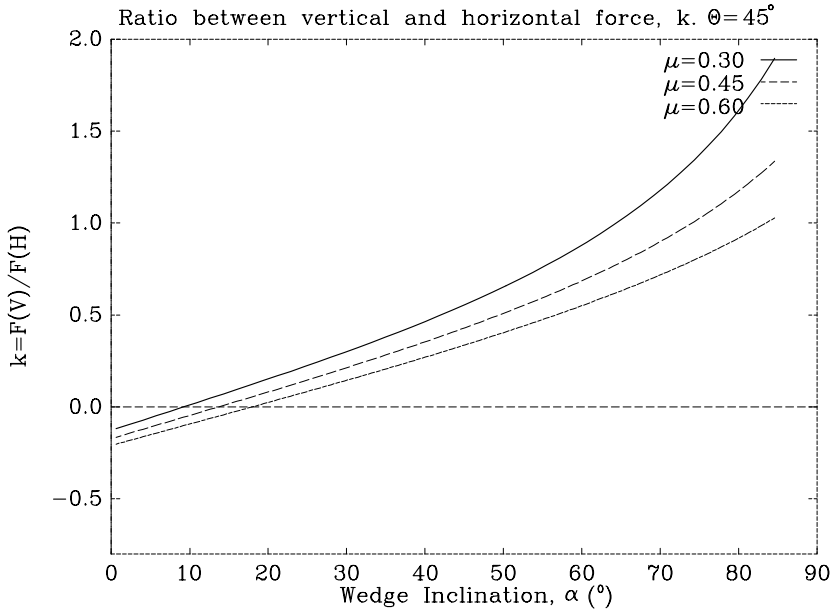

Figure 8.10: *Ratio between the vertical and horizontal force, k.* $\theta = 45^o$ *and* $\mu = 0.3, 0.45, 0.6$.

8.8 Total Reaction and Verification

The problem of two alternative deformation modes in the tip zone in front of the cutting edge was described in Sections 8.5 and 6.4. Below, the resistance force is derived for both alternative modes.

Combining Eqs. (6.1, 8.37, 8.32, 8.28 and 8.38) gives the plastic/fracture resistance force on the plate for the mode where the crack does not run ahead of the wedge:

$$\begin{aligned} F_H &= g(\mu,\theta,\alpha_w)\,\frac{\dot{E}_c+\dot{E}_m+\dot{E}_b}{V} \\ &= g(\mu,\theta,\alpha_w)\,\{\frac{0.64}{\sqrt{3}}\,\sigma_0\,t\,R\,\cos^2\theta\,(1+0.55\,\theta^2)+ \\ &\quad \frac{2}{\sqrt{3}}\,\sigma_0\,t\,B\,\theta+\frac{\sigma_0\,t^2\,(B+R)}{\sqrt{3}\,R\,\cos\theta}\} \end{aligned} \tag{8.42}$$

$$R \le B\,\frac{1}{\pi/2-1} = 1.75\,B \tag{8.43}$$

The limit of R, Eq. (8.43), comes from the general kinematic requirement that the deformed plate flaps must be in contact with the wedge. The rolling radius, R, which gives the lowest resisting force, becomes

$$R = \sqrt{\frac{B\,t}{0.64\,(1+0.55\theta^2)\,\cos^3\theta}} \tag{8.44}$$

In the alternative crack tip deformation mode where the crack runs ahead of the wedge, the rate of energy dissipation in the tip zone is not a function of R and the total rate of energy dissipation does therefore not have a mathematical minimum as above. It is a monotonically decreasing function of the rolling radius. Using the maximum allowable rolling radius for kinematic consistency, Eq. (8.43), with Eqs. (6.1, 6.13, 8.32, 8.28 and 8.38) then gives the resistance force as

$$F_H = g(\mu, \theta, \alpha_w)\,\{R_c\,t + \frac{2}{\sqrt{3}}\,\sigma_0\,t\,B\,\theta + \frac{1.57\,\sigma_0\,t^2}{\sqrt{3}\,\cos\theta}\} \tag{8.45}$$

In order to verify the derived equations, the experimental results shown in Section 8.2 are considered again. Application of Eq. (8.45) raises the difficulty that the fracture parameter, R_c, is unknown. Lu et al., [71], performed an experimental study on tearing energy in splitting metal tubes and presented an expression and test results for mild steel plates, which seems to be independent of plate thickness (at least for thicknesses between 0.5 mm and 1.5 mm):

$$R_c = 8.8mm\,\sigma_u\,\varepsilon_f \tag{8.46}$$

On the assumption that the separation process in plate cutting resembles that of tube splitting, this relation is applied below. However, as also it is stated by Lu et al., the parameter, R_c, is a crude one to use in other problems than the specific one considered in the test because the tearing energy is highly dependent on the detailed stress-strain state in the process. This was also noted by Atkins, [12], who reported values for R_c ranging from 200 - 1000 kJ/m^2 depending on the type of tearing process. Therefore, to apply expressions like Eqs. (8.45, 8.46) really requires further work on the detailed ductile separation process.

The friction factors, g, in the following verification examples are calculated from Eq. (8.38) using $\mu = 0.3$ and $\alpha_w = 10^o$. The fracture strains of the three experiments are assumed to be 0.25, 0.25 and 0.15, respectively, giving fracture toughnesses of $600kJ/m^2$, $600kJ/m^2$ and $700kJ/m^2$.

Table 8.5 shows a comparison between the theoretical prediction of the two presented models and the experimental results which were also presented in Table 8.3.

The theory, Eq. (8.42) with Eq. (8.44), overpredicts the forces of the three reported tests by - 7 %, 41 % and 5 %. Thus, except for the test of Yahiaoui et al. [142], very good agreement between theory and experiments is seen even though the scale of the problems is different by an order of magnitude. Moreover, it is noted that the difference between the two calculation models, Eq. (8.42) and Eq. (8.45), is small. If values for the fracture toughness, R_c, were sufficiently accurate the relative magnitude of the numbers in column four and five would indicate which of the two presented models would develop. The actual numbers

Table 8.5: *Steady-state cutting. Theoretical predictions and experimental results for three tests.*

Experiments by	g from Eq. (6.36)	R (mm) Eq. (8.44)	$F(kN)$ Eq. (8.42)	$F(kN)$ Eq. (8.45)	$F(kN)$ Measured
1. Lu & Calladine, [69]	2.81	3.59	5.58	5.72	6.0
2. Yahiaoui et al., [142]	1.50	4.85	3.53	3.58	2.5
3. Astrup, [10]	1.67	72.3	2372	1722	2250

in Table 8.5 indicate that the plate was cut (purely plastic flow) in the two experiments with thin plates but it fractured in the experiment of Astrup. Actually, this seems to be in accordance with the reported experimental results. It is true to say, however, that the above model with fracture as the material separation process requires further work on quantifying R_c. It is likely that the finite element method can contribute to clarifying points about the energy dissipation at the crack tip.

Table 8.6 shows how the energy dissipation is distributed between deformation mechanisms and friction when the plate resistance is calculated from Eq. (8.42).

Table 8.6: *Partitioning of energy between deformation mechanisms and friction. The calculation model assumes a purely plastic flow at the wedge tip.* $E_{tot} = E_c + E_b + E_m$.

Experiments by	Friction $\frac{(g-1)}{g}$	Front tip $\frac{E_c}{E_{tot}}$	Shear $\frac{E_m}{E_{tot}}$	Bending $\frac{E_b}{E_{tot}}$	$\frac{(E_m+E_b)}{E_c}$
1. Lu & Calladine, [69]	64 %	29 %	22 %	49 %	2.5
2. Yahiaoui et al., [142]	33 %	10 %	74 %	16 %	8.7
3. Astrup, [10]	40 %	17 %	56 %	27 %	4.9

It is interesting to note how differently the energy is distributed in the three examples due to different wedge angles, plate thicknesses and wedge width. This indicates why it is difficult to derive formulas which capture all dependencies on a purely empirical basis. It is noted that the effect of friction is significant. The last column in Table 8.6 shows the importance of the far field deformation relative to the tip zone process. It is clear that the far field energy dissipation is dominant in these examples. The corresponding values for the alternative model with material fracture instead of plastic flow at the crack tip are $\chi = 1.12$, 4.31 and 72.5. These values of χ are the ones to be used in the scaling formula presented by Atkins, Eq. (8.15), assuming a fracture process at the crack tip.

Chapter 9

Internal Mechanics of a Stiffened Ship Bottom on a Conical Rock

9.1 Introduction

As discussed in the previous chapter, most of the work concerning grounding damage has been devoted to the problem of cutting of a bare plate by a wedge. Indeed, this mode of deformation - often referred to as 'bottom raking' - has been observed in accidental groundings but it is only a limited part of the damage processes that can be found in grounding on rocks. The present chapter extends the theory of Chapter 8 to cover more complex structures than just a bare plate. Obviously, it would be desirable to cover the grounding response of all types of ship structures on all types of rock geometries. As the method is based on assumed deformation modes, however, it cannot immediately capture the response of completely new structural arrangements and the types of rocks involved also have to be limited. The group of rock geometries considered here is shown in Figure 9.1. The rocks have a conical base defined by the semi-apex angle, φ, and a rounded tip with radius, R_R.

The typical components of a ship bottom structure are shown in Figure 9.2 for transversely as well as longitudinally stiffened structures. Ships of over about 90 m length are mostly longitudinally stiffened, [88], so ship bottoms of large tankers are typically of the type to the right in Figure 9.2 - possibly without the inner bottom.

The number of parameters necessary to characterise a structure like shown in Figure 9.2 in a general manner is so large that any attempt of mapping the general grounding response experimentally will either fail or be prohibitively costly. For the present simplified approach it is clear that it would be most convenient to develop a theoretical model in which individual structural components can be considered separately and then be consistently assembled. Simplified analyses of specific assembled structures have been developed with great succes,

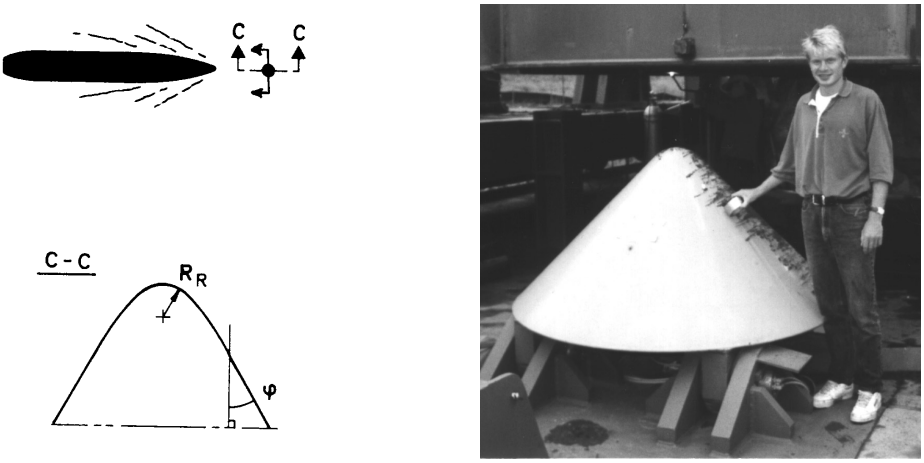

Figure 9.1: *Geometry of the conical rock with a rounded tip. Photo of artificial rock used in the tests conducted by Naval Surface Warfare Centre, USA.*

see for example [125] but it is by no means obvious how such an approach can be extended to cover assembled structures in a general scheme.

The approach taken here is to postulate an overall mode for the deformation zone in which there is compatibility between structural components. By compatibility is meant that intersections between components stay together during the deformation process. The underlying philosophy of this approach is that intersections do not fail but as discussed in Section 6.3, that assumption is not completely undebateable.

9.2 Global Deformation Kinematics

Since principle structural elements are attached to the shell- or the inner bottom plating it is convenient to use the deformation of the plating as the basis for the global deformation mode. Then, to assure compatibility between structural elements, it must be required that all elements attached to the plating, consistently follow the plating during the deformation process. The deforming shape of the hull plating is shown in Figure 9.3. Figure 9.3 *a* and *b* show the deformation modes with and without fracture, respectively.

During passage of the deformation zone, a material element will experience bending, stretching and fracture depending on the deformation mode. As illustrated by Figure 9.3 the mode of deformation and thus the energy dissipation in each of the three mechanisms will depend on whether the plating has fractured and also on the size of the deformation zone. Sections 9.4 and 9.5 of this chapter are devoted to these two aspects of the problem, respectively.

An attempt of describing the displacement field of the deformation shown Figure 9.3 *b* was presented by Jocelyn, [128]. Even very simple trigonometric functions for the displacement

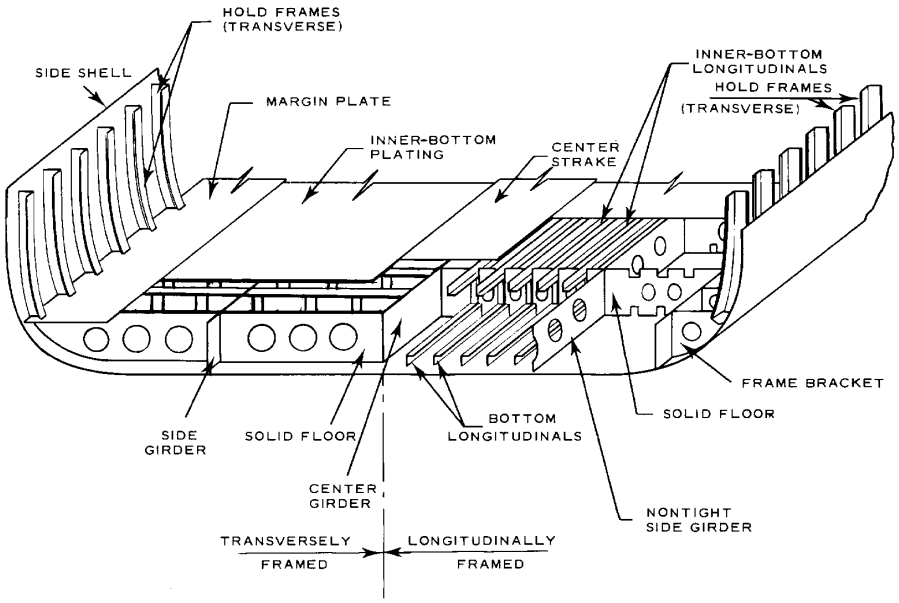

Figure 9.2: *Typical ship bottom structures for longitudinally stiffened ships, [118].*

field appear to give expressions for the rate of energy dissipation that cannot be handled analytically. To get simple closed form solutions, the present approach is therefore based on using two simplified deformation models to quantify the membrane- and the bending deformations, respectively. Refer to [109] and [110] for an overview of the approach.

Figure 9.4 shows the model used to calculate the membrane deformations. The shown geometry can be reproduced by folding a piece of (inextensible) paper cut along the OS- and $Q'P - lines$. It is shown in Appendix B that the longitudinal- and transverse gap openings, u_0 and v_0 respectively, are given by

$$u_0 = B_{de}\sqrt{(1-\cos\alpha)^2\sin^2\theta + (1-\cos\theta)^2\sin^2\alpha} \tag{9.1}$$

$$v_0 = B_{de}\,(1/\cos\alpha - 1) \tag{9.2}$$

where B_{de} is the half width of the deforming zone, α is the angle from horizontal to the 'flaps' and θ is the so-called 'plate split angle'. The model can be used both before and after the plate has fractured at the center line. Before fracture, the plate deformation extends the distance B_{de} away from rock centre and with a rock tip penetration of δ the flap angle becomes, $\alpha = \tan^{-1}\delta/B_{de}$. When the plate has fractured, the plate conforms to the rock so the flap angle becomes equal to $\pi/2$ minus the semi-apex angle, φ, and the width of the deformation, B_{de} becomes equal to the base of the rock in the plate of the undisturbed plate. The plate split angle is indicative of how far the deformation zone extends ahead of the rock. From the width of the deformation zone, B_{de}, the length of the zone, OQ, becomes $L_{de} = B_{de}/\tan\theta$. During the deformation process, the rock is moving through transverse members which will prevent the deformation from extending far ahead - i.e. transverse

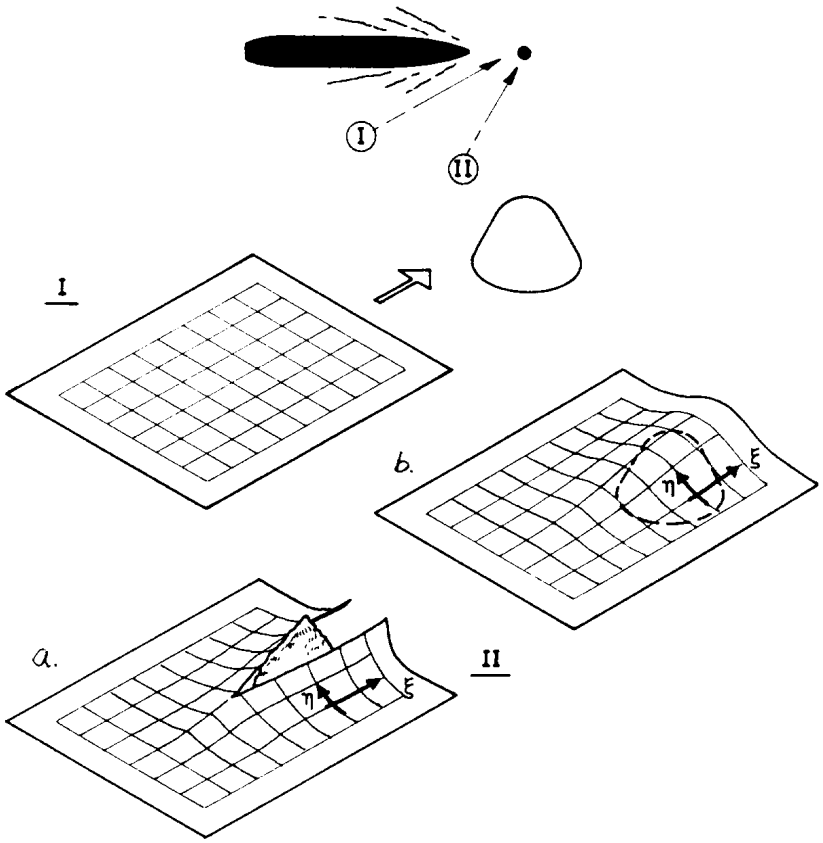

Figure 9.3: *Deformation mode for hull plating, i.e. shell plating and inner bottom plating.*

members will have the effect of increasing the effective plate split angle, θ. The plate split angle, θ, is treated as an unknown variable throughout the theoretical derivations of the following sections. In general, the plastic resistance is a decreasing function of θ and the frictional resistance is an increasing function of θ. The total resistance of the structure therefore normally has a minimum with respect to θ. In the final application of the theory the plate split angle is taken as the value that minimizes the energy dissipation, i.e. the resistance force of the structure.

Experiments show that the plate is unlikely to fail along transverse lines (PQ), so the gap between PQ and PR has to be accomodated by in-plane straining of material. For small penetrations, the plate does not fracture at all so the gap between OQ and OQ' also has to be closed by membrane plate straining. For larger rock penetrations, the plate ruptures at the center line so that OQRS becomes a free edge. However, material continuity over the gap between PQ and PR still has to be accomodated by straining of plate material. The question is which strain field closes the shown gaps. This problem was also discussed in Chapter 8 about plate cutting (see page 133) and it will be touched on again in the sections below about plate resistance. A structure with heavy longitudinal stiffeners is unlikely to

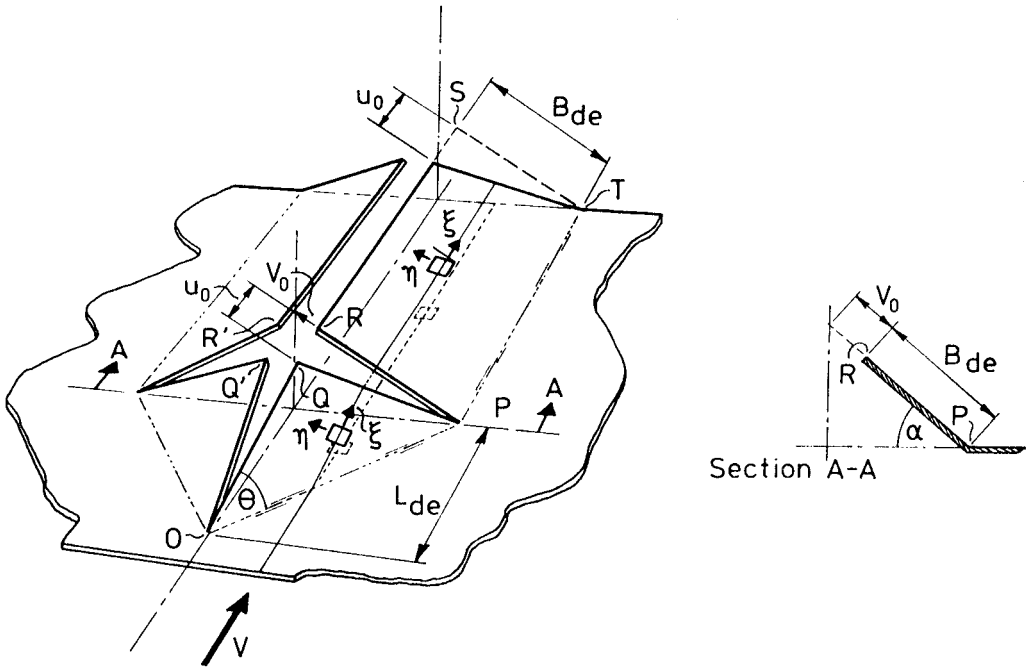

Figure 9.4: *Deformation mode assumed for calculation of membrane straining.*

be stretched in the longitudinal (ξ) direction. The hull plating will rather deform in a mode where longitudinal fibres are predominantly sheared with respect to each other with limited tensile deformation. From a computational point of view, a mode with zero tensile strains in the longitudinal direction is very convenient because no assumptions are necessary of the length over which a material fiber is stretched. Also, examination of the failure modes reported by Rodd and MacCampbell, [106], clearly justify the assumption of dominating shear deformations. Figure 9.5 shows the failure mode of the test reported by Rodd and MacCampbell. Significant shear bands are observed in the bottom plating.

The simplified deformation mode shown in Figure 9.4 is not kinematically admissible since the hinge lines have infinite curvature. To quantify the bending of plating or longitudinals attached to the plating, these curvatures therefore have to be smoothed over the length of the deforming zone. The basic idea of this smoothing is shown for one longitudinal fibre in Figure 9.6. As a structural element passes the first hinge, the longitudinal curvature is changed from 0 to $1/R$. At the second hinge the curvature is reversed to $-1/R$ and at the final hinge the element is straightened out to a curvature of 0. In all, the material element experienced changes of curvature equal to $[\kappa] = 4/R$ as it passed through the deforming zone.

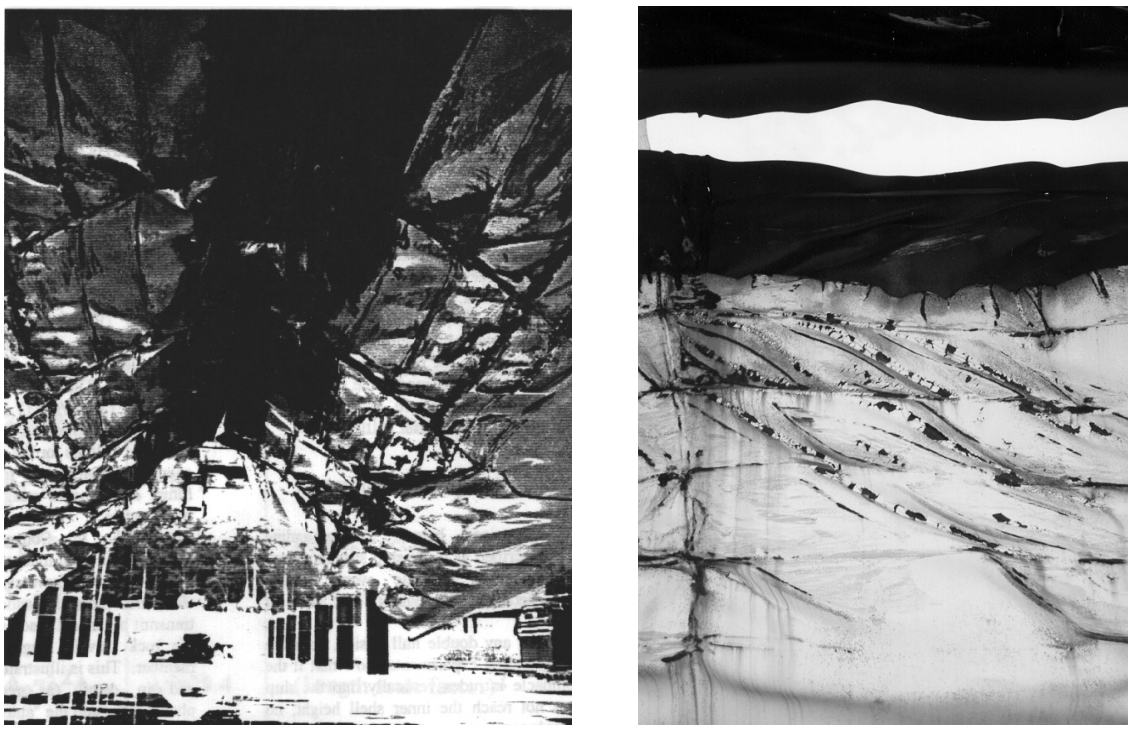

Figure 9.5: *Failure mode of ship bottom observed in NSWC Test no 1, [106], (frog's eye view). The photo to the left shows the path of the rock through the ship bottom. The photo to the right shows a close-up of the shell plate deformation (the rock moved from right to left). The photo to the right shows fracture of both shell and inner bottom plating leaving an opening (horizontal white area) to the tank.*

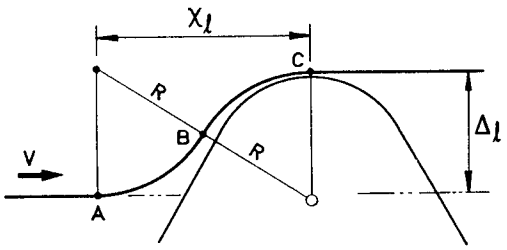

Figure 9.6: *Assumed bending deformation of a longitudinal plate fibre or a longitudinal stiffener.*

Given the length of the deforming zone, χ_l and the vertical displacement at one end, Δ_l the rolling radii, R, produced by the moving hinges can be found from geometrical considerations to be

$$R = \frac{\chi_l^2 + \Delta_l^2}{4\,\Delta_l} \tag{9.3}$$

Now a structural member attached to inner or outer bottom plating is assumed to follow the deformation modes shown in Figure 9.4 and Figure 9.6 and so the plastic resistance of the member can be calculated accordingly. Since longitudinal fibres in the plating are not stretched, the requirement of compatibility between components also prescribe zero extensional deformation of longitudinals attached to the plating. Consequently, the deformation mode of a longitudinal will be pure bending and twisting and the deformation mode of a longitudinal girder fixed between the shell plating and the inner bottom plating will be combined shearing and bending. A transverse member, on the other hand will be deformed in tension (according to the gap v_0 in Figure 9.4) in addition to shearing, bending or twisting.

9.3 Local Deformation Around Rock before Fracture

As discussed above it is possible to get a good estimate of the energy absorption in the structure from a gross overall model, like the one presented above in Figure 9.4. For friction and fracture, however, it is necessary to have one or more refined models for the plate deformation at important details. Below, such a model is derived for the shell plating wrapping on the rock. As they are derived, more local models could be implemented for other important phenomena such as welding failure, failure of shell plating at a bulkhead etc.

The specific problem considered here is that of plating wrapping around a conical rock with a rounded tip. In a ship bottom structure the shell plating is attached to various stiffeners but for simplicity the problem of a bare plate is considered here. Since material flows through the deforming zone it is not immediately possible to derive an exact solution for the mode of deformation. However, careful inspection of plate specimens deformed by a rock moving in the in-plane direction reveals that the mode of deformation in front of the rock resembles that of a plate deformed by an indentor moving in the lateral direction. For the latter axis-symmetric problem an exact rigid-plastic solution can be derived. Due to friction and the incremental nature of plasticity, however, the force levels associated with the two deformation modes cannot be expected to be equal. The idea of the present approach is that the local wrapping of material on the rock tip is the same for the two problems. The punch indentation problem was considered previously for investigation of failure criteria, [144], for collision, [139], and for ballistic limits [57], [58], [59].

9.3.1 Theoretical Solution

Figure 9.7 shows the geometry of the considered problem. The tip of a spherical indentor mounted on a conical base is displaced a vertical distance, δ, into the centre of a circular plate of thickness t and radius R. The problem is axis-symmetric and the deformation is described in a $(w, r)-$coordinate system where w and r are the vertical and the radial coordinates, respectively. The angle from horizontal to the plate at a certain distance from the center, is $\psi(r)$. The radius of the sphere is R_b and the plate is in contact with the indentor from the centre to point C, i.e. for $0 < r < r_C$ and $0 < \psi < \psi_C$. The vertical punch force is P.

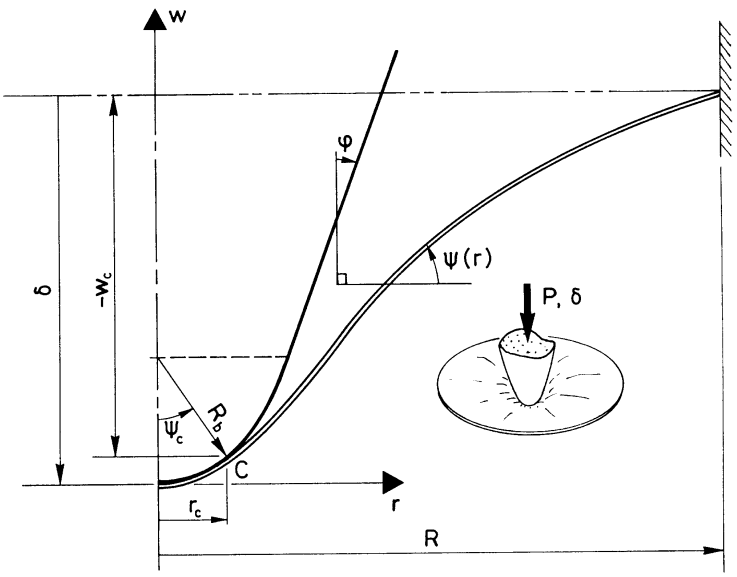

Figure 9.7: *Definition sketch for derivation of plate punch solution.*

The plate is assumed to be in a membrane state (bending is neglected) and material is assumed to be rigid-plastic following von Mises yield locus. The strain hardening characteristics of the material could be taken into account, [58] and [144], but introduction of another uncertain parameter into the present analysis complicates it unnecessarily. Material elements are assumed to be displaced only vertically leading to the following expressions for the natural strain components

$$\varepsilon_{rr} = -\varepsilon_{tt} = \ln\left(\frac{1}{\cos\psi}\right) \tag{9.4}$$

$$\varepsilon_{\psi\psi} = \varepsilon_{\psi r} = 0 \tag{9.5}$$

where t is a thickness coordinate. Vertical equilibrium of the central part of the plate can be stated as

$$P = 2\pi N_0 r \sin\psi(r) \qquad \text{for } r_C < r < R \tag{9.6}$$

where $N_0 = 2\sigma_0 t/\sqrt{3}$ is the plane strain fully plastic membrane force according to von Mises yield locus. According to the assumption of only vertical displacement of material elements, all the deformation takes place outside point C, i.e. for $r_C < r < R$. The present model cannot give information about the pressure distribution within the contact area, $0 < r < r_C$. In particular, at point C, $r = r_C = R_b \sin\psi_C$ and Eq. (9.6) becomes

$$P = 2\pi N_0 R_b \sin^2\psi_C \tag{9.7}$$

With the geometric relation

$$\sin\psi = \frac{dw}{\sqrt{dw^2 + dr^2}} = \frac{dw/dr}{\sqrt{1 + (dw/dr)^2}} \tag{9.8}$$

Eq. (9.6) can be transformed into the differential equation

$$\frac{dw}{dr} = \frac{P/(2\pi N_0 R_b)}{\sqrt{(r/R_b)^2 - (P/(2\pi N_0 R_b)^2}} \tag{9.9}$$

The solution, $w(r)$, is found by separation of variables and the boundary condition $w(r) = 0$ at $r = R$:

$$w = \frac{P}{2\pi N_0} \ln\left[\frac{r + \sqrt{r^2 - (P/(2\pi N_0)^2}}{R + \sqrt{R^2 - (P/(2\pi N_0)^2}}\right] \qquad \text{for } r_C < r < R \tag{9.10}$$

The displacement of the indentor tip, δ is the sum of the plate displacement at C, $w(r = r_C)$ and the height of the sphere from the centre to point C, i.e.

$$\delta = R_b(1 - \cos\psi_C) - w(r = r_C) \tag{9.11}$$

From Eq. (9.10) and Eq. (9.11) the punch displacement is given as a function of ψ_C which is related to the punch force by Eq. (9.7). In non-dimensional form the punch displacement is

$$\frac{\delta}{R_b} = 1 - \cos\psi_C + \sin^2\psi_C \ln\left[\frac{R/R_b + \sqrt{(R/R_b)^2 - \sin^4\psi_C}}{\sin\psi_C\,(1 + \cos\psi_C)}\right] \tag{9.12}$$

With Eq. (9.7) and Eq. (9.12) the indentor displacement is now given as a function of the punch load.

After a certain penetration the plate fails and the load drops. According to the results presented in Section 6.5 and the plane strain condition, Eq. (9.5), the plate will first neck and then fracture. The maximum strain and the initial failure will be at point C when $\varepsilon_{rr} = \varepsilon_{cr} = n$. If the strain at failure is denoted ε_{cr}, Eq. (9.4) gives the wrapping angle at failure:

$$\psi_{C,cr} = \cos^{-1}\left(e^{-\varepsilon_{cr}}\right) \tag{9.13}$$

Note that if the sphere is mounted on a cone with a semi-apex angle φ, the plate does not fail if the cone is sufficiently blunt, i.e. $\varphi > \pi/2 - \psi_{C,cr} = \sin^{-1}[e^{-\varepsilon_{cr}}]$.

Approximations
In the equations above, load, penetration and failure are expressed in terms of the intermediate parameter, ψ_C. As a non-linear equation consequently must be solved to find the load, P, or the wrapping angle, ψ_C, as a function of penetration, the inconvenience of this formulation is obvious. By least squares approximations it is found, however, that the relationship between the wrapping angle and the penetration, Eq. (9.12), is well approximated by the expression

$$\psi_C = 0.883\ (\delta/R)^{0.625}\ (R/R_b)^{0.440} \qquad \text{or} \tag{9.14}$$

$$\frac{\delta}{R} = 1.220\ (R/R_b)^{-0.7032}\ \psi_C^{1.559} \tag{9.15}$$

The error introduced by simplifying the expressions is less than 5 % for the parameter ranges $0.02 < \delta/R < 0.2$, $5 < R/R_b < 40$ and $0 < \psi_C < 50^o$. With the approximations above, the punch load and the penetration to failure become

$$P = 2\,\pi\,N_0\,R_b\,\sin^2\left[0.883\ (\delta/R)^{0.625}\ (R/R_b)^{0.440}\right] \tag{9.16}$$

$$\left(\frac{\delta}{R}\right)_{failure} = 1.220\ (R/R_b)^{-0.7032}\ \left(\cos^{-1}\left(e^{-\varepsilon_{cr}}\right)\right)^{1.559} \tag{9.17}$$

For calculations by hand, the expressions above are convenient and they could even be further simplified as it turns out that the force-penetration relationship is almost linear in the initial stage of the deformation. When they are implemented in a computer program, however, it is not necessary to introduce the approximations, as Eq. (9.12) gives the penetration explicitly for $\psi_C = \cos^{-1}(e^{-\varepsilon_{cr}})$ and as Eq. (9.12) is easily solved numerically for the plate wrapping angle ψ_C given δ, R_b and R.

9.3.2 Comparison to Experiments

Kamano, Kaminishi and co-workers, [59] and [57], published results of steady-state punch indentation into mild steel plates. The main data from the experimental set-up of the three relevant tests is given in Table 9.1.

Table 9.1: *Main data of experimental results given by Kamano, Kaminishi and co-workers, [59] and [57]. In the calculations the indentor radius is taken to be* $R_b + t/2$.

Configuration no	t (mm)	R (mm)	R_b (mm)	σ_y (MPa)	σ_u (MPa)	$\sigma_0 = 0.5(\sigma_y + \sigma_u)$ (MPa)
1	2.1	100	2.75	208	319	264
2	2.1	100	10.0	208	319	264
3	1.0	100	2.75	234	323	279

Figure 9.8 shows the calculated force-displacement relationship for the three test configurations together with the theoretical predictions from Eq. (9.16). Theory overestimates the punch load by only 0 - 10 %. This discrepancy can easily be ascribed to the uncertain choice of flow stress, σ_0, in the rigid-plastic theory.

In connection with application to a theoretical grounding model, prediction of the wrapping angle, ψ_C and prediction of strains and plate failure is most interesting. From Figure 9.8 it is seen that the measured plate resistance force dropped or levelled off abruptly when the penetration reached a distinct level. According to the theory of the previous section, this level of penetration corresponds to the point where the strain at the boundary of the contact zone reaches a value equal to the strain hardening exponent, n. The actual value of n is only given for *Configuration III* as $n = 0.22$ but assuming it is the same for all three configurations gives a theoretical prediction, as shown in the third column of Table 9.2. The actual strain at crack initiation was measured to be about 0.7, so the validity of using this value for the failure strain is also investigated in Table 9.2.

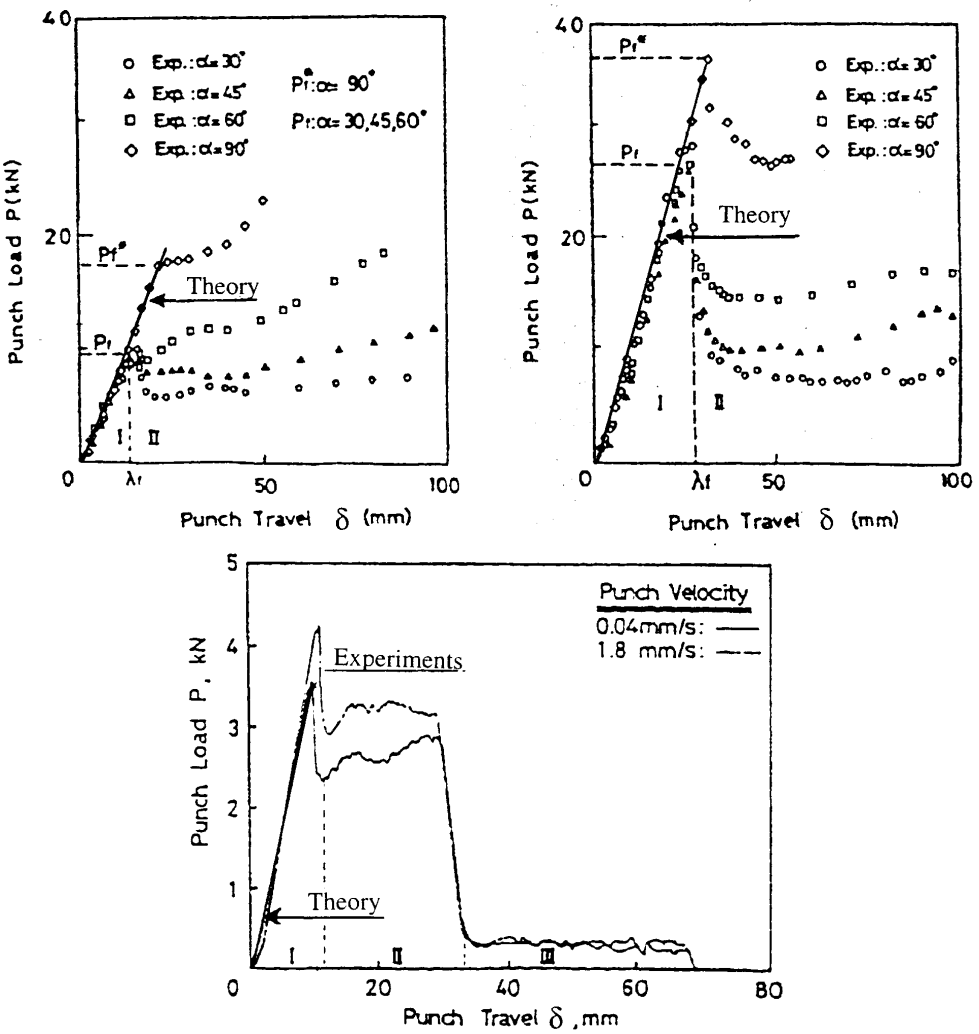

Figure 9.8: *Measured and calculated force-displacement relationships for the three configurations. The experiments were carried out with different cone apex angles, denoted 'α' above, [57], [59].*

Table 9.2: *Penetrations to failure. Experimental values and theory (Eq. (9.17)) with assumed critical strains to failure of* $\varepsilon_{cr} = n = 0.22$ *and* $\varepsilon_{cr} = 0.7$.

Configuration no	Experiment δ_{frac} (mm)	Theory, $\varepsilon_{cr} = n = 0.22$ δ_{frac} (mm)	Theory, $\varepsilon_{cr} = 0.70$ δ_{frac} (mm)
1	13.0	6.0	13.3
2	28.0	13.3	28.1
3	11.0	5.4	11.9

It is seen that, by using the failure criterion, $\varepsilon_{cr} = n = 0.22$, the theory underestimates the penetration to failure severely. The reason for this deficiency of theory emerges from a closer inspection of the experiments of Kawano et al., [59]. The strain field was here measured for experiments with a smaller specimen radius than in the experiments above but otherwise the same material and set-up ($R = 45\ mm$, $t = 2.1\ mm$, $R_b = 2.75\ mm$ and $R_b = 10m\ m$). In Figure 9.9 and Figure 9.10 the measured and calculated strain fields are compared.

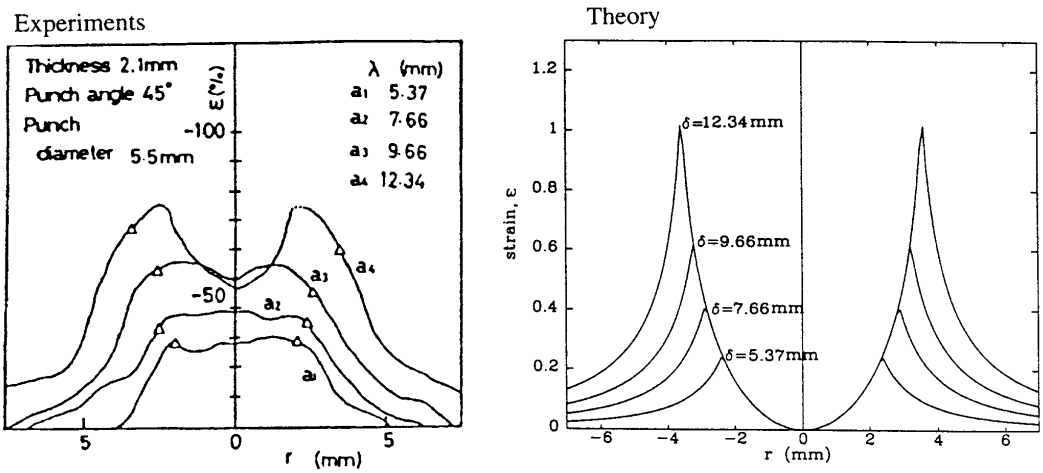

Figure 9.9: *Measured and calculated strain fields for* $R = 45\ mm$, $t = 2.1\ mm$, $R_b = 2.75\ mm$, *[59]. In the left diagram,* λ *denotes penetration, i.e.* $\lambda = \delta$.

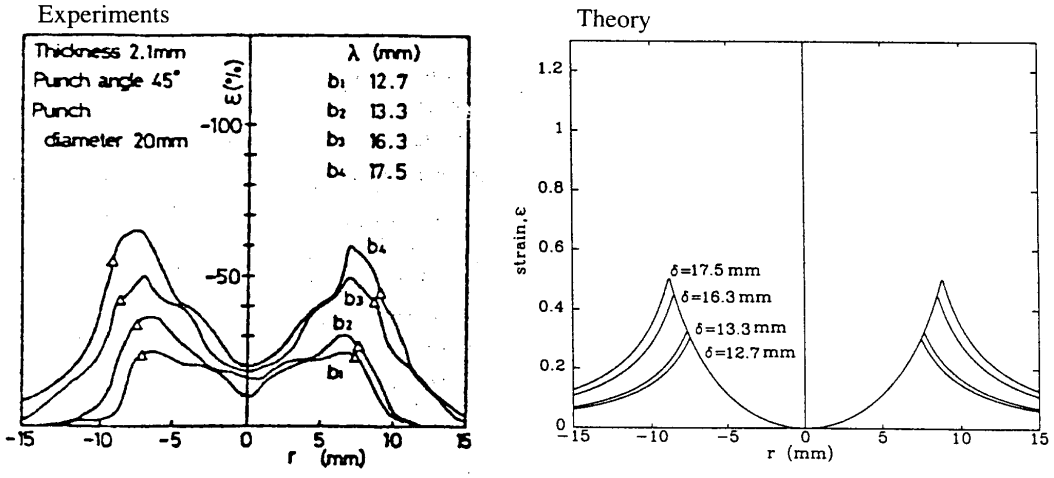

Figure 9.10: *Measured and calculated strain fields for* $R = 45mm$, $t = 2.1mm$, $R_b = 10mm$, *[59]. In the left diagram,* λ *denotes penetration, i.e.* $\lambda = \delta$.

The major conclusions to be drawn are:

1. The experimental results show significant straining at the centre, $r = 0$, indicating that the assumption of no in-plane material displacement is not valid. At a certain penetration, however, it is true to say that the central part is not further strained.

2. The theory predicts a very localised strain distribution over a small width of the plate. This corresponds to the experimental data where a neck was formed around the penetrator. Since the theoretical solution for the strain distribution shows the same kind of localisation as was seen in the experiments, using the theoretical limit of $\varepsilon_{max} = \varepsilon_{cr} = n$ gives a significant underestimation of the penetration to failure (see Table 9.2). The experiments showed maximum strains of about 0.7 and as seen in Table 9.2 use of this critical strain gives very good correspondence between theory and experiments.

3. The discrepancies between measured and calculated strain fields indicate an in-plane displacement of material elements (not only vertical) which causes a circumferential strain. This means that the state of strain is in the stretching region of a fracture forming limit diagram, FFLD, and the assumed necking criterion $\varepsilon_{rr} = n$ corresponding to plane strain is therefore no longer valid.

All in all, it is seen that even for this relatively simple example of punch indentation, prediction of plate failure is by no means simple and the problem needs further investigation for clarification. The results above indicate that the strain limit should be the fracture strain. In a grounding scenario, however, results which are given later show that use of the necking strain, $\varepsilon_{cr} = n$, gives good agreement between theory and measurements for the penetration to fracture.

Figure 9.11 shows a comparison between measured and calculated maximum strains as a function of penetration for the two different indentor radii. The correspondence between theory and experimental results is seen to be fair. This was also to be anticipated since insertion of the measured failure strain into the failure criterion led to a good prediction of penetration to failure, see Table 9.2. The conclusion is that if the failure strain, ε_{cr} of the material is known, the theory presented above, Eq. (9.17), gives the penetration depth at which failure occurs.

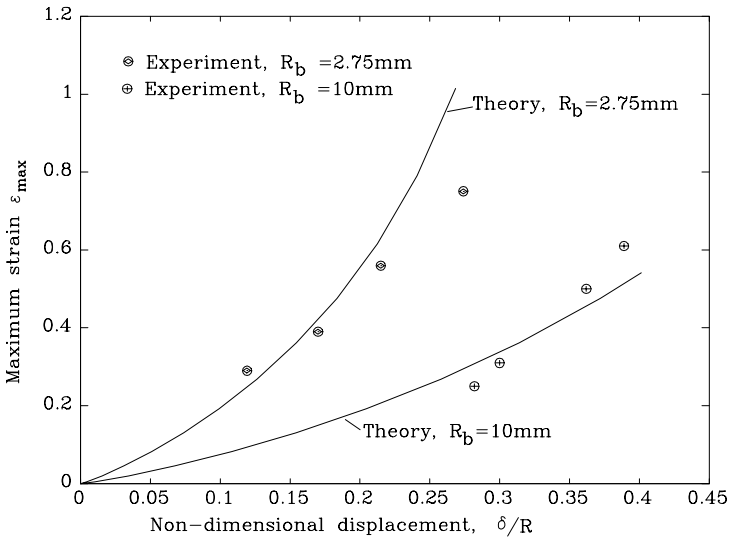

Figure 9.11: *Measured and calculated maximum strains at different levels of penetration.* $R = 45\ mm$, $t = 2.1\ mm$, $R_b = 2.75, 10\ mm$, *[59].*

As it is shown later, the 'wrapping angle', ψ_C, is relevant in connection with prediction of the effect of friction. In the experimental results shown in Figure 9.9 and Figure 9.10, the outer limits of the contact area is indicated by the triangles. Denoting the radial coordinate of the contact zone limit, r_C, the information is easily converted to wrapping angles as $\psi_C = \sin^{-1}(r_C/R_b)$. Then, the experimental wrapping angles of Figure 9.9 and Figure 9.10 can be compared to those predicted by Eq. (9.14). The comparison is shown in Figure 9.12. Theory tends to slightly overestimate the angle for the small indentor but gives very good correspondance for the larger. In view of the uncertainties that must be connected with the measurements, the agreement is very good.

The conclusion to the present analysis of punch indentation into circular plates is that a theory is established which gives the relations between the penetration-maximum strain and the penetration-wrapping angle, respectively. The results will be applied to the grounding problem by assuming that the mode of plate wrapping on the rock is the same as the mode of plate wrapping on the indentor. In the following, Eq. (9.12) can therefore be used with $R = B_{de}$ and $R_b = R_R$.

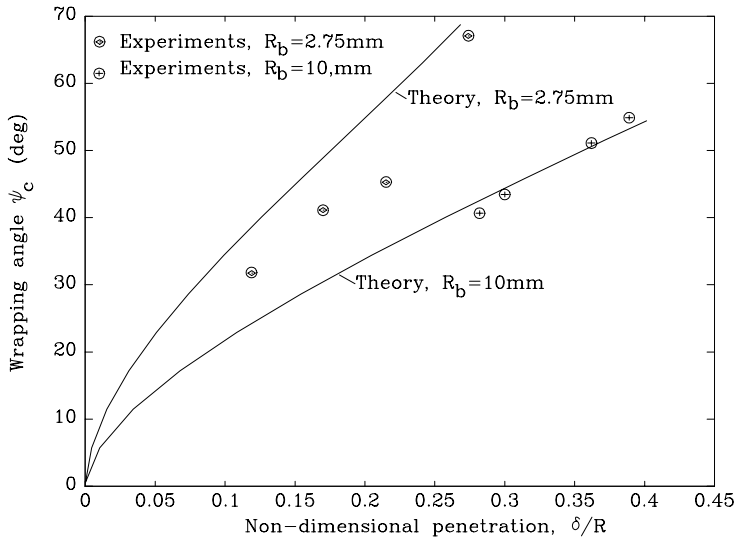

Figure 9.12: *Measured and calculated wrapping angles at different levels of penetration.* $R = 45mm$, $t = 2.1mm$, $R_b = 2.75, 10mm$, *[59].*

9.4 Necking and Fracture of a Plate in Shear and Tension

As discussed in Section 6.5, prediction of fracture is by no means simple. This was illustrated by the difficulties of predicting plate failure in the very 'clean' and simplest possible plate punch problem of the previous section. Compared to this plate punch problem, the problem of fracture in an assembled ship bottom is further complicated by the effect of stiffeners, welds and different kinds of imperfections as well as by the fact that the indentor does not move perpendicularly to the plane of the plate but rather *in* the plane. Successful attempts at modelling the strength of welds and so-called 'hard points' have been presented, but the field has not yet matured for application to a simplified methodology like the present, so welds and component intersections are assumed to stay intact.

The idea of the present approach is that a plate strip in the transverse direction deforms as in the plate punch problem above, with the modification of a superimposed shear strain. This is consistent with the overall 'shear model' presented in Section 9.2 and the approach is illustrated in Figure 9.13. The straining of a material element must be largest when it leaves the deformation zone. Thus, it is sufficient to consider the fracture criterion here - i.e. at the transverse strip shown in Figure 9.13.

In the plate punch problem, material was assumed to be deformed in a state of plane strain. Here, by superimposing a shear strain, both in-plane major strains, ε_1 and ε_2, will be present and proper account has to be taken of the two-dimensional strain limits shown in the fracture forming limit diagram, Figure 6.12.

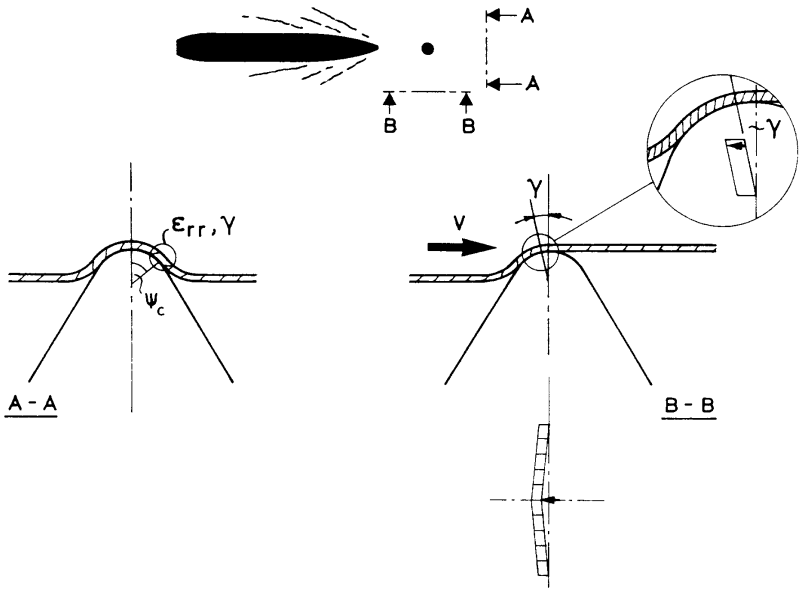

Figure 9.13: *Basic idea of fracture criterion. A transverse plate strip deforms as in the plate punch problem with a superimposed shear deformation.*

In order to use the strain limits given in Figure 6.12, the strain pair $(\varepsilon_{rr}, \varepsilon_{r\theta})$ has to be transformed to the major strain pair $(\varepsilon_1, \varepsilon_2)$. The assumption of proportional strain paths is made here although arguments will be given later in Section 9.7 that this may not be the case:

$$\frac{\varepsilon_{rr}}{\varepsilon_{r\theta}} = \text{Constant} \tag{9.18}$$

Mohr's circle for the strain in a material element therefore expands concentrically as the element passes through the zone of deformation. The radius is given by

$$R = \sqrt{\varepsilon_{rr}^2/4 + \varepsilon_{r\theta}^2} \tag{9.19}$$

and the major strain pair by

$$\varepsilon_1 = \varepsilon_{rr}/2 + R \tag{9.20}$$

$$\varepsilon_2 = \varepsilon_{rr}/2 - R \tag{9.21}$$

It should be noted that the major strains are positive and negative, respectively, indicating a process in the second quadrant in an FFLD. Adding Eq. (9.20) and Eq. (9.21) gives

$$\varepsilon_1 + \varepsilon_2 = \varepsilon_{rr} \tag{9.22}$$

The plate failure locus in the drawing region is given by a similar expression, $\varepsilon_1 + \varepsilon_2 = \varepsilon_{cr}$ (Eq. (6.30)), so that the final failure criterion simply becomes

$$\varepsilon_{rr} = \varepsilon_{cr} \tag{9.23}$$

This is exactly the criterion of the plate punch problem so super imposing a shear strain does not change the fracture criterion. Hence, the expression from the previous section for the penetration to failure directly applies here. If the rock is sufficiently blunt, the strains never reach a critical level. In terms of the cone semi-apex angle, φ, this can be expressed as: no fracture if $\sin\varphi > e^{-\varepsilon_{cr}}$. For smaller cone semi-apex angles, the penetration to failure is

$$\delta_{frac} = R_R \left\{ 1 - \cos\psi_C + \sin^2\psi_C \ln\left[\frac{B_{de}/R_R + \sqrt{(B_{de}/R_R)^2 - \sin^4\psi_C}}{\sin\psi_C\,(1+\cos\psi_C)} \right] \right\} \tag{9.24}$$

where B_{de} is the lateral extent of deformation, R_R is the radius of the rock tip, $\psi_C = \cos^{-1}(e^{-\varepsilon_{cr}})$ and ε_{cr} is the critical plate straining, which should be taken to be $\varepsilon_{cr} = n$. It is noted that with $R_R = 0$ the penetration to failure is zero. Clearly, this is not physical because the mode of deformation will be different from the wrapping mode assumed above for the punch type deformation. However, the penetration to rupture for such a needle type rock is very limited, [83], so in most cases the error of using Eq. (9.24) even for this rock geometry is not large.

9.5 Extent of Deforming Zone and Fracture Criterion

The above sections concerning energy dissipation and fracture are all based on a given extent of the deformation: B_{de} in Figure 9.4, χ_l in Figure 9.6 and R in Figure 9.7. Indeed, the plate of the punch indentation problem had a well defined clamped boundary condition but, for an assembled ship bottom structure as shown in Figure 9.2, boundary conditions are far more complicated.

In many of the previous applications of the upper bound method to crashworthiness, statically determinate problems like axial crushing of columns (for example [5] and [137]) or more complicated structures like a ship bow, [60], have been analysed. When such a statically determinate problem is considered, the size of the deforming zone is known because the deformation takes place in that part of the structure where stresses (which are known by static equilibrium alone) first exceed the strength. For example, in axial crushing of a prismatic beam, the axial force is the same at all cross-sections so that a repeated deformation mode along the length of the beam can be anticipated. In a statically indeterminate system,

however, stresses are unknown unless the stiffness of the structure is taken into account. Thus, in a simplified approach as this one where the flexibility is not considered, the problem of finding the extent of the deforming zone becomes apparent.

In the problem of plate cutting by a wedge, which was treated in Chapter 8, the size of the deforming zone was found by introducing an unknown geometric parameter, the so-called plate rolling radius, and postulating that this rolling radius adjusts itself to giving the lowest instantaneous resistance force of the plate. This approach is in accordance with the idea of finding a least upper bound and it is convenient for the simplest geometries. For an assembled ship bottom structure, however, searching for the deformation mode with the smallest rate of energy dissipation becomes very cumbersome and at present it is not possible.

Figure 9.14: *Frog's eye view of a double bottom deformed by a conical rock with a rounded tip. Example of how strong stiffeners on the longitudinal girders introduce hard points, early shell rupture and possibly bad energy absorption. From experiments conducted by the NSWC, USA, [106].*

In the work of Thunes, [125], which is summarised by Amdahl, [6], a simplified model is presented for the problem of lateral indentation of a cone into a double bottom. It is here assumed that the deformation process extends to the nearest principal stiffeners outside the base of the rock before the plate fractures. This method is the simplest possible and in several cases it has proved to be sufficiently accurate. However, as noted in several analyses of side collisions, for example [28] and [139], membrane forces in the side shell may cause the deformation to extend beyond the nearest stiffeners. This spread of the deforming zone may be important to capture, because it affects the rate of energy dissipation as more material is deformed and it delays the onset of fracture as 'hard points' are not artificially introduced. Figure 9.14 shows an example of a ship bottom which may be well engineered

for the environmental loads but, due to the very rigid stiffening structure on the longitudinal girders, the structure shows early fracture and bad energy absorption capabilities.

The following sections describe how the extent of the deforming zone in the longitudinal and transverse directions is calculated in the present study.

9.5.1 Longitudinal Extent of Deformation

For a double bottom with densely spaced floors and girders, the experiments performed by the NSWC, [106] and [105], showed that the deformed structure conformed closely to the rock on the front face of the rock. For a bottom structure with heavy longitudinals, the deformation is not necessarily confined to a small area between two frames - it may shoot into bays ahead of the rock. Photographic evidence of the damaged hull of the *Exxon Valdez* shows such failure modes where longitudinals are lifted up through the transverse frames. As shown in [139], the same phenomenon is present in a side collision where the finite strength of transverse frames allows the deformation to spread over several frames delaying shell fracture. In order to determine the length of the deformation zone, χ_l in Figure 9.6, consider the two simplified failure modes shown in Figure 9.15.

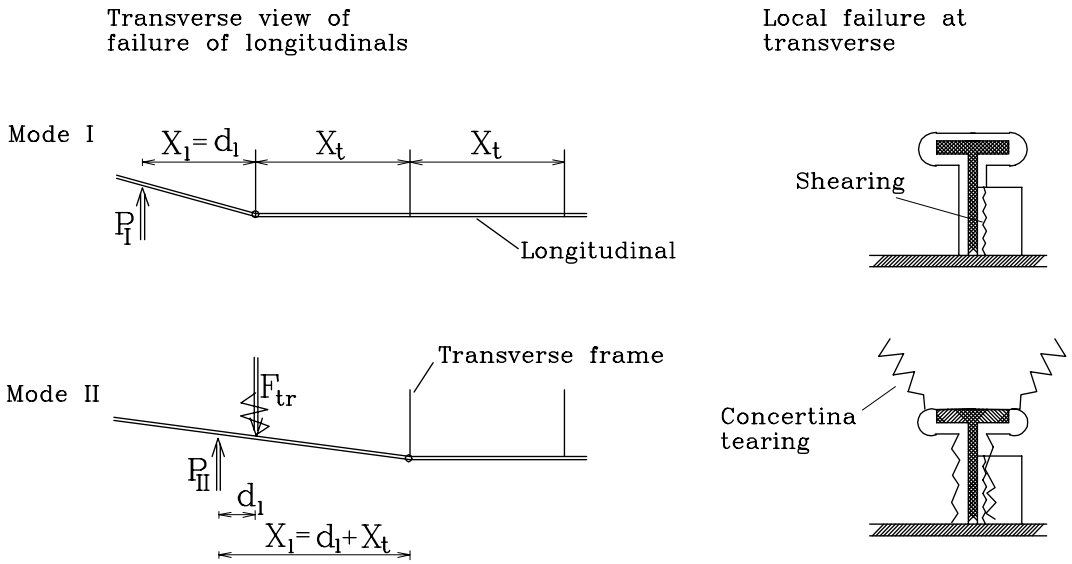

Figure 9.15: *Two of the possible global failure modes for longitudinals and local failure of intersection between longitudinal and transverse.*

In a grounding event, the load is more complex than just a vertical point force, but for estimation of the length of the deformation, the model shown in Figure 9.15 is considered sufficiently accurate. The bending moment capacity of the longitudinal is denoted M_o and the resistance of the transverse frame is F_{tr}. The distance between the frames is χ_t. When

the rock is sufficiently far away from the frame, the deformation mode giving the lowest force, P_I, is *Mode I*. The vertical force is then

$$P_I = \frac{M_0}{d_l} \tag{9.25}$$

At some point as the rock approaches the transverse frame, the bending hinge jumps to the next frame in order to minimise the rate of energy dissipation, Figure 9.15. The force for this *Mode II* is

$$P_{II} = \frac{M_0}{d_l + \chi_t} + \frac{\chi_t}{d_l + \chi_t} F_{tr} \tag{9.26}$$

If it is assumed that the deformation mode adjusts itself to giving the lowest force, the point of transition between modes is found by solving $P_I = P_{II}$ for $d_l = d_{l,0}$. The result is simple:

$$d_{l,0} = \frac{M_0}{F_{tr}} \tag{9.27}$$

The model is only valid for $d_{l,0} \leq \chi_t$.

The connection between the transverse and the longitudinal first fails by shear of the connection to the web, Figure 9.15. On the assumption that the web is effectively welded to the transverse over 2/3 of its height, D_w, the fully plastic resistance becomes

$$F_{tr,shear} = \frac{\sigma_0}{\sqrt{3}} \left(\frac{2}{3} D_w \right) t_t \tag{9.28}$$

This initial failure is followed by contact between the flange of the longitudinal and the transverse and subsequent concertina tearing of the plating in the transverse, see Figure 9.15 and Figure 8.1. The problem of concertina tearing is thoroughly treated by Wierzbicki, [136]. It is shown here that a fair estimate of the load in the initial phase of the deformation is equal to the squash load

$$F_{tr,tear} = \sigma_0 \, d_f \, t_t \tag{9.29}$$

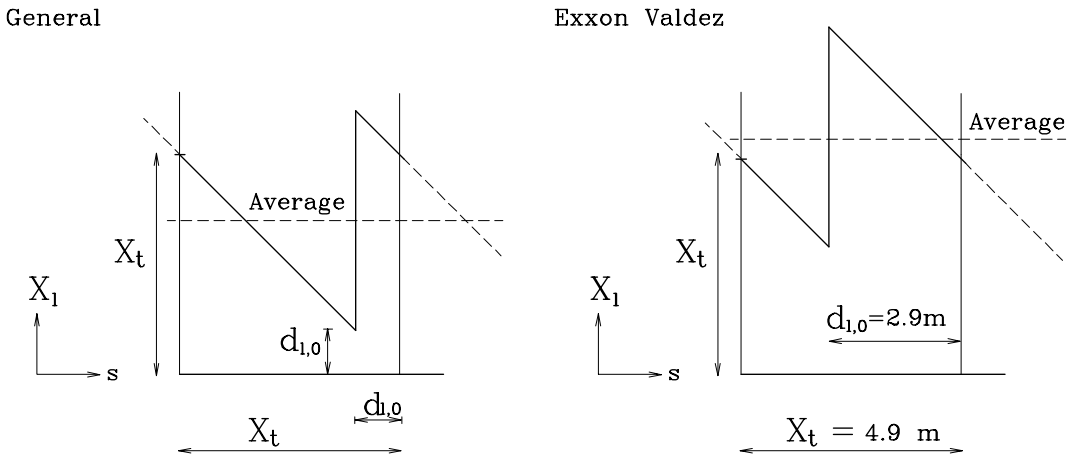

Figure 9.16: *Longitudinal extent of the deformation, χ_l, as a function of the rock position, s, between two frames. The deformation jumps to the next transverse frame when the distance to the frame ahead of the rock is $d_{l,0}$. General and numerical example of the Exxon Valdez.*

where d_f is the width of the flange and t_t is the thickness of the transverse. An estimate of the average resistance of the transverse to the lifting of the longitudinal is here taken to be

$$F_{tr} = \frac{F_{tr,shear} + F_{tr,tear}}{2} = \frac{\sigma_0}{2} \left(\frac{2}{3\sqrt{3}} D_w t_t + d_f t_t \right) \tag{9.30}$$

For a given ship bottom structure with heavy longitudinals, the longitudinal extent of deformation, χ_l, can now be calculated from the theory above. Figure 9.16 depicts χ_l as a function of the rock position between two frames.

The average extent becomes

$$\chi_{l,av} = \int_0^{\chi_t} \chi_l \, ds = \frac{1}{2}\chi_t + d_{l,0} = \frac{1}{2}\chi_t + \frac{M_0}{F_{tr}} \tag{9.31}$$

and according to the limits given for Eq. (9.27) the model is only valid for $\chi_{l,av} \leq 1.5\chi_t$. With the scantlings of the *Exxon Valdez* as an example, the following data can be found;

$$\begin{aligned} \chi_t &= 4.9 \; m \\ M_0 &= 2.20 \; MNm \\ F_{tr,shear} &= 1.13 \; MN \\ F_{tr,tear} &= 1.53 \; MN \\ F_{tr} &= 1.33 \; MN \end{aligned}$$

According to Eq. (9.27) the deformation zone jumps through the transverse frame ahead of the rock when the distance to this frame is $d_{l,0} = 1.7\ m$. Then Eq. (9.31) gives an average length of the deforming zone of $\chi_{l,av} = 4.1\ m$. The length of the deforming zone as a function of the position of the rock is shown in Figure 9.16. With a spacing between frames of 4.9 m, the results above indicate that the average length of the deforming zone is about the same as the spacing between the frames. Thus, it is assumed that $\chi_{l,av} = \chi_t$.

9.5.2 Transverse Extent of Deformation and Fracture Criterion

The simple theoretical model above depicts the observed phenomenon of a larger extension of the deforming zone in the longitudinal direction for weaker supporting structures. As noted in connection with Figure 9.14, the spreading of deformation in the transverse direction may also be important, as membrane stresses in shell plating and transverse members drive the deformation beyond the longitudinal stiffeners pushed directly by the rock. To capture this spreading in a general scheme is not simple by any means. By considering the ship bottom as a grillage - somewhat as indicated in Figure 9.15 - it is possible to find the extent of deformation in a traditionally stiffened single bottom but, for a double bottom with crushable girders and floors and a very strong interaction between outer and inner bottom the problem is exceedingly complex and represents well the type of problems at which the finite element method is superior to the simplified methods.

In order to find a realistic model for the transverse extent of deformation within the framework of the present simplified approach, the results derived in the previous sections about local deformation and fracture should be considered. The strain in the transverse direction is related to the inclination, ψ, of the plate from horizontal via Eq. (9.4). This means that if the cone apex angle is sufficiently large, the inclination of the plate cannot exceed the critical strain, and the plate does consequently not fail. Inserting $\psi = \pi/2 - \varphi_c$ and $\varepsilon_{rr} = \varepsilon_{cr}$ in Eq. (9.4) gives the critical cone semi-apex angle:

$$\cos\psi = e^{-\varepsilon_{cr}} \quad \Rightarrow \tag{9.32}$$

$$\varphi_c = \sin^{-1}\left[e^{-\varepsilon_{cr}}\right] \tag{9.33}$$

Then, if $\varphi > \varphi_c$, the shell never fractures and if $\varphi < \varphi_c$, the plating fractures at a certain penetration. Taking as an example $\varepsilon_{cr} = n = 0.22$ gives $\varphi_c = 53.4^o$. The following considerations are for a rock with $\varphi < \varphi_c$, i.e. the plate fractures at a penetration which can be calculated from Eq. (9.24) given the width of the deforming zone, B_{de}.

For an initial estimate of B_{de}, assume that the deformation of the plating extends to the first principal stiffener outside the base of the rock in the plane of the undeformed plating. In other words, $B_{de} = s_l$ where s_l is the transverse distance to the considered longitudinal stiffener. If the rock tip radius is sufficiently large, longitudinals are pushed by direct contact of the rock before the plate fractures. When the dome of the rock touches a longitudinal

at the position $s_{l,i}$, the maximum inclination of a plate element from horizontal is denoted $\psi_{i,max}$. The geometric relation is

$$\sin \psi_{i,max} = \frac{s_{l,i}}{R_R} \tag{9.34}$$

This relation together with Eq. (9.32) now gives a critical transverse position of a longitudinal stiffener as

$$s_{l,c} = R_R \sqrt{1 - e^{-2\varepsilon_{cr}}} \tag{9.35}$$

so that all stiffeners closer to the rock than $s_{l,c}$ are pushed directly by the rock and the first stiffener outside $s_{l,c}$ is not touched before the plating has fractured.

The present approach for the *outer* bottom is based on the idea that the deformation before fracture extends to the first stiffener outside $s_{l,c}$. After fracture, the structure conforms to the rock so the width of the deformation is simply equal to the base of the rock in the plane of the undeformed plating.

For the *inner* shell, the problem is more complex because it interacts with the outer bottom through floors and girders, even before the rock tip touches the plating. At the same time, it is important to have an accurate prediction of inner bottom fracture because this is the last barrier against outflow of oil. Figure 9.17 shows the deformation mode of a double hull from one of the experiments performed by the NSWC, [105]. The picture shows the deformation at a stage just before fracture of the inner hull but with fracture of the outer bottom.

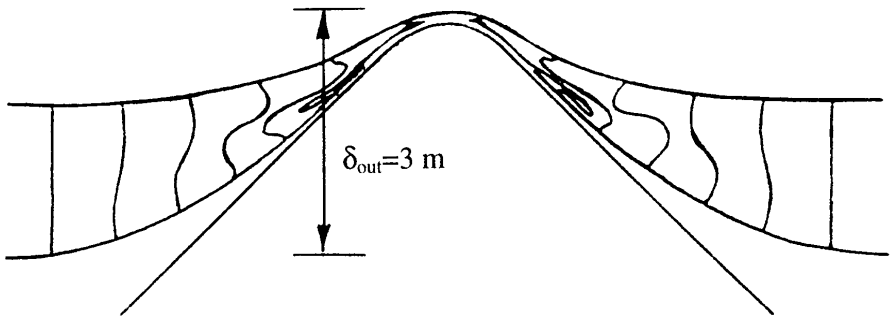

Figure 9.17: *Deformation of double hull ('ADH/PD328 ') just before fracture of the inner hull, [105]. The shell plating is fractured.*

It is clear from Figure 9.17 that there is strong interaction between the deformation of the shell plating and the inner bottom through the girders. Consequently, the assumption for the outer bottom of longitudinals only moving by direct contact with the rock clearly does not

hold true for the inner bottom, because the longitudinals are here pushed from below. The basic assumption here is that the deformation of the inner bottom before fracture extends to the first longitudinal stiffener outside both $s_{l,c}$ and longitudinal girders pushed by the outer bottom, i.e. longitudinal girders within the deformation zone of the outer bottom.

On the basis of the assumptions listed above, the extent of deformation is now defined for both inner and outer bottom before and after fracture is initiated. The procedure is described in detail in the sections containing the summary of calculation routines, Sections C.2.3 and C.3.2.

As an example, consider the grounding event shown in Figure 9.17. The rock tip radius is $R_R = 0.178\ m$ so with $\varepsilon_{cr} = n = 0.22$, the critical position of a longitudinal becomes $s_{l,c} = 0.106\ m$. The distance between the longitudinal girders is $0.17\ m$. The rock tip is at the centre between two girders so that the transverse distances to the girders are $s_{l,1} = 0.085\ m$, $s_{l,2} = 0.255\ m$, $s_{l,3} = 0.425\ m$, $s_{l,4} = 0.595\ m$ etc. According to the assumptions above, the deformation of the outer bottom will extend to the second girder before the plate fractures, i.e.

$$B_{de,out} = s_{l,2} = 0.255\ m \tag{9.36}$$

With $\varepsilon_{cr} = n = 0.22$ the penetration to fracture of the outer hull becomes $\delta_{frac,out} = 0.096\ m$.

When the rock tip touches the inner bottom, the shell plating has fractured so that the width of the deformation is assumed to be equal to the width of the base of the rock, which is $B_{R,out} = B_{de,out} = 0.474\ m$. According to the assumptions above, this implies that the first three girders are pushed by the rock and hence the deformation of the inner bottom extends to the fourth girder, i.e.

$$B_{de,inn} = s_{l,4} = 0.595\ m \tag{9.37}$$

Due to the very dense spacing of girders in this structure, another girder is actually pushed before the inner bottom fractures because the width of the outer bottom deformation has increased to $B_{out} = 0.674\ m$. It is assumed here, however, that the boundary of the inner bottom deformation stays at the fourth girder all the way to fracture. Figure 9.18 shows the assumed deformation compared to the measured deformation mode.

Inserting the width of the deforming zone from Eq. (9.37) in Eq. (9.24) gives a penetration into the inner bottom of $\delta_{frac,inn} = 0.15\ m$. The height of the inner bottom is $0.40\ m$ so the total penetration at fracture is $0.55\ m$. As the experiments were conducted at a scale of 1:5, this corresponds to a full-scale penetration of $2.75\ m$. Rodd, [105], reported the full-scale penetration to fracture to be approx. $3.0\ m$, see Figure 9.18. Thus, the theory predicts

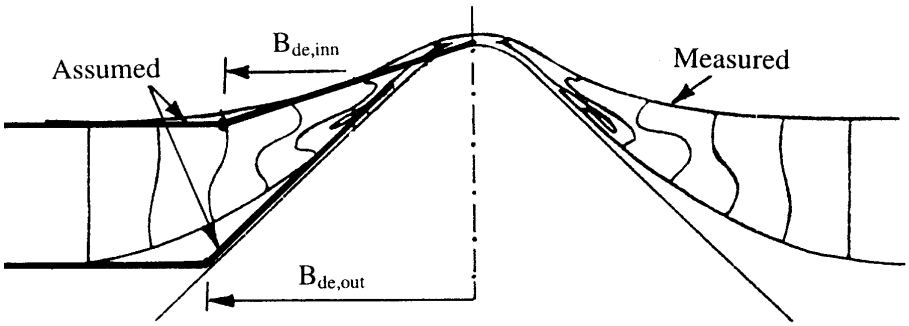

Figure 9.18: *Comparison between measured and assumed deformation modes. The measured deformation mode is from Rodd, [105].*

this penetration with an error of only 8 %. As this comparison is affected by the height of the double bottom, which is 2 m in full scale, it is interesting to compare the penetrations into the inner bottom. The measured penetration into the inner bottom before fracture was 1.0 m whereas the theory gives 0.75 m, so the error is now 25 %, which is still very good, considering the complexity of the problem.

If the specific structure shown in Figure 9.17 should be analysed, it would be reasonable to assume that the plating was deformed all the way to the boundaries because these boundaries are quite close to the rock. If the extent of the deformation zone is taken to be this distance, i.e. $B_{de} = 127\ cm$, Eq. (9.24) gives a penetration into the inner bottom to fracture of $\delta_{frac,inn} = 99.5\ cm$. The result is significant because this is exactly the penetration which was measured in all four tests reported by Rodd, [105]. Results presented below in Section 9.7 indicate an equivalent correspondence between Eq. (9.24) and small scale experiments. Hence, with all available experimental data, there are good reasons to believe in the validity of Eq. (9.24).

9.6 Friction and Vertical Reaction

By use of the approach outlined in Section 6.6, the effect of friction, g, and the ratio, k, between the vertical and the horizontal reaction can be derived for any rock geometry. It is necessary, however, to assume the distribution of pressure (the amplitude comes from the upper bound equations) and the direction of the relative velocity between the rock and the plate. It is assumed that the mode of deformation is determined by the inner or outer bottom plating so it is convenient to divide the analysis, depending on the fracture conditions of this plating.

9.6.1 Intact Plating

When the plating has not fractured, the mode of deformation for the plating in front of the rock is assumed to be equivalent to that found for the plate punch problem in Section 9.3. For this problem contact was found from the tip of the rock to an angle, ψ_C, from vertical. Consider now a longitudinal plate strip in front of the rock, Figure 9.19.

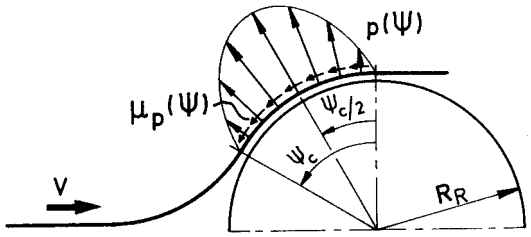

Figure 9.19: *Side view of the contact area and distribution of the normal pressure, p, and the frictional stresses, $\tau = \mu\, p$, on the rock when the plating is intact.*

The rock is in contact with the plate for $0 < \psi < \psi_C$. The normal pressure on the rock from the plate is distributed as $p(\psi) = Ap'(\psi)$. The amplitude, A, cancels in the final expressions for the friction factor and the ratio between vertical and horizontal forces, k. Equilibrium in the direction of motion can be expressed as

$$F_H = A \int_0^{\psi_C} [p' \sin\psi + \mu p' \cos\psi]\, R d\psi \tag{9.38}$$

The friction factor, g, which is the ratio between the total horizontal force and the plastic resistance force can now be found from Eq. (6.1) and Eq. (9.38) to be

$$g = \frac{F_H}{F_P} = \left(1 - \frac{\int_0^{\psi_C} \mu\, p'(\psi)\, d\psi}{\int_0^{\psi_C} [\sin\psi\, p'(\psi) + \mu\, \cos\psi\, p'(\psi)]\, d\psi}\right)^{-1} \tag{9.39}$$

The vertical force on the plate is

$$F_V = A \int_0^{\psi_C} [p'(\psi)\, \cos\psi - \mu p'(\psi) \sin\psi]\, R\, d\psi \tag{9.40}$$

The vertical to horizontal force ratio, k, emerges as the ratio between Eq. (9.40) and Eq. (9.38). For any shape of pressure distribution $p'(\psi)$, g and k can now be evaluated. It turns out that, if $p'(\psi)$ is symmetric about $\psi_C/2$, the pressure can be assumed to be condensed in a point at $\psi = \psi_C/2$ with a very good accuracy. The error of this simplification

for the friction factor and the vertical force is less than 2 % for any reasonable pressure distribution. Thus, assuming that the normal pressure is symmetrically distributed about $\psi = \psi_C/2$ the expressions for the friction factor and the force ratio are simplified to the convenient forms:

$$g = \frac{F_H}{F_P} = \left(1 - \frac{\mu}{\sin(\psi_C/2) + \mu\,\cos(\psi_C/2)}\right)^{-1} \tag{9.41}$$

$$k = \frac{F_V}{F_H} = \frac{1 - \mu\tan(\psi_C/2)}{\tan(\psi_C/2) + \mu} \tag{9.42}$$

The wrapping angle, ψ_C, is found by solving Eq. (9.12) for ψ_C. As the penetration approaches zero the wrapping angle also approaches zero and g and k go towards infinity. Since the basic assumption of the model is rigid-plasticity, however, it is only valid after a certain penetration corresponding to full plastification. At present this is taken into account by introducing a simple lower limit for the wrapping angle, $\psi_{C,min} = \sqrt{2\sigma_y/E}$. The wrapping angle should not be taken less than $\psi_{C,min}$.

The friction factor and the vertical to horizontal force ratio given in Eq. (9.41) and Eq. (9.42) are shown in Figure 9.20 and Eq. (9.21) as a function of the plate wrapping angle, ψ_C for two different values of the coefficient of friction.

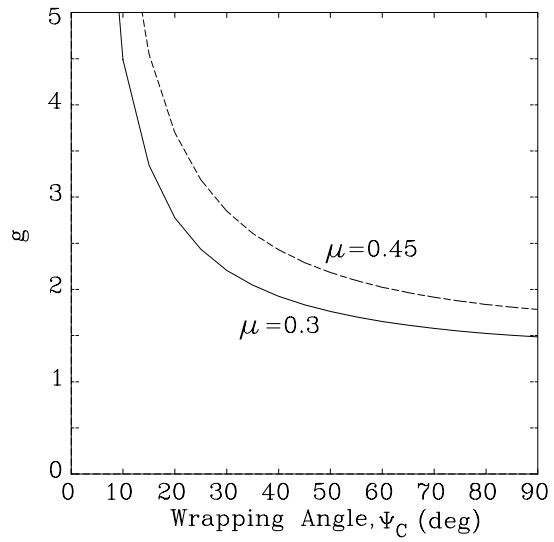

Figure 9.20: *Friction factor g as a function of the plate wrapping angle for two values of the coefficient of friction.*

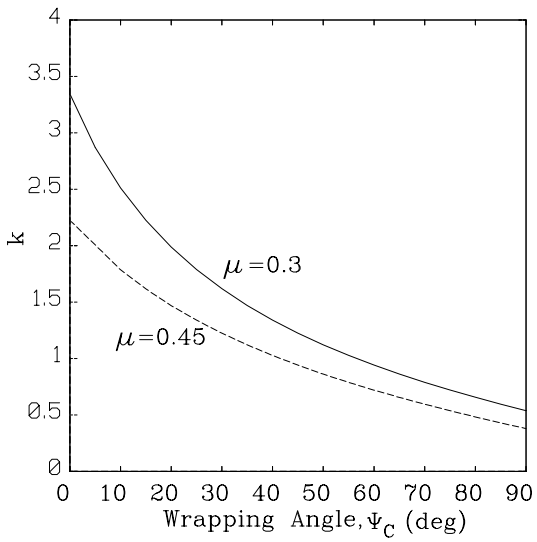

Figure 9.21: *Force ratio k as a function of the plate wrapping angle for two values of the coefficient of friction.*

9.6.2 Fractured Hull Plating

When the plate fractures, stresses in the transverse direction are brought to zero and, instead of only touching the rock in a small area near the tip, the bottom structure conforms more to the rock. Again, to derive expressions for the friction factor and the vertical to horizontal force ratio, it is necessary to assume or calculate a pressure distribution over a certain contact area. Experiments reveal a quite complex process of plate wrapping on the cone and deriving a local plate wrapping solution as it was done for the deformation before fracture, seems to be a very difficult task. Instead, to be consistent with the assumed overall mode of deformation, it is here assumed that the contact area between rock and plate is equal to the contact area between the conical rock shown in Figure 9.1 and the simplified mode of deformation shown in Figure 9.3. This is a line contact along a generator of the cone. Figure 9.22 shows the geometry of the problem.

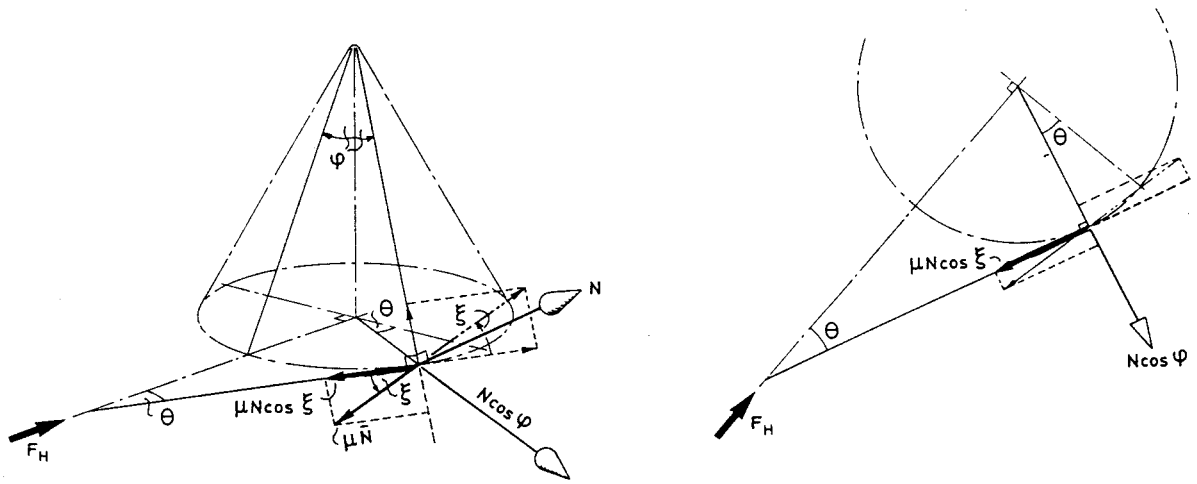

Figure 9.22: *Sketch of geometry for the derivation of the friction factor, $g = F_H/F_P$, and force ratio, $k = F_V/F_H$.*

The undeformed plate is moving horizontally at a velocity $\vec{V}$, but the relative motion between the rock and the deformed plate is displaced an angle ξ from $\vec{V}$ in the plane of the plate 'flap'. Horizontal equilibrium for the plate can be expressed as

$$F_H = N(\cos\varphi \sin\theta + \mu \cos\xi \cos\theta) \tag{9.43}$$

Insertion into Eq. (6.1) then gives the friction factor as

$$g = \frac{F_H}{F_P} = \left(1 - \frac{\mu}{\cos\varphi \sin\theta + \mu \cos\theta \cos\xi}\right)^{-1} \tag{9.44}$$

The ratio between the vertical and the horizontal force becomes

$$k = \frac{F_V}{F_H} = \frac{\sin\varphi - \mu \sin\xi \cos\varphi}{\cos\varphi \sin\theta + \mu \cos\theta \cos\xi} \tag{9.45}$$

From geometrical considerations, it can be found that the angle ξ between $\vec{V}$ and the relative velocity in the contact area must be bound, $0 < \xi < \theta$. As in the wedge cutting problem, a value of $\xi = \theta/2$ is used here. The friction factor and the vertical to horizontal force ratio given in Eq. (9.44) and Eq. (9.45) are shown in Figure 9.23 and Figure 9.24 as a function of the plate splitting angle, θ for two different values of the coefficient of friction μ and the cone semi-apex angle, φ.

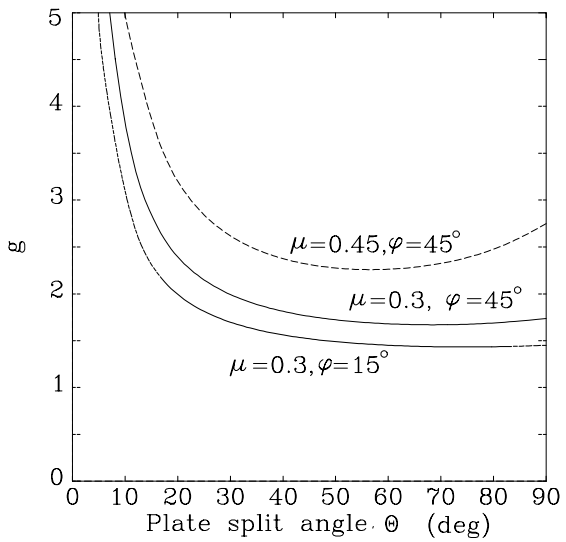

Figure 9.23: *Friction factor g for fractured plating as a function of the plate split angle for different values of the coefficient of friction μ and the cone semi-apex angle, φ.*

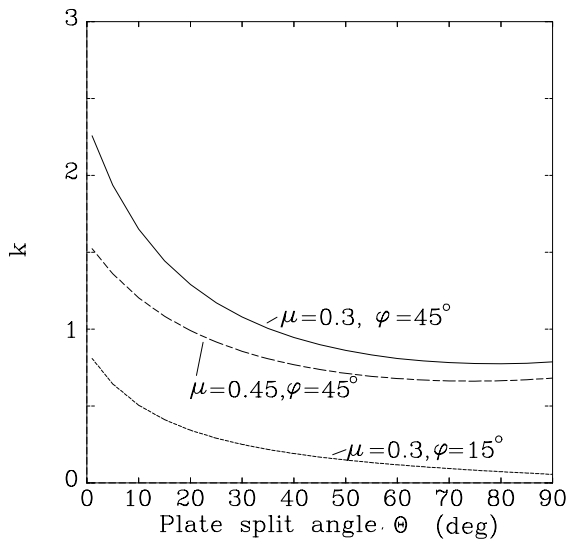

Figure 9.24: *Force ratio k for fractured plating as a function of the plate split angle for different values of the coefficient of friction μ and the cone semi-apex angle, φ.*

9.7 Plate Resistance before Fracture

With the basic theory for plasticity and friction given in Chapter 6 and the modes of deformation shown above in Figure 9.4 and Figure 9.6, the basis is made for calculating the resistance of the inner and the outer bottom plating. In the present section the resistance of an unstiffened plate is considered but the assumed mode of deformation is kept in the analysis of stiffeners so that their resistance can be added subsequently, see also [111].

9.7.1 Membrane Deformation

It is assumed that the deformation takes place within the triangular area OPQ in Figure 9.4. Unfortunately, very few results have been presented about the strain field in a moving plastic zone like this one. In metal forming, it is common practice to consider only the final state of the deformation and assume proportional strain paths. The membrane deformation of the present problem, however, should probably be considered at two stages at least: As a material element passes the OP-line it is assumed to be strained to a direct strain of $\varepsilon_{\eta\eta} = v_0/B_{de}$ and a shear angle of $\varepsilon_{\xi\eta} = -v_0/(2L_{de})$. The final deformation is assumed to be the direct strain $\varepsilon_{\eta\eta} = v_0/B_{de}$ and the shear angle $\varepsilon_{\xi\eta} = u_0/(2B_{de})$, so a strain field has to connect these two states. Figure 9.25 shows how the strains are assumed to change as a material element passes through the deformation zone.

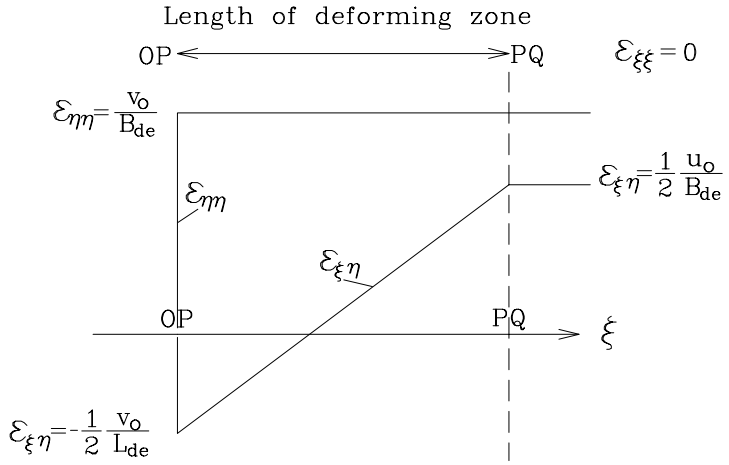

Figure 9.25: *Strain path of a plate material element passing through the zone of deformation, see also Figure 9.4. As a material element passes over the OP line it is assumed to be strained to a transverse direct strain of $\varepsilon_{\eta\eta} = v_0/B_{de}$ and a shear strain of $\varepsilon_{\xi\eta} = -v_0/(2L_{de})$. The final strain is $\varepsilon_{\eta\eta} = v_0/B_{de}$ and the shear strain $\varepsilon_{\xi\eta} = u_0/(2B_{de})$.*

The total change in equivalent strain should be calculated in two steps, one contribution as the material element passes the OP line and one contribution as the element passes through the deformation zone from OP to PQ. With proportional strain paths over the OP-line and linear strain paths through the deforming zone, as shown in Figure 9.25, the strain rates over the deforming zone become constant. Eqs. (6.6 - 6.10) then give the total energy equivalent strain to be

$$[\varepsilon]_{eq} = [\varepsilon]_{eq,OP} + [\varepsilon]_{eq,OP-PQ} = \frac{2}{\sqrt{3}}\left\{\sqrt{\left(\frac{v_0}{B_{de}}\right)^2 + \frac{1}{4}\left(\frac{v_0}{L_{de}}\right)^2} + \frac{1}{2}\left(\frac{v_0}{L_{de}} + \frac{u_0}{B_{de}}\right)\right\} \quad (9.46)$$

It is true to say that much work is needed to understand fully the strain field and the associated energy dissipation in a moving plastic zone. Some longitudinal straining

is invariably present and transverse members have a significant influence on the mode of deformation. According to Eq. (6.9) and with $B_{de}/L_{de} = \tan\theta$, the rate of energy dissipation in plastic membrane deformation on both sides of the symmetry line becomes

$$\dot{E}_m = \frac{4}{\sqrt{3}}\,\sigma_0\,t\,v_0\,V\left\{\sqrt{1+\frac{1}{4}\,\tan^2\theta}+\frac{1}{2}\left(\frac{u_0}{v_0}+\tan\theta\right)\right\} \tag{9.47}$$

9.7.2 Bending Deformation

The plate is bent both longitudinally and transversely and the energy dissipation for these two bending processes is considered separately.

A transverse strip fixed at the outer boundaries and deformed at the mid span, has been subjected to a total bending angle of $\Delta\psi = 4\,\tan^{-1}(\delta/B_{de})$. The energy absorbed per unit length is therefore $4\,M_0\,\tan^{-1}(\delta/B_{de})$ and as deformed material leaves the deforming zone at a velocity of V, the rate of energy dissipation for the transverse bending becomes

$$\dot{E}_{b,t} = 4\,M_0\,V\,\tan^{-1}\left(\delta/B_{de}\right) \tag{9.48}$$

The rate of energy dissipation for a longitudinal strip should be calculated according to Eq. (6.11) and the mode of deformation shown in Figure 9.6. The jump in plate curvature over one of the four hinges is $[\kappa] = [\kappa_{nn}] = 1/R$. The rate of energy dissipation is a decreasing function of χ_l so - as in the case of a stationary deformation zone - the deformation of a longitudinal tends to extend as far ahead as possible. As discussed in Section 9.5 transverse bulkheads and frames prevent the deformation from extending far ahead and, due to these supporting structures, the length of the deforming zone is not constant over time. It is assumed here, however, that the length of the deforming zone is $L_{de} = B_{de}/\tan\theta$ so that it is included in the choice of θ. In order to calculate the total rate of bending energy dissipation over the width of the deforming zone, it is convenient to introduce a coordinate, s, at the boundary of the deforming zone pointing towards the symmetry axis of the rock. Figure 9.26 shows two models for the longitudinal bending deformation modes. The functions for the longitudinal extent of deformation, χ_l, and the lifting, Δ_l, as a function of the transverse coordinate, s, are given in the figure.

More advanced models could be found but the two models shown in Figure 9.26 seem to resemble the actual deformation pattern well and they give analytically integrable expressions for the jump in curvature, $[\kappa](s)$:

$$\int_0^{B_{de}}[\kappa]\,ds = \int_0^{B_{de}}\frac{4\,\Delta_l}{\Delta_l^2+\chi_l^2}\,ds = \frac{2\,B_{de}}{\delta}\,\ln\left[\left(\frac{\delta}{L_{de}}\right)^2+1\right] \qquad \text{for Model 1} \tag{9.49}$$

$$\int_0^{B_{de}}[\kappa]\,ds = \int_0^{B_{de}}\frac{4\,\Delta_l}{\Delta_l^2+\chi_l^2}\,ds = \frac{4\,\delta\,B_{de}}{L_{de}\,\sqrt{\delta^2+B_{de}^2}} \qquad \text{for Model 2} \tag{9.50}$$

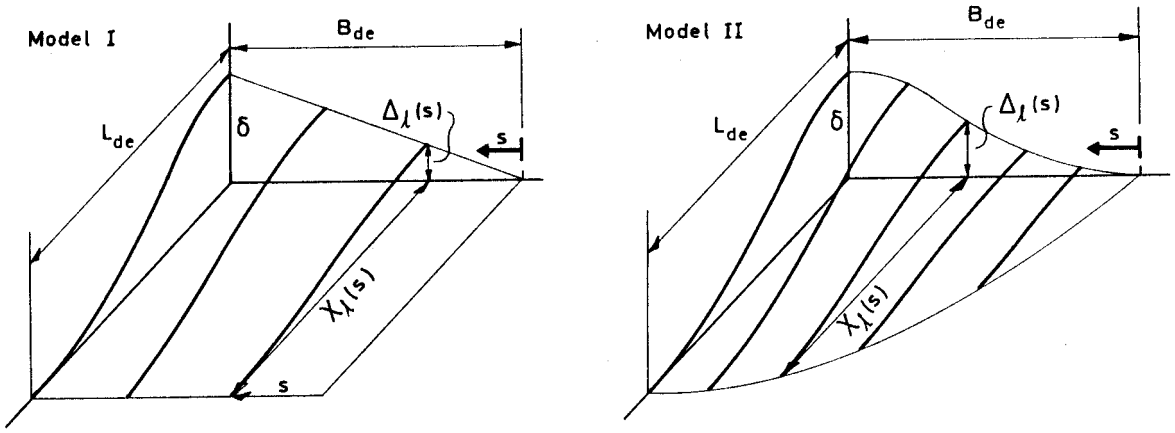

$$\Delta_l(s) = \frac{\delta}{B_{de}}\, s \qquad \Delta_l(s) = \frac{\delta}{2}\left(1 - \cos\frac{\pi\, s}{B_{de}}\right)$$

$$\chi_l(s) = L_{de} \qquad \chi_l(s) = L_{de} \sin\left(\frac{\pi\, s}{2\, B_{de}}\right)$$

Figure 9.26: *Models for longitudinal bending deformation.*

The jump in curvature, $[\kappa]$, and the energy dissipation are very sensitive to the choice of χ_l and Δ_l. To compare Eq. (9.49) and Eq. (9.50), it can be assumed that $L_{de} = B_{de}$. A Taylor expansion with respect to δ/L_{de} then reveals that *Model 2* gives a rate of energy dissipation in bending which is twice as high as that of *Model 1*. A close inspection of *Model 2* shows that for some penetrations, $[\kappa]$ is greater at $s = 0$ than at the rock tip. This counter-intuitive behaviour of $[\kappa(s)]$ is found for several of the deformation modes which, at first glance seem to resemble the actual deformation well. In conclusion, *Model 1* will be used in the following. With Eq. (6.11) the total rate of energy dissipation for the longitudinal bending deformation on both sides of the symmetry line becomes

$$\begin{aligned}
\dot{E}_{b,l} &= 2 \int_0^{B_{de}} 4\,[\kappa]\, M_0\, V\, ds \\
&= 8\, M_0\, V \int_0^{B_{de}} [\kappa] ds \\
&= \frac{16\, M_0\, V\, B_{de}}{\delta} \ln\left[\left(\frac{\delta}{L_{de}}\right)^2 + 1\right]
\end{aligned} \tag{9.51}$$

9.7.3 Total Resistance and Comparison to Experiments

The total plastic resistance of the plating can be calculated from Eqs. (6.1), (9.47), (9.48) and (9.51):

$$\begin{aligned} F_P = \frac{\dot{E}_m + \dot{E}_{b,l}}{V} &= 2\,N_0\,v_0\,\left\{\sqrt{1+\frac{1}{4}\,\tan^2\theta}+\frac{1}{2}\,\left(\frac{u_0}{v_0}+\tan\theta\right)\right\} \\ &+ 4\,M_0\,\tan^{-1}\left(\frac{\delta}{B_{de}}\right)+\frac{16\,M_0\,B_{de}}{\delta}\,\ln\left[\left(\frac{\delta}{L_{de}}\right)^2+1\right] \end{aligned} \tag{9.52}$$

where $N_0 = 2\sigma_0 t/\sqrt{3}$ and $M_0 = \sigma_0 t^2/(2\sqrt{3})$. All expressions are now derived for calculating the total horizontal and vertical reaction forces including plasticity and friction. In summary, the equations to be applied together with Eq. (9.52) are

$$u_0 = B_{de}\,\sqrt{(1-\cos\alpha)^2\sin^2\theta+(1-\cos\theta)^2\sin^2\alpha} \tag{9.53}$$

$$v_0 = B_{de}\,(1/\cos\alpha - 1) \tag{9.54}$$

$$\alpha = tan^{-1}\,(\delta/B_{de}) \tag{9.55}$$

$$F_H = g\,F_P \tag{9.56}$$

$$F_V = k\,F_H = g\,k\,F_P \tag{9.57}$$

$$g = \left(1-\frac{\mu}{\sin\,(\psi_C/2)+\mu\,\cos(\psi_C/2)}\right)^{-1} \tag{9.58}$$

$$k = \frac{1-\mu\,\tan(\psi_C/2)}{tan(\psi_C/2)+\mu} \tag{9.59}$$

$$\psi_C = 0.883\,\left(\delta/B_{de}\right)^{0.625}\,\left(B_{de}/R_b\right)^{0.440} \tag{9.60}$$

$$\delta_{frac} = \begin{cases} 1.22\,B_{de}\,\left(R_R/B_{de}\right)^{0.7032}\,\left(\cos^{-1}\left(e^{-\varepsilon_{cr}}\right)\right)^{1.559} & \text{for } \sin\varphi < e^{-\varepsilon_{cr}} \\ \infty & \text{for } \sin\varphi \geq e^{-\varepsilon_{cr}} \end{cases} \tag{9.61}$$

Note that the approximations for ψ_C and δ_{frac} are not generally valid but they are applicable to the experiments considered below. The general expressions are given in Section 9.3.

Unfortunately, the amount of experimental data published on the subject of the present problem is very limited. Turgeon, [128], investigated the problem of a transversely stiffened plate deformed by a parabolic rock both theoretically and experimentally. The theoretical model was based on an assumed deformation mode and rigid-plastic theory. All displacement functions u, v and w were described by trigonometric functions. Bending curvatures and membrane straining were quantified by theory for moderately large deflections. Assuming

rigid-plastic material Turgeon found that the bending energy could be neglected and that the plastic resistance of the plating for the membrane deformation (both tension and shear) was well approximated by the expression

$$F_P = 2.25\,\sigma_0\,t\,\delta^2/B_{de} \tag{9.62}$$

The formula is compared to Eq. (9.52) below. The experiments showed a very strong influence of the transverse stiffeners and, for the present problem, it is difficult to separate the plate resistance from the total measured forces. The study of Turgeon indicated that the effect of friction is significant and as in the present analysis it was found difficult to quantify theoretically frictional effects, due to uncertainties in determination of the wrapping angle, ψ_C. Force ratios, $k = F_V/F_H$, of up to 6 were measured indicating a coefficient of friction of maximum $\mu = 1/6 = 0.17$ (!) according to Eq. (9.58).

Muscat-Fenech, [82], conducted experiments with indentation of a spherical indentor into mild steel plates. The principal idea of the experimental set-up is shown in Figure 9.27.

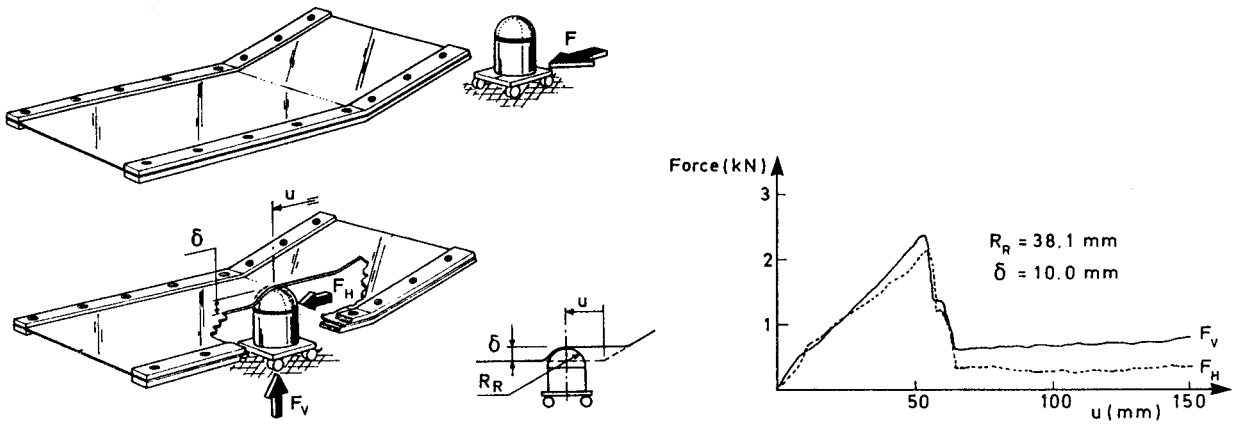

Figure 9.27: *Sketch of the experimental set-up used by Muscat-Fenech, [82], to investigate the plate resistance before fracture.*

The main data for the experiments are given in Table 9.3.

For comparison with theory - and for use in general - a proper value for the plate split angle, θ, has to be selected, see Figure 9.4. Figure 9.28 shows the plastic resistance, F_P, from Eq. (9.52) as a function of the plate split angle, θ, and the penetration, δ. Note that with the present modelling the plastic resistance is not a function of the radius of the rock.

As θ approaches zero, the plastic resistance of the plate approaches a value corresponding to only transverse bending and stretching. Taylor expansions of the trigonometric functions give a simple expression for the plastic resistance:

$$F_{P,min} = N_0\,\delta^2/B_{de} + 4\,M_0\,\delta/B_{de} \tag{9.63}$$

Table 9.3: *Main data for experiments performed by Muscat-Fenech, [82].*

Radius of rock tip, R_R	12.7-50.8 mm
Penetration, δ	0-50 mm
Half width of deformation, B_{de}	150 mm
Plate thickness, t	0.80 mm
Material	'Mild Steel'
Yield stress, σ_y	214 MPa
Flow stress (assumed), σ_0	275 MPa
Coefficient in Power law, Eq. (6.20), C	548 MPa
Parameter in Power law, Eq. (6.20), B	0 .
Strain hardening exponent, n	0.21 .
Ductile fracture toughness, R	240 kJ/m^2

If the transverse bending, which accounts for less than 3 % of the energy absorption in the present problem, is neglected, Eq. (9.63) is further simplified to

$$F_{P,min} = \frac{2}{\sqrt{3}}\,\sigma_0\,t\,\delta^2/B_{de} = 1.15\,\sigma_0\,t\,\delta^2/B_{de} \tag{9.64}$$

This equation has the same form as the expression found by Turgeon, Eq. (9.62), but the magnitude of Eq. (9.64) is only about half of Turgeon's result, due to the neglect of shear deformation. Table 9.4 shows a comparison between measured and calculated values for the horizontal and vertical forces reported by Muscat-Fenech, [82]. Since θ is basically unknown, the theoretical results are presented for both $\theta = 0$ and $\theta = 20^o$.

The comparison between measured and calculated results does not immediately reveal a very convincing performance of the derived theory. For $\theta = 20^o$ the present theory generally overestimates the forces seriously. However, a closer look at the experimental results in Table 9.4 reveals tendencies which call for further experimental investigation. For example, it is surprising if, at one particular penetration ($\delta = 10\ mm$) the resistance is first an increasing function of the penetrator radius (tests nos. 1 and 2) then a decreasing (test no. 2 and 4) and finally an increasing (tests nos. 4 and 6). In connection with the comparison between theory and tests some points concerning the experimental results should be emphasised:

- Elastic effects. With a plate thickness of $t = 0.8\ mm$, a span of $2B_{de} = 300\ mm$ and a deformation of only $\delta = 10 - 20\ mm$, elasticity might have a significant effect and use of a rigid-plastic model is questionable. Due to the boundary conditions of the present problem, it is not immediately possible to quantify accurately the elastic deformation. However, a simple string model ($\varepsilon = \frac{1}{2}(\delta/B_{de})^2$) predicts full plastification when $\delta = B_{de}\sqrt{2\sigma_y/E} \approx 0.045 B_{de}$. With $B_{de} = 150mm$ this gives $\delta = 6.7mm$ so

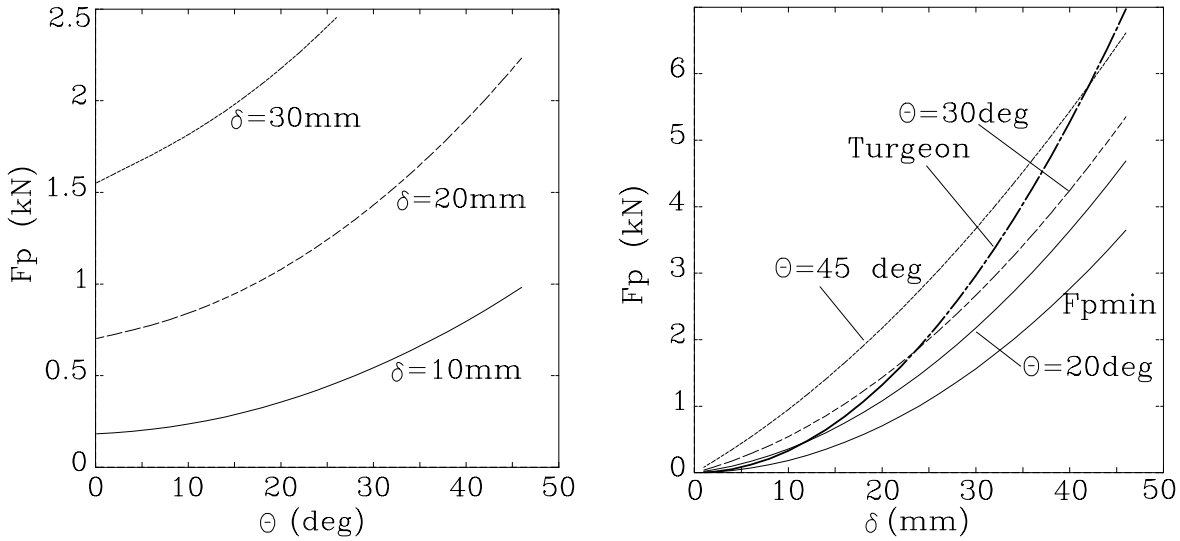

Figure 9.28: *Plastic resistance of plating, F_P Eq. (9.52), as a function of plate split angle, θ, and penetration, δ.*

although this is a crude estimate, it indicates an effect of elasticity which may be significant. Accurate solutions for a circular plate of radius B_{de} predict an equivalent level of elastic deformation, [127].

- Boundary Slippage. The initial tests performed at MIT showed that it is difficult to provide a fully clamped boundary condition for the plate, see [142]. At MIT it was found necessary to provide the plate support with draw beads, i.e. during mounting the plate is plastically deformed into a recess in the support structure. Such a fixation was not provided in the tests presented by Fenech-Muscat so it is likely that the plate has slipped a bit from the support. Note that if the deformation shape was triangular, the plate only had to slide 0.3 mm at the support to give zero membrane deformation at $\delta = 10$ mm!

With the derived theory and the points above in mind, it would be very interesting to conduct more tests. Muscat-Fenech performed tests with different penetrations, so that the penetrations to fracture can be extracted from the test results. These measured penetrations to failure and the corresponding values calculated by Eq. (9.61) are given in Table 9.5.

It is seen that, except for one configuration ($R_R = 38.1$ mm) the theoretically determined penetrations to fracture agree with the experimental bounds when a failure strain of $\varepsilon_{cr} = n$ is used in Eq. (9.61).

Table 9.4: *Experimental results reported by Muscat-Fenech, [82], and corresponding theoretical values, which are based on a coefficient of friction of $\mu = 0.3$. Numbers in brackets correspond to deviation from experimental values.*

Experimental Results:

Test No	R_R mm	δ mm	F_H kN	F_V kN	$k = F_V/F_H$
1	12.7	10.0	0.28	0.70	2.5
2	25.4	10.0	0.63	1.1	1.8
3	25.4	20.0	1.8	3.3	1.8
4	38.1	10.0	0.32	0.69	2.1
5	38.1	20.0	1.4	2.6	1.8
6	50.8	10.0	1.2	2.0	1.7

Theoretical Prediction:

			$\theta = 20^o$		$\theta = 0^o$	
Test No	g	k	F_H kN	F_V kN	F_H kN	F_V kN
1	2.3	1.7 (-32 %)	0.82 (+192 %)	1.4 (+100 %)	0.42 (+50 %)	0.72 (+3 %)
2	2.7	2.0 (+14 %)	0.98 (+56 %)	1.9 (+73 %)	0.50 (-21 %)	0.99 (-10 %)
3	2.2	1.6 (-11 %)	2.3 (+28 %)	3.7(+12 %)	1.5 (-17 %)	2.4 (-27 %)
4	3.1	2.1 (+0 %)	1.1 (+244 %)	2.3 (+233 %)	0.56 (+75 %)	1.2 (+74 %)
5	2.4	1.7 (-6 %)	2.6 (+86 %)	4.5 (+73 %)	1.7 (+21 %)	2.9 (+12 %)
6	3.3	2.2 (+29 %)	1.2 (+0 %)	2.6 (+30 %)	0.61(-49 %)	1.4 (-30 %)

Table 9.5: *Penetration to fracture. Experiments by Muscat-Fenech, [82], and theory from Eq. (9.61).*

R_R (mm)	Experiments	Eq. (9.61) $\varepsilon_{cr} = n = 0.21$ δ_{frac} (mm)	Eq. (9.61) $\varepsilon_{cr} = 0.7$ δ_{frac} (mm)
12.7	$10mm < \delta_{frac} < 20mm$	15.9 mm	35.2 mm
25.4	$20mm < \delta_{frac} < 30mm$	25.8 mm	57.2 mm
38.1	$40mm < \delta_{frac} < 50mm$	34.3 mm	75.9 mm
50.8	$40mm < \delta_{frac} < 50mm$	41.9 mm	92.9 mm

9.8 Plate Resistance after Fracture

After the plate has fractured, stresses in the transverse direction are released and instead of being stretched all the way to the remote boundaries, the plate conforms to the rock. Theoretical analysis of this problem is performed in a manner similar to that for cutting by a wedge presented in Chapter 8. There are differences, however, which complicate the analysis of plate cutting by a cone: The prismatic wedge has a well defined plate splitting angle, θ (see Figure 8.2), and since the wedge faces are plane, the direction of the normal and the frictional forces is uniquely determined. For the present problem the deformation mode shown in Figure 9.4 is still applied but the plate split angle, θ, is now basically unknown. It is shown below, however, that by choosing the plate split angle which minimises the horizontal resistance, the horizontal and vertical cutting forces can be determined theoretically with very good accuracy.

9.8.1 Energy Dissipation by Plasticity, Fracture and Friction

The plate separates in front of the cone, and since the cone does not have a sharp well defined cutting edge, the material separation process must be one of ductile fracture. For the wedge cutting problem analysed in Chapter 8, it was noted that some experiments revealed a crack process of pure plastic flow around the cutting edge rather than fracture. With a fracture toughness of R_c, the rate of energy dissipation for the crack tip process becomes

$$\dot{E}_c = R_c\, t\, V \tag{9.65}$$

To calculate the rate of energy dissipation for the membrane deformation, Figure 9.4 is used. The plate fractures along the centre line but the $PQ-PR$ gap has to be accommodated by straining for material continuity. The strain field requiring least energy is shearing of longitudinal fibres to a shear angle of $\gamma = 2\,\varepsilon_{\xi\eta} = u_0/B_{de}$. According to Eqs. (6.9, 6.10), the rate of energy dissipation for the membrane straining becomes

$$\dot{E}_m = 2\,\sigma_0\, t\, B_{de}\,[\varepsilon_{eq}]\, V = 2\,\sigma_0\, t\, B_{de} \left(\frac{2}{\sqrt{3}}\,\frac{1}{2}\,\frac{u_0}{B_{de}}\right) V = N_0\, u_0\, V \tag{9.66}$$

where the gap width, u_0, is calculated from Eq. (9.1) with $\alpha = \pi/2 - \varphi$ and $B_{de} = \delta\, \tan\varphi$.

In a simplified method like the present, taking improper account of the interaction between individual failure modes may lead to erroneous results. Eqs. (9.65, 9.66) were derived on the assumption that fracture and membrane deformation could be considered as separate processes. The problem with this approach is that a part of the fracture energy included

in R_c is actually plastic membrane deformations at the crack tip. This means that the energy absorbed by plastic deformations at the crack tip is included in both Eq. (9.65) and Eq. (9.66). Instead of Eq. (9.66) the membrane energy dissipation rate is therefore taken to be

$$\dot{E}_m = \begin{cases} 0 & \text{if } N_0\, u_0 < R_c\, t \\ (N_0\, u_0 - R_c\, t)\, V & \text{if } N_0\, u_0 > R_c\, t \end{cases} \tag{9.67}$$

For large scale problems like grounding on a rock $R_c\, t << N_0\, u_0$ so the modification in Eq. (9.67) is neglectable. For the small scale experimental results referred to later, however, the modification is important.

The deformed plate in the wake of the cone has been bent from horizontal to an angle of $\pi/2 - \varphi$, so the rate of energy dissipation for this bending process is

$$\dot{E}_b = 2\, M_0\ (\pi/2 - \varphi)\ V \tag{9.68}$$

where φ is the semi-apex angle of the cone, see Figure 9.1. Longitudinal bending is present as well but, the contribution for a bare plate is small. The contribution of plate bending is further discussed in Section 9.8.2 concerning longitudinal stiffeners. The total plastic resistance of the plate can now be obtained from Eqs. (9.65, 9.67, 9.68):

$$F_P = \frac{\dot{E}_c + \dot{E}_m + \dot{E}_b}{V} = \begin{cases} R_c\, t + 2\, M_0\ (\pi/2 - \varphi) & \text{if } N_0\, u_0 < R_c\, t \\ N_0\, u_0 + 2\, M_0\ (\pi/2 - \varphi) & \text{if } N_0\, u_0 > R_c\, t \end{cases} \tag{9.69}$$

With Eq. (9.69), Eq. (9.44) and Eq. (9.45), the horizontal and vertical reaction forces can be calculated in the usual manner as $F_H = g\, F_P$ and $F_V = k\, F_H = k\, g\, F_P$.

9.8.2 Comparison to Experimental Results

Muscat-Fenech, [83], conducted experiments with cutting of a thin plate by a cone. The experimental set-up is shown schematically in Figure 9.29 together with two force-displacement plots for ($2\varphi = 45^o$, $\delta = 10mm$) and ($2\,\varphi = 60^o$,$\delta = 40mm$). Of interest here is the steady state force which is reached after a certain penetration. As indicated by the lower of the force-displacement plots in Figure 9.29 the steady-state forces were not unambiguously extracted from the all the tests.

The data of the experimental set-up is identical to that given in Table 9.3, except that the indentor was conical with cone apex angles of $2\,\varphi = 30^o, 45^o$ and 60^o, respectively.

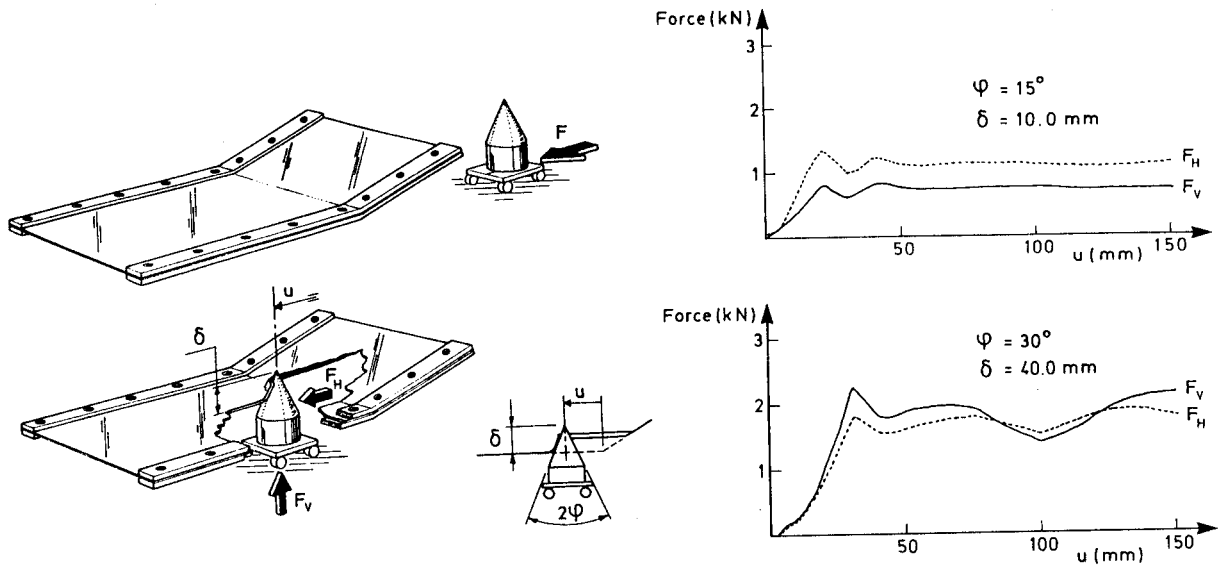

Figure 9.29: *Sketch of experimental set-up to investigate the resistance of plating cut by a cone together with two force-displacement plots:* ($2\varphi = 45^o$,$\delta = 10mm$) *and* ($2\,\varphi = 60^o$, $\delta = 40\ mm$). *Results from Muscat-Fenech, [83].*

Typical measured force-displacement plots are shown in Figure 9.29. The main results of the force-displacement measurements are given in Table 9.6.

In order to compare the results of Table 9.6 with the theory derived above, the plate split angle, θ, must be determined. Since the current theoretical approach is a kind of 'upper bound method', θ is here taken to be the value which minimises the resistance force of the plating - i.e. with this value of the plate split angle, the theoretical solution is a 'least upper bound'. Figure 9.30 shows the horizontal resistance force as a function of θ for a cone with a semi-apex angle of $\varphi = 22.5^o$. Depending on the penetration, the plate split angle giving the least resistance is seen to vary over a small interval from 5^o to 14^o.

The dependence of the resistance on θ is seen to be relatively weak around the minima, Figure 9.30. As it also turns out that the variation of the optimum value for θ is a weak function of cone geometry, the following analysis is based on a constant value of θ, namely the average value for all the experimental configurations. With this average value of $\theta = 9.7^o$ the theoretical model is fully defined by Eqs. (9.44, 9.45, 9.69).

Table 9.6: *Measured steady-state forces in cutting of a plate by a cone, Muscat-Fenech, [83].*

Indentor semi-apex angle	δ mm	F_H kN	F_V kN	$k = F_H/F_V$
$\varphi = 15^o$	10	1.25	0.80	0.64
	20	1.30	0.90	0.69
	30	1.25	0.90	0.72
	40	1.35	0.90	0.67
	50	1.20	1.20	1.00
$\varphi = 22.5^o$	10	1.00	0.80	0.80
	20	1.30	1.00	0.77
	30	1.20	1.00	0.83
	40	1.60	1.30	0.81
	50	1.60	1.25	0.78
$\varphi = 30^o$	10	1.10	1.10	1.0
	20	1.10	1.10	1.0
	30	1.30	1.30	1.0
	40	1.70	1.70	1.0
	50	2.00	2.00	1.0

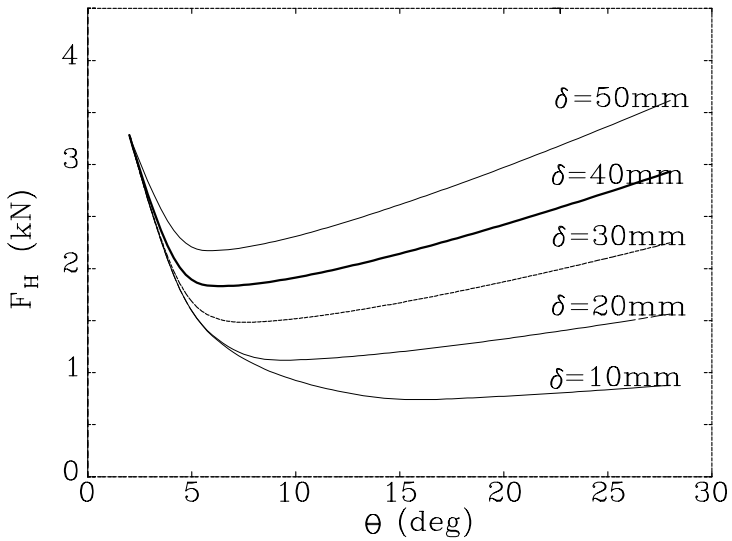

Figure 9.30: *Theoretical horizontal resistance of a cone with $\varphi = 22.5^o$ as a function of θ, at different levels of penetration.*

To verify the theoretical model for the friction factor, g, and the vertical to horizontal force ratio, k, Figure 9.31 compares measured and calculated values for k as a function of the cone semi-apex angle, φ.

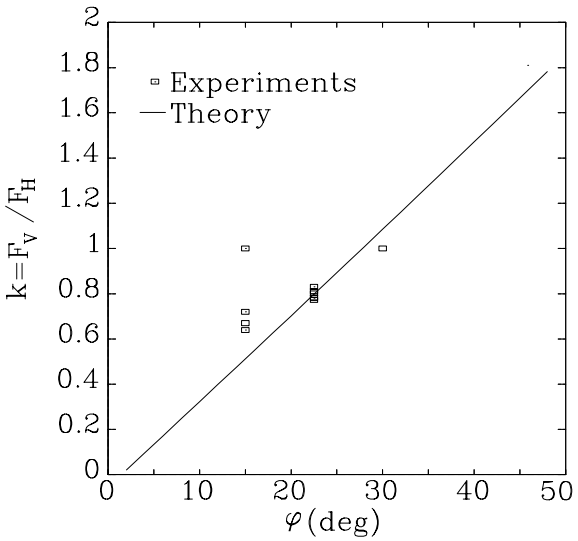

Figure 9.31: *Measured and calculated ratios of vertical to horizontal reaction force, k, vs. cone semi-apex angle, φ. $\theta = 9.7^o$ and $\mu = 0.3$.*

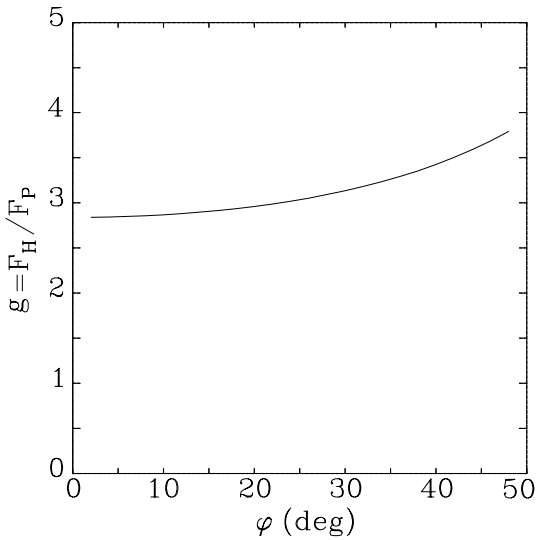

Figure 9.32: *Friction factor, g, vs. cone semi-apex angle, φ for $\theta = 9.7^o$ and $\mu = 0.3$.*

The theoretical curve in Figure 9.31 shows a steeper behaviour than the experimental data but the overall agreement is good. If the variation of plate split angle with penetration was taken into account, k would be an increasing function of penetration which does not seem to be the case for the experimental data of Table 9.6. A good prediction of the vertical to horizontal force ratio, k, as shown in Figure 9.31 indicates a good estimate of the point of attack for the forces on the cone. It is consequently reasonable to assume an equally good prediction of the friction factor, g. As shown in Figure 9.32 g is about 3 for $\theta \approx 10^o$ indicating a very significant contribution of friction.

Figures 9.33 - 9.38 show comparisons between measured and calculated horizontal and vertical forces. If the minimum resistance force was taken at all penetrations, the horizontal force in Figure 9.37 would vary between $0.73\,kN$ and $2.2\,kN$ (see Figure 9.30) instead of $1\,kN$ and $2.5\,kN$.

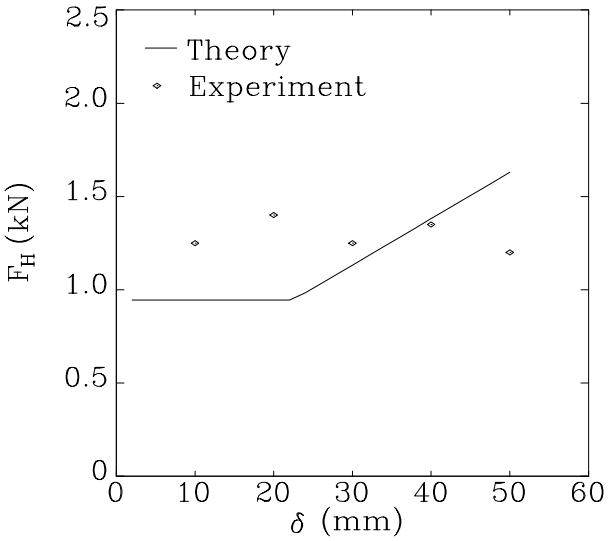

Figure 9.33: *Horizontal plate resistance force as a function of the penetration. The cone semi-apex angle is* $\varphi = 15^o$.

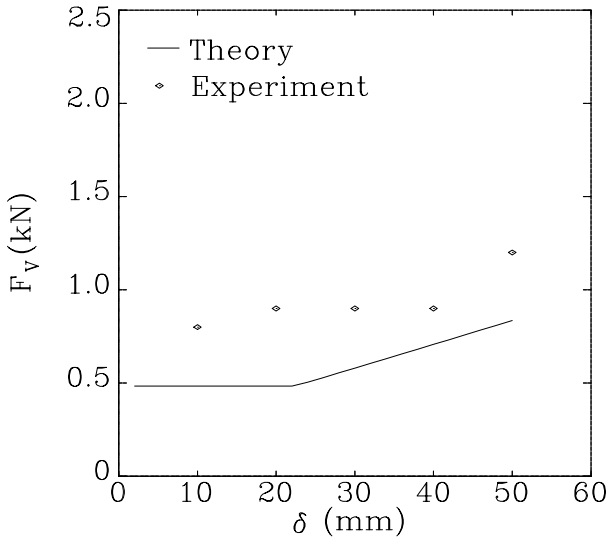

Figure 9.34: *Vertical plate reaction force as a function of the penetration. The cone semi-apex angle is* $\varphi = 15^o$.

Considering the complexity of the problem, the agreement between theory and experimental results is seen to be very good. Even the kink predicted by the theory can be observed in some of the tests. It is true to say that the present method for taking into account the interaction between the fracture process and the membrane deformation zone can be modified according to other hypotheses but it is seen to work well for the considered scale. Part of the reason why the theoretical model performs so well must be ascribed to the fact that most of the energy in plasticity and fracture is dissipated by the fracture process and the fracture toughness, R_c, was measured directly. With $g = 3$, friction accounts for two thirds of the energy, however, and thus friction is apparently predicted equally well. It would be interesting to see how well the theoretical model performs on a larger scale where the crack tip process is of minor importance. All in all it can be concluded that the major effects of plasticity, fracture and friction in the cutting of a plate by a cone has been quantified in a simple closed form mathematical model which gives excellent prediction of the vertical and the horizontal forces in model scale.

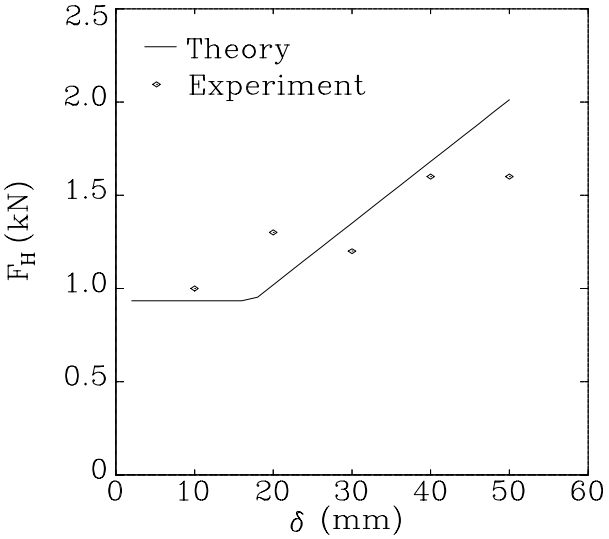

Figure 9.35: *Horizontal plate resistance force as a function of the penetration. The cone semi-apex angle is* $\varphi = 22.5^o$.

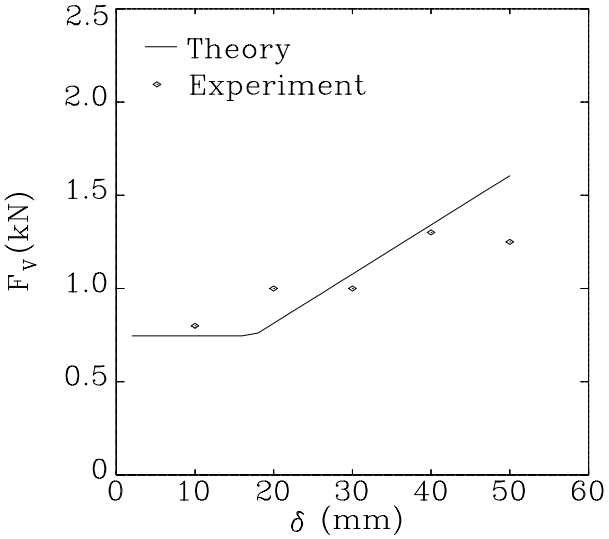

Figure 9.36: *Vertical plate reaction force as a function of the penetration. The cone semi-apex angle is* $\varphi = 22.5^o$.

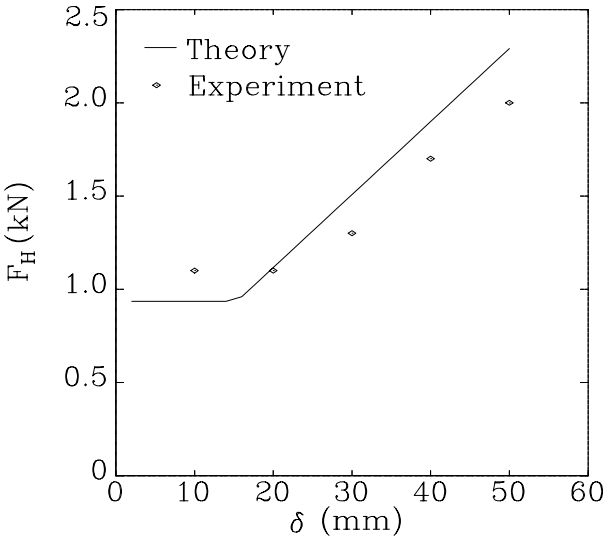

Figure 9.37: *Horizontal plate resistance force as a function of the penetration. Cone semi-apex angle is* $\varphi = 30^o$.

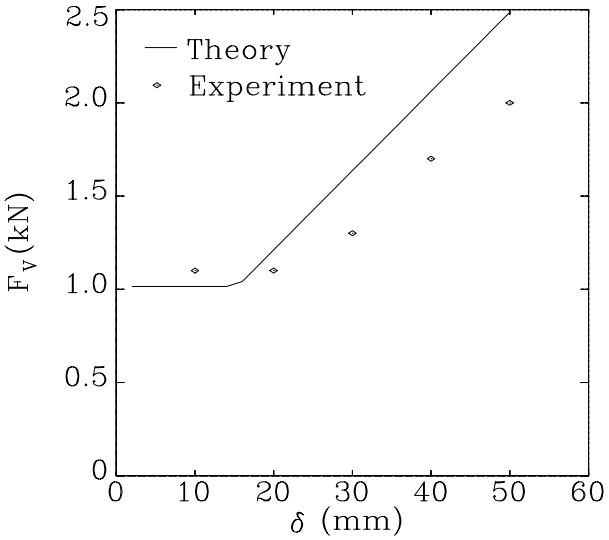

Figure 9.38: *Vertical plate reaction force as a function of the penetration. Cone semi-apex angle is* $\varphi = 30^o$.

9.9 Resistance of Longitudinal Members

Tests and accidental grounding events show that longitudinal members are twisted, bent and locally crushed during a grounding event. An example is given in Figure 9.39, which shows a photo of the bottom of the *Sea Empress* after a grounding event.

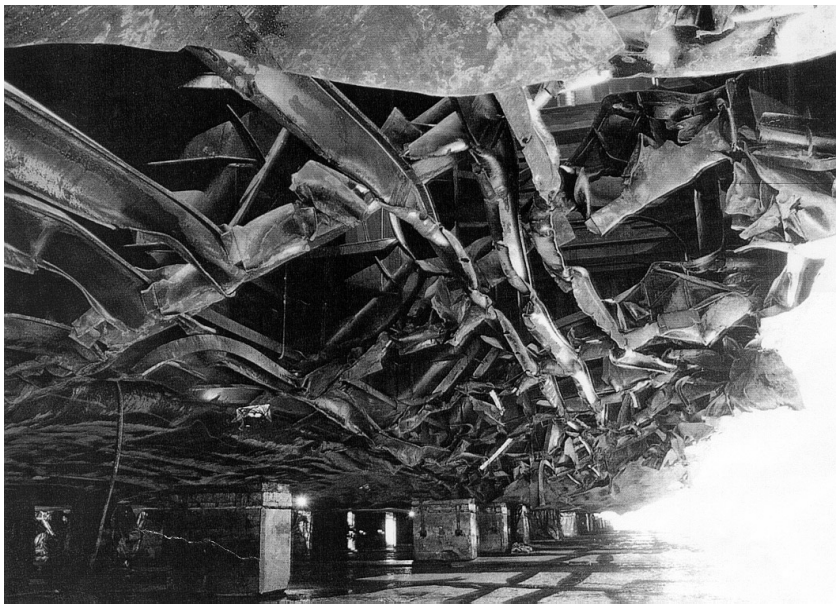

Figure 9.39: *Damage to the starboard side of the 'Sea Empress' after multiple grounding events on the rocks off Milford Haven, [23].*

The response of the longitudinals depends on their scantlings, boundary conditions and the nature of the load, so that formulation of a general theory for longitudinals becomes quite complicated. In this section, the grounding resistance of the three most typical types of longitudinal members is considered:

1. Web girder connecting the inner and outer bottom in a double bottom.
2. Longitudinal bulkhead.
3. Longitudinal stiffener attached to either outer or inner bottom.

All three types of longitudinal members can be seen in Figure 9.2.

9.9.1 Web Girders

When a longitudinal web girder is forced past the rock, it collapses and energy is dissipated in bending, membrane deformation and friction. For simplicity the following analysis considers

a bare unstiffened girder although - as it was illustrated by Figure 9.14 - the stiffening may have decisive influence on the grounding response.

The present approach is based on the assumption that the membrane deformation of the girder is the major energy-absorbing mechanism. Out-of-plane bending could easily be included as well but due to the high in-plane strains, the contribution would be small. The girder is mounted between the outer and inner bottoms which are both assumed to deform as illustrated in Figure 9.4. Figure 9.40 shows a longitudinal girder or bulkhead attached to the shell plating.

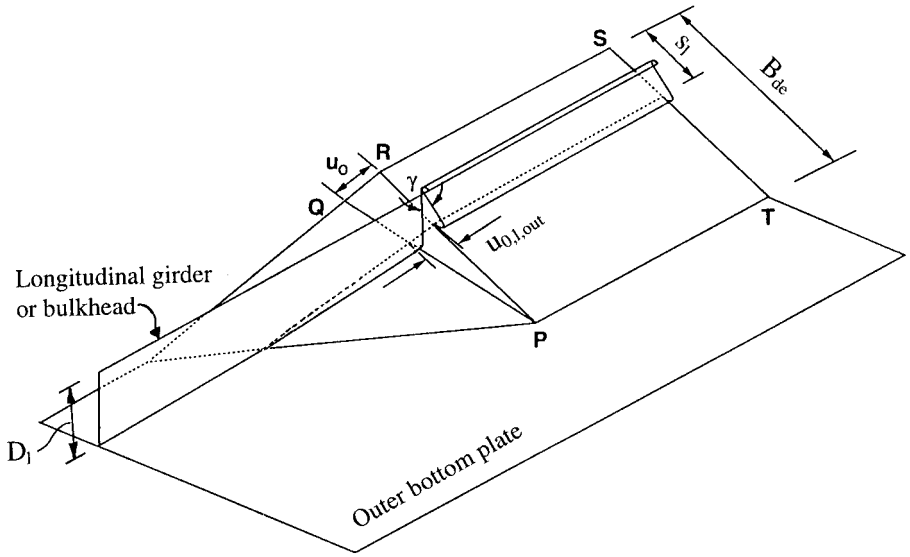

Figure 9.40: *Deformation mode of a longitudinal girder or bulkhead passing through the deformation zone. Deformation of the shell plating corresponds to the global deformation mode of Figure 9.4.*

As it is assumed that longitudinal fibres in the bottom plating are not stretched, fibres in a longitudinal web girder are not stretched either. Instead, the gap openings shown in Figure 9.40 are accommodated by shear straining as for the bottom plating. The average change in shear angle as a girder material element passes through the deformation zone is

$$[\gamma] = \frac{u_{0,l,out} - u_{0,l,inn}}{D_l} \tag{9.70}$$

where D_l is the height of a longitudinal girder (or the height of the deformation in a bulkhead), and $u_{0,l,out}$ and $u_{0,l,inn}$ are the longitudinal gap openings in the outer and inner hull platings in the position of the web girder, see Figure 9.40. Application of Eq. (6.10) with $\varepsilon_{\eta\xi} = \gamma/2$ and with $\varepsilon_{\xi\xi} = \varepsilon_{\eta\eta} = 0$ gives a mean jump in equivalent strain over the

deformation zone of $[\varepsilon_{eq}] = [\gamma]/\sqrt{3}$. Eq. (6.9) then gives the rate energy dissipation for the membrane deformation of the girder as

$$\dot{E}_l = \frac{\sigma_0}{\sqrt{3}}\, t_l\, D_l\, V\, [\gamma] = \frac{\sigma_0}{\sqrt{3}}\, t_l\, \left(u_{0,l,out} - u_{0,l,inn}\right)\, V \tag{9.71}$$

where t_l is the plate thickness of the web plating. The plastic resistance is now

$$F_{P,l} = \frac{\dot{E}_l}{V} = \frac{\sigma_0}{\sqrt{3}}\, t_l\, \left(u_{0,l,out} - u_{0,l,inn}\right) \tag{9.72}$$

and the associated horizontal and vertical forces can be calculated as $F_H = g\, F_P$ and $F_V = g\, k\, F_P$, where g and k are calculated from Eqs. (9.41, 9.42, 9.44, 9.45). The gap widths in the plating in the position of the considered longitudinal should be calculated depending on whether the plating has fractured. The transverse distance from the rock tip to the considered longitudinal is denoted s_l. According to Eq. (9.1), the gap width in the position of a longitudinal with the transverse coordinate s_l becomes

$$u_{0,l} = (B_{de} - s_l)\, \sqrt{(1-\cos\alpha)^2 \sin^2\theta + (1-\cos\theta)^2 \sin^2\alpha} \tag{9.73}$$

The angle, α, from horizontal to the plate flaps shown in Figure 9.4 depends on the fracture state of the plating. Before fracture, the deformation spreads out and after fracture the plate conforms to the rock. As discussed in Section 9.5 this is quantified by the 'flipping angle' as

$$\alpha = \begin{cases} \tan^{-1}\left(\delta_R / B_{de}\right) & \text{no fracture, i.e. } \delta_R < \delta_{frac} \\ \pi/2 - \varphi & \text{fracture, i.e. } \delta_R \geq \delta_{frac} \end{cases} \tag{9.74}$$

Before fracture, α remains relatively small, so the trigonometric functions can be accurately represented by their Taylor expansions. All in all, the gap width at the outer bottom, $u_{0,l,out}$, can then be calculated as

$$u_{0,l,out} = \begin{cases} 0 & \text{for } s_l \geq B_{de,out} \\ \dfrac{\delta_{R,out}(1 - s_l/B_{de,out})\cdot}{\sqrt{\frac{1}{4}\left(\delta_{R,out}/B_{de,out}\right)^2 \sin^2\theta + (1-\cos\theta)^2}} & \text{for } s_l < B_{de,out} \text{ and } \delta_{R,out} < \delta_{frac,out} \\ \dfrac{(B_{de,out} - s_l)\cdot}{\sqrt{(1-\sin\varphi)^2 \sin^2\theta + \cos^2\varphi (1-\cos\theta)^2}} & \text{for } s_l < B_{de,out} \text{ and } \delta_{R,out} \geq \delta_{frac,out} \end{cases} \tag{9.75}$$

where $\delta_{frac,out}$ is the penetration into the outer bottom causing rupture, $B_{de,out}$ is the width of the deformation in the outer bottom and $\delta_{R,out}$ is the rock tip penetration into the outer bottom. The gap width at the inner bottom in the position of the considered longitudinal girder is

$$u_{0,l,inn} = \begin{cases} 0 & \text{for } s_l \geq B_{de,inn} \\ \delta_{R,inn}(1 - s_l/B_{de,inn}) \cdot \\ \sqrt{\frac{1}{4}\left(\delta_{R,inn}/B_{de,inn}\right)^2 \sin^2\theta + (1-\cos\theta)^2} & \text{for } s_l < B_{de,inn} \text{ and } \delta_{R,inn} < \delta_{frac,inn} \\ (B_{de,inn} - s_l) \cdot \\ \sqrt{(1-\sin\varphi)^2 \sin^2\theta + \cos^2\varphi(1-\cos\theta)^2} & \text{for } s_l < B_{de,inn} \text{ and } \delta_{R,inn} \geq \delta_{frac,inn} \end{cases} \tag{9.76}$$

The plastic resistance of a longitudinal web girder can now be calculated from Eq. (9.72), Eq. (9.75) and Eq. (9.76). The associated horizontal and vertical forces can be calculated as $F_H = g\,F_P$ and $F_V = g\,k\,F_P$, where g and k are calculated from Eqs. (9.41, 9.42, 9.44, 9.45).

9.9.2 Longitudinal Bulkheads

The response of a longitudinal bulkhead is the same as in a longitudinal girder, except that the height is unlimited. The equations above can therefore be applied with $u_{0,l,inn} = 0$. The plastic resistance of a bulkhead is thus:

$$F_{P,l} = \frac{\dot{E}_l}{V} = \frac{\sigma_0}{\sqrt{3}}\, t_l\, u_{0,l,out} \tag{9.77}$$

and the associated horizontal and vertical forces can be calculated as $F_H = g\,F_P$ and $F_V = g\,k\,F_P$, where g and k are calculated from Eqs. (9.41, 9.42, 9.44, 9.45). The gap width $u_{0,l,out}$ is calculated from Eq. (9.75).

9.9.3 Longitudinals

Photographic evidence from accidental grounding events indicates that bending is the major energy-dissipating mechanism for longitudinal stiffeners. The overall mode of deformation for longitudinals was discussed in Section 9.2 (see p. 147) and it was shown in Section 9.5 how the average length of the deforming zone $\chi_{l,av}$ can be calculated.

According to the deformation mode shown in Figure 9.6, the deformation zone is assumed to consist of three moving hinges. The forward hinge changes the curvature of the undeformed longitudinal from 0 to $1/R$, the intermediate hinge reverses the curvature from $1/R$ to $-1/R$ and the aft hinge changes the curvature from $-1/R$ to 0. According to Eq. (6.11) the rate of internal energy dissipation for a longitudinal in this deformation mode becomes

$$\dot{E}_b = V \sum_{i=1}^{3} M_{0,l}^i [\kappa]^i \tag{9.78}$$

where V is the forward velocity and $M_{0,l}^i$, $[\kappa]^i$ is the fully plastic bending moment and the jump in curvature of the i'th hinge, respectively. During the deformation process, the longitudinals deform out of their original plane in the so-called tripping mode which changes the plastic bending moment capacity. Therefore, depending on this tripping deformation, the plastic bending moment might be different for each of the three moving hinges. In the following, it is assumed that the bending moment capacity is the same at each of the hinges and the longitudinal is assumed to lay down - trip - so that the bending moment of the longitudinal is minimised. The expression for the rate of energy dissipation then becomes

$$\dot{E}_b = V\, M_{0,l}\{[\kappa] + 2[\kappa] + [\kappa]\} = 4\, M_{0,l}\, [\kappa]\, V \tag{9.79}$$

With a length of the deforming zone equal to $\chi_{l,av}$, Eq. (9.3) and Eq. (9.78) give the rate of energy dissipation for bending of a longitudinal:

$$\dot{E}_b = 16\, V\, M_{0,l} \frac{\Delta_l}{\chi_{l,av}^2 + \Delta_l^2} \tag{9.80}$$

where Δ_l is the maximum lifting of the longitudinal in the plane of bending, see Figure 9.6. In the calculation of the fully plastic bending moment, $M_{0,l}$, it should be noted that as the shell plating is already in a state of full plastification it should not be fully included in the bending moment capacity. When the web of the longitudinal is perpendicular the bending moment capacity is minimum:

$$M_{0,l} = \frac{\sigma_0}{4} \left(t_f\, d_f^2 + \, D_w\, t_w^2 \right) \tag{9.81}$$

where d_f is the width of the flange, t_f is the thickness of the flange, D_w is the height of the web and t_w is the thickness of the web. Brackets are normally mounted to the longitudinals to prevent tripping but they do not prevent tripping under the extreme deformations considered here, see Figure 9.39.

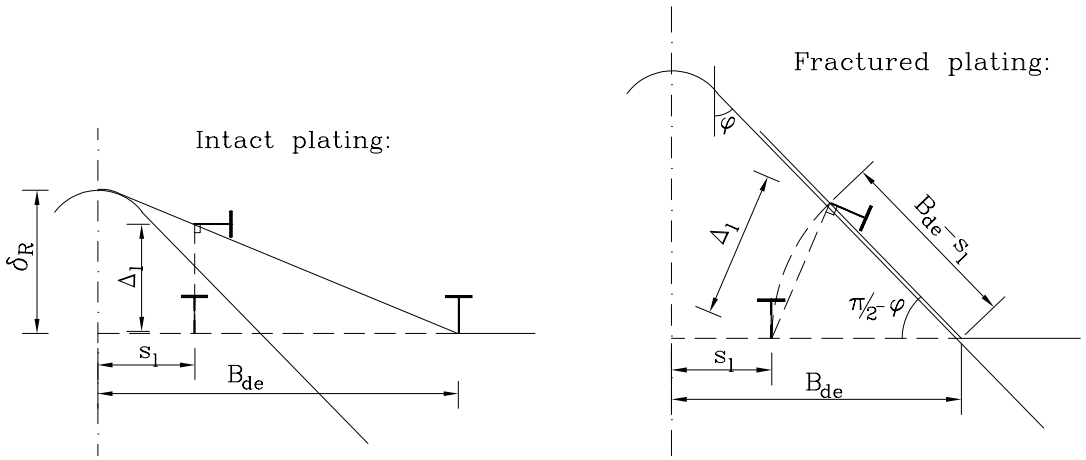

Figure 9.41: *Lifting of a longitudinal for intact and fractured bottom plating respectively.*

To derive the final expressions for the plastic resistance, consider first the state before fracture, i.e. $\delta_R < \delta_{R,frac}$. Figure 9.41 shows the mode of deformation in a transverse section. As the shell plating is stretched, the longitudinal is displaced vertically upwards.

According to the deformation mode shown in Figure 9.41, the lifting of a longitudinal is

$$\Delta_l = \delta_R \frac{(B_{de} - s_l)}{B_{de}} = \delta_R \left(1 - s_l/B_{de}\right) \tag{9.82}$$

The plastic resistance can now be expressed as

$$F_P = \frac{4\,\sigma_0\,\delta_R\,\left(1 - s_l/B_{de}\right)\left(t_f\,d_f^2 + D_w\,t_w^2\right)}{\delta_R^2\left(1 - s_l/B_{de}\right)^2 + \chi_{l,av}^2} \tag{9.83}$$

and the horizontal and vertical forces can be calculated as $F_H = g\,F_P$ and $F_V = g\,k\,F_P$, where g and k are calculated from Eqs. (9.41, 9.42).

After the bottom plating has fractured, $\delta_R > \delta_{R,frac}$, the plate is assumed to conform to the rock. Figure 9.41 shows the deformation mode in a transverse section.

The lifting, Δ_l, in the plane of the bending is

$$\Delta_l = 2\,\left(B_{de} - s_l\right)\tan\left(\frac{\pi}{4} - \frac{\varphi}{2}\right) \tag{9.84}$$

so the plastic resistance of the longitudinal becomes

$$F_P = \frac{8\,\sigma_0\,(B_{de}-s_l)\left(t_f\,d_f^2+\,D_w\,t_w^2\right)\tan\left(\frac{\pi}{4}-\frac{\varphi}{2}\right)}{4(B_{de}-s_l)^2\,\tan^2\left(\frac{\pi}{4}-\frac{\varphi}{2}\right)+\chi_{l,av}^2} \tag{9.85}$$

and the horizontal and vertical forces can be calculated as $F_H = g\,F_P$ and $F_V = g\,k\,F_P$ where g and k are calculated from Eqs. (9.44, 9.45).

9.10 Resistance of Transverse Members

For relatively large ships the transverse stiffening structure attached to the bottom shell plating is primarily bulkheads, deep frames in single bottom ships and solid floors in double bottom ships. Examples of solid floors in a double bottom ship are seen in Figure 9.2 and Figure 9.42 shows the transverse framing in a longitudinally stiffened single hull ship.

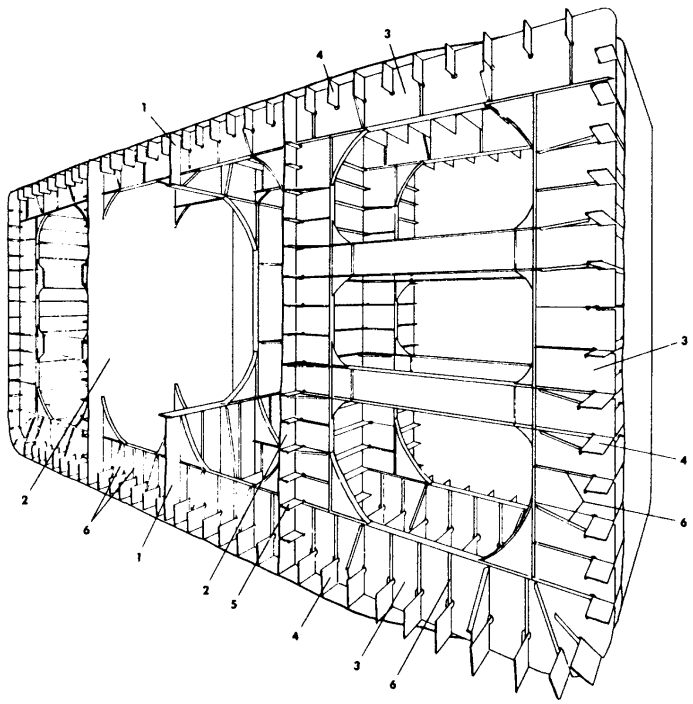

Figure 9.42: *Example of transverse frames in a single hull ship, [44].*

These transverse components are seldom just bare plates but are normally fitted with stiffeners or reduced by cutouts for weight saving or pipe tunnels. As for longitudinal girders and bulkheads, the secondary stiffeners may have significant influence on the structural

response. When well engineered, they increase the energy absorption of the components but bad designs introduce hard points and induce early fracture, see Figure 9.14. For the present analysis the transverse is assumed to be a bare homogenous plate. The basic deformation mode is depicted in Figure 9.43 and it is seen to be fully compatible with the plate deformation mode shown in Figure 9.3.

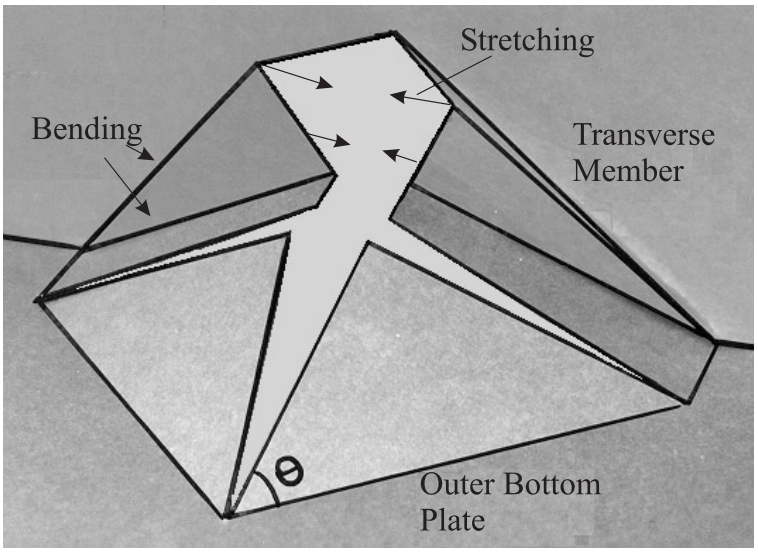

Figure 9.43: *Assumed deformation mode for transverse structures. The bottom plating follows the global deformation mode shown in Figure 9.4.*

Theoretical and experimental investigation of the response of a web girder was previously conducted at MIT, see [29], [30], [34], [138]. In the work by Wierzbicki and Simonsen, [139], the geometric description of the girder folding was simplified and the idea of the mean crushing force with respect to the deformation depth $2H_t$ was adapted. The present work is a further development of the analysis [139] as the geometric description is enhanced, theory is compared to experiments, girders of finite depth are considered and fracture is included.

Figure 9.43 shows that the energy-absorbing mechanisms are again bending and membrane deformation and possibly fracture. As the component is deformed by an indentor moving in the longitudinal direction friction is also present.

For unfractured plating, the gap width shown in Figure 9.43 illustrates necessary membrane straining of the material. It is seen that this gap width is largest in the middle of the buckle, and it is even larger here than in the plating. This simple model therefore helps to explain the experimental evidence, [106], that transverse members may serve as crack initiators.

9.10.1 Energy Dissipation in Plastic Deformation

Below, the plastic resistance is derived for a girder with a flange being deformed at the midspan, Figure 9.44.

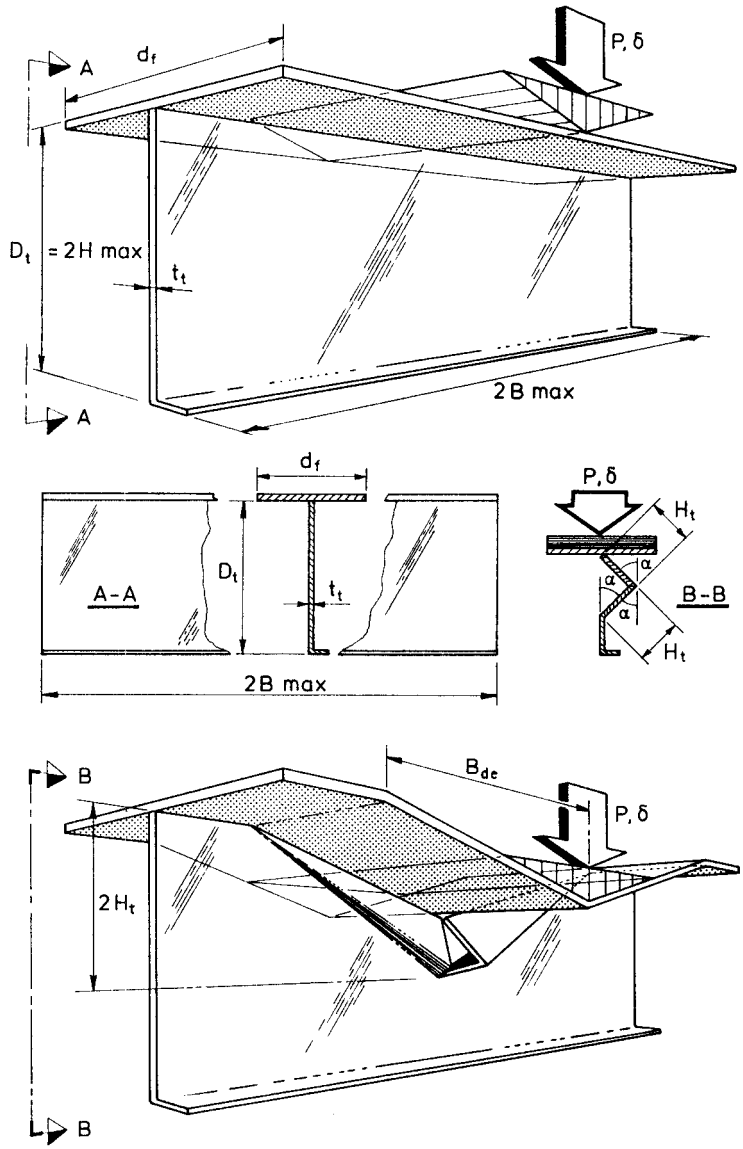

Figure 9.44: *Definition sketch for crushing of a web girder. In a grounding scenario the penetration and the crushing force are in a direction opposite to that shown here.*

The deformation is idealised by 6 hinge lines and a membrane deformation zone. The deformation takes place within an area of $2B_{de}$ by $2H_t$. The maximum possible extent of the deformation is given by the boundaries and is equal to $2B_{max}$ by $2H_{max}$. The wave length of the plastic buckle is $2H_t$ so, when the deformation of the first fold is fully exhausted, the penetration depth is $\delta = 2H_t$.

Global equilibrium can be expressed by the principle of virtual work:

$$P\,\dot{\delta} = \dot{E}_b + \dot{E}_m \tag{9.86}$$

where indices b and m indicate bending and membrane deformation respectively. The mean crushing force, P_m, can be found from the total energies at the end of the deformation process when $\delta = 2H_t$:

$$P_m\,2H_t = E_b + E_m \tag{9.87}$$

The bending hinge lines each have a length of approximately B_{de} so, with a plastic bending moment per unit length of $M_0 = \sigma_0 t^2/(2\sqrt{3})$, the rate of energy dissipation for the bending becomes

$$\dot{E}_b = 8\,M_0\,B_{de}\,\dot{\alpha} \tag{9.88}$$

where α is the angle of bending, see Figure 9.44. Penetration depth and bending angle are geometrically related as $\delta = 2H_t(1-\cos\alpha)$. Hence, the rate of the bending angle becomes

$$\dot{\alpha} = \frac{\dot{\delta}}{2\,H_t}\left(1 - \left(1 - \frac{\delta}{2H_t}\right)^2\right)^{-1/2} \tag{9.89}$$

Integration of Eq. (9.88) up to the point where the first fold is fully exhausted ($\alpha = \pi/2$) gives a total bending energy of

$$E_b = 4\,\pi\,M_0\,B_{de} \tag{9.90}$$

For the membrane deformation, only direct strains in the transverse direction are considered so the rate of energy dissipation for this process can be expressed as

$$\dot{E}_m = \int_S \sigma_0\,t_t\,\dot{\varepsilon}_{yy}\,ds \tag{9.91}$$

where $S = 4H_tB_{de}$ in the area of deformation. For the flange and the upper fibre in the web, the strain and the strain rate can according to the theory of moderately large deflections, be calculated as

$$\varepsilon_{yy,f} = \frac{1}{2}\left(\frac{\delta}{B_{de}}\right)^2 \tag{9.92}$$

$$\dot{\varepsilon}_{yy,f} = \frac{\delta\,\dot{\delta}}{B_{de}^2} \tag{9.93}$$

When the deformation mode is fully exhausted at $\delta = 2H_t$, the gap width from the plate flap edge to the midspan is constant and equal to $B_{de}\varepsilon_{yy,f}$ between the two upper hinge lines and zero at the lower hinge line. The average gap width and the average strain are therefore only 3/4 of the values at the upper fibre. With an average strain rate of $\dot{\varepsilon}_{yy,av} = 3/4\,\dot{\varepsilon}_{yy,f}$, the rate of membrane energy dissipation for the entire zone of deformation becomes

$$\dot{E}_m = 4B_{de}H_t\sigma_0 t_t\dot{\varepsilon}_{yy,av} = \frac{3\sigma_0 t_t H_t\delta\,\dot{\delta}}{B_{de}} \tag{9.94}$$

When the fold is completely folded at $\delta = 2H_t$ the energy absorbed by the membrane deformation is

$$E_m = \frac{6\,\sigma_0\,t_t\,H_t^3}{B_{de}} \tag{9.95}$$

For comparison of the theory with experiments performed at MIT, the flange shown in Figure 9.44 has to be included in the theory. With a strain and strain rate given by Eqs. (9.92, 9.93) and a volume of deformation of $2B_{de}d_f t_f$, the rate of energy dissipation and the total deformation energy at $\delta = 2H_t$ becomes

$$\dot{E}_{m,f} = 2\,\frac{\sigma_0\,t_f\,d_f\,\delta}{B_{de}}\,\dot{\delta} \tag{9.96}$$

$$E_{m,f} = 4\,\frac{\sigma_0\,t_f\,d_f\,H_t^2}{B_{de}} \tag{9.97}$$

The instantaneous and the mean crushing forces can now be expressed as

$$P = \frac{\dot{E}_b + \dot{E}_m + \dot{E}_{m,f}}{\dot{\delta}} = \frac{4\,M_0\,B_{de}}{H_t\sqrt{1-\left(1-\frac{\delta}{2H_t}\right)^2}} + \frac{3\,\sigma_0\,t_t\,H_t\,\delta}{B_{de}} + \frac{2\,\sigma_0\,t_f\,d_f\,\delta}{B_{de}} \tag{9.98}$$

$$P_m = \frac{E_b + E_m + E_{m,f}}{2\,H_t} = \frac{2\,\pi\,M_0\,B_{de}}{H_t} + \frac{3\,\sigma_0\,t_t\,H_t^2}{B_{de}} + 2\,\frac{\sigma_0\,t_f\,d_f\,H_t}{B_{de}} \tag{9.99}$$

The values of H_t and B_{de} are yet to be determined. The experiments performed at MIT indicate that once a deformation mode is initiated, the hinges are stationary until the mode is exhausted. In the tests at MIT the deformation was seen to extend all the way to the vertical boundaries ($B_{de} = B_{max}$), but not all the way to the horizontal boundary as $2H_t$ was only about 2/3 of the depth of the girder. This indicates that the deformation in general extends at least to one boundary. The present approach is then based on the idea that the deformation buckle extends to one boundary, and that the extent in the other direction adjusts itself so that the mean indentation force is minimised as given by Eq. (9.99). On the assumption that the deformation extends over the depth of the girder ($H_t = H_{max}$) the width of deformation, B_{de}, which minimises the mean crushing force, is

$$\left.\frac{\partial\,P_m}{\partial\,B_{de}}\right|_{H_t=H_{max}} = 0 \qquad \Rightarrow \tag{9.100}$$

$$B_{opt} = H_{max}\sqrt{\frac{\sqrt{3}}{\pi}\left(3\,\frac{H_{max}}{t_t} + \frac{2\,d_f\,t_f}{t_t^2}\right)} \tag{9.101}$$

Likewise, if the deformation extends all the way to the vertical boundaries, the depth of deformation minimising the mean crushing force can be found by minimisation of Eq. (9.99) with respect to H_t. In this case, however, the deformation of the flange is completely kinematically defined so the minimisation should only be performed for the energy absorption in the girder, i.e. for the first two terms in Eq. (9.99). Minimising these with respect to H_t for $B_{de} = B_{max}$ gives a half folding wave length of

$$H_{opt} = \left(\frac{\pi}{6\sqrt{3}}B_{max}^2\,t_t\right)^{1/3} = B_{max}\left(\frac{\pi}{6\sqrt{3}}\,\frac{t_t}{B_{max}}\right)^{1/3} \tag{9.102}$$

The procedure for finding the extent of the deformation ($2H_t, 2B_{de}$) is then to compare the optimum values with the maximum possible values defined by the boundaries:

$$H_t = min\,(H_{max}, H_{opt}) \tag{9.103}$$

$$B_{de} = min\,(B_{max}, B_{opt}) \tag{9.104}$$

When the deformation extends to the vertical boundary, $H_t = H_{max}$, Eq. (9.99) and Eq. (9.101) give the mean crushing force

$$P_m = 2\sqrt{\left(\pi/\sqrt{3}\right)}\sigma_0\, t_t^{3/2}\, H_{max}^{1/2}\, \sqrt{3 + 2\frac{t_f\, d_f}{t_t\, H_{max}}} \tag{9.105}$$

With no flange the mean resistance of the transverse becomes $P_m = 4.67\,\sigma_0\, t^{3/2}\, H_{max}^{1/2}$. If the deformation extends to the vertical boundaries, the deformation is defined by $B_{de} = B_{max}$ and $H_t = H_{opt}$ and the mean crushing force up to a penetration of $\delta = 2\,H_{opt}$ is given by Eq. (9.99) and Eq. (9.102):

$$P_m = 4.05\,\sigma_0\, t_t^{5/3}\, B_{max}^{1/3} + 1.34\,\sigma_0\, t_f\, d_f\, \left(\frac{t_t}{B_{max}}\right)^{1/3} \tag{9.106}$$

9.10.2 Comparison to Experiments

The problem of web crushing was extensively investigated at MIT. Main data of the experiments is given in Table 9.7.

Table 9.7: *Main data of web crushing experiments performed at MIT. The flow stress was determined from a calculated mean strain and a uniaxial tension test, [29].*

Yield stress, σ_y	175 MPa
Flow stress, σ_0	236 MPa
Girder depth, $D = 2H_{max}$	41.7 mm
Half girder width, $B_{max} = 2H_{max}$	83.4 mm
Flange width, d_f	41.7 mm
Plate thickness, $t_t = t_f$	0.737 mm

First, to find whether the deformation extends to the sides or to the horizontal boundary, insert into Eqs. (9.101, 9.102):

$$B_{opt} = 217.9\ mm$$
$$H_{opt} = 11.6\ mm$$

With $B_{max} = 83.4\ mm$ and $H_{max} = 20.85\ mm$ this means that the deformation should extend to the sides, $B_{de} = B_{max} = 83.4\ mm$, but not all the way to the horizontal boundary, $H_t = H_{opt} = 11.6\ mm$. Comparison to the experimental results of Choi et al., [29], reveals a surprisingly good agreement, as the experiments showed that the girder was stretched all the way to the sides and the depth of deformation was about 2/3 of the girder depth, in other words, $B_{de} = B_{max} = 83.4\ mm$, $H_t = 13.9\ mm$. In the theoretical model presented previously by Choi et al, [29] and [30], the depth of the deformation was taken from the experimental observations to be one third of the girder depth, $H_t = D/3 = 13.9\ mm$. Obviously, it is highly advantageous to be able to *calculate* the extent of the deformation from minimisation rather than assume it.

Now given $B_{de} = B_{max}$ and $H_t = H_{opt}$, the instantaneous and the mean crushing forces can be calculated from Eq. (9.98) and Eq. (9.106), respectively. The mean crushing force becomes

$$P_m = 4520\ N \tag{9.107}$$

Figure 9.45 shows a comparison between the force measurements reported in [30] and the calculated crushing forces from Eq. (9.98) and Eq. (9.106).

During the initial stage of deformation, the rate of energy dissipation for the bending decreases from infinity (see Eq. (9.89)) so the theoretical model does not capture this first part of the process accurately. The problem could be solved by introducing an initial plate imperfection or by considering the elastic buckling limit but, for the present analysis, it is irrelevant as the energy of this first phase is small. The agreement for the remaining part of the process is seen to be excellent with a slight tendency of overestimation by theory. By choosing a lower flow stress (for example 180 MPa as in [30]) a perfect agreement can be obtained but as seen, it is not necessary for validation of the model. In conclusion, the proposed mathematical model is assumed to be sufficiently accurate for further development and application to the theoretical grounding model.

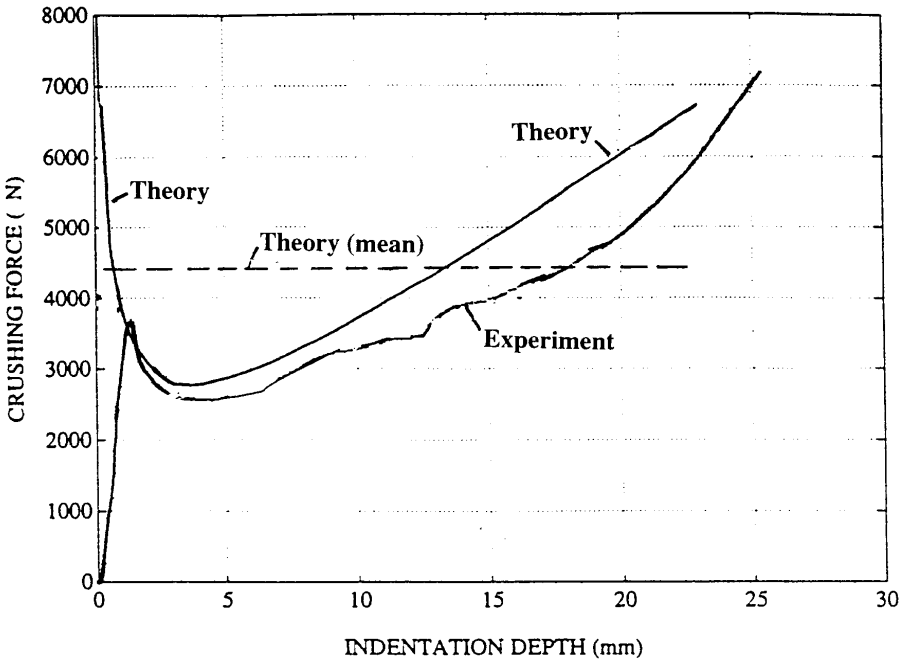

Figure 9.45: *Comparison between measured and calculated crushing forces for a web girder.*

9.10.3 Subsequent Folding and Members of Limited Height

As the transverse is deformed beyond the first fold, subsequent buckles are formed. Figure 9.46 shows a photo of a solid floor in a double bottom deformed by a conical rock and several folds are seen. At the midspan of the girder the rock tip has penetrated past the inner bottom, leaving the floor in a state of complete compression.

As seen from the example of the previous section and as seen in Figure 9.46, the deformation extends to the side boundaries, even for very shallow girders. The following developments are therefore based on the assumption that the half width and depth of the deformation are respectively $B_{de} = B_{max}$ and $H_t = H_{opt}$. As the energy dissipation of the plating is considered separately elsewhere, the flange which was included in the theory above is not considered in the following. The flange is only deformed in membrane straining and has no influence on the deformation mode of the girder so it could very easily be included later if web crushing was to be analysed.

The theory derived above is valid only up to the point of total compression of the first fold. As this height is quite limited the theory has to be extended to cover the response in the process of forming subsequent folds. At some level of penetration, the material ruptures and instead of membrane deformation, fracture is the major energy-dissipating mechanism.

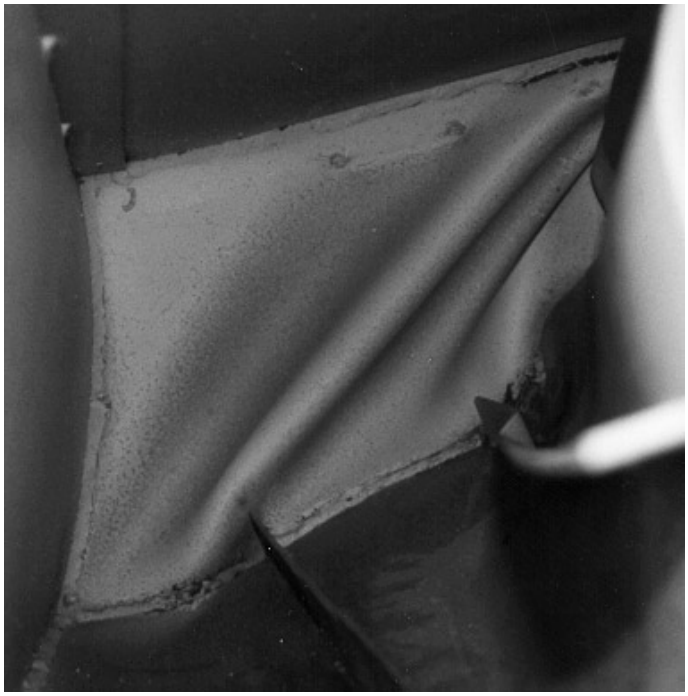

Figure 9.46: *Floor in a double bottom after grounding on a conical rock. From the 1:5 scale test series performed by the NSWC, USA, [106].*

After the first fold has been formed, $\delta = 2\,H_{opt}$ the maximum strain is approximately

$$\varepsilon_{max} = \frac{1}{2}\left(\frac{\delta}{B_{max}}\right)^2 = \frac{1}{2}\left(\frac{2H_{opt}}{B_{max}}\right)^2 \approx 0.9\left(\frac{t_t}{B_{max}}\right)^{2/3} \tag{9.108}$$

where H_{opt} was given by Eq. (9.102). For the example shown in Figure 9.46, plate thickness and floor width were $t_t = 3\ mm$ and $B_{max} = 1.27\ m$ respectively. These values give a maximum strain of $\varepsilon_{max} = 0.016$. Although local strains are larger there is a large reserve before fracture and so - as seen - subsequent folds will form.

To derive the theory for subsequent folding, consider first a girder of infinite depth. The basic assumption is that the subsequent folds have the same geometry as the first, depicted in Figure 9.43. When a fold is deformed beyond its total collapse it only dissipates energy in membrane straining so if the deformation extends over several folds, the bending energy can be neglected as a good approximation. With the optimum buckle depth, H_{opt}, from Eq. (9.102) and retaining only the second term in Eq. (9.98), the crushing resistance of the girder becomes

$$P = \frac{3\,\sigma_0\,t_t\,\delta}{B_{max}}\,B_{max}\left(\frac{\pi}{6\sqrt{3}}\,\frac{t_t}{B_{max}}\right)^{1/3} = 2.0\,\sigma_0\,t_t^2\left(\frac{B_{max}}{t_t}\right)^{2/3}\,\frac{\delta}{B_{max}} \tag{9.109}$$

The load is seen to be proportional to the penetration as for a plastic string. The non-dimensional load can be defined from Eq. (9.109) as

$$\bar{P} = \frac{P}{2.0\,\sigma_0\,t_t^2\,\left(\frac{B_{max}}{t_t}\right)^{2/3}} \tag{9.110}$$

According to the idea of folds being subsequently formed and strained during the progressive folding process, the force-penetration relationship up to the folding of the N'th fold can be expressed as

$$\bar{P} = \begin{cases} \frac{1}{B_{max}}\delta & \text{in first fold, } 0 < \delta < 2H_t \\ \frac{1}{B_{max}}(\delta + \delta - 2\,H_t) & \text{in second fold, } 2H_t < \delta < 4H_t \\ \frac{1}{B_{max}}(\delta + \delta - 2\,H_t + \delta - 4\,H_t) & \text{in third fold, } 4H_t < \delta < 6H_t \\ \frac{N}{B_{max}}(\delta - (N-1)\,H_t) & \text{in } N'\text{th fold, } 2(N-1)\,H_t < \delta < 2\,N\,H_t \end{cases} \tag{9.111}$$

This successive inclusion of new material in the stretching area gives a piecewise linear behaviour of the force as depicted in Figure 9.47.

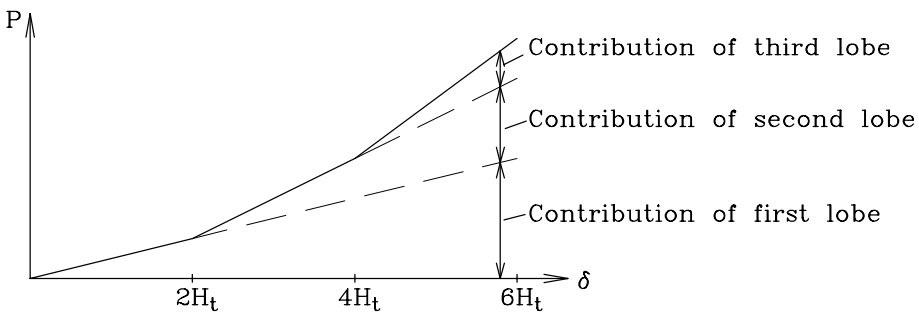

Figure 9.47: *Force penetration relationship as new folds are formed. Neglecting bending deformation gives piecewise linear behaviour.*

For deformation over several buckles the number of buckles is most conveniently taken to be a continuous function of the penetration, $N = \delta/(2\,H_t)$. For transverse components limited in the vertical extent by their height, D_t, such as the frame in Figure 9.42 or the floor in Figure 9.46, the maximum number of folds is $N = D_t/(2H_t)$. With this formulation it is now possible to consider a component of limited height simply by limiting the number of buckles formed and contributing to the resistance:

$$N = \begin{cases} \frac{\delta}{2\,H_t} & \text{for } \delta \le D_t \\ \frac{D_t}{2\,H_t} & \text{for } \delta > D_t \end{cases} \tag{9.112}$$

Inserting Eq. (9.112) into Eq. (9.111) now gives the crushing force as a function of penetration in a very convenient form for components of arbitrary height, D_t:

$$\bar{P} = \begin{cases} \frac{1}{B_{max}} \left\{ \frac{\delta^2}{4\,H_t} + \frac{\delta}{2} \right\} & \text{for } \delta < D_t \\ \frac{1}{B_{max}} \left\{ \frac{D_t\,\delta}{2\,H_t} + \frac{D_t}{2} - \frac{D_t^2}{4\,H_t} \right\} & \text{for } \delta \geq D_t \end{cases} \tag{9.113}$$

The force is seen to increase parabolically up to $\bar{P} = D_t^2/(4H_t) + D_t/2$ at $\delta = D_t$ and it then increases linearly from there, see also Figure 9.47.

Eq. (9.113) can be integrated to give the energy dissipation in the unfractured plating corresponding to a rock penetration of δ_R:

$$\begin{aligned} \bar{E}_t &= E_t / \left(2.0\,\sigma_0\,t_t^2 \left(\frac{B_{max}}{t_t} \right)^{2/3} \right) \\ &= \int_0^{\delta_R} \bar{P}\,d\delta \\ &= \begin{cases} \frac{1}{B_{max}} \left[\frac{\delta_R^3}{12 H_t} + \frac{\delta_R^2}{4} \right] & \text{for } \delta_R \leq D_t \\ \frac{1}{B_{max}} \left[\frac{D_t^3}{12 H_t} - \frac{D_t^2}{4} + \frac{D_t \delta_R^2}{4 H_t} + \left(\frac{D_t}{2} - \frac{D_t^2}{4 H_t} \right) \delta_R \right] & \text{for } \delta_R > D_t \end{cases} \end{aligned} \tag{9.114}$$

9.10.4 Resistance of a Fractured Transverse

It was observed by Rodd and MacCampbell, [106], that once a fracture is initiated it rapidly travels from the shell plating to the transverse and vice verse. Hence, the fracture criterion for the transverse is here assumed to be the same as for the shell plating. It is assumed that when the transverse component has fractured a crack extends as far into the member as the rock tip. Due to the rupture the transverse opens up as illustrated by the gaps in Figure 9.43. Expressed by the fracture toughness, R_c, the energy to form the crack is

$$E_c = \begin{cases} R_c t \delta_R & \text{for } \delta_R \leq D_t \\ R_c t D_t & \text{for } \delta_R > D_t \end{cases} \tag{9.115}$$

Eq. (9.115) represents a first estimate of the energy absorbed by the transverse. As shown in Section 9.8 about plate resistance after fracture, some additional membrane straining which is neglected here should be taken into account. On the assumption of the same type of deformation with six hinge lines per fold and the same length of the folds, H_t, the bending energy is

$$E_b = 4\,\pi\,M_0\,B_{max}\,N \tag{9.116}$$

where the number of folds is given by Eq. (9.112).

9.10.5 Application to Theoretical Grounding Model

Eq. (9.113) gives the force-penetration relationship for crushing of a transverse component of height D_t before fracture is induced. The load considered was moving in the plane of the plate so it would be the type of load experienced in a stranding scenario. For a longitudinal bottom raking process, however, the rock moves in the perpendicular (longitudinal) direction, so the indentation into the transverse is a result of lifting of longitudinals and inclined faces of the rock. Despite these apparent differences in the origin of the load, the results derived above can be applied consistently to the present grounding analysis.

Consider any transverse member which, at a rock indentation of δ_R, has absorbed the energy E_t after passage of the rock. This energy is dissipated over a certain length which could conveniently be taken to be the distance between transverse members, χ_t. The time it takes to dissipate this energy is then $\Delta t = \chi_t / V$, so the mean rate of plastic energy dissipation due to the deformation of the transverse becomes

$$\dot{E}_t = \frac{E_t}{\Delta t} = \frac{E_t}{\chi_t} V \tag{9.117}$$

The so-called plastic force (see Eq. (6.1)) is consequently

$$F_P = \frac{E_t}{\chi_t} \tag{9.118}$$

and the associated horizontal and vertical forces can be calculated as $F_H = g\, F_P$ and $F_V = g\, k\, F_P$, where g and k can be calculated from Eqs. (9.41 9.42, 9.44, 9.45).

By application of Eqs. (9.118, 9.114), the plastic force before fracture can now be expressed as

$$F_P = \frac{E_t}{\chi_t} = \frac{2.0\, \sigma_0\, t_t^2}{\chi_t\, B_{max}} \left(\frac{B_{max}}{t_t} \right)^{2/3} \left[\frac{\delta_R^3}{12 H_t} + \frac{\delta_R^2}{4} \right] \qquad \text{for } \delta_R \leq D_t \tag{9.119}$$

and the plastic resistance after fracture is given by

$$F_P = \frac{2.0\, \sigma_0\, t_t^2}{\chi_t\, B_{max}} \left(\frac{B_{max}}{t_t} \right)^{2/3} \left[\frac{D_t^3}{12 H_t} - \frac{D_t^2}{4} + \frac{D_t \delta_R^2}{4 H_t} + \left(\frac{D_t}{2} - \frac{D_t^2}{4 H_t} \right) \delta_R \right] \text{ for } \delta_R > D_t \tag{9.120}$$

The half folding wave length is taken to be the optimum wave length, given the width of the deformation zone, i.e.

$$H_t = H_{opt} = \left(\frac{\pi}{6\sqrt{3}} B_{max}^2\, t_t\right)^{1/3} = B_{max}\left(\frac{\pi}{6\sqrt{3}}\,\frac{t_t}{B_{max}}\right)^{1/3}. \tag{9.121}$$

The associated horizontal and vertical forces can be calculated as $F_H = g\,F_P$ and $F_V = g\,k\,F_P$, where g and k can be calculated from Eq. (9.41) and Eq. (9.42).

From Eqs. (9.118, 9.115, 9.116) the plastic resistance force for a fractured transverse member becomes

$$F_P = \frac{E_c + E_b}{\chi_t} = \begin{cases} \left(R_C\, t_t + \frac{2\,\pi\, M_0\, B_{max}}{H_t}\right)\frac{\delta_R}{\chi_t} & \text{for } \delta_R \le D_t \\ \left(R_C\, t_t + \frac{2\,\pi\, M_0\, B_{max}}{H_t}\right)\frac{D_t}{\chi_t} & \text{for } \delta_R > D_t \end{cases} \tag{9.122}$$

where H_t is calculated from Eq. (9.121). The associated horizontal and vertical forces can be calculated as $F_H = g\,F_P$ and $F_V = g\,k\,F_P$, where g and k are given by Eq. (9.44) and Eq. (9.45). The resistance is seen to be a linear function of penetration up to a penetration corresponding to the depth of the girder. For larger penetration the transverse offers no additional resistance.

This page is intentionally left blank

Chapter 10

Verification of Theoretical Hard Grounding Model

A full verification of the theoretical model presented in the previous three chapters would require an extensive effort in the sense that the number of theoretical elements to verify is large and in the sense that performing full-scale grounding experiments is extremely labour and cost intensive. Parts of the theoretical model were already compared to experiments, however, and good agreement was found in the specific paragraphs concerning:

1. Plate cutting by a wedge in Chapter 8.
2. Punch plate deformation and fracture in Section 9.3.
3. Extent of deformation and penetration to fracture in Section 9.5.
4. Plate resistance before fracture in Section 9.7.
5. Plate resistance after fracture in Section 9.8.
6. Resistance of transverse members in Section 9.10.

The present chapter is devoted to verification of the theory for an assembled ship bottom structure. In the first part, the 1:5 scale grounding tests of the Naval Surface Warfare Centre, Carderock Division, USA, are considered. The idea behind these tests is to force an assembled ship bottom structure over a rock in a horizontal fixed-pitch motion, so the coupling of the damage process to the heave, roll and pitch motion is excluded. As discussed earlier, it is difficult to scale the energy absorption of a process like the present in which there is both plastic flow and fracture. The idea here is, however, that if the theory performs well in a scale of 1:5, it also works in full scale.

In the second part of the chapter, the accidental grounding of a large oil tanker on a reef off the coast of Singapore in 1973 is reconstructed by use of the theoretical model.

Refer to [110] for further validation and for application in terms of calculation of probabilistic extents of damage in the ship bottom.

10.1 Grounding Tests by the NSWC

10.1.1 Experimental Set-up

The grounding tests were performed by the Naval Surface Warfare Centre, Carderock Division, at the HI-Test Laboratories in Arvonia, Virginia, USA. The testing facilities were developed to simulate grounding of an assembled ship bottom structure on a pinnacle rock at a scale of 1:5 corresponding to an oil tanker of about 30,000 to 40,000 DWT. Figure 10.1 shows the experimental set-up schematically.

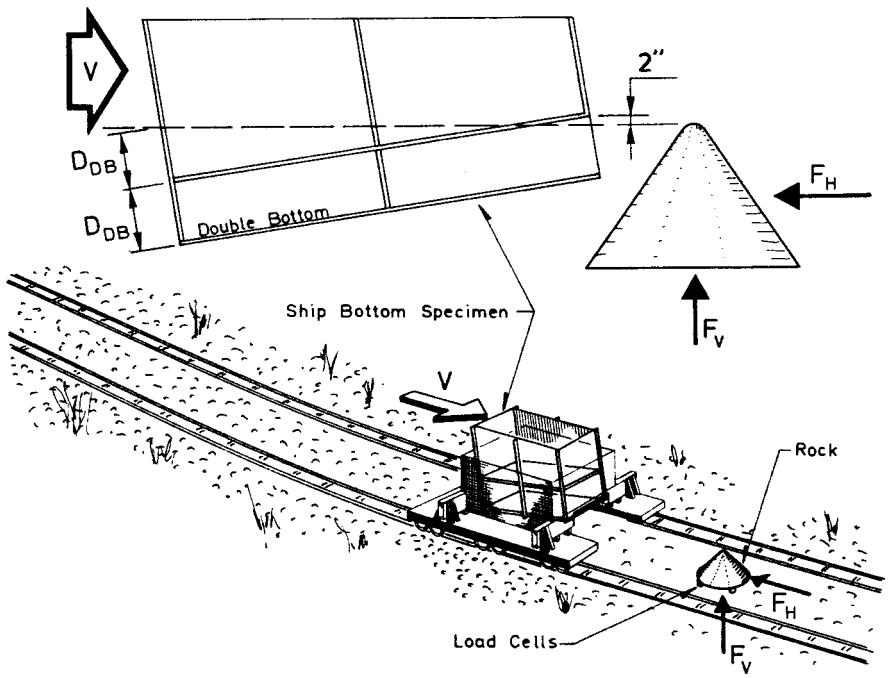

Figure 10.1: *Experimental set-up of the grounding tests conducted by the Naval Surface Warfare Centre (NSWC) at the HI-Test Labaratories, Virginia, USA.*

The ship bottom test specimen is mounted to a railway car which is pulled to the top of a hill to accumulate potential energy. The idea of the tests is to release the car from the hill and let it run over an artificial rock which is connected to vertical and horizontal load cells. The test specimens have a length of approximately 6-7 m, a width of about 2.5 m and a double

bottom height of about 0.4 m (corresponding to 2.0 m in a scale of 1:5). The specimens are mounted to the railway car such that the rock tip enters the model structure about 5 cm (2 inches) below the inner shell. The inclination of the double bottoms to horizontal is so that when the rock is at the aft bulkhead, the rock tip penetration into the inner bottom is equal to the double bottom spacing, Figure 10.1 . This set-up ensures that rupture of the inner hull is initiated as the rock passes through the specimen. Table 10.1 gives main data of the experimental set-up.

Table 10.1: *Main data of the grounding tests by the NSWC, USA. (*: assumed values).*

Weight of test vehicle	223 *tons*
Impact speed of test vehicle, V	12 *knots*
Rock tip radius, R_R	0.17 m
Rock semi-apex angle, φ	45^o
Material	ASTM A569
Material yield strength, σ_y	283 MPa
Material ultimate strength, σ_u	345 MPa
Material flow stress, $\sigma_0 = (\sigma_y + \sigma_u)/2$	314 MPa
Material fracture toughness*, R_c	240 kJ/m^2
Material strain hardening*, n	0.22

The results of four tests were reported by Rodd in [105] and these results will be compared to the corresponding theoretical predictions in the following. The four test specimens are shown in Figures 10.2 - 10.4. Main characteristics are[1]:

NSWC 1 Conventional double bottom construction with floors, girders and longitudinal stiffeners on both inner and outer bottom plating, Figure 10.2.

NSWC 2 Advanced Double Hull Design. The structure has no floors between the transverse bulkheads, Figure 10.3.

NSWC 3 Advanced Double Hull Design further developed from the ADHD above. Compared to the *NSWC 2* structure this structure has tighter girder spacing and stiffened double-plated transverse bulkheads. Longitudinal girders are stiffened with horizontal flat bar stiffeners and the inner bottom plating is thicker than the shell plating, Figure 10.4.

NSWC 4 Essentially like the *NSWC 3* structure but with tight vertical spacing on the longitudinal girders instead of the horizontal stiffening and with an increase in girder thickness from 3 mm in *NSWC 3* to 3.4 mm, Figure 10.4.

[1] The *NSWC* numbering neither corresponds to NSWC's own numbering nor to a chronological order of the tests.

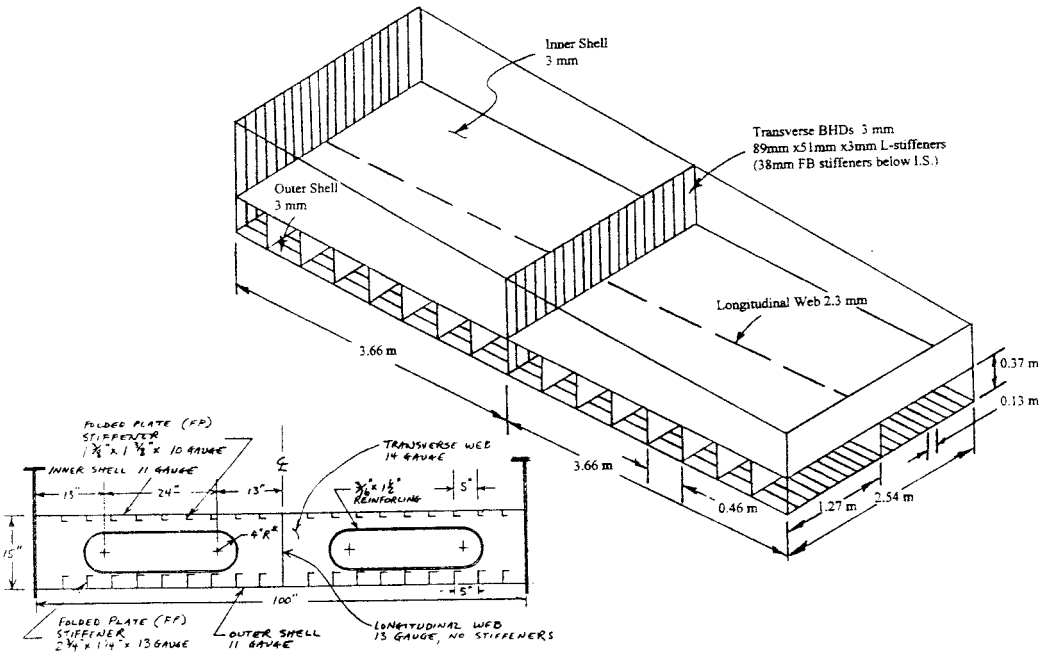

Figure 10.2: *Main characteristics of the NSWC 1 structure ("CONV/PD328").*

Before comparing the experimental results with theory, it is interesting to consider the energy absorbed in the four tests and see if these could have been predicted by the formula presented by Minorsky in 1959, [80], see Figure 6.2. If the off-set in the formula is neglected, it writes $E = 415.5 R_T$, where the energy is in $ton\, knots^2$ and the deformed steel volume R_T is in $ft^2\, in.$ By transformation of the formula to SI-units it becomes

$$E = 46.6\, MJ/m^3\, R_T \tag{10.1}$$

Since the energy absorbed in plastic flow is $E = \sigma_0\, \bar{\varepsilon}\, R_T$, the formula can be converted to an average effective strain if the flow stress, σ_0, is known. The ships analysed by Minorsky were built before 1959 so they were built of mild steel, i.e. it can be assumed that $\sigma_0 = 250\ MPa$, corresponding to a mean effective strain of $\bar{\varepsilon} = 0.19$. Since the necking limit is about 0.22, a mean strain of 0.19 seems unrealistically high. The high level of strain indicated by Eq. (10.1) can be due to underestimation of the actual volume of deformed material, overestimation of the energy or due to the neglect of fracture energy (Vaughan included this energy later, [132] and [133]). Table 10.2 lists the energy absorbed in the four NSWC tests over the first 5.46 m of contact, the volume of the test specimens (which is equal to R_T as all of the structure was deformed) and the energy absorbed per volume of test specimen steel.

Since the energy per steel volume, E/R_T, is seen to vary between 11.3 MJ/m^3 and 20.3 MJ/m^3 there is not immediately good correlation to Minorsky's value of 46.6 MJ/m^3 - i.e. the mean effective strain was far below the Minorsky value of $\bar{\varepsilon} = 0.19$. As proposed in

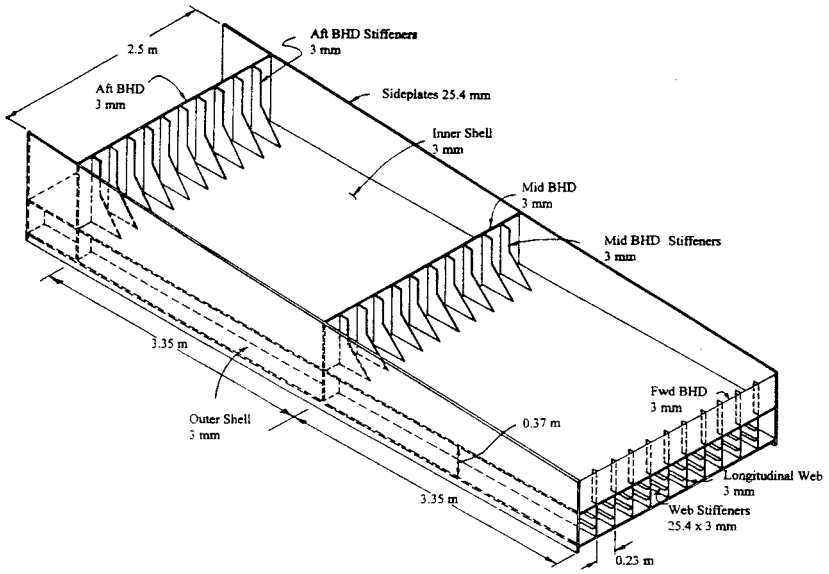

Figure 10.3: *Main characteristics of the NSWC 2 structure ("ADH/PB").*

Table 10.2: *Measured energy E over the first 17.9 feet (5.46 m) of contact, steel volume of each test specimen R_T, energy per cubic meter steel E/R_T.*

	Energy $E(MJ)$	Steel Volume $R_T(m^3)$	Energy pr Steel Volume $E/R_T(MJ/m^3)$
NSWC 1	3.25	0.245	13.3
NSWC 2	2.65	0.235	11.3
NSWC 3	5.34	0.277	19.3
NSWC 4	6.03	0.297	20.3

the approach taken by Choi and Wierzbicki, [31], the analysis above could be enhanced by taking only the material in the direct path of the rock as R_T. Although this approach is not consistent with Minorsky's measurements (R_T was the total volume of deformed material in an accident), it would take into account the increasing resistance with penetration. In conclusion, an approach like Minorsky's can give an estimate of the energy absorption in the right order of magnitude. However, the results in Table 10.2 clearly show the often proved fact that the energy absorption capability of a given structure depends not only on the amount of material deformed (as suggested by Minorsky's formula Eq. (10.1)) but also on the geometry of the structure. In order to optimise a structure with respect to its crashworthiness, it is therefore necessary to have a theory which is more advanced than Minorsky's.

In the following, the measured forces and absorbed energies will be compared to the corresponding values calculated with the theory derived in the present thesis. The main scantlings used in the numerical modelling of the experiments are given in Table 10.3. Tertiary stiffeners

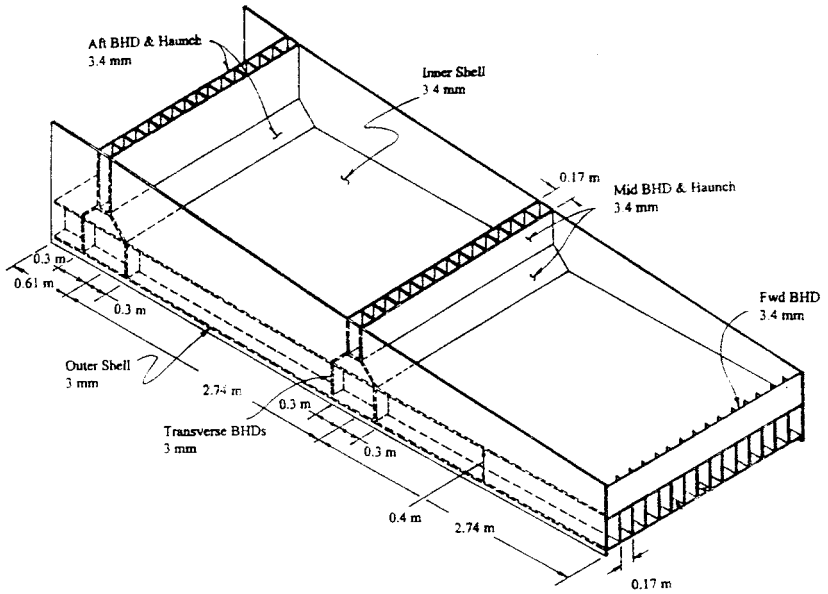

Figure 10.4: *Main characteristics of the NSWC 3 and NSWC 4 structures ("ADH/PD328" and " ADH/PD328V").*

are taken into account by increasing the plate thickness of girders and bulkheads according to a volumewise smearing.

In the theoretical model derived in Chapter 9 and summarised in Appendix C there are only three parameters which are not fully known for the present modelling:

1. The ductile material fracture toughness, R_c.
2. The coefficient of friction, μ.
3. The plate splitting angle, θ.

The ductile material fracture toughness, R_c, was not measured for the used material and as shown in Table 10.3 it is assumed here to be $R_c = 240\ kJ/m^2$, according to the small-scale tests of Atkins. A sensitivity analysis with respect to this parameter reveals that the energy absorption is very insensitive to R_c. The reason for this is that the energy dissipation of the crack tip process is small when the zone of deformation is wider than a few plate thicknesses. A rough estimate of the scale of problems at which fracture energy dominates can be found by assuming a uniform plane straining up to fracture in an area of width kt. The energy dissipation rates for plastic flow and fracture are then respectively $V\sigma_0\varepsilon_{cr}t(kt)$ and $V\,R_c\,t$. The deformation width at which fracture and plastic flow energy are equal becomes $kt = R_c/(\sigma_0\varepsilon_{cr})$. For the numerical example below $k = 1.2$, which means that when the width of the deformation is larger than 1.2 plate thicknesses (3.6 mm) plastic flow dominates. In the NSWC tests the width of deformation is in the order of one metre so it

Table 10.3: *Main scantlings used in numerical modelling of the four tests performed by the NSWC, [105]. Notice that component plate thicknesses are increased according to a volume wise smearing.*

	NSWC 1	*NSWC 2*	*NSWC 3*	*NSWC 4*
Length (m)	7.32	7.30	6.09	6.09
Width (m)	2.54	2.50	2.55	2.55
DB spacing (m)	0.38	0.37	0.40	0.40
Pitch angle (deg)	3.38	3.59	4.69	4.69
Plate thickness inner bottom (mm)	3.0	3.0	3.4	3.4
Plate thickness of shell (mm)	3.0	3.0	3.0	3.0
Plate thickness of floors (mm)	2.3	-	-	-
Plate thickness of girders (mm)	2.3	3.4	3.4	4.0
Pl. thickness of transv. blkh. (mm)	6.0	6.0	10.0	10.0

is clear that membrane deformation dominates. As a numerical example of the insensitivity, increasing R_c from 240 kJ/m^2 to 600 kJ/m^2 as suggested in Chapter 8, increases the energy absorption in the *NSWC 1* specimen by only 0.4 %. The uncertainty of the parameter has therefore no practical influence on the theoretical modelling.

As the coefficient of friction is relatively simple to measure (standard techniques are developed within plate forming technology) it is unfortunate that it must be estimated here. Future tests should exclude this uncertainty. The present theoretical analysis is performed with two values for the coefficient of friction, $\mu = 0.3$ and $\mu = 0.4$.

The plate split angle, θ, is related to the plate deformation around the rock, see Figure 9.4, and it cannot immediately be determined from simple geometrical considerations. As it was shown in Section 9.8 about plate resistance after fracture, the resistance of the structure has a minimum with respect to θ so the analysis below uses this optimum value of θ. The plate split angle is assumed to be the same throughout each test. Figure 10.5 shows the energy absorbed over the first 17.9 feet (5.46 m) of contact as a function of the plate splitting angle for $\mu = 0.4$.

The calculated absorbed energy is seen to have a well defined minimum for θ between 10^o and 20^o. These optimum values of the plate split angle are used in the following, $\theta = \theta_{opt}$. The only completely free parameter of the theory has thus been fixed.

Table 10.4 compares measured and calculated results for energy absorption and for penetration to inner bottom rupture.

The exact measured penetrations to fracture were not published explicitly but it is stated in [105] that in all four tests, the penetration to inner plate fracture was about 3 m in full scale, i.e. 0.6 m in model scale. The theoretical predictions of $\delta_{frac,out}$ given in the last

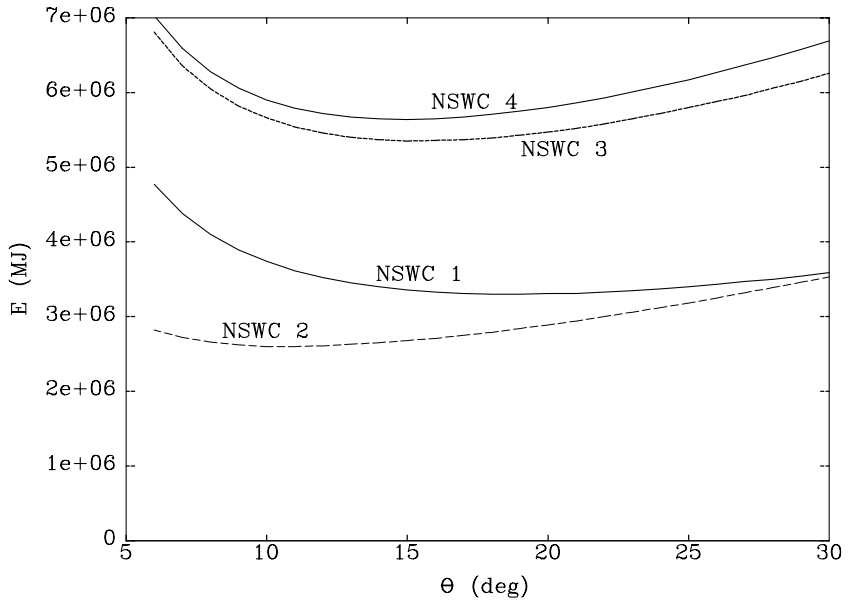

Figure 10.5: *Energy absorbed over the first 5.46 m of contact as a function of plate split angle, θ. The coefficient of friction is $\mu = 0.4$.*

column of Table 10.4 therefore indicate a maximum deviation from experiments of 10 - 15 %, theory underestimating the penetration to fracture. The penetration to fracture of $\delta_{frac,out} = 0.55m$ for *NSWC 3, 4* was also calculated in Chapter 9, Section 9.5.2.

With $\mu = 0.4$ the deviations between theoretical and experimental energies are only 1.5 %, 1.9 %, 0.3 % and 6.5 %. Such agreement between calculated and measured energies is well within the uncertainty of the input data and it indicates a surprisingly good performance of the theory.

More verification examples are needed however, before the model can be claimed to have a general accuracy of about 5 %, but the results of Table 10.4 are certainly very encouraging.

Figure 10.6 shows comparisons between measured and calculated forces. As there was

Table 10.4: *Measured and calculated absorbed energies, E, over the first 17.9 feet (5.46 m) of contact. Also measured and calculated rock tip penetrations, $\delta_{frac,out}$, into outer bottom at fracture of inner bottom plating.*

	Experiment	Theory, $\mu = 0.3$		Theory, $\mu = 0.4$		Experiment	Theory
	E/MJ	$\theta_{opt}/^o$	E/MJ	$\theta_{opt}/^o$	E/MJ	$\delta_{frac,out}$/m	$\delta_{frac,out}$/m
NSWC 1	3.25	18	2.71	19	3.30	0.6	0.52
NSWC 2	2.65	10	2.08	11	2.60	0.6	0.52
NSWC 3	5.34	14	4.34	15	5.36	0.6	0.55
NSWC 4	6.03	14	4.57	15	5.64	0.6	0.55

good agreement between energies it is not surprising that the agreement between horizontal forces is also good. The hump on the curves which is due to the transverse is seen to be slightly underestimated by theory.

There is seen to be very good agreement between vertical forces also. As seen in Figure 9.21 and Figure 9.24 the ratio of vertical to horizontal force is quite sensitive to the coefficient of friction. Therefore, the fact that there is good agreement between vertical to horizontal force ratios indicates that the coefficient of friction is really abuout 0.4 as assumed.

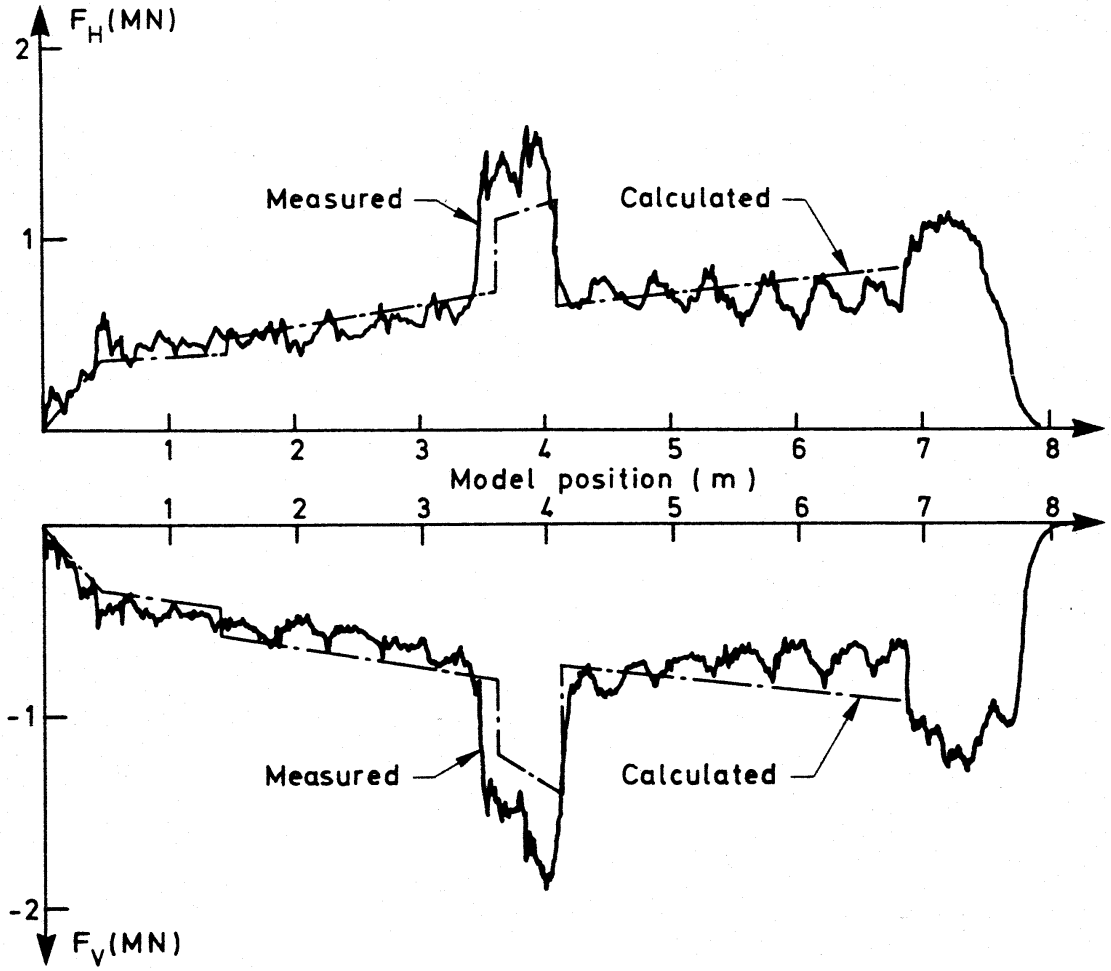

Figure 10.6: *Calculated ($\mu = 0.4$) and measured horizontal and vertical forces for the NSWC 1 specimen.*

10.2 Actual Grounding of Single Skin VLCC

Being able to predict the internal mechanics it is relevant to consider the full grounding problem including the coupling of internal mechanics to external dynamics. Many real accidental grounding accidents have occurred over time but, due to lack of information about ship and ground, few of them can be used for verification purposes. Kuroiwa, [63], published the data of an accidental grounding event together with calculated results of finite element simulations. The grounding accident occurred on January 6 1975 as a 240,000 d.w.t. single skin oil tanker ran onto the *Buffolo Reef* off the coast of Singapore. Figure 10.7 shows the reported damage to the hull structure. The bottom of the ship was torn about 180 m from the bow to the middle of centre tank no 3. The ship was stuck 10 days on the reef expanding the damage around centre tank no. 3. More than 10,000 tons of oil was spilled.

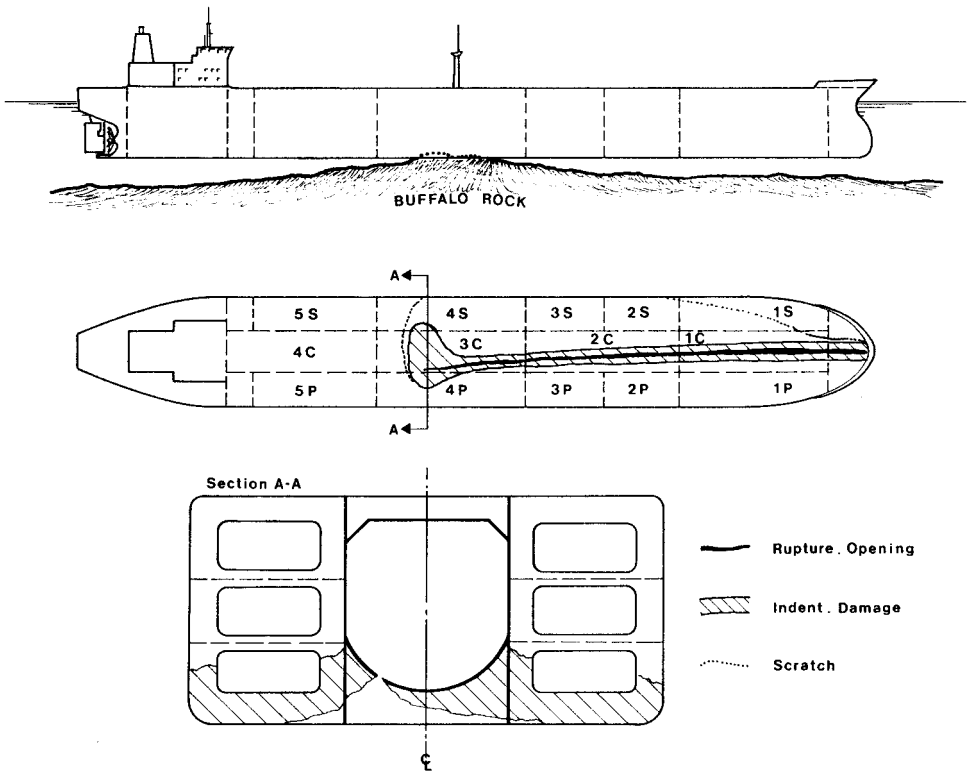

Figure 10.7: *Ship bottom damage to a single skin VLCC due to grounding on Buffalo Reef on January 6, 1975. From [63].*

Figure 10.8 shows a photo of the damaged hull. The grounding was simulated successfully with $LS-DYNA3D$ by Kuroiwa and co-workers, [63], and part of the simulation result is shown in Figure 10.9.

Figure 10.8: Picture of damaged hull of single hull VLCC. From [63].

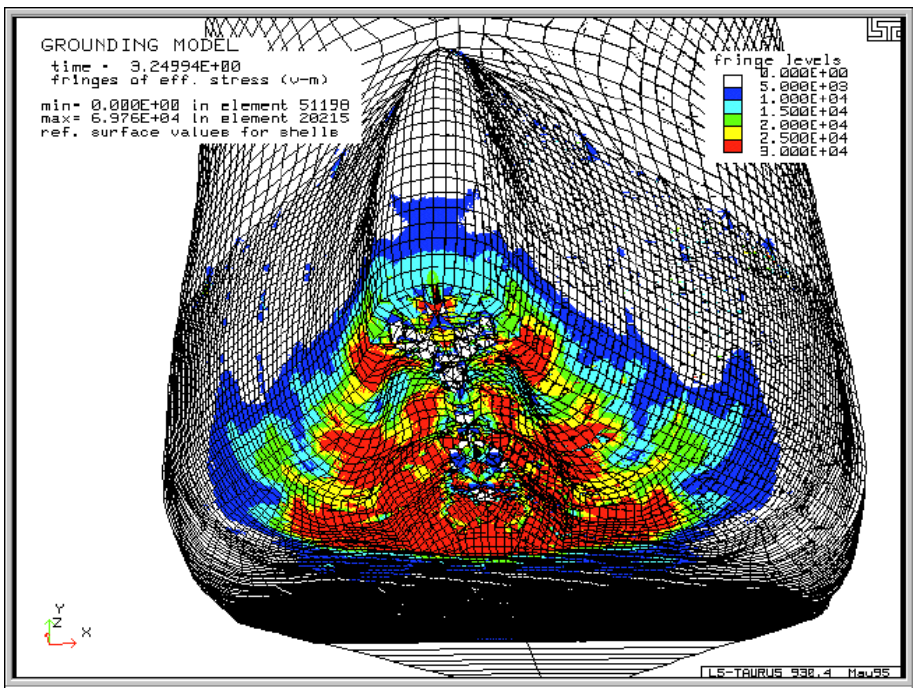

Figure 10.9: $LS-DYNA3D$ simulation of ship grounding.

As mentioned in Chapter 6 the computational effort in a finite element calculation as shown in Figure 10.9 is enormous - even by current computer standards. With the fastest of the workstations at the Department of Naval Architecture and Offshore Engineering, DTU, (HP 735 rated *SPECfp92=201*), the CPU time for one grounding calculation would be about 6.7 weeks. Table 10.5 lists the data used in the present numerical modelling of the accident. With the present implementation of theory it takes about 20 minutes to input the data and the CPU time for one grounding calculation is 0.3 s.

Table 10.5: *Data used in numerical modelling of grounding accident on Buffalo Reef.*

Length, L	304 m
Beam, B	53.4 m
Depth, D	25.7 m
Design draught, T	19.8 m
Displacement, M_S	273,000 t
Longitudinal Centre of Flotation aft of midship, LCF	-4.4 m
Longitudinal Metacentric Height, GM_L	330 m
Transverse Metacentric Height, GM_T	5.3 m
Impact velocity, V	12 knots
Rock penetration amidships, δ_{R0}	3-5 m
Rock eccentricity, s	3.0 m
Trim, $T_{AP} - T_{FP}$	0 m
Coefficient of friction, μ	0.4
Bottom plate thickness, t_{out}	35.0 mm
Bottom plate flow stress, σ_0	275 MPa
Bottom plate strain hardening, $n = \varepsilon_{cr}$	0.22
Spacing between transverse frames	5.0 m
Plate thickness of transverse frames, t_t	15 mm
Flow stress of transverse frames, σ_0	275 MPa
Spacing between longitudinals	1.0 m
Longitudinal web plate height, D_w	840 mm
Longitudinal web plate thickness, t_w	17.5 mm
Longitudinal flange width, d_f	200.0 mm
Longitudinal flange thickness, t_f	30.0 mm
Flow stress of longitudinals, σ_0	315 MPa

The shell plate thickness was 28.5 mm but due to smearing of the deformed part of the keel plate, it was taken to be 35 mm in the calculations. The plate split angle, θ, was found as in the previous section from minimisation to be $\theta = 7^o$. The rock shape and height[2] are not known. As seen in Table 10.5 the rock is modelled as conical with a rounded tip with radius $R_R = 1\ m$ and a semi-apex angle of $\varphi = 50^o$. Figure 10.10 shows the calculated

[2]The 'rock height' or 'reference rock penetration' δ_{R0} refers to the rock penetration amidships if the ship was not allowed to heave, roll or pitch.

damaged length of the hull as a function of the rock height together with the measured damage length of 180 m.

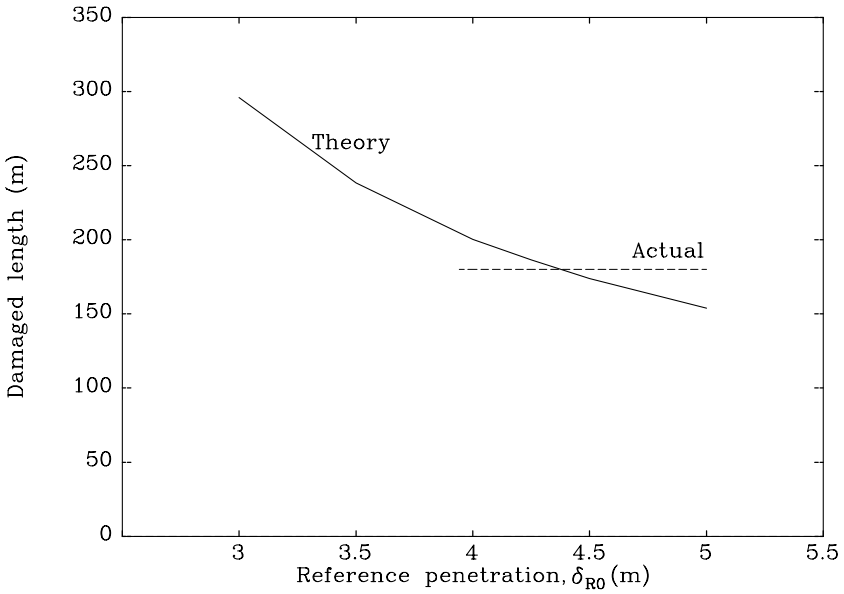

Figure 10.10: *Damage length to a single hull VLCC vs. reference rock penetration.*

As expected, the damage length is a decreasing function of rock penetration and it is seen that the observed damage length of 180 m is obtained from theory with a rock penetration of about 4.4 m. From the transverse section in Figure 10.7 it can be found that the actual maximum rock penetration was around 5 m. However, since the ship was stuck to the reef for 10 days, the measured damage path in the given transverse section was expanded after the grounding so the measured rock penetration of 5 m represents an absolute upper bound. Hence, although very accurate comparisons are impossible due to the uncertain shape of the rock, there is very good agreement between the damage seen in the actual grounding and the corresponding calculated damage. With a reference rock penetration of 4.4 m the initial kinetic energy is absorbed in the following way: 0.2 % is stored as potential energy, 35 % is absorbed by the shell plating, 47 % is absorbed by longitudinals and 18 % is absorbed by transverse frames and bulkheads. The following section further discusses how different structural members contribute differently to the energy absorption.

To illustrate the importance of the coupling between external dynamics and internal mechanics, Figure 10.11 shows the rock path through the hull for different transverse rock positions, s. If the ship was locked in a horizontal motion without heave, roll and pitch, its kinetic energy would be dissipated in only 145 m. As seen in Figure 10.11 the damage length becomes significantly larger when the ship is free to heave, roll and pitch.

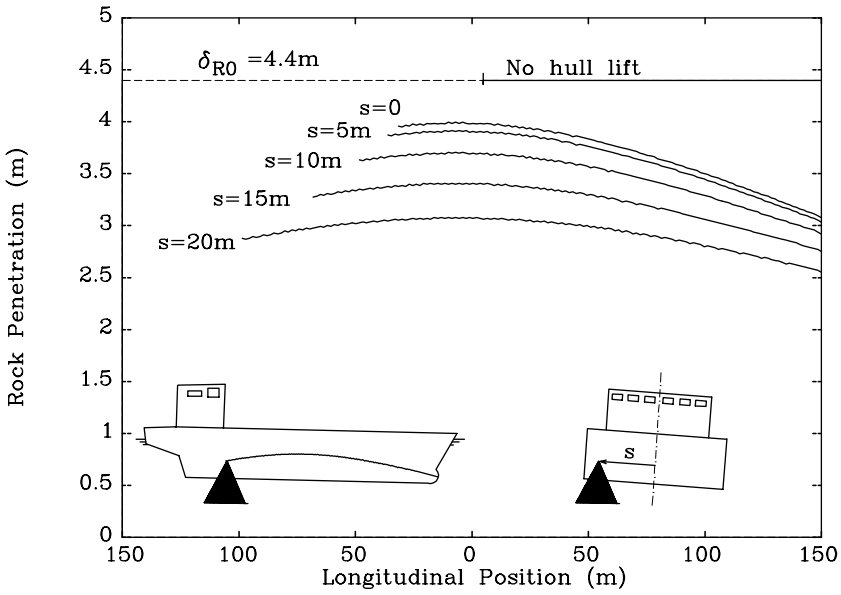

Figure 10.11: *Rock penetration into hull for different values of the rock eccentricity. Rock height is* $\delta_{R0} = 4.4m$.

10.3 Design for Ship Bottom Raking

With confidence in the theory it can be used to optimise the crashworthiness of ship bottom structures. It is not the purpose of the present thesis to give guidelines for such an optimization but rather to show, how different structural members contribute more or less effectively to the energy absorption of the structure.

Moreover, if operational data of a ship can be obtained in terms of probability density functions (p.d.f.s) for ship velocity, draught etc. and the hit grounds can be characterised correspondingly by p.d.f.s, the theoretical model can be used to *calculate* the extents of damage in a probabilistic format, see [110], instead of basing the oil outflow calculation on damage statistics obtained from existing ships. Ultimately, such a probabilistic calculation extended to cover the oil outflow could replace existing rules for ship design (e.g. the double hull requirement) to prevent environmental damage due to tanker operation.

Table 10.6 shows how the energy was distributed very differently between structural components in the four NSWC tests. For optimisation of the structure with respect to the energy absorption capabilities, it is essential that the distribution of energy among structural members is calculated accurately. It is very difficult in experiments to quantify the energy absorption of the individual members, however. A possible future method of verifying the numbers in Table 10.6 would be to tune a finite element model to give the measured absorbed energy and then from the finite element solution extract the energy absorption of individual members.

It is clear that optimisation with respect to crashworthiness has to consider also the

Table 10.6: *Contribution of the structural members to the energy absorption.*

	NSWC 1	*NSWC 2*	*NSWC 3*	*NSWC 4*
Outer plate (%)	29.9	29.7	18.9	17.9
Longitudinals on shell plate (%)	28.3	-	-	-
Transverse members (%)	18.9	29.5	42.6	40.5
Longitudinal girders (%)	6.2	31.0	30.3	33.9
Inner bottom plate (%)	9.8	9.9	8.2	7.8
Longitudinals on inner btm. (%)	7.0	-	-	-

traditional design loads but it is interesting to see how effective the different structural members in the four NSWC tests were in terms of energy absorption per unit volume of steel, Table 10.7. Conclusions about the most effective use of steel with respect to energy absorption could be derived from Table 10.7 but considerations should also be given to fracture resistance of the structure so such important conclusions are left for future studies.

Table 10.7: *Energy absorption per unit volume of steel for each class of structural members in the four NSWC tests.*

	NSWC 1	*NSWC 2*	*NSWC 3*	*NSWC 4*
Outer plate (MJ/m^3)	17.7	14.0	21.5	21.5
Longitudinals on shell plate (MJ/m^3)	23.1	-	-	-
Transverse members (MJ/m^3)	9.6	22.9	37.1	37.1
Longitudinal girders (MJ/m^3)	31.7	8.7	14.0	13.9
Inner bottom plate (MJ/m^3)	5.8	4.7	8.3	8.3
Longitudinals on inner btm. (MJ/m^3)	8.7	-	-	-

This page is intentionally left blank

Chapter 11

Conclusions and Recommendations for Further Work

11.1 Conclusion

The purpose of the present thesis has been to contribute to the understanding of *The Mechanics of Ship Grounding*. The overall objective of this study is to develop rational procedures for design of ship structures for accidental loads. In other areas of the transportation industry - especially automotive and aviation - design for accidental loads have long been mandatory and a branch of engineering has evolved around this topic. In naval architecture, design for the so-called crash-worthiness of a structure has not traditionally been considered extensively. Recent large grounding accidents, in particular that of the *Exxon Valdez*, and subsequent governmental requirements have lead to an intense international focus on the topic, however. To assess the risks associated with shipping, it is necessary to have procedures for quantifying both the frequency and the consequences of accidents. According to the title, the present thesis focuses on the consequences of grounding events but a few results have been included to illustrate the application of a method for quantifying the frequency and likelihood of grounding events.

The first part of the thesis describes such a procedure for calculating the frequency of grounding events for a certain traffic in a certain geographic area. Comparison of the calculated expected number of grounding events for the *Esbjerg - Fanø* ferry route in Denmark with the number of observed grounding events over three years shows an encouraging agreement.

For prediction of the consequences several approaches can be taken. General-purpose non-linear finite element codes have proved their ability to simulate grounding events but application of these programs for design is still prohibitively expensive in terms of man hours and computer power. The objective of the main part of the thesis has been to derive theoretical models which capture the grounding response in detail without tremendous modelling

effort. This objective has been achieved through a series of simplifications and by replacing generality with a limited number of degrees of freedom based on observed behaviour. The main steps taken to arrive at a rational basis for calculating the ship response to a given grounding event are:

- Establishment of a theoretical model for calculating the ship behaviour in grounding on soft sea beds. The overall approach is time simulation, i.e. the equations of motion for the ship surge, heave and pitch are solved in time. The hull girder is modelled by linear elastic Timoshenko beam theory and the loads considered are gravity, hydrostatic pressure, hydrodynamic pressure and the ground reaction. The major difficulty is calculating the ground response to the intruding bow. Based on results of model tests, a simple, yet effective, phenomenological model for the ground reaction is derived, which takes into account the strong influence of pore water.
- Establishment of a theoretical model for calculating the grounding bottom damage and ship motion over a pinnacle shaped rock. The overall approach is to divide the problem into external dynamics and internal mechanics and couple these two problems through equilibrium of contact forces. The model for the external dynamics is based on a pseudo time integration scheme where vertical inertia forces are neglected and the surge motion is found from energy considerations. The model for the internal mechanics is based on the so-called "upper bound approach" - i.e. the structural resistance force in the direction of motion is calculated from the energy dissipation rate of an assumed mode of deformation. Several theoretical solutions which are further described below are derived to the involved problems of plasticity, fracture and friction.

The following main conclusions can be drawn from this thesis:

1. A relatively simple rational model for estimation of grounding frequency has been presented. As the model is based on a series of estimates concerning events leading to a grounding event there are uncertainties associated with the model which need further investigation but the first results of the model are very encouraging.
2. The consequences regarding structural failure associated with ship grounding on soft sea beds can be calculated. The proposed theoretical model was verified by measurements of small scale tests and controlled large scale tests. Calculations for a VLCC and six different fast vessels show that the grounding induced sectional forces may exceed the hull girder strength. Indeed, the accidental grounding of the Alvenus on a sand bar in 1984 demonstrated the potential seriousness of this type of accident.
3. The consequences in terms of hull damage associated with ship grounding on a pinnacle-shaped rock can be calculated. The derived theoretical model for the internal mechanics was compared to four grounding tests performed by the NSWC, USA. A remarkable accuracy was found as the energy absorption and the penetration to fracture was predicted with maximum errors of respectively 6 % and 13 %. The model has only one

'free' parameter, the coefficient of friction, which was set to 0.4 (which is very reasonable) to give the above-mentioned accuracy. The performance of the total grounding model was checked against an accidental grounding event on a reef off the coast of Singapore in 1975. The shape of the underwater rock was unknown but use of a rock shape estimated from the damage path of the deformed ship led to very good agreement between calculated and the observed ship damage. The derivation of the theoretical model for grounding on a pinnacle brought about several partial results:

- In a study of the global ship motion, it was found that even if the rock is at the side of the ship, the induced sway and yaw motion can be neglected - at least if the damage length is less than half the ship length. If the damage length is larger, the induced horizontal rotation of the ship tends to cause the rock to leave the ship hull.
- A theoretical solution was derived for steady-state plate cutting by a wedge. The mechanisms of plasticity, fracture and friction were quantified and it was shown that the derived model can predict the forces of three cutting experiments with plate thicknesses varying from 0.7 mm to 25 mm. The errors of the predictions were 7 %, 41 % and 5 % but the coefficients of friction were not measured, so this uncertainty may explain the discrepancy between theory and measurements.
- A global deformation mode for a ship bottom deformed by a longitudinally moving rock was proposed. Description of the deformation was based on assumed deformation modes for the inner and outer bottom plating. All members attached to the plating were assumed to follow the plating in a compatible manner so that component intersections stayed intact.
- A theoretical solution for punch indentation of a sphere into a circular plate was considered with the objective of finding a solution for the local plate deformation around a conical rock with a rounded tip. The theoretical solution was compared to experiments and good agreement was found for both forces, strain fields and penetrations to fracture. It was noted, however, that work is still needed before the onset of fracture can be accurately predicted.
- A theoretical model was derived for resistance of a plate which has not fractured. By comparing the theoretical model with experimental results, errors of up to 75 % were found but this discrepancy can be ascribed to the test specimen slipping at the boundary or to elastic effects.
- A theoretical model was derived for plate 'cutting' by a cone. Since the cone does not have a sharp cutting edge, the material separation process must be ductile fracture. Based on the assumed global mode of deformation the energy dissipation rate for plasticity, fracture and friction could be quantified and the resistance force could be calculated. An agreement of about +/- 15 % between theory and experimental results was found both for the horizontal and the vertical forces.
- A theoretical model for the resistance of longitudinal members (bulkheads, girders and stiffeners) was derived. The expressions cannot immediately be verified as no

usable experimental results seem to be available.

- A theoretical model was derived for the resistance of transverse members. The problem of web girder crushing was considered and based on a very simple mode of deformation compatible to the plate deformation, the expressions for crushing force and energy absorption of a transverse member were derived. The length or the width of the plastic buckle was found by minimisation of the mean crushing force. Comparison of the theoretical model to results of model-scale experiments showed very good agreement both as regards the plastic wave length and between the measured and the calculated crushing force. The theory was extended to cover deformation of members of finite height, deformation over several buckles, and deformation after fracture.

11.2 Recommendations for Future Work

With the long term objective of making *Rational Design of Ship Structures for Accidental Loads*, the list of possible research topics for future work seems endless. Within the framework of grounding, the present study has pinpointed a number of topics which need to be further investigated for clarification of associated risks. First the results for both soft and hard grounding should be implemented in an integrated risk analysis model. In addition to frequency estimation and grounding response, such a model should include the post-accident behaviour, i.e. residiual hull girder strength, oil outflow, damage stability etc.

11.2.1 Grounding on Soft Sea Beds

- For the soft-grounding analysis, a further study of rupture of sand would be relevant. Understanding this phenomenon and being able to quantify it would also help in other areas of engineering where submerged foundations or piles are rapidly - for example accidentally - loaded.

- For verification of the theoretical model for soft grounding, data of the Alvenus accident has been obtained from the United States Coast Guard through Lt. Daniel Pippenger. The Alvenus suffered serious hull girder failure due to grounding on a sand bar and theoretical reconstruction of this accident would shed light on hull girder failure in soft grounding events.

- In several areas around the world (for example India) large tankers are scrapped by running them at full speed up on beaches. It is very likely that valuable information about ship motion and hull girder damage could be obtained by observing and maybe monitoring these grounding events.

11.2.2 Grounding on Rocks

The developed model for the internal mechanics was shown to predict the energy absorption of four experiments with an error of less than 6 %. Such agreement is remarkable and taking into account the complexity of the problem, it cannot be expected that theoretical solutions will ever come closer than this. In fact, even a similar experiment could not be expected to reproduce the results with such accuracy.

Although the agreement is encouraging for these specific four tests, there are yet many problems which need clarification, however:

- It is essential that the extent of damage around the rock can be accurately determined. The extent of damage has influence both on the resistance of the structure and on the penetration to fracture. At present the damage is assumed to extend to certain primary stiffeners away from the rock, but this assumption should probably be replaced by an evaluation of the strength of the structure around the rock. Good understanding of the spread of deformation could also be applied to simplified models for damage to a ship side in a collision.

- The fracture criterion should be developed further both in terms of determining the strain path up to fracture and in terms of finding a proper fracture locus. Results derived for the metal forming industry such as fracture forming limit diagrams should be further investigated. The possibility of transverse members acting as crack initiators should be investigated. Strength of weldings should also be further investigated.

- For prediction of fracture and energy dissipation, the strain field in plate deformation before fracture should be further studied.

- For quantification of frictional effects, the coefficient of friction should be measured for rock/ship-bottom contact. Applicable experimental set-ups were developed within the area of sheet forming.

- The presented study of web crushing (resistance of transverse members) should be followed up by more experiments to see if the theory works as well as indicated for other plate aspect ratios. If it does, the solution can be widely applied to collision and grounding problems.

- The developed solutions for longitudinal members are based on quite simplistic deformation modes. It would be interesting to study further their contribution to the structural response.

- Dynamic effects have been neglected despite numerous observations indicating their possible importance. Dynamic effects should be considered, possibly with the objective of justifying their future neglect.

- As they are released, the large-scale tests of the NSWC should be used for verification of the model for the internal mechanics. Valuable results were also produced in grounding tests conducted by the the Association for Structural Improvement of Shipbuilding Industry in the Netherlands in 1994.
- The grounding model should be extended to cover other rock geometries - for example a two-dimensional wide rock (like a beach).
- As for soft grounding events it would be very interesting to perform full-scale grounding tests with tankers which are going to be scrapped.

Most of the topics suggested above concerning grounding on rock can be produced in very simple experiments. However, it is often difficult - not to say impossible - to determine from a deformed specimen how the absorbed energy is distributed between the various deformation mechanisms and what the local strain fields are. For such quantification of strain fields and energy dissipation, the finite element method could prove to be very useful together with experiments.

Appendix A

Geometry for Plate Cut by Wedge

The objective of this section is to find the gap openings u_0 and $2v_0$ shown in Figure 8.7 expressed in terms of the rolling radius, $R(= R_t/cos\theta)$, the wedge shoulder width, $2B$ and the wedge semi angle, θ.

Gap opening at wedge front

It is convenient to introduce two coordinate systems, a global system, $(X, Y, Z)_G$, and a local system, $(x, y, z)_l$, both with origin at point O. The $z-$ and Z-axes point vertically upwards, the X_G-axis is in the symmetri line pointing towards the wedge tip and the x_l-axis is in the bending hinge line, OP. The y_l- and Y_G-axes are defined from the other axes. An arc line coordinate, s, which follows the curling edge of the plate is also introduced, see Figure A.1. The s-axis also has origin at point O.

A point on the edge with the arc line coordinate, s, has the local coordinates

$$\begin{aligned} x_l &= s\,cos\theta \\ y_l &= -R_t\,sin\left(\frac{s\,sin\theta}{R_t}\right) \\ z_l &= R_t\left(1 - cos\left(\frac{s\,sin\theta}{R_t}\right)\right) \end{aligned} \tag{A.1}$$

The general relation between local and global coordinates is given by the transformation

$$
\begin{aligned}
X_G &= x_l\, cos\theta - y_l\, sin\theta \\
Y_G &= x_l\, sin\theta + y_l\, cos\theta \\
Z_G &= z_l
\end{aligned}
\tag{A.2}
$$

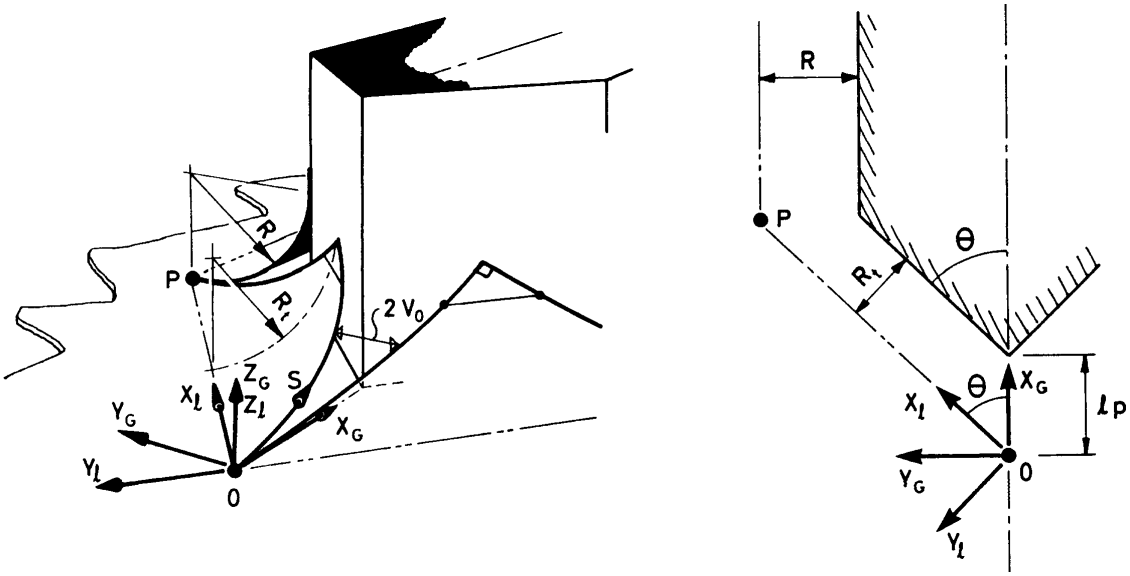

Figure A.1: *Definitions used for finding the gap width at the wedge tip.*

Inserting Eq. (A.1) into Eq. (A.2) gives the global coordinates for a point on the plate edge with coordinate s;

$$
X_G = (s\, cos\theta)\, cos\theta - \left(-R_t\, sin\left(\frac{s\, sin\theta}{R_t}\right)\right) sin\theta \tag{A.3}
$$

$$
Y_G = (s\, cos\theta)\, sin\theta + \left(-R_t\, sin\left(\frac{s\, sin\theta}{R_t}\right)\right) cos\theta \tag{A.4}
$$

$$
Z_G = z_l \tag{A.5}
$$

Since the gap opening is $2\, v_0 = 2\, Y_G$ it is now given from Eq. (A.4) as a function of s, R and θ;

$$
2\, v_0 = 2\left(s\, cos\theta\, sin\theta - R\, cos^2\theta\, sin\left(\frac{s}{R} tan\theta\right)\right) \tag{A.6}
$$

The objective is to find the gap width at the cutting edge, i.e. at the point where $X_G = l_p = R_t/sin\theta = R/tan\theta$, see Figure A.1. Eq. (A.3) is too complex to be solved in a closed form for s, otherwise this value of s should be inserted into Eq. (A.6) giving the final expression sought. It has to be done numerically.

As an initial guess we could calculate the gap width at $s = l_p = R/tan\theta$. From Eq. (A.6) the expression becomes

$$2\,v_0 = 2\,R\,cos^2\theta\,(1 - sin1) = 0.317\,R\,cos^2\theta \tag{A.7}$$

By comparing this expression to the exact solution found from numerical solution of Eqs. (A.3, A.6) it is found that the final exression for the gap width, $2v_0$ at the cutting edge is very well approximated by the expression

$$2\,v_0 = 0.317\,R\,cos^2\theta\left(1 + 0.55\,\theta^2\right) \tag{A.8}$$

The error of Eq. (A.8) at 10^o, 30^o, 45^o is respectively 0.25 %, 1.3 % and 0.18 %.

Gap opening at wedge shoulders

It is convenient to define a coordinate system, (X, Y, Z), at the shoulder in the plane of the undeformed plate. The Z-axis points vertically upwards along the shoulder line, the Y-axis is in the plane of the undeformed plate and it is perpendicular to the Z-axis and to the wedge sides. The X-axis is defined from the $Y-$ and Z axes, see Figure A.2.

The total width of the deformed plate on one side of the symmetry line is $R + B$ and the length of the curved part of the flap is $\pi R/2$ so the width of the straight part of the flap at the wedge sides becomes

$$b_{fs} = (R + B) - \pi R/2 = B - R(\pi/2 - 1) \tag{A.9}$$

Likewise, it can be shown that the width of the straight part of the flap at the wedge front becomes

$$b_{ff} = cos\theta\,(B - R(\pi/2 - 1)) \tag{A.10}$$

We require the tangent of the deformed plate flaps to conform to the wedge as shown in Figure A.2 giving the requirement

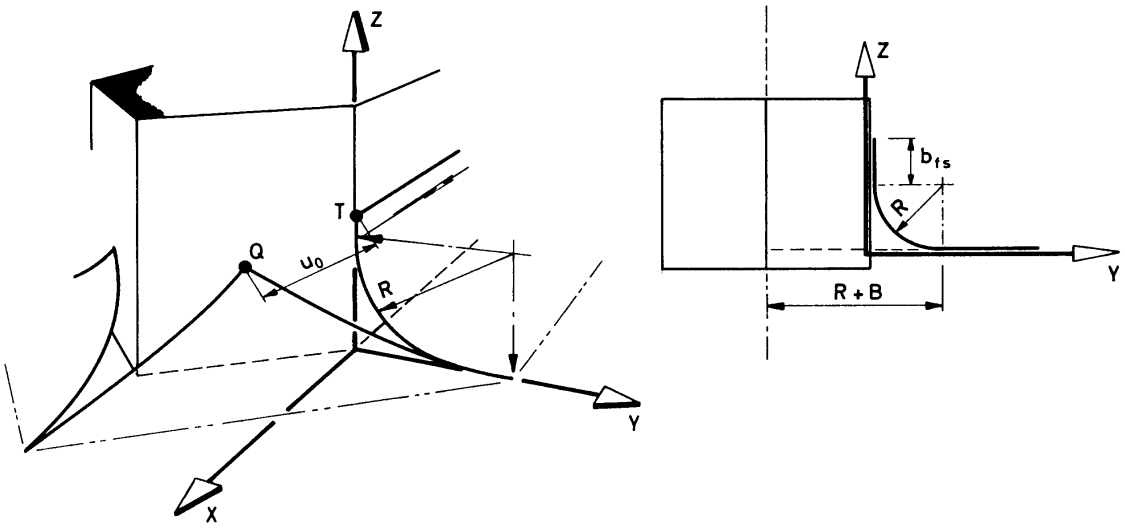

Figure A.2: *Definitions used for finding the gap width at the wedge sides.*

$$b_f \geq 0 \Rightarrow \tag{A.11}$$

$$R \leq \frac{B}{\pi/2 - 1} \approx 1.75\, B \tag{A.12}$$

The position of point T is

$$\begin{pmatrix} X \\ Y \\ Z \end{pmatrix}_T = \begin{pmatrix} 0 \\ 0 \\ B + R(2 - \pi/2) \end{pmatrix} \tag{A.13}$$

and the position of point Q is

$$\begin{pmatrix} X \\ Y \\ Z \end{pmatrix}_Q = \begin{pmatrix} B\, sin\theta\, cos\theta \\ -B\, sin^2\theta \\ (B + R(2 - \pi/2))\, cos\theta \end{pmatrix} \tag{A.14}$$

The distance between T and Q is then given by

$$\begin{aligned} u_0 &= \left((X_T - X_Q)^2 + (Y_T - Y_Q)^2 + (Z_T - Z_Q)^2 \right)^{0.5} \\ &= \left(B^2\, sin^2\theta + (1 - cos\theta)^2\, (B + R(2 - \pi/2))^2 \right)^{0.5} \end{aligned} \tag{A.15}$$

Figure A.3 and Figure A.4 show the variation of the gap width with rolling radius and wedge angle from Eq. (A.15).

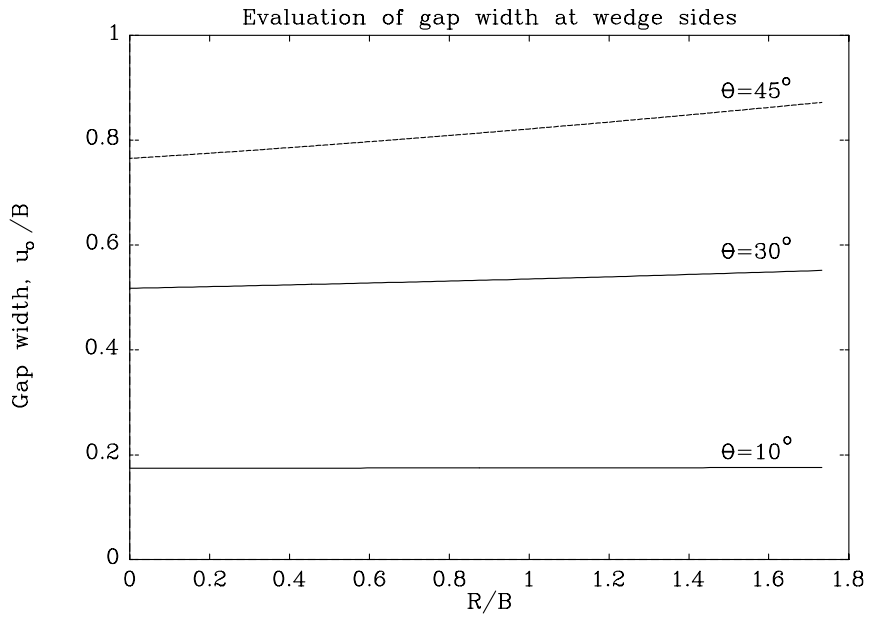

Figure A.3: *Variation of gap width with rolling radius.*

It is seen from Figure A.3 that u_0/B is a very weak function of the rolling radius and Figure A.4 illustrates that Eq. (A.15) is well approximated by the expression

$$u_0 = B\,\theta \tag{A.16}$$

for the considered ranges of θ and R.

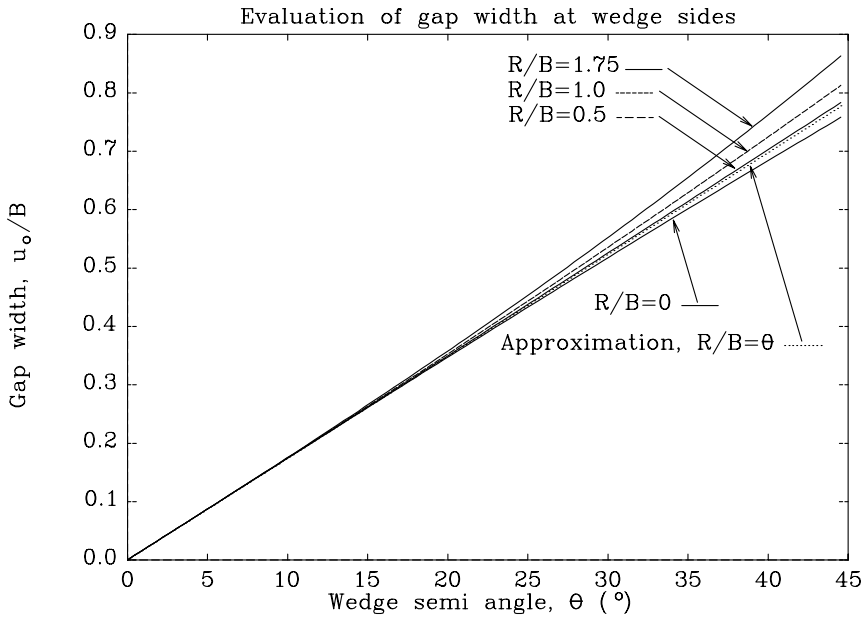

Figure A.4: *Variation of gap width with wedge angle.*

Appendix B

Geometry of Plane Flap Model

Derivation of geometric properties for the straight flap model. The following properties are introduced (Figure 9.4 and B.1).

$u_0(\alpha, \theta, B_{de})$	maximum width of a 'side gap', i.e. distance between Q and R in Figure 9.4 ,
$v_0(\alpha, \theta, B_{de})$	half width of center gap, i.e. distance between R and center plane in the direction of the plate flap,
α	angle from horizontal to flaps measured in a plane perpendicular to the hinges,
θ	plate splitting angle,
B_{de}	flap width.

The rock penetration causes the two flaps, QPR and $PRST$, to rotate an angle, α, from the horizontal about the lines OP and PT repectively. The objective is to find the distance, u_0, between Q and R and the distance, v_0, between the center plane and Q as a function of α, θ and B_{de}.

A Cartesian coordiante system, xyz, is introduced, Figure B.1. Its origin is at P, the x-axis is parallel to the symmetry plane, it points forward and lies in the plane of the undeformed plate. The y-axis is also in the plane of the undeformed plate and it points towards the symmetry plane. The z-axis points upwards.

Consider two vectors, $\vec{a}$ and $\vec{b}$. The vector $\vec{a}$ is in the plane of the front flap, QPR. Its origin is at the OP-line, it is perpendicular to OP, and its endpoint is at Q. The vector $\vec{b}$ connects points P and R. The idea of the following derivation is to rotate $\vec{a}$ and $\vec{b}$ around OP and PT and find the distance between the endpoints.

Supscript '0' is used for the origin of a vector, and subscript '1' is used for the endpoint of a vector. As an example, $\vec{a} = \vec{a}_1 - \vec{a}_0$.

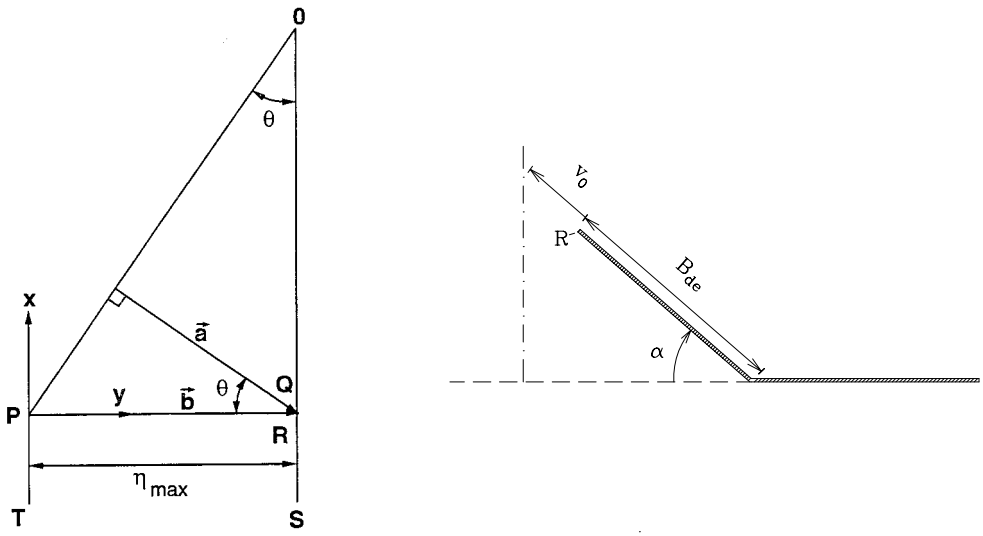

Figure B.1: *Geometry of half of the deformation pattern (aerial view)*

The origins of the vectors are;

$$\vec{a}_0 = \begin{pmatrix} x \\ y \\ z \end{pmatrix} = B_{de} \begin{pmatrix} \cos\theta \sin\theta \\ 1 - \cos^2\theta \\ 0 \end{pmatrix}, \qquad \vec{b}_0 = \begin{pmatrix} x \\ y \\ z \end{pmatrix} = B_{de} \begin{pmatrix} 0 \\ 0 \\ 0 \end{pmatrix}$$

Before rotation, the vectors are;

$$\vec{a}' = \begin{pmatrix} x \\ y \\ z \end{pmatrix} = B_{de} \begin{pmatrix} -\cos\theta \sin\theta \\ \cos^2\theta \\ 0 \end{pmatrix}, \qquad \vec{b}'_0 = \begin{pmatrix} x \\ y \\ z \end{pmatrix} = B_{de} \begin{pmatrix} 0 \\ 1 \\ 0 \end{pmatrix}$$

Rotating $\vec{a}'$ and $\vec{b}'_0$ an angle, α, from horizontal gives;

$$\vec{a} = \begin{pmatrix} x \\ y \\ z \end{pmatrix} = B_{de} \begin{pmatrix} -\cos\theta \sin\theta \cos\alpha \\ \cos^2\theta \cos\alpha \\ \cos\theta \sin\alpha \end{pmatrix}, \qquad \vec{b}_0 = \begin{pmatrix} x \\ y \\ z \end{pmatrix} = B_{de} \begin{pmatrix} 0 \\ \cos\alpha \\ \sin\alpha \end{pmatrix}$$

The coordinates of the endpoints are now given as;

$$\vec{a}_1 = \vec{a}_0 + \vec{a} = B_{de} \begin{pmatrix} -\cos\theta \sin\theta(1 - \cos\alpha) \\ 1 - \cos^2\theta(1 - \cos\alpha) \\ \cos\theta \sin\alpha \end{pmatrix}, \qquad \vec{b}_1 = \vec{b}_0 + \vec{b} = B_{de} \begin{pmatrix} 0 \\ \cos\alpha \\ \sin\alpha \end{pmatrix}$$

The distance between these endpoints is

$$u_0(\alpha, \theta, B_{de}) = B_{de}\sqrt{\left((1-\cos\alpha)^2 \sin^2\theta + (1-\cos\theta)^2 \sin^2\alpha\right)}$$

From Figure B.1 it can be found that the distance from point R to the symmetry plane in the direction of the tilted plate flap is

$$v_0 = B_{de}\left(\frac{1}{\cos\alpha} - 1\right)$$

This page is intentionally left blank

Appendix C

Summary of Calculation Routines

The present chapter presents a summary of calculation routines for analysis of grounding of a ship on a conical rock with a rounded tip. Previously derived formulas [114], were implemented in the computer program *DAMAGE* under the *Joint MIT-Industry Program on Tanker Safety*. An overview of implementation of theory and use of *DAMAGE* is given by Sinmao, Abramowicz and Wierzbicki, [115]. The present theory is implemented in a FORTRAN computer program.

The following sections list necessary equations for calculating the force from the rock to the structure given structural data and the penetration of the rock into the ship bottom. Coupled with the model for the external dynamics given in Chapter 7 this set of equations represent all necessary expressions for calculating the grounding response of the considered ship-rock configuration.

C.1 Input Parameters

Input to the problem is conveniently separated into four categories;

1. Structure
2. Rock Geometry
3. Global Ship Parameters
4. Ship-Rock Interaction

Structure The structure is defined by the geometry and the material of inner and outer bottom plating and all connected stiffeners. The level of detail is limited to principal dimensions of primary and secondary structure.

Rock. The rock is defined by the type and the geometry. A conical rock with a rounded tip is defined by the cone semi-apex angle, φ, and the tip radius, R_R.

Global Ship Parameters. Corresponding to the simple model for the external dynamics, the necessary global ship parameters are: mass M_{XX}, length between perpendiculars L_{pp}, beam B, longitudinal centre of floatation, LCF, water line area A_w, longitudinal metacentric height GM_L and transverse metacentric height GM_T.

C.2 Internal Mechanics for a Single Bottom deformed by a Conical Rock

The following sections summarize how the horizontal and vertical forces from the rock are calculated given the penetration, δ_{out} into the outer hull. All formulas for the structural resistance are expressed in terms of the plate split angle, θ. The used value of θ is the one that minimizes the total resistance of the structure.

The basic idea is to find the extent of deformation and add the resistance of all structural components within the zone of deformation.

C.2.1 Nomenclature

B_{de}	Width of deformation,
D_{DB}	Spacing between inner and outer bottom,
d_f	Width of flange,
D_w	Height of a web, for example of a longitudinal,
E	Young's modulus,
F_H	Horizontal resistance force,
F_P	Plastic resistance force,
F_V	Vertical reaction force,
g	friction factor,
M_0	Fully plastic bending moment of plate, $2/\sqrt{3}\sigma_0 t^2/4$,
n	Material strain hardening. Often $\varepsilon_{cr} = n$,
N_0	Fully plastic membrane force of plate, $2/\sqrt{3}\sigma_0 t$,
k	Vertical to horizontal force ratio,
R_c	Ductile fracture toughness of material,

s_l	Distance from rock tip to a longitudinal,
t_f	Thickness of flange,
t_t	Thickness of a transverse member,
t_w	Thickness of a web,
R_R	Radius of rock tip,
χ_l	Longitudinal extent of deformation for a longitudinal,
δ	Penetration of rock into ship bottom,
δ_R	Penetration of rock into ship bottom,
$\delta_{R,out}$	Penetration of rock into outer ship bottom,
$\delta_{R,inn}$	Penetration of rock into inner ship bottom,
δ_{frac}	Penetration to fracture,
φ	Semi-apex angle of rock cone,
ψ_C	Wrapping (contact) angle for plate on rock tip,
σ_y	Yield strengt of material,
σ_0	Flow stress of material,
ε_{cr}	Critical strain to rupture,
$\chi_{l,av}$	Average longitudinal extent of deformation for a longitudinal,

C.2.2 Basic Geometric Parameters

The penetration into the outer bottom is $\delta = \delta_{out}$. The half width of the rock in the base of the undeformed bottom plating is

$$B_{out} = \begin{cases} \sqrt{R_R^2 - (\delta_{out} - R_R)^2} & \text{for } \delta_{out} < R_R(1 - \sin\varphi) \\ \tan\varphi\,(\delta_{out} + R_R(1/\sin\varphi - 1)) & \text{for } \delta_{out} \geq R_R(1 - \sin\varphi) \end{cases} \tag{C.1}$$

C.2.3 Penetration to Fracture and Lateral Extent of Damage

If the rock is sufficiently blunt, the plating will never fracture. The critical cone semi-apex angle is $\varphi_c = \sin^{-1}(e^{-n})$ so if $\varphi < \sin^{-1}(e^{-n})$ the plating will fracture at a certain penetration, δ_{frac}.

The following equations are for $\varphi < \sin^{-1}(e^{-n})$. A critical transverse position, $s_{l,c}$ for a longitudinal is calculated as

$$s_{l,c} = R_R\sqrt{1 - e^{-2n}} \tag{C.2}$$

Before fracture, the deformation will extend to the first longitudinal stiffener outside - i.e. further away from the rock tip than - $s_{l,c}$. The distance to this stiffener is denoted $s_{l,f}$. I.e. before fracture the width of deformation is $B_{de,out} = s_{l,f}$.

The penetration to fracture is

$$\delta_{frac} = R_R \left\{ 1 - \cos\psi_C + \sin^2\psi_C \ln\left[\frac{s_{l,f}/R_R + \sqrt{(s_{l,f}/R_R)^2 - \sin^4\psi_C}}{\sin\psi_C\,(1+\cos\psi_C)} \right] \right\} \tag{C.3}$$

where $\psi_C = \cos^{-1}(e^{-n})$. The width of the deformation is

$$B_{de} = B_{de,out} = \begin{cases} s_{l,f} & \text{for } \delta_{out} < \delta_{frac} \\ B_{out} & \text{for } \delta_{out} \geq \delta_{frac} \end{cases} \tag{C.4}$$

C.2.4 Friction factor g, and Force Ratio k

g and k for Intact Shell Plating

The wrapping angle, ψ_C is calculated by solving the equation

$$\delta = R_R \left\{ 1 - \cos\psi_C + \sin^2\psi_C \ln\left[\frac{B_{de}/R_R + \sqrt{(B_{de}/R_R)^2 - \sin^4\psi_C}}{\sin\psi_C\,(1+\cos\psi_C)} \right] \right\} \tag{C.5}$$

Since the model is only considered after full plastification, it is only valid after a certain penetration. The wrapping, ψ_C therefore has a finite minimum value and it should not be taken less than $\psi_{C,min} = \sqrt{2\sigma_y/E}$.

The friction factor and force ratio are calculated as

$$g = \frac{F_H}{F_P} = \left(1 - \frac{\mu}{\sin(\psi_C/2) + \mu\,\cos(\psi_C/2)} \right)^{-1} \tag{C.6}$$

$$k = \frac{F_V}{F_H} = \frac{1 - \mu\tan(\psi_C/2)}{\tan(\psi_C/2) + \mu} \tag{C.7}$$

g and k for Fractured Shell Plating

$$g = \frac{F_H}{F_P} = \left(1 - \frac{\mu}{\cos\varphi\sin\theta + \mu\cos\theta\cos(\theta/2)} \right)^{-1} \tag{C.8}$$

$$k = \frac{F_V}{F_H} = \frac{\sin\varphi - \mu\,\sin(\theta/2)\,\cos\varphi}{\cos\varphi\,\sin\theta + \mu\,\cos\theta\,\cos(\theta/2)} \tag{C.9}$$

C.2.5 Resistance of Plating

Intact Plating

$$F_P = 2\,N_0\,v_0\,\left\{\sqrt{1+\frac{1}{4}\,\tan^2\theta}+\frac{1}{2}\,\left(\frac{u_0}{v_0}+\tan\theta\right)\right\} \tag{C.10}$$

$$u_0 = s_{l,f}\,\sqrt{(1-\cos\alpha)^2\sin^2\theta+(1-\cos\theta)^2\sin^2\alpha} \tag{C.11}$$

$$v_0 = s_{l,f}\,(1/\cos\alpha-1) \tag{C.12}$$

where $\alpha = \tan^{-1}(\delta_{out}/s_{l,f})$.

The horizontal resistance of the plating can now be calculated as $F_H = g\,F_P$ and the vertical reaction is calculated as $F_V = k\,F_H = g\,k\,F_P$ where g and k are calculated from Eq. (C.6) and Eq. (C.7).

Fractured Plating

$$F_P = \begin{cases} R_c\,t+2\,M_0\,(\pi/2-\varphi) & \text{if } N_0\,u_0 < R_c\,t \\ N_0\,u_0+2\,M_0\,(\pi/2-\varphi) & \text{if } N_0\,u_0 > R_c\,t \end{cases} \tag{C.13}$$

where

$$u_0 = B_{out}\,\sqrt{(1-\sin\varphi)^2\sin^2\theta+(1-\cos\theta)^2\cos^2\varphi} \tag{C.14}$$

The horizontal resistance of the plating is calculated as $F_H = g\,F_P$ and the vertical reaction is calculated as $F_V = k\,F_H = g\,k\,F_P$ where g and k are calculated from Eq. (C.8) and Eq. (C.9).

C.2.6 Resistance of Longitudinal Bulkheads

Intact Plating

$$F_P = \begin{cases} 0 & \text{for } s_l \geq s_{l,f} \\ \sigma_0\, t_l\, \delta_{out}(1 - s_l/B_{de,out})/\sqrt{3}\ \cdot & \\ \sqrt{\frac{1}{4}\left(\delta_{out}/B_{de,out}\right)^2 \sin^2\theta + (1-\cos\theta)^2} & 0 < s_l < s_{l,f} \end{cases} \tag{C.15}$$

The horizontal resistance of the plating can now be calculated as $F_H = g\, F_P$ and the vertical reaction is calculated as $F_V = k\, F_H = g\, k\, F_P$ where g and k are calculated from Eq. (C.6) and Eq. (C.7).

Fractured Plating

$$F_P = \begin{cases} 0 & \text{for } s_l \geq B_{out} \\ \sigma_0\, t_l\, (B_{out} - s_l)/\sqrt{3}\ \cdot & \\ \sqrt{(1-\sin\varphi)^2 \sin^2\theta + \cos^2\varphi(1-\cos\theta)^2} & \text{for } s_l < B_{out} \end{cases} \tag{C.16}$$

The horizontal resistance of the plating is calculated as $F_H = g\, F_P$ and the vertical reaction is calculated as $F_V = k\, F_H = g\, k\, F_P$ where g and k are calculated from Eq. (C.8) and Eq. (C.9).

C.2.7 Resistance of Longitudinal Stiffeners

Each longitudinal stiffener within the deformation zone (i.e. $s_l < B_{de}$) is considered separately and its resistance and vertical reaction is added to the total quantities. The mean longitudinal extent of deformation for the considered longitudinal is assumed to be equal to the distance between major transverse members:

$$\chi_{l,av} = \chi_t \tag{C.17}$$

Intact Plating

$$F_P = \frac{4\,\sigma_0\,\delta_R\,\left(1 - s_l/B_{de}\right)\left(t_f\,d_f^2 + D_w\,t_w^2\right)}{\delta_R^2\left(1 - s_l/B_{de}\right)^2 + \chi_{l,av}^2} \tag{C.18}$$

The total horizontal resistance of the considered longitudinal is calculated as $F_H = g\,F_P$ and the vertical reaction is calculated as $F_V = k\,F_H = g\,k\,F_P$ where g and k are calculated from Eq. (C.6) and Eq. (C.7).

Fractured Plating

$$F_P \;=\; \frac{8\,\sigma_0\,\left(B_{de} - s_l\right)\,\left(t_f\,d_f^2 + \,D_w\,t_w^2\right)\tan\left(\frac{\pi}{4} - \frac{\varphi}{2}\right)}{4(B_{de} - s_l)^2\,\tan^2\left(\frac{\pi}{4} - \frac{\varphi}{2}\right) + \chi_{l,av}^2} \tag{C.19}$$

The total horizontal resistance of the considered longitudinal is calculated as $F_H = g\,F_P$ and the vertical reaction is calculated as $F_V = k\,F_H = g\,k\,F_P$ where g and k are calculated from Eq. (C.8) and Eq. (C.9).

C.2.8 Resistance of Transverse Bulkheads, Floors or Frames

Intact Plating

$$F_P = \begin{cases} \frac{2.0\,\sigma_0\,t_t^2}{\chi_t\,B_{de}}\left(\frac{B_{de}}{t_t}\right)^{2/3}\left[\frac{\delta_{out}^3}{12H_t} + \frac{\delta_{out}^2}{4}\right] & \text{for } \delta_{out} \le D_t \\ \frac{2.0\,\sigma_0\,t_t^2}{\chi_t\,B_{de}}\left(\frac{B_{de}}{t_t}\right)^{2/3}\left[\frac{D_t^3}{12H_t} - \frac{D_t^2}{4} + \frac{D_t\delta_{out}^2}{4H_t} + \left(\frac{D_t}{2} - \frac{D_t^2}{4H_t}\right)\delta_{out}\right] & \text{for } \delta_{out} > D_t \end{cases} \tag{C.20}$$

where the optimum half folding wave length is

$$H_t = B_{de}\left(\frac{\pi}{6\sqrt{3}}\,\frac{t_t}{B_{de}}\right)^{1/3} \tag{C.21}$$

The horizontal resistance of the plating can now be calculated as $F_H = g\,F_P$ and the vertical reaction is calculated as $F_V = k\,F_H = g\,k\,F_P$ where g and k are calculated from Eq. (C.6) and Eq. (C.7).

Fractured Plating

$$F_P = \begin{cases} \left(R_C\, t_t + \frac{2\,\pi\, M_0\, B_{de}}{H_t}\right) \frac{\delta_{out}}{\chi_t} & \text{for } \delta_{out} \le D_t \\ \left(R_C\, t_t + \frac{2\,\pi\, M_0\, B_{de}}{H_t}\right) \frac{D_t}{\chi_t} & \text{for } \delta_{out} > D_t \end{cases} \tag{C.22}$$

$$H_t = B_{de} \left(\frac{\pi}{6\sqrt{3}} \frac{t_t}{B_{de}}\right)^{1/3} \tag{C.23}$$

The horizontal resistance of the plating is calculated as $F_H = g\, F_P$ and the vertical reaction is calculated as $F_V = k\, F_H = g\, k\, F_P$ where g and k are calculated from Eq. (C.8) and Eq. (C.9).

C.3 Modification from Single Bottom to Double Bottom

The following sections summarize how the horizontal and vertical forces from the inner bottom and the members attached to the inner bottom are calculated given the penetration, δ_{out} into the outer hull. All formulas for the structural resistance are expressed in terms of the plate split angle, θ. The used value of θ is the one that minimizes the total resistance of the structure.

The basic idea is to find the extent of deformation and add the resistance of all structural components within the zone of deformation.

C.3.1 Basic Geometric Parameters

The penetration into the outer bottom is $\delta = \delta_{out}$ and the penetration into the inner hull is then

$$\delta_{inn} = \begin{cases} 0 & \text{for } \delta_{out} - D_{db} \le 0 \\ \delta_{out} - D_{db} & \text{for } \delta_{out} - D_{db} > 0 \end{cases} \tag{C.24}$$

where D_{db} is the spacing between inner and outer bottom plating. The half width of the rock in the base of the undeformed inner bottom plating is then

$$B_{inn} = \begin{cases} \sqrt{R_R^2 - (\delta_{inn} - R_R)^2} & \text{for } \delta_{inn} < R_R(1 - \sin\varphi) \\ \tan\varphi\,(\delta_{inn} + R_R(1/\sin\varphi - 1)) & \text{for } \delta_{inn} \ge R_R(1 - \sin\varphi) \end{cases} \tag{C.25}$$

C.3.2 Penetration to Fracture and Lateral Extent of Damage

If the rock is sufficiently blunt, the plating will never fracture. The critical cone semi-apex angle is $\varphi_c = \sin^{-1}(e^{-n})$ so if $\varphi < \sin^{-1}(e^{-n})$ the plating will fracture at a certain penetration, $\delta_{frac,inn}$.

The following equations are for $\varphi < \sin^{-1}(e^{-n})$. A critical transverse position, $s_{l,c,inn}$ for a longitudinal is calculated as

$$s_{l,c,inn} = R_R \sqrt{1 - e^{-2n}} \tag{C.26}$$

To determine the extent of deformation before fracture find the longitudinal girders closer to the rock than B_{out}. These girders are pushed by the rock from below so the deformation for the inner bottom extends further out than these stiffeners. Then determine the transverse position of the first longitudinal stiffener outside $s_{l,c,inn}$ and outside the girders pushed by the rock from below. The position of this longitudinal stiffener is denoted $s_{l,f,inn}$. The width of the deforming zone before fracture is then $B_{de,inn} = s_{l,f,inn}$.

The penetration into the inner bottom to fracture of the inner bottom is

$$\delta_{frac,inn} = R_R \left\{ 1 - \cos\psi_C + \sin^2\psi_C \ln\left[\frac{s_{l,f,inn}/R_R + \sqrt{(s_{l,f,inn}/R_R)^2 - \sin^4\psi_C}}{\sin\psi_C\,(1+\cos\psi_C)} \right] \right\} \tag{C.27}$$

where $\psi_C = \cos^{-1}(e^{-n})$. The width of the deformation is

$$B_{de,inn} = \begin{cases} s_{l,f,inn} & \text{for } \delta_{inn} < \delta_{frac,inn} \\ B_{inn} & \text{for } \delta_{,inn} \geq \delta_{frac,inn} \end{cases} \tag{C.28}$$

C.3.3 Friction Factor g, and Force Ratio k

The state of the inner bottom plating determines the g and k factors for inner plating and stiffeners attached to only the outer bottom.

g and k for Intact Shell Plating

The wrapping angle, ψ_C is calculated by solving the equation

$$\delta = R_R \left\{ 1 - \cos\psi_C + \sin^2\psi_C \ln\left[\frac{B_{de}/R_R + \sqrt{(B_{de}/R_R)^2 - \sin^4\psi_C}}{\sin\psi_C\,(1+\cos\psi_C)} \right] \right\} \tag{C.29}$$

Since the model is only considered after full plastification, it is only valid after a certain penetration. The wrapping, ψ_C therefore has a finite minimum value and it should not be taken less than $\psi_{C,min} = \sqrt{2\sigma_y/E}$.

The friction factor and force ratio are calculated as

$$g = \left(1 - \frac{\mu}{\sin(\psi_{C,inn}/2) + \mu\,\cos(\psi_{C,inn}/2)} \right)^{-1} \tag{C.30}$$

$$k = \frac{1 - \mu\tan(\psi_{C,inn}/2)}{tan(\psi_{C,inn}/2) + \mu} \tag{C.31}$$

g and k for Fractured Shell Plating

$$g = \frac{F_H}{F_P} = \left(1 - \frac{\mu}{\cos\varphi\sin\theta + \mu\cos\theta\cos(\theta/2)} \right)^{-1} \tag{C.32}$$

$$k = \frac{F_V}{F_H} = \frac{\sin\varphi - \mu\,\sin(\theta/2)\,\cos\varphi}{\cos\varphi\,\sin\theta + \mu\,\cos\theta\,\cos(\theta/2)} \tag{C.33}$$

C.3.4 Resistance of Plating

Intact Plating

$$F_P = 2\,N_0\,v_0 \left\{ \sqrt{1 + \frac{1}{4}\,\tan^2\theta} + \frac{1}{2}\,\left(\frac{u_0}{v_0} + \tan\theta \right) \right\} \tag{C.34}$$

where

$$u_0 = s_{l,f,inn}\sqrt{(1-\cos\alpha)^2\sin^2\theta + (1-\cos\theta)^2\sin^2\alpha} \tag{C.35}$$

$$v_0 = s_{l,f,inn}\,(1/\cos\alpha - 1) \tag{C.36}$$

and $\alpha = \tan^{-1}(\delta_{inn}/s_{l,f,inn})$.

The horizontal resistance of the plating can now be calculated as $F_H = g\,F_P$ and the vertical reaction is calculated as $F_V = k\,F_H = g\,k\,F_P$ where g and k are calculated from Eq. (C.30) and Eq. (C.31).

Fractured Plating

$$F_P = \begin{cases} R_c\,t + 2\,M_0\,(\pi/2 - \varphi) & \text{if } N_0\,u_0 < R_c\,t \\ N_0\,u_0 + 2\,M_0\,(\pi/2 - \varphi) & \text{if } N_0\,u_0 > R_c\,t \end{cases} \tag{C.37}$$

$$u_0 = B_{inn}\sqrt{(1-\sin\varphi)^2\sin^2\theta + (1-\cos\theta)^2\cos^2\varphi} \tag{C.38}$$

The horizontal resistance of the plating is calculated as $F_H = g\,F_P$ and the vertical reaction is calculated as $F_V = k\,F_H = g\,k\,F_P$ where g and k are calculated from Eq. (C.32) and Eq. (C.33).

C.3.5 Resistance of Longitudinal Web Girders

The plastic resistance is

$$F_{P,l} = \frac{\sigma_0}{\sqrt{3}}\,t_l\,(u_{0,l,out} - u_{0,l,inn}) \tag{C.39}$$

where

$$u_{0,l,out} = \begin{cases} 0 & \text{for } s_l \geq B_{de,out} \\ \delta_{out}(1 - s_l/B_{de,out})\cdot \\ \sqrt{\frac{1}{4}\left(\delta_{out}/B_{de,out}\right)^2\sin^2\theta + (1-\cos\theta)^2} & \text{for } s_l < B_{de,out} \text{ and } \delta_{out} < \delta_{frac,out} \\ (B_{de,out} - s_l)\cdot \\ \sqrt{(1-\sin\varphi)^2\sin^2\theta + \cos^2\varphi(1-\cos\theta)^2} & \text{for } s_l < B_{de,out} \text{ and } \delta_{out} \geq \delta_{frac,out} \end{cases} \tag{C.40}$$

and

$$u_{0,l,inn} = \begin{cases} 0 & \text{for } s_l \geq B_{de,inn} \\ \delta_{inn}(1 - s_l/B_{de,inn})\cdot \\ \sqrt{\frac{1}{4}\left(\delta_{inn}/B_{de,inn}\right)^2\sin^2\theta + (1-\cos\theta)^2} & \text{for } s_l < B_{de,inn} \text{ and } \delta_{inn} < \delta_{frac,inn} \\ (B_{de,inn} - s_l)\cdot \\ \sqrt{(1-\sin\varphi)^2\sin^2\theta + \cos^2\varphi(1-\cos\theta)^2} & \text{for } s_l < B_{de,inn} \text{ and } \delta_{inn} \geq \delta_{frac,inn} \end{cases} \tag{C.41}$$

If $\delta_{out} < \delta_{frac,out}$, the horizontal resistance of the plating is calculated as $F_H = g\,F_P$ and the vertical reaction is calculated as $F_V = k\,F_H = g\,k\,F_P$ where g and k are calculated from Eq. (C.6) and Eq. (C.7).

If $\delta_{out} > \delta_{frac,out}$, the horizontal resistance of the plating is calculated as $F_H = g\,F_P$ and the vertical reaction is calculated as $F_V = k\,F_H = g\,k\,F_P$ where g and k are calculated from Eq. (C.8) and Eq. (C.9).

C.3.6 Resistance of Longitudinal Stiffeners

Each longitudinal stiffener within the deformation zone (i.e. $s_l < B_{de}$) is considered separately and its resistance and vertical reaction is added to the total quantities. The mean longitudinal extent of deformation for the considered longitudinal is assumed to be equal to the distance between major transverse members:

$$\chi_{l,av} = \chi_t \tag{C.42}$$

Intact Plating

$$F_P = \frac{4\,\sigma_0\,\delta_R\,\left(1 - s_l/B_{de}\right)\left(t_f\,d_f^2 + D_w\,t_w^2\right)}{\delta_R^2\left(1 - s_l/B_{de}\right)^2 + \chi_{l,av}^2} \tag{C.43}$$

The total horizontal resistance of the considered longitudinal is calculated as $F_H = g\,F_P$ and the vertical reaction is calculated as $F_V = k\,F_H = g\,k\,F_P$ where g and k are calculated from Eq. (C.30) and Eq. (C.31).

Fractured Plating

$$F_P = \frac{8\,\sigma_0\,\left(B_{de} - s_l\right)\left(t_f\,d_f^2 + D_w\,t_w^2\right)\tan\left(\frac{\pi}{4} - \frac{\varphi}{2}\right)}{4(B_{de} - s_l)^2\,\tan^2\left(\frac{\pi}{4} - \frac{\varphi}{2}\right) + \chi_{l,av}^2} \tag{C.44}$$

The total horizontal resistance of the considered longitudinal is calculated as $F_H = g\,F_P$ and the vertical reaction is calculated as $F_V = k\,F_H = g\,k\,F_P$ where g and k are calculated from Eq. (C.32) and Eq. (C.33).

Bibliography

[1] M. A. Abkowitz. Lectures on ship hydrodynamics - steering and manoeuvrability. Technical Report HY-5, Hydro- og Aerodynamisk Laboratorium, Lyngby, 1964.

[2] W. Abramowicz and T. Wierzbicki. Axial crushing of foam filled columns. *Int. J. of Mech. Sci.*, 30(3/4):263–271, 1988.

[3] Y. Akita, N. Ando, Y. Fujita, and K. Kitamura. Studies on collision-protective structures in nuclear-powered ships. *Nucl. Engng Design*, 19(365), 1972.

[4] Y. Akita and K. Kitamura. A study on collision by an elastic stem to a side structure of ships. *J. of the Society of Naval Architects of Japan*, 131:307–317, 1972.

[5] J.M. Alexander. An approximate analysis of the collapse of thin cylindrical shells under axial loading. *Quart. J. Mechanics Applied Mathematics*, 13:10–15, 1969.

[6] J. Amdahl. Mechanics of grounding - bottom damage estimations. Technical report, 22nd WEGEMT Graduate School, Technical University of Denmark, April 1995. Course on Accidental Loadings on Marine Structures.

[7] J. Amdahl and D. Kavlie. Experimental and numerical simulation of double hull stranding. *DNV-MIT Workshop on Mechanics of Ship Collision and Grounding*, 1, 1992. Edited by O. Astrup.

[8] J. Amdahl, D. Kavlie, and A. Johansen. Tanker grounding resistance. In *Proceedings of The Sixth International Symposium on Practical Design of Ships and Mobile Units, (PRADS95)*, pages 2.1072–2.1083, Seoul, Korea, 1995.

[9] ASIS. Large scale grounding tests and numerical simulation. Technical report, The Association for Structural Improvement of Shipbuilding Industry, 1994.

[10] O. Astrup. Cutting of thick plates by a wedge. *Joint MIT-Industry Project on Tanker Safety*, 27, Jan 1994.

[11] A.G. Atkins. Scaling in combined plastic flow and fracture. *Int. J. Mech. Sci.*, 30(173), 1988.

[12] A.G. Atkins. Tearing of thin metal sheets. In T. Wierzbicki and N. Jones, editors, *Structural Failure*, pages 107–132. John Wiley & Sons, 1989.

[13] A.G. Atkins. Letter to the editor. *Int. J. Mech. Sci.*, 33(1):69 – 71, 1991.

[14] A.G. Atkins. Deformability versus fracture limit diagrams. Technical report, Department of Engineering, University of Reading, 1993.

[15] A.G. Atkins and Y.W. Mai. *Elastic and Plastic Fracture.* Ellis Horwood/John Wiley, Chichester, 1985.

[16] A.G. Atkins and Y.W. Mai. Fracture strains in sheet metalforming and specific essential work of fracture. *Engng. Fract. Mech.*, 27, 1987.

[17] J. Atmadja. Weld failures in oil tankers due to groundings - finite element approach. Technical Report 51, Joint MIT-Industry Program on Tanker Safety, August 1995.

[18] Y. Bai et al. Collapse analysis of ship hulls. *Marine Structures*, 6:485–507, 1993.

[19] J. Bay, S. Spangenberg, N.H. Olsen, and P. Terndrup Pedersen. Ship simulation as an integrated part of the design process for bridges crossing waterways. *Permanent Int. Ass. of Navigation Congress, Bulletin 72*, 1991.

[20] M.A. Biot. Theory of three-dimensional consolidation. *J. of Applied Physics*, 12:155 – 164, 1941.

[21] M.A. Biot. Mechanics of deformation and acoustic propagation in porous media. *J. of Applied Physics*, 33:1483 – 1498, 1960.

[22] T.Z. Blazynski, editor. *Plasticity and modern metal-forming technology.* Elsevier Applied Science, 1985.

[23] J. Bond. Recent activity at harland and wolff. *Drydock*, pages 37–39, June 1996.

[24] E. Booth, E. Collier, and J. Miles. Impact scalability of plated steel structures. In N. Jones and T. Wierzbicki, editors, *Structural Crashworthiness*, pages 136–174. Butterworths Eds., 1983.

[25] A. Brown and M. Amrozowicz. Tanker environmental risk - putting pieces together. In *Int. Conference on Designs and Methodologies for Collision and Grounding Protection of Ships*, pages 15.1 – 15.13, San Francisco, 1996. SNAME, SNAJ.

[26] J.B. Caldwell. Ultimate longitudinal strength. *Trans. of the Royal Institution of Naval Architects*, 107:411–430, 1965.

[27] J.C. Card. Effectiveness of double bottoms in preventing oil outflow from tanker bottom damage incidents. *Marine Technology*, 12(1), 1975.

[28] J. Che and G. Jang. Numerical Simulation of Structural Response of Double Hull VLCC in Collision. In *Proceedings of The Sixth International Symposium on Practical Design of Ships and Mobile Units, (PRADS95)*, pages 2.1036 – 2.1047, Seoul, Korea, 1995.

[29] S. K. Choi, T. Wierzbicki, and J. Culbertson-Driscoll. Crushing strength of a web girder. *Joint MIT-Industry Project on Tanker Safety*, 23, 1994.

[30] S. K. Choi, T. Wierzbicki, Oystein Goksyr, and J. Culbertson-Driscoll. Crushing resistance of a web girder with application to ship structures. *Joint MIT-Industry Project on Tanker Safety*, 38, 1994.

[31] S.K. Choi and T. Wierzbicki. Correlation of NSWC Grounding Tests with Minorsky/Vaughan Method. Technical Report 39, Joint MIT-Industry Program on Tanker Safety, January 1995.

[32] A. Consideré. . *Ann. des Ponts et Chausées*, 9:574, 1885.

[33] National Research Counsil. Tanker spills; prevention by design. Technical report, Commitee on Tank Vessel Design National Academy Press, Washington, 1991.

[34] J. Culbertson-Driscoll. Crushing characteristics of web girders in unidirectionally stiffened double hull structures. *Joint MIT-Industry Project on Tanker Safety*, 10, 1992.

[35] J. Danckert. Flydekriterier og flydelove for anisotrope materialer. Technical Report 2, Institut for Production, AUC, 1989. In Danish.

[36] D. Dudzinski and A. Molinari. Pertubation analysis of thermoviscoplastic instabilities in bi-axial loading. *Int. J. Solids Structures*, 27:601–628, 1991.

[37] F. Engelund. On the laminar and turbulent flows of ground water through homogeneous sand. *Trans. Dan. Acad. Tech. Sc.*, 3, 1953.

[38] G. Ferron and A. Zeghloul. Strain localization and fracture in metal sheets. In Norman Jones and Tomasz Wierzbicki, editors, *Structural Crashworthiness and Failure*, pages 131–163. Elsevier Applied Science, London and New York, 1993.

[39] Y. Fujii. Integrated study on marine traffic accidents. In *IABSE Colloquium on Ship Collision with Bridges and Offshore Structures*, pages 91–98, 1983. Vol. 42.

[40] Y. Fujii and R. Shiobara. The analysis of traffic accidents. *J. of Navigation*, 24:534, 1971.

[41] Y. Fujii, H. Yamanouchi, and N. Mizuki. I- Some Factors Affecting the Frequency of Accidents in Marine Traffic. II - The Probability of Stranding. III - The Effect of Darkness on the Probability of Collision and Stranding. *J. of Navigation*, 27:235–247, 1974.

[42] Y. C. Fung. *A first course in continuum mechanics.* Prentice Hall, New Jersey, 3 edition, 1990.

[43] E.M. Goodwin and J.F. Kemp. Collision risks for fixed offshore structures. *J. of Navigation*, 33:351–356, 1980.

[44] H.E. Guldhammer and F. Miller. *Søredning, Skibsbygning, Styrkeberegning.* Bogfondens Forlag, København, 1983.

[45] A. L. Gurson. Continuum theory of ductile rupture by void nucleation and growth: Part 1 - yield criteria and flow rules for porous ductile media. *ASME, J. Eng. Materials and Technology*, 99, 1977.

[46] A.M. Hansen. *Reliability Methods for the Longitudinal Strength of Ships.* PhD thesis, Technical University of Denmark, Department of Naval Architecture and Offshore Engineering, 1995.

[47] P. Harremoes, Krebs Ovesen, and Moust Jacobsen. *Lærebog i Geoteknik*, volume 2. Polyteknisk Forlag, 4 edition, 1980.

[48] P. Harremoes, Krebs Ovesen, and Moust Jacobsen. *Lærebog i Geoteknik*, volume 1. Polyteknisk Forlag, 5 edition, 1984.

[49] R. Hill. On discontinuous states, with special reference to localized necking in thin sheets. *J. Mech. Phys. Solids*, 1:19–30, 1952.

[50] R. Hill. A theoretical perspective on in-plane forming of sheet metal. *J. Mech. Phys. Solids*, 39:295–307, 1991.

[51] J.W. Hutchinson and K.W. Neale. Sheet necking - 11. time-independent behaviour. es in bi-axial loading. In D.P. Koistinen and N.M. Wang, editors, *Mechanics of sheet-metal forming*, pages 127–153. Plenum Press, New York, 1978.

[52] N. Jones. Scaling of inelastic structures loaded dynamically. *Structural Impact and Crashworthiness*, 1:45–74, 1984. G.A.O. Davies, Ed., Elsevier Applied Science Publishers.

[53] N. Jones. *Structural Impact.* Cambridge University Press, 1989.

[54] N. Jones. Quasi-static analysis of structural impact damage. *J. Construct. Steel Research*, 33:151–177, 1995.

[55] N. Jones and W. S. Jouri. A study of plate tearing for ship collision and grounding damage. *J. Ship Res.*, 31(253), 1987.

[56] N. Jones, W.S. Jouri, and R.S. Birch. On the scaling of ship collision damage. In *3rd International Congress on Marine Technology*, pages 287–294, Athens, Greece, 1984. International Maritime Association of East Mediterranean, Phivos Publishing Co.

[57] K. Kaminishi et al. Dependence of energy-absorbing capacity on mechanical properties under penetration. *JSME International Journal*, 33(3):297 – 302, 1990.

[58] K. Kaminishi et al. Crack initiation and extension under penetration of thin metal plates. *JSME International Journal*, 35(4):475 – 481, 1992.

[59] S. Kawano et al. Energy-absorbing capacity of ductile thin metal sheet under quasi-statical penetration by a conical punch. *JSME International Journal*, 31(1):108 – 116, 1988.

[60] H Kierkegaard. Ship collisions with icebergs. *Marine Structures*, 6:359–376, 1993.

[61] J.H. Kim, I.H. Choi, and O.H. Kim. Bow collision behaviour of high-speed catamaran. *Hyundai Engineering Review*, 15(2), 1996.

[62] S. Kristiansen. Platform collision risk on the norwegian continental shelf. In *IABSE Colloquium on Ship Collision with Bridges and Offshore Structures*, pages 163–172, 1983. Vol. 42.

[63] T. Kuroiwa. Numerical simulation of actual collision and grounding accidents. In *Int. Conference on Designs and Methodologies for Collision and Grounding Protection of Ships*, pages 7.1 – 7.12, San Francisco, 1996. SNAME, SNAJ.

[64] T. Kuroiwa, Y. Kawamoto, and T. Yuhara. Study on damage of ship bottom structures due to grounding. *DNV-MIT Workshop on Mechanics of Ship Collision and Grounding*, 1, 1992. Edited by O. Astrup.

[65] Sir Horrace Lamb. *Hydrodynamics*. Cambridge, 3 edition, 1935.

[66] L. Landweber and M. Macagno. Added mass of a rigid prolate spheroid oscillating horizontally in a free surface. *J. of Ship Research*, pages 30 – 36, 1960.

[67] H. Lenselink and K.G. Thung. Numerical simulations of the dutch-japanese full scale ship collision tests. *DNV-MIT Workshop on Mechanics of Ship Collision and Grounding*, 1, 1992. Edited by O. Astrup.

[68] F.M. Lewis. The inertia of the water surrounding a vibrating ship. *Trans. SNAME*, 37:1 – 20, 1929.

[69] G. Lu and C. R. Calladine. On the cutting of a plate by a wedge. *Int. J. Mech. Sci.*, 32:295–313, 1990.

[70] G. Lu and C. R. Calladine. Author's reply. *Int. J. Mech. Sci.*, 33(1):73–74, 1991.

[71] G. Lu et al. An experimental study on tearing energy in splitting square metal tubes. *Int. J. Mech. Sci.*, 36(12):1087–1097, 1994.

[72] M. Böckenhauer and E.D. Egge. Assessment of collision resistance of ships for classification purposes. Technical report, 22nd WEGEMT Graduate School, Technical University of Denmark, April 1995. Course on Accidental Loadings on Marine Structures.

[73] J. Macduff. The probability of vessel collision. *Ocean Industry*, September 1974.

[74] N. Fl. Madsen. *Vibrations of Ships*. PhD thesis, The Technical University of Denmark, Department of Ocean Engineering, 1977. In Danish.

[75] L.E. Malvern. *Introduction to the Mechanics of a Continuum Medium*. Prentice Hall, Inc., New Jersey, 1969.

[76] Z. Marciniak and K. Kuczunski. Limit strains in the process of stretch-forming sheet metal. *Int. J. Mech. Sci.*, 9:609–620, 1967.

[77] L.M. Maxwell. Effect of rock geometry on the failure modes of plates and the forces in grounding experiments. Technical Report 15, Joint MIT-Industry Program on Tanker Safety, May 1993.

[78] F. McClintock and J. Atmadja. Hard point fracture of shell plating. Technical Report 4, Rupture Analysis of Oil Tankers in a Side Collision, MIT, September 1996.

[79] P.B. Mellor. Tensile instability in thin-walled tubes. *J. Mech. Engng. Sci.*, 4:251–256, 1962.

[80] V. U. Minorsky. An analysis of ship collisions with reference to protection of nuclear power plants. *Journal of Ship Research*, 3:1–4, 1959.

[81] M. Mizukami et al. Collision simulation of a double-hulled structure with unidirectional girder system. In *Proc. of the Sixth Int. Offshore and Polar Engineering Conference*, volume 4, pages 523 – 528, 1996.

[82] C. Muscat-Fenech. The tearing of ships plating upon grounding. Technical Report 1, Dept. of Engineering, University of Reading, 1996.

[83] C. Muscat-Fenech. The tearing of ships plating upon grounding. Technical Report 2, Dept. of Engineering, University of Reading, 1996.

[84] J.N. Newman. *Marine Hydrodynamics*. The MIT Press, Cambridge, Massachusetts, 1977.

[85] A. Nitta et al. Basis of iacs longitudinal strength standard. *Marine Structures*, 5:1–21, 1992.

[86] NMA. Report concerning safety onboard fast vessels. Technical report, Norwegian Maritime Authority, 1994. In Norwegian.

[87] P. Bettess O.C. Zienkiewicz, C.T. Chang. Drained, undrained, consolidating, and dynamic behaviour assumptions in soils, limits of validity. *Geotechnique*, 30:385 – 395, 1980.

[88] P. Terndrup Pedersen og J. Juncher Jensen. *Styrkeberegning af maritime konstruktioner*, volume 1. Den Private Ingeniørfond, 1983.

[89] P. Terndrup Pedersen og J. Juncher Jensen. *Styrkeberegning af maritime konstruktioner, Numeriske Metoder*, volume 2. Den Private Ingeniørfond, 1983.

[90] H. Ohtsubo and G. Wang. An upper-bound solution to the problem of plate tearing. *J Mar Sci technol*, 1(1), 1995.

[91] D.F. Olsen, H.H Gotfredsen, and Y. Fujii. Risk reducing effect of the great belt vts system. In *7th Int. VTS Symp.*, Vancouver, Canada, June 1992.

[92] G. Oortmerssen. The motions of a ship in shallow water. *Ocean Engng.*, pages 221–255, 1976.

[93] N.E. Ottesen Hansen, B. Cerup Simonsen, and M.J. Sterndorff. The ship impact protection of the great belt suspension bridge. *Third Symposium on Strait Crossings*, 1, 1994.

[94] N.E. Ottesen Hansen, B. Cerup Simonsen, and M.J. Sterndorff. The soil mechanics of ship beaching. In *Proceedings of the 24th International Conference on Coastal Engineering*, Kobe, Japan, 1994. Paper no. 235.

[95] J.K. Paik. Cutting of a longitudinally stiffened plate by a wedge. *J. of Ship Research*, 38(4):340–348, 1994.

[96] J.K. Paik and T.K. Lee. Cutting tests for a stiffened plate by a wedge. In *MARIENV*, Tokyo, September 1995.

[97] J.K. Paik and P.Terndrup Pedersen. Modeling of the internal mechanics in ship collisions. *Ocean Eng.*, 23(2):107–142, 1996.

[98] P. Terndrup Pedersen. *Collision and Grounding Mechanics*, pages 125–158. Danish Society of Naval Architecture, Copenhagen, May 1995.

[99] P. Terndrup Pedersen and B. Cerup Simonsen. Dynamics of ships running aground. *J. Mar. Sci. Technol.*, 1(1), 1995.

[100] P. Terndrup Pedersen, S. Valsgaard, D. Olsen, and S. Spangenberg. Ship impacts - bow collisions. *Int. J. Impact Engng.*, 13:163 – 187, 1993.

[101] M. J. Petersen. Dynamics of ship collisions. *Ocean Engineering*, 9(4):295–329, 1982.

[102] M.J. Petersen. *Ship Collisions.* PhD thesis, The Technical University of Denmark, Department of Ocean Engineering, 1980. In Danish.

[103] D. Pippenger. Coupled vertical and horizontal resistance of hull girder in grounding accidents. Technical Report 46, Joint MIT-Industry Program on Tanker Safety, May 1995.

[104] C.W. Prohaska. The vertical vibration of ships. *The Shipbuilder and Marine Engine-Builder*, Oct. 1947.

[105] J.L. Rodd. Observations on conventional and advanced double hull grounding experiments. In *Int. Conf. on Designs and Methodologies for Collision and Grounding Protection of Ships*, pages 13.1 – 13.13, San Francisco, USA, 1996.

[106] J.L. Rodd and S. MacCampbell. Double hull tanker grounding experiments. In *The Advanced (unidirectional) Double-Hull Technical Symposium*, Gaithersburg, Maryland, 1994.

[107] S.E. Rutherford and J.B. Caldwell. Ultimate longitudinal strength of ships: A case study. *Trans. of the Society of Naval Architects and Marine Engineers*, 98:441–471, 1990.

[108] S.L. Semiatin and J.J. Jonas. *Formability and Workability of Metals.* American Society for Metals, 1984.

[109] B. Cerup Simonsen. Internal Mechanics of a Stiffened Ship Bottom in a Grounding Accident: I - Theory. *Submitted to Marine Structures*, 1997.

[110] B. Cerup Simonsen. Internal Mechanics of a Stiffened Ship Bottom in a Grounding Accident: II - Validation and Application. *Submitted to Marine Structures*, 1997.

[111] B. Cerup Simonsen. Plate tearing by a cone. *Submitted for publication in Int. J. Mech. Sci.*, 1997.

[112] B. Cerup Simonsen and P. Terndrup Pedersen. Analysis of ship groundings on sand beds. In *Proceedings of The Sixth International Symposium on Practical Design of Ships and Mobile Units, (PRADS95)*, Seoul, Korea, 1995. Submitted for publication in Journal of Ship and Ocean Technology, 1997.

[113] B. Cerup Simonsen and P. Terndrup Pedersen. On grounding of fast ships. *Submitted for publication in Marine Structures*, 1997.

[114] B. Cerup Simonsen, T. Wierzbicki, and S.K. Choi. Theoretical Manual on Grounding Damage of a Hull Bottom Structure - Vol. I. Technical Report 52, Joint MIT-Industry Program on Tanker Safety, June 1995.

[115] M.V. Sinmao, W. Abramowicz, and T. Wierzbicki. User's manual and modeling guide for the program DAMAGE. Technical Report 54, Joint MIT-Industry Program on Tanker Safety, June 1995.

[116] C.S. Smith. Influence of local compressive failure on ultimate longitudinal strength of a ship's hull. In *Proc. of the International Symposium on Practical Design in Shipbuilding, PRADS*, pages 72–79, Tokyo, Japan, 1977.

[117] M.J. Sterndorff and P. Terndrup Pedersen. Grounding experiments on soft bottoms. *J. Mar. Sci. Technol.*, 1:174–181, 1996.

[118] S.G. Stiansen. Structural components, chapter 7. In R. Taggart, editor, *Ship Design and Construction*, pages 275–338. The Society of Naval Architects and Marine Engineers, 1980.

[119] S. Storen and J.R. Rice. Localized necking in thin sheets. *J. Mech. Phys. Solids*, 23:421–441, 1975.

[120] W.J. Stronge, T.X. Yu, and W. Johnson. *Energy dissipation by splitting and curling tubes*, volume 2, pages 576–587. Applied Science, London, 1983. (edited by J. Morton).

[121] W.J. Stronge, T.X. Yu, and W. Johnson. Long stroke energy dissipation in splitting tubes. *Int. J. Mech. Sci.*, 25:637–647, 1984.

[122] P. Terndrup Pedersen. Ship grounding and hull girder strength. *Marine Structures*, 7:1–29, 1994.

[123] P.F. Thomas. Application of plate cutting mechanics to damage prediction in ship grounding. *Joint MIT-Industry Project on Tanker Safety*, 8, May 1992.

[124] J.H. Thomsen. Hurtige skibes bovkollisioner. Master's thesis, Technical University of Denmark, Department of Naval Architecture and Offshore Engineering, 1996. In Danish.

[125] R. Thunes. Development of analytical models of wedge indentation into unidirectionally stiffened and orthogonally stiffened double hulls. Technical Report 21, Joint MIT-Industry Report, Tanker Safety, 1994.

[126] L.J. Tick. Differential Equations with Frequency-Dependent Coefficients. *Journal of Ship Research*, pages 45–46, Oct. 1959.

[127] S.P Timoshenko and S. Woinowsky-Krieger. *Theory of Plates and Shells*. McGraw-Hill Book Company, 1959.

[128] J. Turgeon. Analysis of hull damage without fracture in single-bottom transversally framed ships subjected to grounding. Technical Report 48, Joint MIT-Industry Program on Tanker Safety, May 1995.

[129] Y. Ueda and S.M.H. Rashed. An ultimate transverse strength analysis of ship structures. *Selected papers from J. of Soc. of Nav. Arch. of Japan*, 13:87 – 104, 1975.

[130] Pieter J. van der Weijde and Eberhart Haug. A concept of hybrid analytical-numerical method for collision and grounding simulations. *DNV-MIT Workshop on Mechanics of Ship Collision and Grounding*, 1, 1992. Edited by O. Astrup.

[131] G. van Oortmerssen. *The Motions of a Moored Ship in Waves*. Netherlands Ship Model Basin Wageningen, The Netherlands, 1976. Publication no 510.

[132] H. Vaughan. Bending and tearing of plate with application to ship bottom damage. *The Naval Architect*, 3:97–99, May 1978.

[133] H. Vaughan. The tearing of mild steel plate. *J. Ship Research*, 24(96), 1980.

[134] Det Norske Veritas. Tentative rules for classification of high speed and light craft. Technical report, DNV, 1993.

[135] T. Wierzbicki. Concertina tearing of metal plates - improved solution and comparison. *Joint MIT-Industry Project on Tanker Safety*, 22, 1994.

[136] T. Wierzbicki. Concertina tearing of metal plates. *Int. J. Solid Structures*, 19:2923–2943, 1995.

[137] T. Wierzbicki and W. Abramowicz. On the crushing mechanics of thin-walled structures. *J. Appl. Mech.*, 5, 1983.

[138] T. Wierzbicki and J. Driscoll. Crushing characteristics of a web girder. *J. of Construct. Steel Research*, 33:199 –235, 1995.

[139] T. Wierzbicki and B. Cerup Simonsen. Global structural model of bow indentation into ship side. Technical Report 2, MIT, 1996.

[140] T. Wierzbicki and P. Thomas. Closed-form solution for wedge cutting force through thin metal sheets. *Int. J. Mech. Sci.*, 35(3), 1993.

[141] G. Woisin. Comments on Vaughan: the tearing strength of mild steel plate. *J. Ship Res.*, 26(1):50–52, 1987.

[142] M. Yahiaoui, M. Bracco, P. Little, and K. Trauth. Experimental studies on scale models for grounding. Technical Report 18, Joint MIT-Industry Program on Tanker Safety, Jan 1994.

[143] T. Yao and P.I. Nikolov. Progressive collapse analysis of ship's hull under longitudinal bending. *Journal of the Society of Naval Architects of Japan*, 170:200–214, 1991.

[144] X. Yu. *Structural Analysis with large deformations until fracture and with dynamic failure*. PhD thesis, Hamburg University, 1996.

[145] Z.M. Zheng and T. Wierzbicki. A theoretical study on the steady-state wedge cutting through thin metal plates. *Int. J. of Fracture*, 78, 1996.

Ph.d. Theses
Department of Naval Architecture and Offshore Engineering, DTU

1961 **Strøm-Tejsen, J.:** "Damage Stability Calculations on the Computer DASK".

1963 **Silovic, V.:** "A Five Hole Spherical Pilot Tube for three Dimensional Wake Measurements".

1964 **Chomchuenchit, V.:** "Determination of the Weight Distribution of Ship Models".

1965 **Chislett, M.S.:** "A Planar Motion Mechanism".

1965 **Nicordhanon, P.:** "A Phase Changer in the HyA Planar Motion Mechanism and Calculation of Phase Angle".

1966 **Jensen, B.:** "Anvendelse af statistiske metoder til kontrol af forskellige eksisterende tilnærmelsesformler og udarbejdelse af nye til bestemmelse af skibes tonnage og stabilitet".

1968 **Aage, C.:** "Eksperimentel og beregningsmæssig bestemmelse af vindkræfter på skibe".

1972 **Prytz, K.:** "Datamatorienterede studier af planende bådes fremdrivningsforhold".

1977 **Hee, J.M.:** "Store sideportes indflydelse på langskibs styrke".

1977 **Madsen, N.F.:** "Vibrations in Ships".

1978 **Andersen, P.:** "Bølgeinducerede bevægelser og belastninger for skib på lægt vand".

1978 **Römeling, J.U.:** "Buling af afstivede pladepaneler".

1978 **Sørensen, H.H.:** "Sammenkobling af rotations-symmetriske og generelle tre-dimensionale konstruktioner i elementmetode-beregninger".

1980 **Fabian, O.:** "Elastic-Plastic Collapse of Long Tubes under Combined Bending and Pressure Load".

1980 **Petersen, M.J.:** "Ship Collisions".

1981 **Gong, J.:** "A Rational Approach to Automatic Design of Ship Sections".

1982 **Nielsen, K.:** "Bølgeenergimaskiner".

1984 **Rishøj Nielsen, N.J.:** "Structural Optimization of Ship Structures".

1984 **Liebst, J.:** "Torsion of Container Ships".

1985 **Gjersøe-Fog, N.:** "Mathematical Definition of Ship Hull Surfaces using B-splines".

1985 **Jensen, P.S.:** "Stationære skibsbølger".

1986 **Nedergaard, H.:** "Collapse of Offshore Platforms".

1986 **Junqui, Y.:** "3-D Analysis of Pipelines during Laying".

1987 **Holt-Madsen, A.:** "A Quadratic Theory for the Fatigue Life Estimation of Offshore Structures".

1989 **Vogt Andersen, S.:** "Numerical Treatment of the Design-Analysis Problem of Ship Propellers using Vortex Latttice Methods".

1989 **Rasmussen, J.:** "Structural Design of Sandwich Structures".

1990 **Baatrup, J.:** "Structural Analysis of Marine Structures".

1990 **Wedel-Heinen, J.:** "Vibration Analysis of Imperfect Elements in Marine Structures".

1991 **Almlund, J.:** "Life Cycle Model for Offshore Installations for Use in Prospect Evaluation".

1991 **Back-Pedersen, A.:** "Analysis of Slender Marine Structures".

1992 **Bendiksen, E.:** "Hull Girder Collapse".

1992 **Buus Petersen, J.:** "Non-Linear Strip Theories for Ship Response in Waves".

1992 **Schalck, S.:** "Ship Design Using B-spline Patches".

1993 **Kierkegaard, H.:** "Ship Collisions with Icebergs".

1994 **Pedersen, B.:** "A Free-Surface Analysis of a Two-Dimensional Moving Surface-Piercing Body".

1994 **Friis Hansen, P.:** "Reliability Analysis of a Midship Section".

1994 **Michelsen, J.:** "A Free-Form Geometric Modelling Approach with Ship Design Applications".

1995 **Melchior Hansen, A.:** "Reliability Methods for the Longitu-dinal Strength of Ships".

1995 **Branner, K.:** "Capacity and Lifetime of Foam Core Sandwich Structures".

1995 **Schack, C.:** "Skrogudvikling af hurtiggående færger med henblik på sødygtighed og lav modstand".

1997 **Cerup Simonsen, B.:** "Mechanics of Ship Grounding".

1997 **Riber, H.J.:** "Response Analysis of Dynamically Loaded Composite Panels".

DEPARTMENT OF NAVAL ARCHITECTURE AND OFFSHORE ENGINEERING
TECHNICAL UNIVERSITY OF DENMARK
UILDING E
DK YNG Y
DENMARK
HONE
TELEFA
EMAIL ish@ish.dtu.dk
NTERNET http://www.ish.dtu.dk

N 87-89502-34-5